DISCRETE ELEMENT MODELING OF THE BRITTLE-DUCTILE TRANSITION IN STRENGTH TESTS FOR QUASI-BRITTLE MATERIALS

A Thesis
Presented to
The Academic Faculty

by

Yifei Ma

In Partial Fulfillment
of the Requirements for the Degree
Doctor of Philosophy in the
School of Civil and Environmental Engineering

Georgia Institute of Technology
May 2017

DISCRETE ELEMENT MODELING OF THE BRITTLE-DUCTILE TRANSITION IN STRENGTH TESTS FOR QUASI-BRITTLE MATERIALS

Approved by:

Dr. Haiying Huang, Advisor
School of Civil and Environmental Engineering
Georgia Institute of Technology

Dr. Susan Burns
School of Civil and Environmental Engineering
Georgia Institute of Technology

Dr. David Frost
School of Civil and Environmental Engineering
Georgia Institute of Technology

Dr. Leonid Germanovich
School of Civil and Environmental Engineering
Georgia Institute of Technology

Dr. David McDowell
School of Mechanical Engineering
Georgia Institute of Technology

Date Approved: 03/28/2017

To my beloved wife,

Jiyu He

for her endless support and love.

ACKNOWLEDGEMENTS

The path to the completion of the thesis has been circuitous. I am fortunate to have had many individuals who encouraged, challenged, supported, and inspired me along the way.

I would like to thank my advisor, Dr. Haiying Huang, for her guidance and critique throughout my research and study at Georgia Institute of Technology. Her ingenious perspective and rigorous attitude towards scientific research have set up a good example for me to follow in my future career.

I also would like to express my gratitude to my thesis committee: Dr. David Frost, Dr. Susan Burns, Dr. Leonid Germanovich, and Dr. David McDowell. I sincerely appreciate their invaluable comments and suggestions, which make the thesis more decent and complete.

The completion of this research was not possible without the contributions of many other individuals. Special thanks to Dr. Qing Lin, Dr. Joseph Labuz, and Dr. Martin Schöpfer for their valuable discussion and mentorship.

Lastly, I want to express my immeasurable appreciation and deepest gratitude to my incredible wife, Jiyu He, for her unwavering support and love during my Ph.D. study. This work would never have been completed without her joyful inspiration.

Partial financial support from the National Science Foundation through grant NSF/CMMI-1055882 and the Sand Control Client Advisory Board of Schlumberger is gratefully acknowledged.

TABLE OF CONTENTS

LIST OF TABLES

LIST OF FIGURES

SUMMARY

Tensile and compressive strengths of quasi-brittle materials such as rocks and concretes are often obtained indirectly from laboratory tests, for example, the Brazilian test and three-point bending for tensile strength, and four-point bending and the scratch test for the compressive strength. Compared with the direct uniaxial tests, these tests have distinct advantages from the experimental standpoint, e.g., robustness or being non-destructive. Nevertheless, these tests are indirect since the stress states at the locations, where failure initiates and progresses, could be complex and non-uniform. Depending on the material properties and sample size, both the ductile mode, associated with crushing and decohesion of grains, and the brittle mode, associated with crack initiation and propagation, could be involved. Interpretation of the experimental results is therefore complicated by the progressive failure, manifested through the development of fracture process zones, and the existence of the dual failure modes.

Over the last two decades, discrete element method (DEM) has become an indispensable numerical tool to model the failure behaviors in quasi-brittle materials. Calibration of the material properties is a necessary step for DEM modeling of any engineering problems. Perhaps out of necessity for matching the experimental data, strength calibration in the literature is also sometime performed with the indirect test configurations, even though the direct tests are easier to interpret and to perform numerically. A long-standing well-known issue in DEM modeling with bonded spherical particles in random dense packing is that the ratio between the compressive and tensile strengths, as determined from the unconfined tests, are much lower than those of realistic values of rocks and concretes. We should then ask the questions: How are the failure mechanisms in the indirect tests affected by the low strength ratio? What are the differences in calibrating the material strengths of a particle assembly by using the indirect and direct tests?

In this study, a novel displacement-softening contact model is first proposed and implemented in the DEM code PFC2D/3D to model the failure behaviors of quasi-brittle materials. By adjusting the softening coefficient, which defines the ratio between the unloading and loading contact stiffnesses, we show that the softening model can not only yield realistic compressive over tensile strength ratios as high as about 30, but also capture the highly nonlinear failure envelope at the low confining stress range. Numerical analyses of the aforementioned four laboratory tests suggest that the softening coefficient as a proxy of the compressive over tensile strength ratio affects the brittle-ductile transition in the failure mechanisms, and that the nominal material strengths may exhibit size effect if both the ductile and brittle modes are involved in the same test. In the Brazilian test, both diametrical splitting from a center crack and the indentation-type of failure are successfully reproduced numerically. The numerical simulations suggest that if the strength ratio is low, the indentation-type of failure is more likely to occur. Depending on the failure mechanisms and the sample size, the nominal Brazilian tensile strength based on the peak load could either overestimate or underestimate the intrinsic tensile strength. If the sample fails according to the center crack splitting scenario, the nominal strength based on the crack initiation stress yields a better prediction of the tensile strength. Similar connection between the brittle-ductile failure mode transition and the size effect is also found in the three-point bending and four-point bending for shear strength tests. In the scratch test, dependence of the critical depth of cut, which governs the transition from a ductile shear failure mode to a brittle tensile fracture mode, on the strength ratio is verified. The numerical simulations confirm that the scratch test in the ductile shear failure mode could be a non-destructive alternative for measuring the uniaxial compressive strength.

CHAPTER I

INTRODUCTION

1.1 Motivations and Objectives

Tensile and compressive strengths of quasi-brittle materials such as rocks and concretes are often obtained indirectly from laboratory tests, for example, the Brazilian test and three-point bending for tensile strength and four-point bending and the scratch test for the compressive strength. Compared with the direct uniaxial tests, these tests have distinct advantages from the experimental standpoint, e.g., robustness or being non-destructive. Nevertheless, these tests are indirect since the stress states at the locations, where failure initiates and progresses, could be complex and non-uniform. Depending on the material properties and sample size, both the ductile mode, associated with crushing and decohesion of grains, and the brittle mode, associated with crack initiation and propagation, could be involved. Interpretation of the experimental results is therefore complicated by the progressive failure, manifested through the development of fracture process zones, and the existence of the dual failure modes.

It has been shown that the brittle-ductile failure mechanism transition in triaxial/uniaxial tests is governed by the confinement level. In direct tension, the sample typically fails as a result the development of mode I fracture. In uniaxial compression, a sample could be split vertically or fail due to development of shear bands, depending on the material properties as well as the sample/platen contact condition. In triaxial compression, failure in form of shear bands is generally observed. The existence of the failure mechanism transition has also been observed in a variety of loading configurations, e.g., the Brazilian test, the scratch test, and three-point bending. In the Brazilian test, experimental results suggest that the sample may fail from the center by tensile crack growth or from the loading point by emanating of micro-cracks. In three-point bending with longitudinal rebars, the brittle-ductile transition is governed by shear cracks or shear bands, depending on the span depth ratio. In

rock scratch test, both brittle failure, associated with crack propagation, and ductile failure, corresponding to grain crushing and grinding, are observed. Besides, the transitioning is related to the depth of cut.

Discrete element method (DEM) has become an indispensable numerical tool to model the failure behaviors in quasi-brittle materials. An essential prerequisite in DEM modeling is to calibrate the material properties by identifying a set of micro-scale parameters for the particles and the contact to yield desirable properties at the macro-scale. Given a quasi-brittle material governed by a single failure mechanism, it is sufficient to calibrate the compressive or tensile strength only according to the failure mechanism [61]. However, it is necessary to calibrate the strength ratio for a complex failure process governed by dual failure mechanisms, such as rock cutting and indentation. A long-standing well-known issue in DEM modeling with bonded spherical particles in random dense packing is that the ratio between the compressive and tensile strengths, as determined from the unconfined tests, are much lower than those of realistic values of rocks and concretes. We should then ask the questions: How are the failure mechanisms in the indirect tests affected by the low strength ratio? What are the differences in calibrating the material strengths of a particle assembly by using the indirect and direct tests?

In this study, a novel displacement-softening contact model is first formulated and implemented in PFC2D/3D to resolve the issue of the low strength ratio. Then we numerically investigate the failure mechanism transitions in indirect rock strength testing methods using DEM. The issues pertaining to this topic, such as brittle-ductile transition, size effect, and the relationship between the nominal and intrinsic strengths are discussed . Specifically, the following subjects are investigated.

1. A displacement-softening contact law is investigate. The dependence of the macro-scale properties and failure mechanisms on the softening coefficient β is examined.

2. The failure mechanism transition in Brazilian test and the effects of the failure mechanisms on the nominal strength and size effect are explored.

3. The failure mechanism transition from shear cracks to shear bands are investigated

by performing three-point and four-point bending tests. The effect of the loading condition and failure mechanism on the size effect is discussed.

4. The rock scratch test is modeled to investigate the variation of the cutting force signal with respect to the failure mechanism. The effect of the cutting velocity, geometry of the cutter, cutting depth, rock heterogeneity and softening coefficient β on the cutting behavior is also discussed.

1.2 Research Outline

The thesis is structured as follow:

Chapter I depicts a full picture of this research, including the motivations and objectives.

Chapter II introduces the displacement-softening model that is capable of capturing a realistic strength ratio of quasi-brittle materials while reproducing the macro-scale failure mechanism transition in triaxial/uniaxial tests. Material properties of Lac du Bonnet granite and Berea sandstone are both calibrated.

Chapter III presents a comprehensive study of the Brazilian test. The failure mechanism transition and its impact to the Brazilian tensile strength (BTS), size effect and the comparison between BTS and uniaxial tensile strength are analyzed. Implications of this numerical analysis to laboratory testing, and more importantly, to the calibration of material properties in DEM modeling in general are also discussed.

Chapter IV investigates the brittle to ductile shear transition in three-point and four-point bending tests. The effect of the failure mechanisms on the size effect is explored.

Chapter V examines the variation of the cutting force signal with respect to different failure mechanisms. The effect of the cutting velocity, cutter depth, and softening coefficient β on the failure mechanisms is elaborated. Then the method of using scratch test to probe rock heterogeneity and the sensitivity of the cutting force to rock stratification are also investigated.

Chapter VI summarizes the findings in this work and gives some suggestions to the future work.

CHAPTER II

CONTACT LAW FOR DEM MODELING OF QUASI-BRITTLE MATERIALS

2.1 Introduction

Discrete element method (DEM) has been widely used to simulate the mechanical behaviors of quasi-brittle materials, such as rocks and concretes. DEM models solid as a collection of particles and therefore allows it to capture the micro-scale failure mechanisms in such materials [31]. As a prerequisite for DEM modeling, it is essential to calibrate the micro-scale parameters against macro-scale properties. Often in literature, only the uniaxial compressive strength (UCS) is calibrated. However, it is well known that the failure mechanism of intact rock is complex under compression. At low confining stress, the failure mechanism is dominated by tensile fractures in the form of wing cracks [17, 53] while at high confining stress, shear fractures govern the strength. Extensive experimental studies of rocks [54, 66, 7, 37] suggest the existence of a strong nonlinear failure envelope when the stress state varies from confined tension to confined compression, as summarized in Figure 2.1(a). Current DEM models are still deficient in capturing the rock failure behaviors at low confining stress range. In particular, the compressive over tensile strength ratio from DEM models of a particle assembly in random dense packing is relatively low [60, 98], see Figure 2.1(b), compared with experimental values which are typically in the range from 10–30. Their corresponding failure envelopes [60, 98] are rather linear and fail to capture the strong nonlinearity of the failure envelope at low confinement. Nevertheless, rock behavior under low confining stress is critical in many engineering applications, for example, excavation induced damage and borehole breakout.

In this work, we show that the high strength ratio and the nonlinear failure envelope at low confinement can be modeled by implementing a displacement-softening contact law in DEM. Previous numerical techniques such as clustering particles [26], increasing the particle

interaction range [110] or using multiscale representation of the rock fabric [95, 34, 99] have been proposed to address the issue of low compressive over tensile strength ratio. DEM modeling with spherical particles having only short range interactions has its appeal over polygonal particles in its computational efficiency. By implementing the displacement-softening contact law, the conventional DEM framework [32] is maintained with only the particle contact law changed.

2.2 Contact Model

Numerical analysis in this work is performed using the discrete element code PFC2D/3D. The contact model is modified from the default parallel bond model option by including a softening force-displacement relationship. A parallel bond in PFC can be envisioned as a series of elastic springs distributed over the contact area between a pair of particles in contact. Schematics of the particle-particle interactions are shown in Figure 2.2. In addition to the normal and shear contact forces, bending moments can be transmitted through the contact between particles.

The default parallel bond contact model has two components and can be described by two groups of micro-scale parameters: 1) particle-particle contact (point contact): normal and shear stiffnesses, K_n and K_s ([F/L]), and friction coefficient μ; 2) the parallel bond (area contact): apparent normal and shear stiffnesses, $\bar{k}_n$ and $\bar{k}_s$ ([F/L^3]), the normal and shear bond strengths, $\bar{\sigma}_c$ and $\bar{\tau}_c$ ([F/L^2]), and the parallel bond radius multiplier $\bar{\lambda}$. The radius multiplier $\bar{\lambda}$ defines the contact area radius for the parallel-bond via $\bar{R} = \bar{\lambda}\min(R_A, R_B)$, where R_A and R_B are the radii of the two particles in contact. These two types of contact act in parallel. Since the stiffnesses for the two types of contact differ in dimensions, it is more convenient to specify apparent moduli as the input parameters instead. For example, the normal stiffnesses K_n for the point contact between particles and $\bar{k}_n$ for the parallel-bond can be determined from,

$$K_n = 2E_c(R_A + R_B) \qquad \bar{k}_n = \frac{\bar{E}_c}{R_A + R_B} \tag{1}$$

where E_c and $\bar{E}_c$ are the apparent moduli for the particle-particle contact and the parallel-bond, respectively. Assuming compression positive, the point contact model relates the

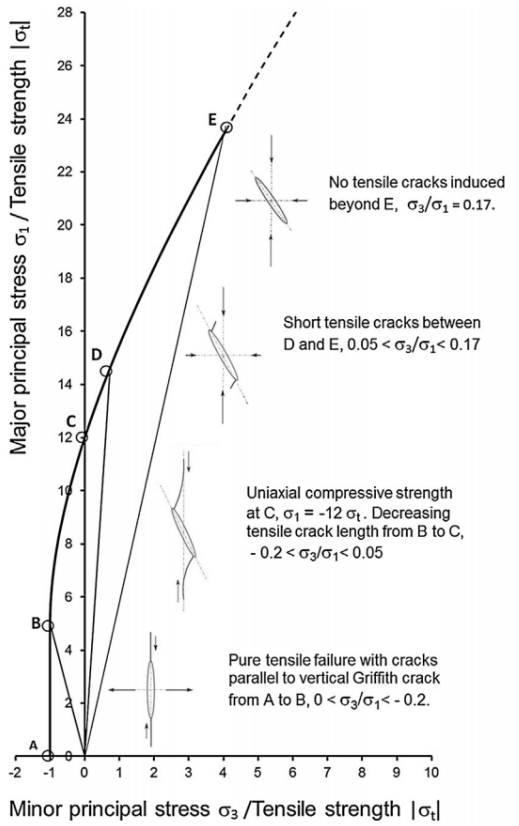

(a) Schematic of a nonlinear failure envelope and the corresponding failure mechanisms for rocks [53].

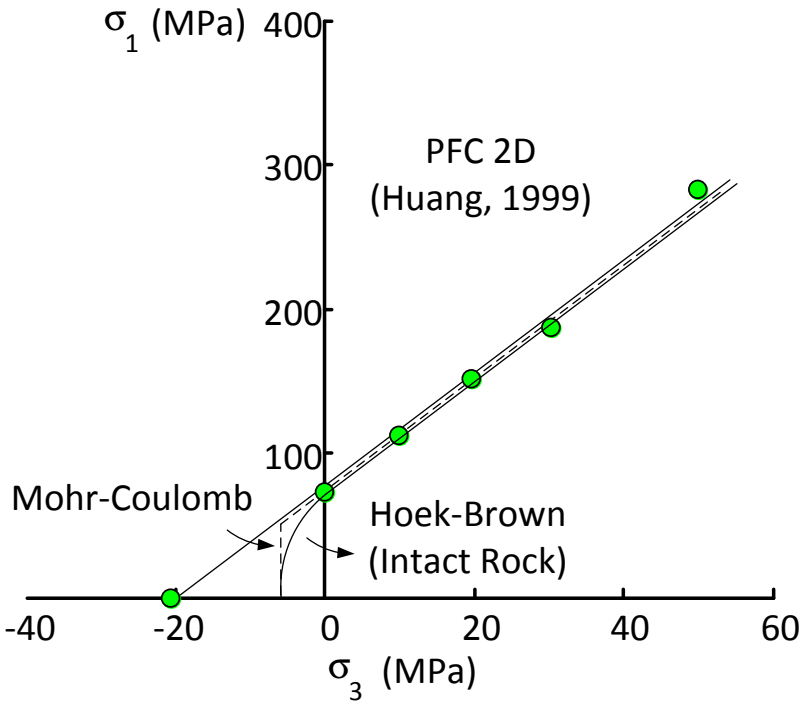

(b) Failure envelope from a DEM analysis; fitted by a Mohr-Coulomb and a Hoek-Brown criterion.

Figure 2.1: Failure envelope of quasi-brittle materials.

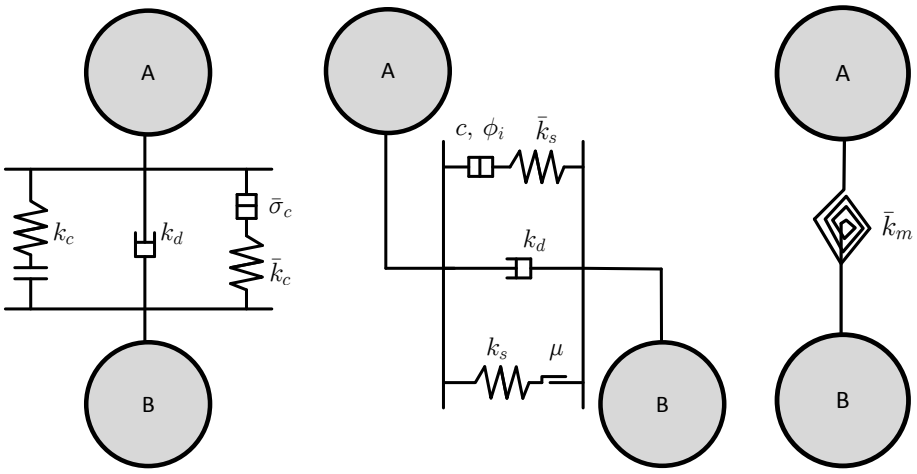

(a) normal (b) tangential (c) rotational

Figure 2.2: Schematic representation of particle interactions in the parallel bond model.

forces and displacements through,

$$F_n = -K_n \delta_n \qquad \Delta F_s = -K_s \Delta \delta_s \tag{2}$$

and follows Coulomb's law of friction,

$$|F_s| \leq \mu F_n \text{ if } \delta_n \leq 0, \qquad F_n = F_s = 0 \text{ if } \delta_n > 0 \tag{3}$$

where F_n and F_s denote the normal and shear contact forces in the point contact, respectively; δ_n is the overlap ($\delta_n > 0$ indicates a gap at the contact) and δ_s is the slip between a pair of particles.

For the area contact component, before reaching the softening condition, the contact forces, $\bar{F}_n$ and $\bar{F}_s$, and the bending moment, $\bar{M}$, follow the linear relationships with the parallel bond stretch $\bar{\delta}_n$, slip $\bar{\delta}_s$ and the angle of relative particle rotation $\bar{\theta}$,

$$\bar{F}_n = -\bar{k}_n A \bar{\delta}_n \qquad \Delta \bar{F}_s = -\bar{k}_s A \Delta \bar{\delta}_s \qquad \Delta \bar{M} = -\bar{k}_n I \Delta \bar{\theta} \tag{4}$$

where A is the cross sectional area of the parallel bond, $A = 2\bar{R}t$ (2D; $t = 1$) or $A = \pi \bar{R}^2$ (3D), and I is the moment of inertia, $I = 2\bar{R}^3 t/3$ (2D) and $I = \pi \bar{R}^4/4$ (3D).

The softening force-displacement relationship is implemented in the normal component of the contact (see Figure 2.3). Softening occurs when the normal contact force $\bar{F}_n$ in a parallel bond reaches a limit defined by the normal bond strength, i.e.,

$$\bar{F}_{n\ \max} = -\bar{\sigma}_c A \tag{5}$$

The force-displacement relationship during the softening stage can be expressed as,

$$\bar{\delta}_n = \frac{\bar{\sigma}_c}{\bar{k}_n} + \frac{\bar{\sigma}_c + \bar{F}_n/A}{\beta \bar{k}_n} \tag{6}$$

where the softening coefficient β defines the ratio between the loading and softening stiffnesses, i.e., $\beta = \bar{k}_u/\bar{k}_l$ and $\bar{k}_l = \bar{k}_n A$. The perfectly brittle case when $\beta \to \infty$ is the default parallel bond option in PFC and has often been used in DEM studies in the literature [32, 98]. The parallel bond fails if one of the criteria below is satisfied,

$$\bar{\delta}_n + \bar{R}\left|\bar{\theta}\right| \geq \bar{\delta}_c \qquad \text{or} \qquad \frac{\left|\bar{F}_s\right|}{A} \geq \bar{\tau}_c \tag{7}$$

If we use the beam theory as an analogy for the parallel bond, the normal bond failure criterion means that the bond fails if the stretch at the edge of the bond reaches the threshold value $\bar{\delta}_c$. In this model, we set,

$$\bar{\delta}_c = \bar{\delta}_2 = \frac{\bar{\delta}_c}{\bar{k}_n}\left(\frac{1+\beta}{\beta}\right) \tag{8}$$

When the parallel bond breaks, the bond stretch at a contact is,

$$\bar{\delta}_n = \bar{\delta}_* = \frac{\bar{\delta}_c}{\bar{k}_n}\left(\frac{1+\beta}{\beta}\right) - \bar{R}\left|\bar{\theta}\right| \tag{9}$$

Since the rotational contribution is included in the bond failure condition (Eq. 7), for large β, it is possible that the bond failure condition actually precludes the occurrence of softening. Both the normal and shear forces, $\bar{F}_n$ and $\bar{F}_s$, in the parallel bond reduce to zero, when the bond fails.

In this work, breakage of a parallel bond, when the failure criteria, Eq. 7, are met at a contact, is termed a micro-crack event. Note that the micro-scale failure mechanism of whether the bond fails in tension or in shear does not directly translate to a tensile or shear failure mechanism at the macro-scale [59, 62]. The micro-scale bond strengths affect the macro-scale failure behaviors via macro-scale properties such as the strength ratio σ_c/σ_t. For the sake of simplicity in formulating the contact model, we assume that the micro-scale failure mechanism is inherently tensile, which is reasonable for quasi-brittle materials such as rocks. Therefore, the softening model is only implemented in the normal direction. Only the coefficient β in addition to the normal bond strength $\bar{\sigma}_c$ and $\bar{k}_n$ is needed to describe

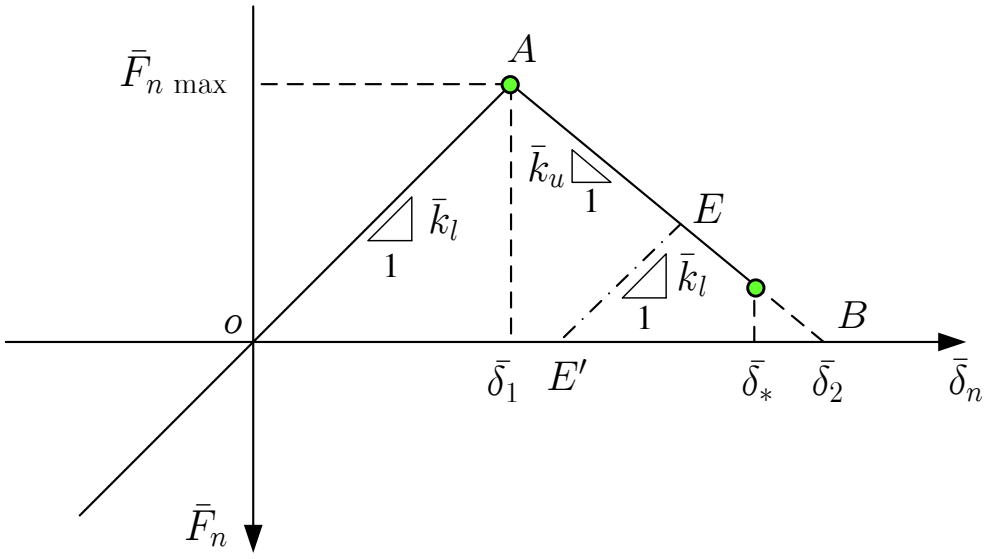

Figure 2.3: Force-displacement law.

the softening behavior. The softening law accounts for the progressive failure of the bonds and also increases the range of interaction between particles.

2.3 Effect of the Softening Coefficient

Effects of the softening coefficient β on the stress-strain behaviors, the compressive over tensile strength ratio, and the failure envelope are investigated in this section. Within the framework of PFC, the scaling laws between the micro-scale parameters and the macro-scale material properties have been studied previously for the contact bond model and parallel bond model ($\beta \to \infty$), e.g., [98, 61, 59]. One of the issues with DEM modeling using circular/spherical particles with perfectly brittle contact models is that the macro-scale strength ratio σ_c/σ_t, as determined from the peak stresses in the unconfined tests, is much lower than those of real rocks. As have shown in [61, 59], for the perfectly brittle contact bond model, when the shear over normal bond strength ratio is relatively small ($\bar{\tau}_c/\bar{\sigma}_c \lesssim 0.5$), the micro-scale failure is mostly in shear and the macro-scale strength ratio $\sigma_c/\sigma_t \sim 1$. The strength ratio σ_c/σ_t increases nearly linearly with the bond strength ratio when $0.5 \lesssim \bar{\tau}_c/\bar{\sigma}_c \lesssim 2$. When $\bar{\tau}_c/\bar{\sigma}_c \gtrsim 2$, the micro-scale failure is predominantly in tension and the strength ratio reaches more or less a constant $\bar{\tau}_c/\bar{\sigma}_c \sim 4$. The strength ratio can be viewed as a measure of material brittleness. A high strength ratio means that, in low

confining stress range, the material is more likely to fail in the form of tensile fracture at the macro-scale, while a low strength ratio means that the material is more likely to fail in shear. A realistic strength ratio is critical to quantitatively model any problems involving both shear and tensile mode of failure at the macro-scale.

Table 2.1: Baseline micro-scale parameters (2D & 3D).

Particle radii (mm)	0.8-1.66
Density ρ (kg/m^3)	2630
Point contact modulus E_c (GPa)	50
Stiffness ratio k_n/k_s	4.0
Friction coefficient μ	0.5
Parallel bond modulus $\bar{E}_c$ (GPa)	50
Bond stiffness ratio $\bar{k}_n/\bar{k}_s$	4.0
Radius multiplier $\bar{\lambda}$	1

2.3.1 Stress-strain Curves

A series of uniaxial compression and tension tests with a rectangular sample of $W \times H = 60 \times 120$ mm in 2D and a cylindrical sample of $D \times H = 40 \times 80$ mm in 3D is performed to determine the effect of the softening coefficient on material strengths. A set of baseline micro-scale parameters for the particles and contacts is listed in Table 2.1. Particles of uniform size distribution are generated randomly within the rectangular domain using a procedure similar to that in [98]. The bond strengths follow Gaussian distributions, where the standard deviations are 10% of the mean, see Table 2.2 for 2D and Table 2.3 for 3D. The mean normal bond strength for $\beta \to \infty$ is set to be $\bar{\sigma}_c = 50$ MPa. For finite β, $\bar{\sigma}_c$ is chosen such that the area of ΔoAB in Figure 2.3 remains the same,

$$\bar{\sigma}_{c,\,\beta} = \sqrt{\frac{\beta}{1+\beta}}\bar{\sigma}_{c,\,\beta\to\infty} \tag{10}$$

The area of ΔoAB can be considered a nominal measure of the energy loss due to each bond breakage. The shear bond strength in this model is set to be much larger than the normal bond strength so that at the micro-scale the bond breaks in tension only.

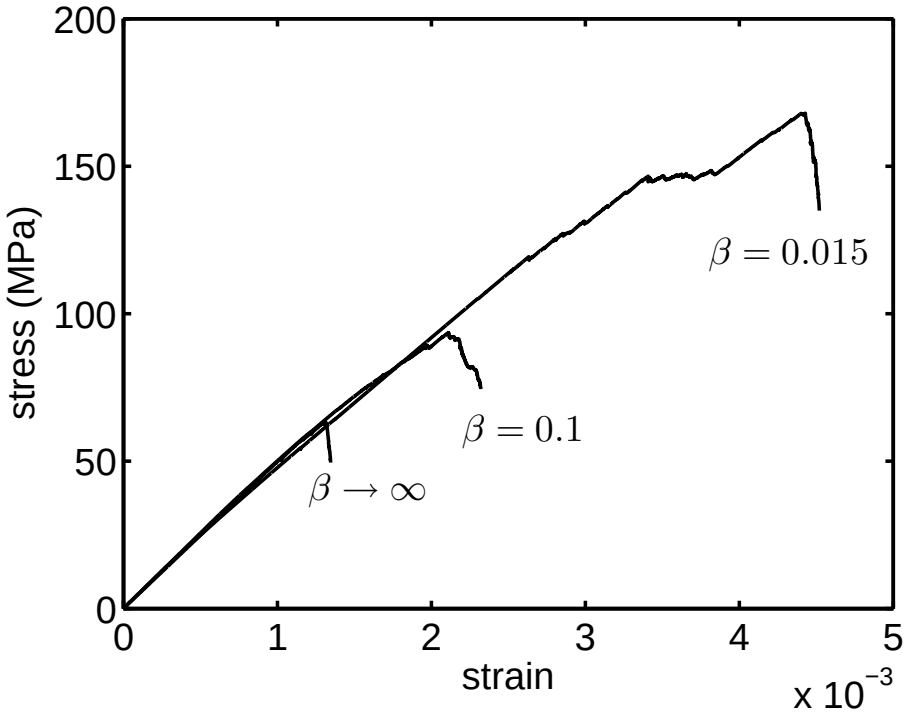

(a) uniaxial compression tests

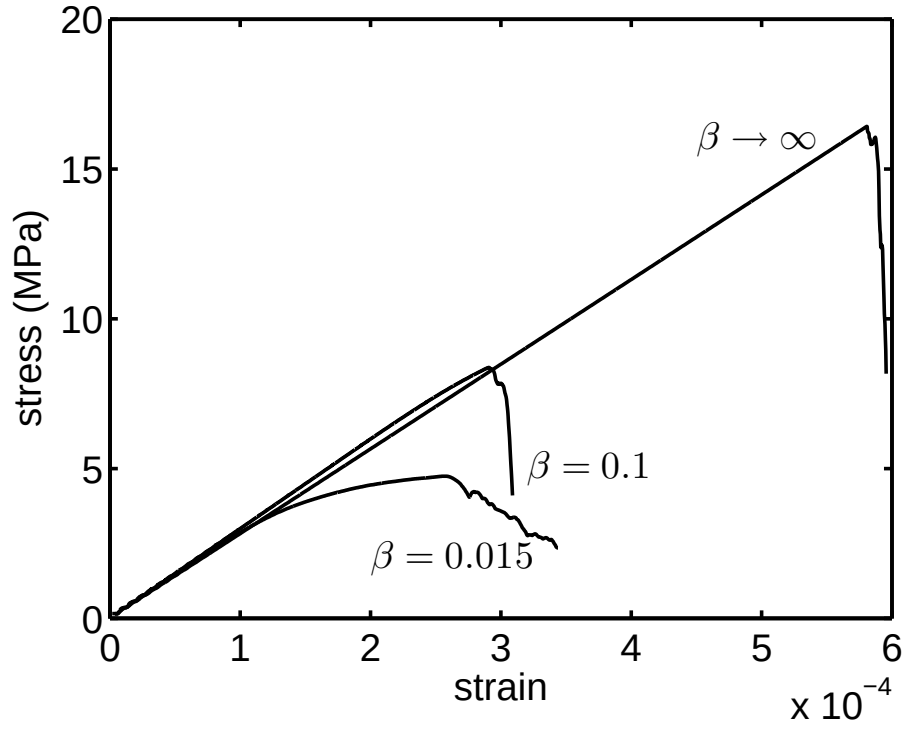

(b) direct tension tests

Figure 2.4: Stress-strain curves; sample size $W \times H = 60 \times 120$ mm (2D).

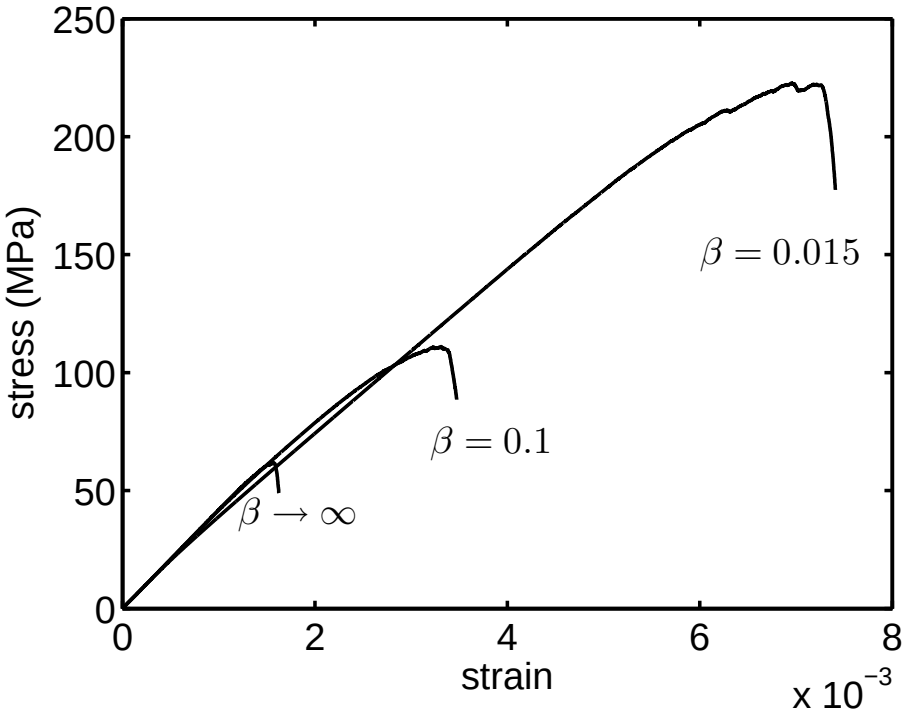

(a) uniaxial compression tests

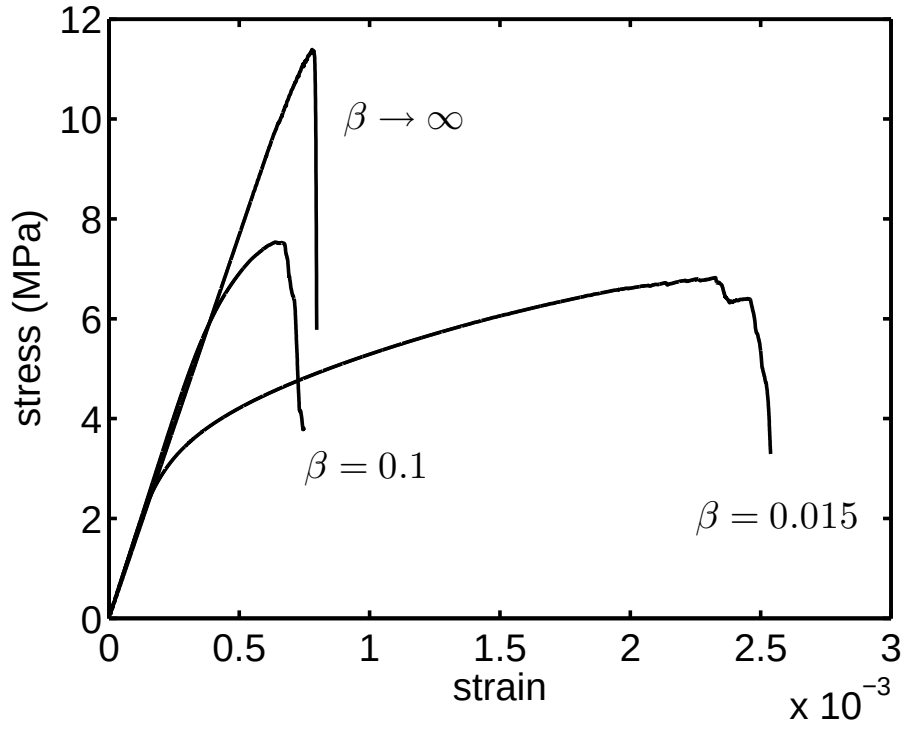

(b) direct tension tests

Figure 2.5: Stress-strain curves; sample size $D \times H = 40 \times 80$ mm (3D).

Table 2.2: Bond strengths in the contact model and macro-scale material properties (2D).

β	0.015	0.1	∞
Normal bond strength $\bar{\sigma}_c$ (MPa)	6±0.6	15±1.5	50±5
Shear bond strength $\bar{\tau}_c$ (MPa)	320±32	320±32	320±32
Elastic modulus E' (GPa)	47.40	51.18	49.56
Poisson's ratio ν'	0.31	0.29	0.29
Uniaxial compressive strength σ_c (MPa)	167.93	93.53	63.05
Uniaxial tensile strength σ_t (MPa)	4.75	8.37	16.42
Strength ratio σ_c/σ_t	35.35	11.17	3.84

Table 2.3: Bond strengths in the contact model and macro-scale material properties (3D).

β	0.015	0.1	∞
Normal bond strength $\bar{\sigma}_c$ (MPa)	6±0.6	15±1.5	50±5
Shear bond strength $\bar{\tau}_c$ (MPa)	320±32	320±32	320±32
Elastic modulus E (GPa)	41.70	40.86	42.03
Poisson's ratio ν	0.39	0.35	0.32
Uniaxial compressive strength σ_c (MPa)	222.68	111.02	61.62
Uniaxial tensile strength σ_t (MPa)	6.82	7.53	15.57
Strength ratio σ_c/σ_t	32.60	14.70	4.18

The 2D and 3D stress-strain curves for $\beta = 0.015$, 0.1 and ∞ from the unconfined tests are shown in Figures 2.4 and 2.5, respectively. The corresponding macro-scale properties are given in Tables 2.2 and 2.3. As expected, the stress-stain curves display rather brittle behaviors at $\beta \to \infty$. The stresses drop almost instantaneously once the peaks are reached. However, nonlinear behaviors in the pre-peak are observed when β decreases. As the softening coefficient β decreases, the stress-strain curves become relatively ductile. However, even at $\beta = 0.015$, the stress-strain curves are far from becoming "perfectly plastic". Indeed, as β decreases from ∞ to 0.015, the critical bond stretch at failure $\bar{\delta}_c$ increases from $0.002\bar{R}$ to $0.0165\bar{R}$ only. The stress-strain curves at low β also exhibit strain softening characteristics in post-peak stage (Figure 2.4(b)).

Since the micro-scale modulii and the stiffness ratios are the same for the three cases, the slopes of the stress-strain curves prior to the peaks are roughly the same for different β. The magnitude of the uniaxial compressive strength increases from 61.62 MPa to 222.68 MPa when β decreases from ∞ to 0.015. Meanwhile, the tensile strength decreases from 15.57

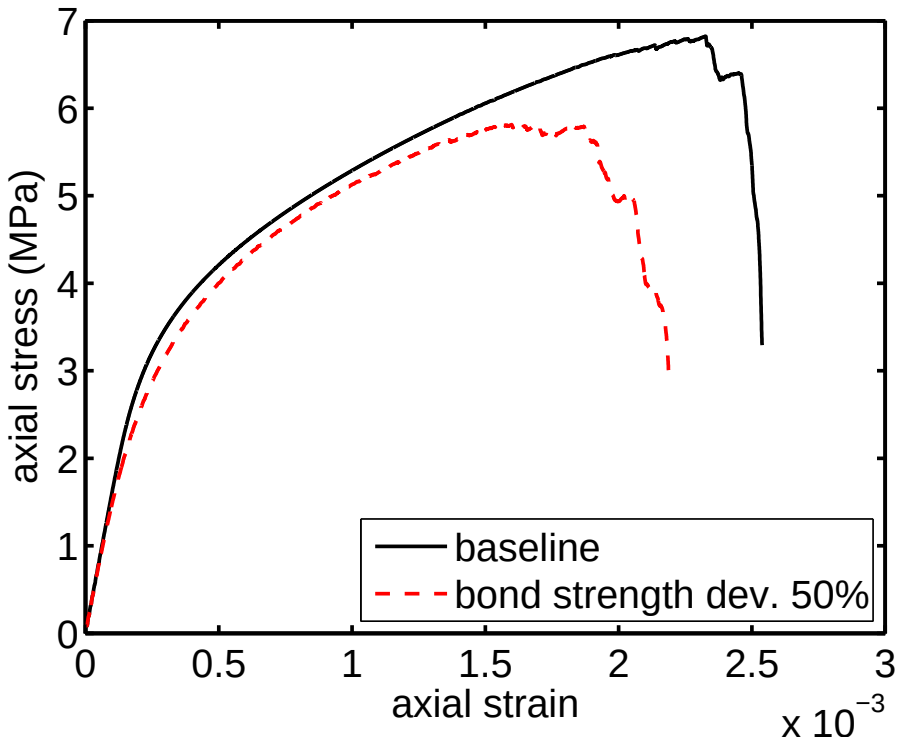

Figure 2.6: Effect of the bond strength deviation on the stress-strain curve in direct tension with $\beta = 0.015$; sample size $D \times H = 40 \times 80$ mm (3D).

MPa to 6.82 MPa. Besides, the overall shapes of the stress-strain curves are reasonable for rocks.

At $\beta = 0.015$, the nonlinear portion is rather pronounced. The stress-strain curve in 2D deviates from linear elastic behaviors at about 50% of the peak strain. This is consistent with the experimental observations from [82] where the crack initiation stress is at 40% of peak stress (45% of peak strain) of Lac du Bonnet granite. In 3D, when $\beta = 0.015$, the nonlinear behavior takes about 90% of the strain prior to the peak. Stress-strain curves from direct tension are hard to find in literature. Nevertheless, strong nonlinear behavior has been observed in materials such as Tage tuff, where the strain corresponding to the nonlinear portion is about 4 times of the strain from the linear elastic portion [89]. Indeed, the nonlinear portion can be adjusted by tuning the micro-scale contact parameters, e.g., the standard deviations of the normal bond strength. By increasing the bond strength deviation from 10% to 50%, the strain from the nonlinear portion of the curve is reduced to about 7 times of the strain from the linear portion, see Figure 2.6.

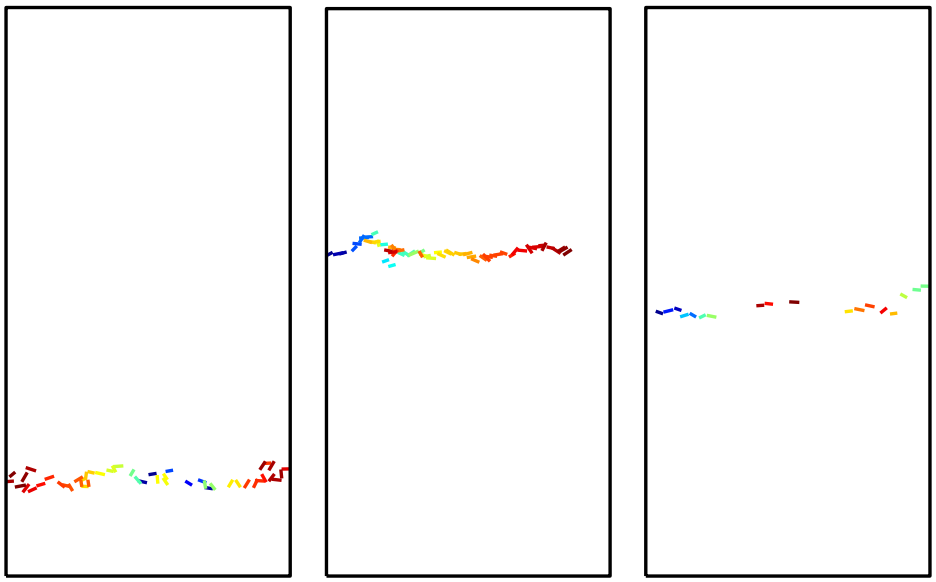

Figure 2.7: Distribution of the micro-cracks at 60% of the loading level after the peak in direct tension; sample size $W \times H = 60 \times 120$ mm.

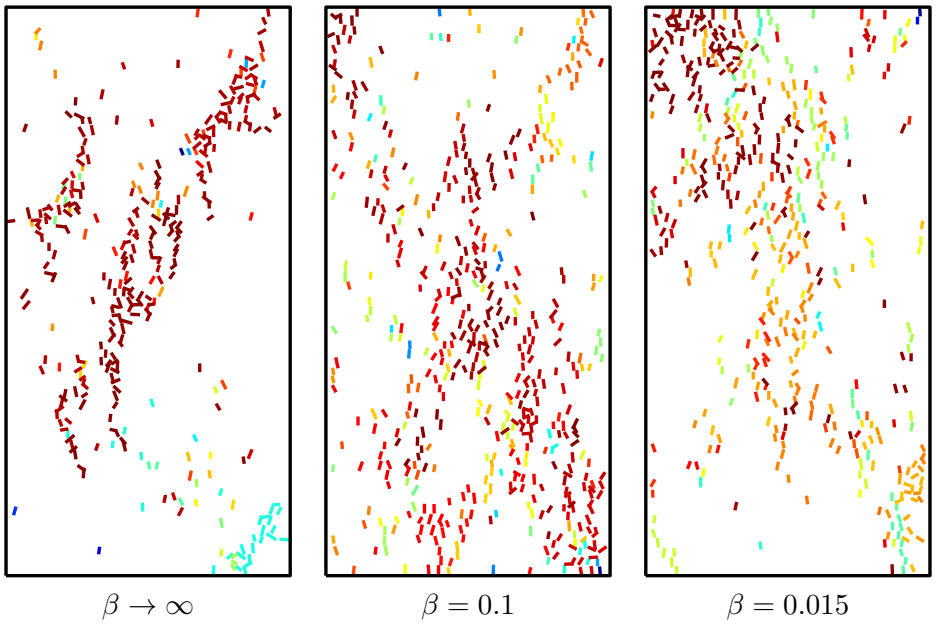

Figure 2.8: Distribution of the micro-cracks at 90% post-peak in uniaxial compression; sample size $W \times H = 60 \times 120$ mm.

In a DEM simulation, localization and coalescence of the micro-scale cracks along a plane can be interpreted as development of a macro-scale crack or a shear band, while clustering of the micro-scale cracks in the bulk can be considered equivalent to growth of a crushed or damaged zone. The particle assemblies fail as a result of localization in form of a mode-I crack in the direct tension tests and shear bands in the unconfined compression tests, respectively.

UCS and UTS exhibit different relationships with respect to β. The different trend may be attributed to the differences in the process of micro-crack evolutions. The softening coefficient β does not seem to have a significant influence on the overall failure mechanisms at the macro-scale. In the direct tension tests, the sample fails as a mode I crack grows across the whole cross-sectional area, see Figure 2.7. In uniaxial compression tests, shear bands can be clearly observed when $\beta \to \infty$ and as β decreases to 0.1 and 0.015, see Figure 2.8.

At the micro-scale, there are barely any micro-scale cracks at the peak in 2D direct tension tests, (see Figure 2.9). The number of micro-cracks is $N = 3$ when $\beta = 0.1$ or ∞, and $N = 0$ when $\beta = 0.015$. But the number of micro-cracks jumps up immediately after the peak. Since the stress field is rather uniform, the micro-cracks appear nearly simultaneously across the width, suggesting that UTS depends strongly on the mean bond strength $\bar{\sigma}_c$. Meanwhile, in the uniaxial compression tests, there is considerable accumulation of micro-cracks prior to the peak. Since the nominal energy loss for a bond failure is set to be the same for all β, the total number of micro-cracks or bond failures at the peak becomes the primary factor influencing the UCS. At the peak, the total number of micro-cracks increases from $N = 67$ at $\beta \to \infty$ to 202 and 362 at $\beta = 0.1$ and 0.015, respectively. Consequently, UCS increases from 63.05 MPa to 167.93 MPa as β decreases from ∞ to 0.015. In addition, the differences in the micro-scale failure behaviors also suggest that while the pre-peak nonlinearity in direct tension is mostly a manifestation of the softening effect, where the apparent stiffness of the whole sample is decreasing because some of the contact bonds are in softening, the nonlinearity in uniaxial compression is a combined effect of both bond breakage and bond strength softening. The overall trends in the variations of the unconfined

strengths with β in 3D are consistent with those in 2D, see Figure 2.10.

Dependence of the unconfined strengths, σ_c and σ_t, on micro-scale failure mechanisms could be further understood from analyzing the contacts in softening. For the bonds in softening, the degree of damage for each bond can be measured by using a parameter defined as,

$$\xi = \frac{\bar{\delta}_n - \bar{\delta}_1}{\bar{\delta}_2 - \bar{\delta}_1} \times 100\% \tag{11}$$

Where $\bar{\delta}_1$, $\bar{\delta}_2$ and $\bar{\delta}_n$ are shown in Figure 2.3. Based on the definition, ξ is in the range from 0 to 1. $\xi = 0$ means the bond is at the peak of the force-displacement curve between two particles, and $\xi = 100\%$ means the bond is broken. ξ is also a measure of the degree of energy release due to bond softening.

Take the example of the 2D direct tension test with $\beta = 0.015$. All micro-scale bond damages are recorded and sorted based on their respective ξ at the peak (see Figure 2.11(a)). The result suggests that most of the bonds in softening at the peak stage are only slightly damaged with $\xi < 20\%$. The total number of the damaged bonds with $\xi < 20\%$ takes nearly 95% of the total number of damaged bonds, while the number of high energy dissipation events with $\xi > 60\%$ takes less than 1%. The histogram in Figure 2.11(b) shows that most of the events are distributed in the range $\xi < 20\%$. The peak tensile strength is dominated by those events with high ξ, because the sample collapses as soon as micro-cracks appear. It therefore explains that the tensile strength is primarily related to the bond strength.

On the other hand, in the uniaxial compression tests, the distribution of the damaged bonds shows a different pattern. The percentage of damaged bonds with $\xi \simeq 5\%$ to $\xi \simeq 60\%$ is nearly constant at about 5%, see Figure 2.12(a). The histogram shows that the number of low energy dissipation events takes about 60% of total number of damaged bonds. This is consistent with the observation from experiments [82]. In the uniaxial compression tests, the fracture initiation usually happens at about 40%-50% of the peak. The sample fails only after the damaged bonds accumulate to form a shear band. Thus, the uniaxial compressive strength is significantly affected by the number of softening bonds.

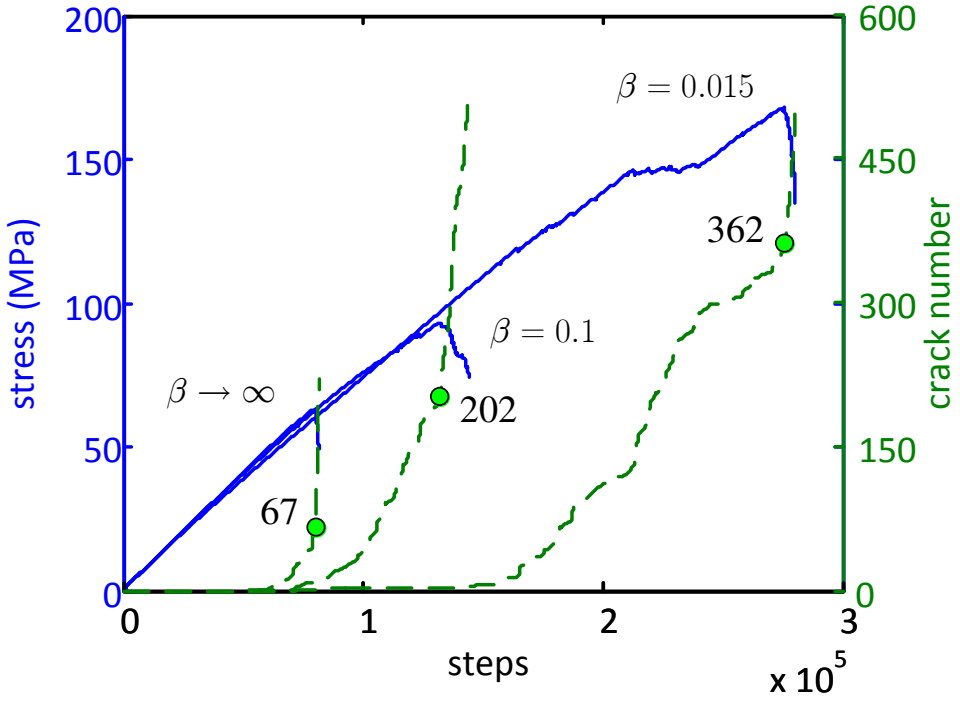

(a) uniaxial compression tests

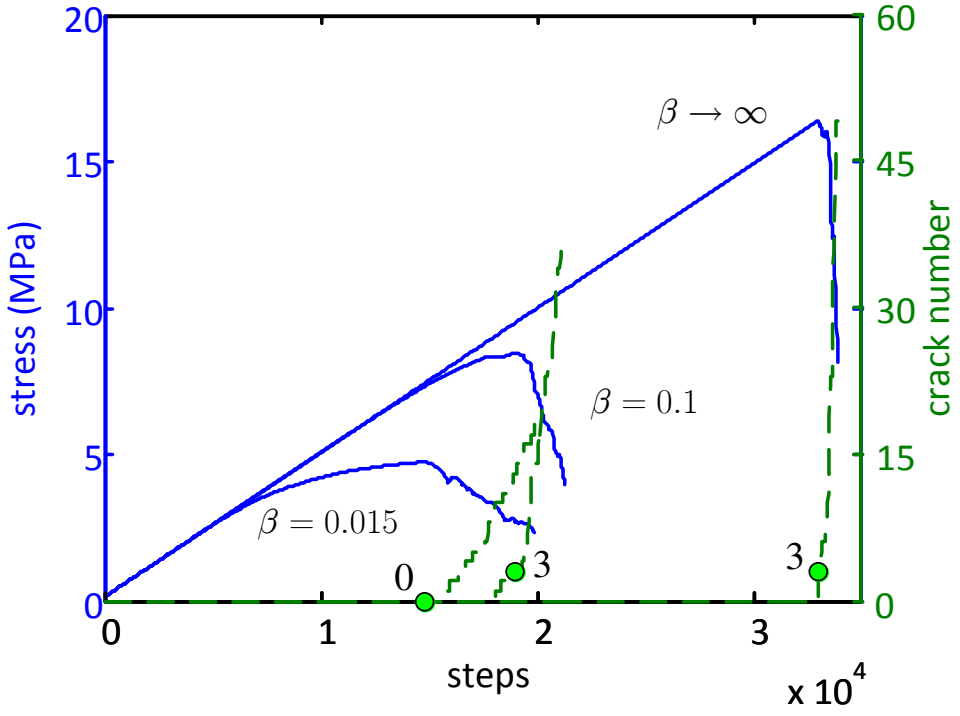

(b) direct tension tests

Figure 2.9: Histories of the loading stresses and the micro-crack numbers in 2D; sample size $W \times H = 60 \times 120$ mm.

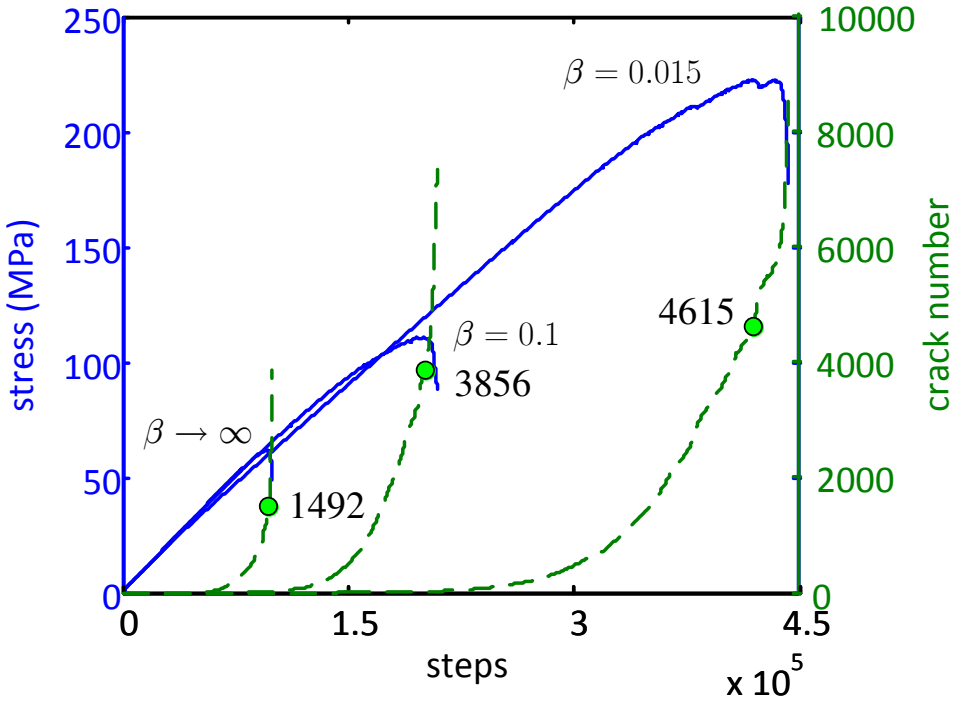

(a) uniaxial compression tests

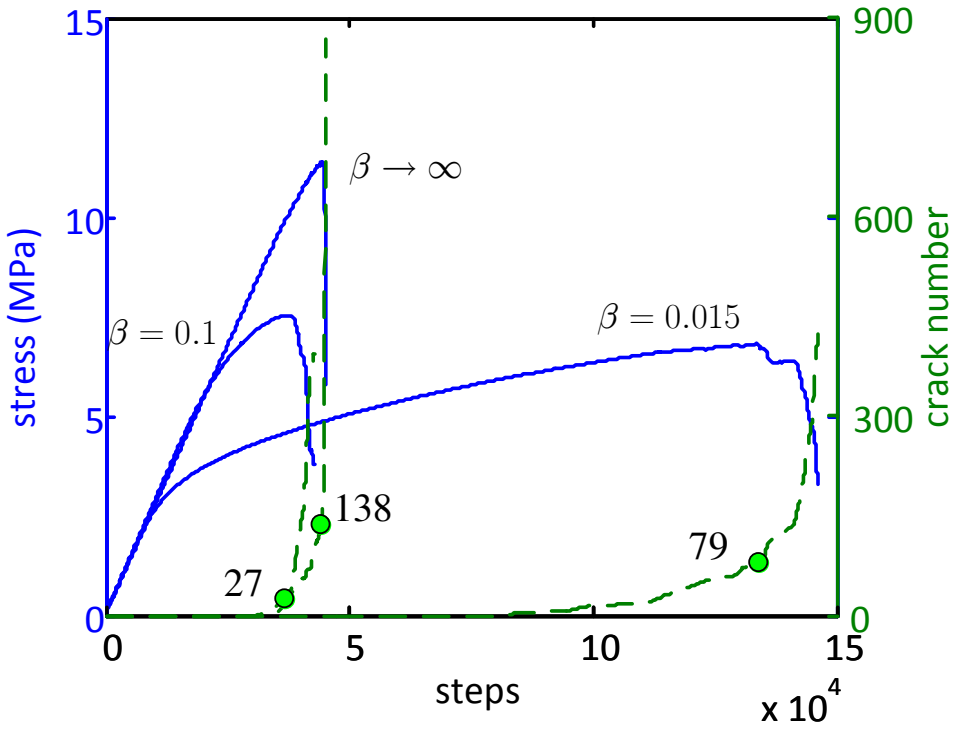

(b) direct tension tests

Figure 2.10: Histories of the loading stresses and the micro-crack numbers in 3D; sample size $W \times H = 60 \times 120$ mm.

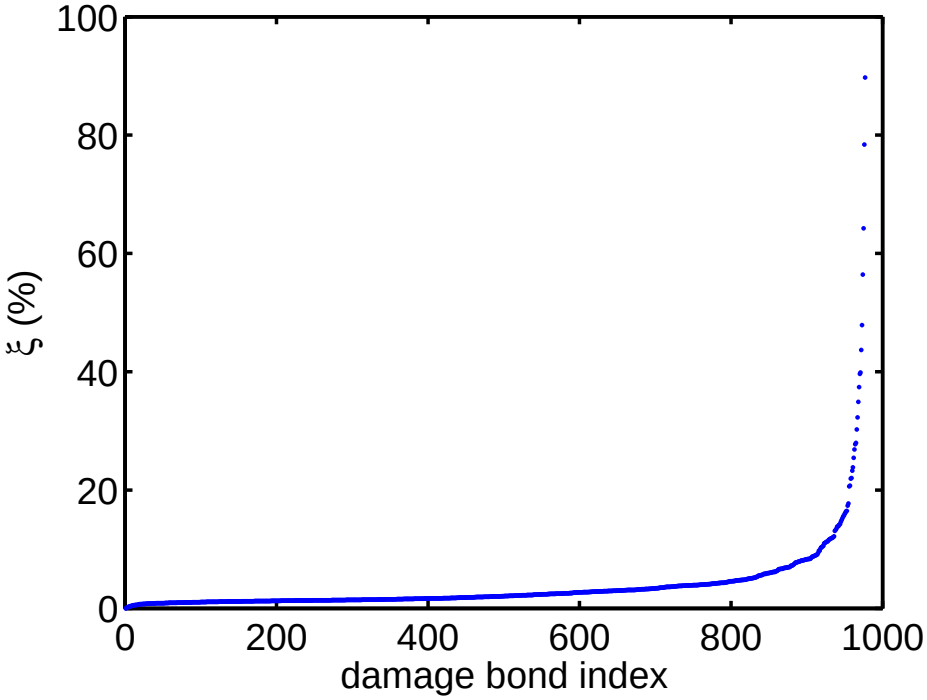

(a)

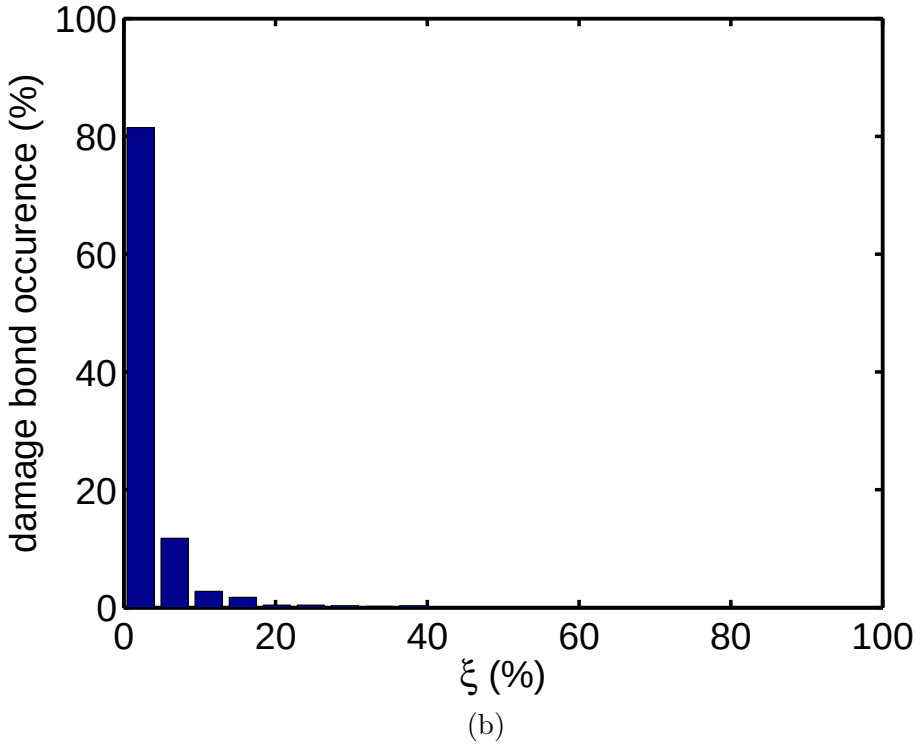

(b)

Figure 2.11: 2D direct tension test at peak, $\beta = 0.015$.

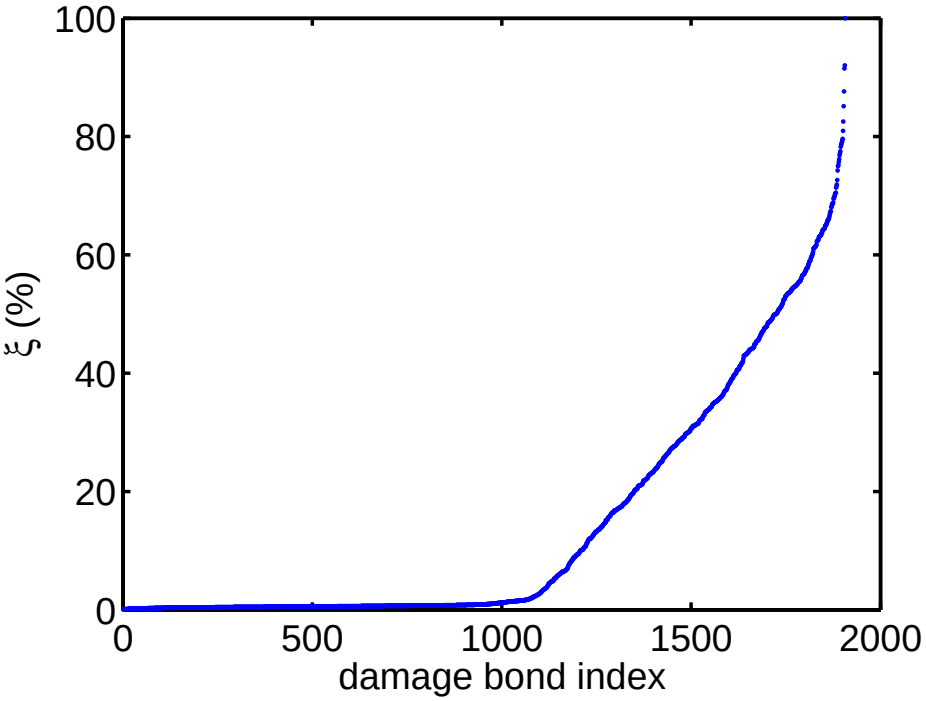

(a)

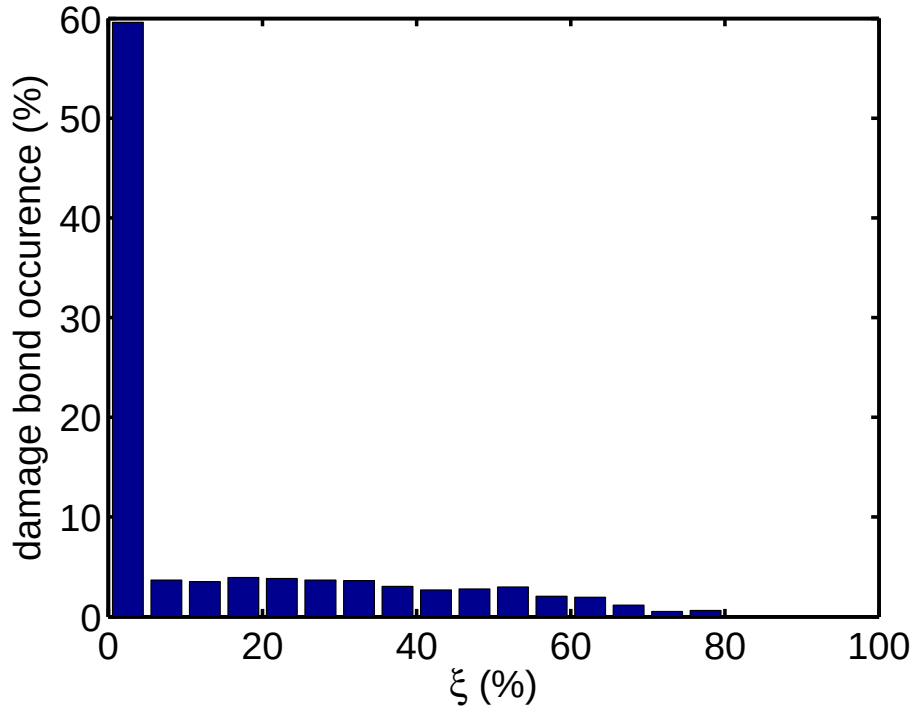

(b)

Figure 2.12: 2D uniaxial compression test at peak, $\beta = 0.015$.

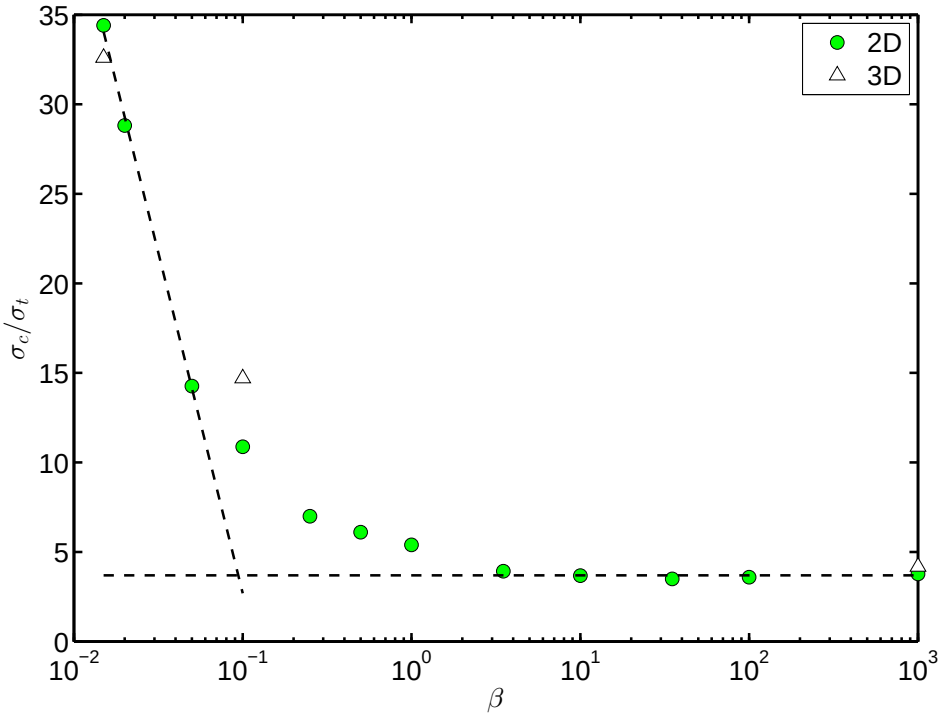

Figure 2.13: Strength ratio vs. the softening coefficient.

2.3.2 Strength Ratio

Because of the different mechanisms governing the uniaxial compressive and tensile strength, the softening coefficient β can effectively adjust the compressive to tensile strength ratio σ_c/σ_t. Variation of the strength ratio σ_c/σ_t as a function of β is shown in Figure A.4. When $\beta \geq 3.5$ in 2D, the strength ratio remains almost constant, $\sigma_c/\sigma_t \simeq 3.7$. This observation at large β agrees with [60] in that behaviors of a particle assembly are affected by the softening law only when the softening stiffness k_u is lower than a threshold value. Otherwise, the softening contact model is effectively the same as the perfectly brittle model. As β decreases further, UTS decreases, but UCS increases. The strength ratio $\sigma_c/\sigma_t = 11.17$ at $\beta = 0.1$ and $\sigma_c/\sigma_t = 14.26$ at $\beta = 0.05$, are reasonably close to many rocks. At $\beta = 0.015$, $\sigma_c/\sigma_t = 35.35$ is perhaps about the upper limit for most rocks [36]. The softening coefficient β indeed has a significant influence on the strength ratio when $\beta < 3.5$. In 3D, the correlation between strength ratio σ_c/σ_t and softening coefficient β is similar to that in 2D, $\sigma_c/\sigma_t = 14.7$ at $\beta = 0.1$.

2.3.3 Failure Envelope

Hoek *et al.* [55] introduced a nonlinear failure criterion based on experimental data for the design of excavation of hard rocks. The criterion is initially constructed for intact rocks and is subsequently modified to account for the existence of joints in rock mass. The Hoek-Brown failure criterion can be expressed as,

$$\sigma_1 = \sigma_3 + \sigma_c \left(m\frac{\sigma_3}{\sigma_c} + s \right)^{0.5} \tag{12}$$

where σ_1 and σ_3 are the major and minor principal stresses at failure; σ_c is the uniaxial compressive strength of the intact rock; and m and s are material constants, where $s = 1$ for intact rock.

A series of confined compression and tension tests are performed to obtain the failure envelope using the micro-scale parameters listed in Tables 2.1–2.3 with $\beta = 0.1$. Sample dimensions same as those in the previous section are used. In this study, we also calculate the equivalent friction angle ϕ for the Mohr-Coulomb criterion by matching the area under the failure envelopes in the range of $\sigma_3 \in [0,\ \sigma_{3,\max}]$, see details in [55].

From Figure 2.14, we can see that the nonlinear failure envelope in the confined tension stage is properly captured by the softening model. Furthermore, the strength ratio σ_c/σ_t is approximately 14 in 3D and 11 in 2D, comparable to general rocks. The simulation results are fitted by Hoek-Brown criterion (see Eq. 12), and the parameters are listed in Table 2.4. The constants m and s obtained from the 2D and 3D simulations are comparable to that for a wide range of medium to high strength rocks, e.g., gneiss [44], marble [38, 43, 65], and sandstone [91, 94, 65].

The failure mechanism transition from tensile to shear failure with respect to the ratio of σ_3/σ_1 is demonstrated in Figure 2.15. In the confined tension test with confinement $\sigma_1 = 10$ MPa, $\sigma_1/\sigma_3 < -0.2$, the failure is in a brittle mode in form of a tensile crack. All the micro-cracks are nearly perpendicular to the loading direction, suggesting a brittle failure mode. As the confinement increases to $\sigma_1 = 60$ MPa, $-0.2 < \sigma_1/\sigma_3 < 0.05$, the macro-scale

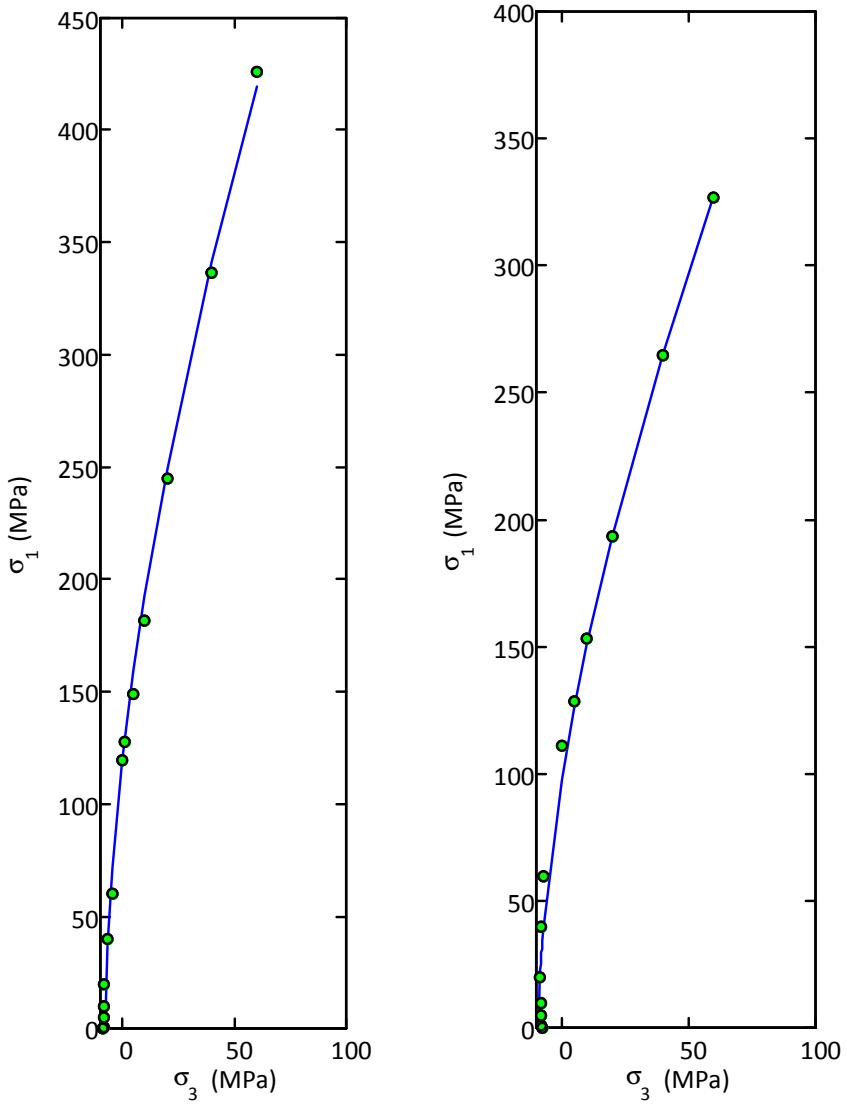

(a) 2D results (b) 3D results

Figure 2.14: Complete failure envelopes. Dots represent the simulation results, while the blue line is the regression curve based on Hoek-Brown Criterion. Fitting parameters are listed in Table 2.4.

Table 2.4: Hoek-Brown criterion parameters and fitting results.

Parameters	2D	3D
m	20.44	9.29
s	0.993	0.774
σ_c (MPa)	93.53	111.02
ϕ (degree)	42.88	37.36
σ_t (MPa)	8.42	7.53
Strength ratio σ_c/σ_t	11.11	14.74

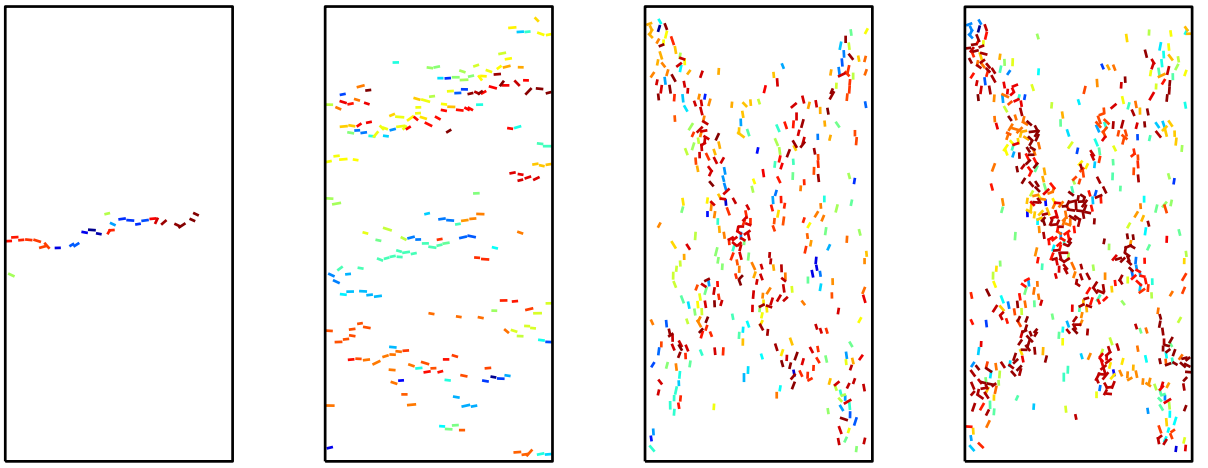

Figure 2.15: Distribution of micro-cracks at 90% of post-peak under different confinements in 2D; sample size $W \times H = 60 \times 120$ mm.

failure is still governed by tensile cracks. It is interesting to note that most of the micro-cracks are oriented along the loading direction (splitting type). However, the macro-scale tensile cracks are inclined with respect to the horizontal direction, indicating a mixed mode characteristics. In confined compression test when $\sigma_3 = 10$ MPa, $0.05 < \sigma_1/\sigma_3 < 0.17$, the localized micro-cracks can be observed along the diagonals of the sample. Meanwhile, no mode I tensile fractures can be observed under this condition. The failure of the sample is now governed by the macro-scale shear bands. When confinement increases to $\sigma_3 = 60$ MPa, the failure pattern is similar to that of $\sigma_3 = 10$ MPa. The strength of the sample is governed by the formation of the shear bands, or in other words, a ductile failure mode. This failure mechanism transition from brittle to ductile in confined compression and tension tests is corroborated by experimental results reported in [100].

2.4 Material Properties Calibration for LdB Granite and Berea Sandstone

The numerical simulation results from the previous section demonstrate that the displacement-softening contact model is able to capture the characteristics of quasi-brittle materials, e.g., uniaxial compressive to tensile strength ratio and the macro-scale failure patterns. In this section, we will apply the proposed model to simulate two different types of rocks, Lac du

Table 2.5: Material properties of Lac du Bonnet granite [83].

Elastic modulus E_c (GPa)	60 - 70
Uniaxial compressive strength σ_c (MPa)	136 - 250
Uniaxial tensile strength σ_t (MPa)	6 - 12
Strength ratio σ_c/σ_t	20 - 30

Table 2.6: Material properties of Berea sandstone [18, 39].

Elastic modulus E_c (GPa)	8 - 24
Uniaxial compressive strength σ_c (MPa)	79
Uniaxial tensile strength σ_t (MPa)	4.9 - 7.3
Strength ratio σ_c/σ_t	10 - 16

Bonnet (LdB) granite and Berea sandstone. The properties of Lac du Bonnet granite have been extensively studied as part of the Underground Research Laboratory (URL) project in Canada [101, 84]. Experimental results, including unconfined and confined tests, are well documented in [83] and the references therein. Berea sandstone is a sedimentary rock where the grains are predominantly sand-sized and are composed of quartz held together by silica. The relatively high porosity and permeability of Berea Sandstone makes it a good reservoir rock. Compared with Lac du Bonnet granite, the grains of Berea sandstone are less angular.

Material properties of LdB granite [83, 82] and Berea sandstone [18] are listed in Tables 2.5 and 2.6, respectively.

2.4.1 LdB Granite

In this section, both unconfined and confined numerical simulations are conducted with samples $W \times H = 60 \times 150$ mm in 2D and $D \times H = 40 \times 100$ mm in 3D. The aspect ratio of 2.5, instead of the typical ratio of 2, is employed to match that from the experiments in [82]. Micro-scale parameters of the numerical models for LdB granite are listed in Table 2.7. Since no attempt is made to match the similarity in grain size and shape with actual grains, the average grain size in all numerical models in this study is kept at $d \simeq 1$ mm.

As expected, the stress-strain curve is linear elastic in the pre-peak. The stress level drops nearly instantaneously once the peak is reached. Since the unconfined compressive to

Table 2.7: Calibrated micro-scale parameters for LdB granite.

	2D	3D
Softening coefficient β	0.03	0.045
Normal bond strength $\bar{\sigma}_c$ (MPa)	13±1.3	15±1.5
Shear bond strength $\bar{\tau}_c$ (MPa)	320±32	320±32
Point contact modulus E_c (GPa)	67.59	78.79
Parallel bond modulus $\bar{E}_c$ (GPa)	67.59	78.79
Elastic modulus $E_c^{'}$ (GPa)	67.52	69.08
Uniaxial compressive strength σ_c (MPa)	218.6	230.0
Uniaxial tensile strength σ_t (MPa)	9.05	11.3
Strength ratio σ_c/σ_t	24.15	20.35

Table 2.8: Hoek-Brown criterion parameters and results for LdB granite and PFC models.

Parameters	LdB granite	2D	3D
m	26.19	24.25	18.14
s	1	1	1
σ_c (MPa)	229.45	229.28	211.90
ϕ (degree)	52.16	51.41	50.83
σ_t (MPa)	8.75	9.44	11.65
Strength ratio σ_c/σ_t	26.22	24.29	18.19

tensile strength ratio of LdB granite is up to 30, the softening coefficient is calibrated to be $\beta = 0.03$. However, even β is at such a low level, the stress-strain curve, see Figure 2.16(a), still shows the the strain softening characteristics in post-peak stage. At the initial loading stage, the stress-strains curve from the experiment exhibits a relatively low modulus, caused by the initial closure of the flaws in the rock sample. No attempt is made in this study to simulate this nonlinear portion. As such, the numerical results show a nearly constant elastic modulus prior to crack initiation.

Figure 2.17 shows a comparison of the failure envelope of LdB granite and the models. Curve fitting of the experimental data with Hoek-Brown criterion shows that σ_c/σ_t for LdB granite is 26.22 with friction angle $\phi = 52.16°$. For PFC2D, the envelope shows an excellent agreement. In particular, the high strength ratio and a realistic friction angle are both captured by the softening model, i.e., $\sigma_c/\sigma_t = 24.29$ and $\phi = 51.41°$. On the other hand, the envelope obtained from PFC3D exhibits a slightly low friction angle, $\phi = 50.83°$. It is important to note that granite usually consist of angular grains, which leads to a higher

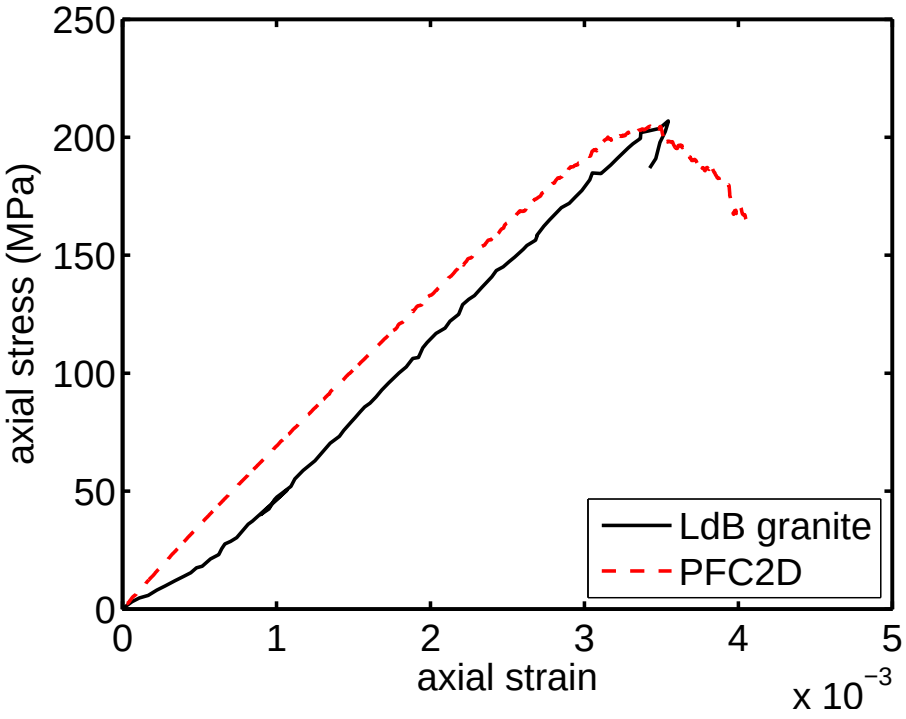

(a)

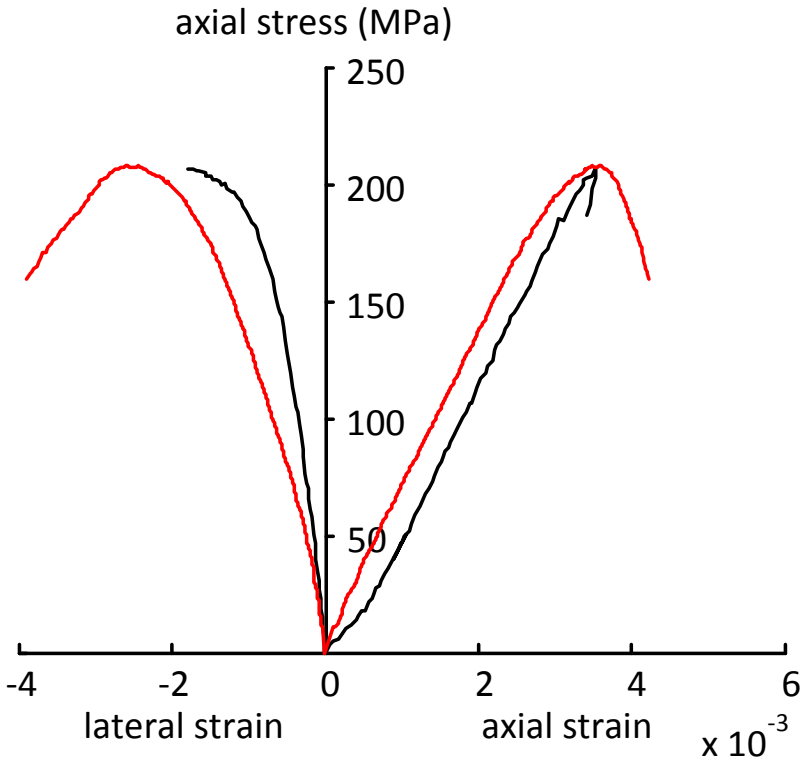

(b)

Figure 2.16: Comparison of stress-strain curves between simulations and experiments; experimental results of LdB granite are digitized from [82].

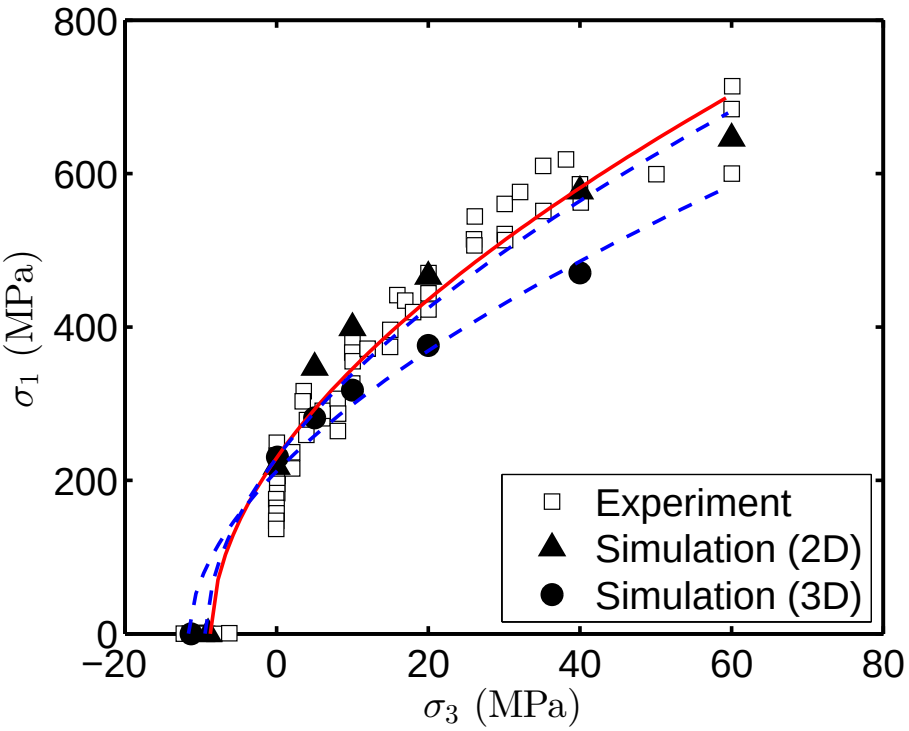

Figure 2.17: Failure envelopes of LdB granite vs. simulations. Experimental results of LdB granite is digitized from [83]; blue dashed lines and red solid line represent the regression curves of simulations and experiments based on Eq. 12, respectively; the parameters and results are summarized in Table 2.8.

friction angle ($\phi \in [45°, 65°]$) than that in rocks consisting of round grains, e.g., sandstone. Nevertheless, the unconfined compressive to tensile strength ratio from 3D simulations is still in a reasonable range compare to experimental results, i.e., $\sigma_c/\sigma_t \in [20, 30]$. Furthermore, it is expected that a higher friction angle could be obtained by the softening model coupled with some other techniques, e.g., flat-joint model [99] or rolling resistance model [1], which could introduce angularity to the grains.

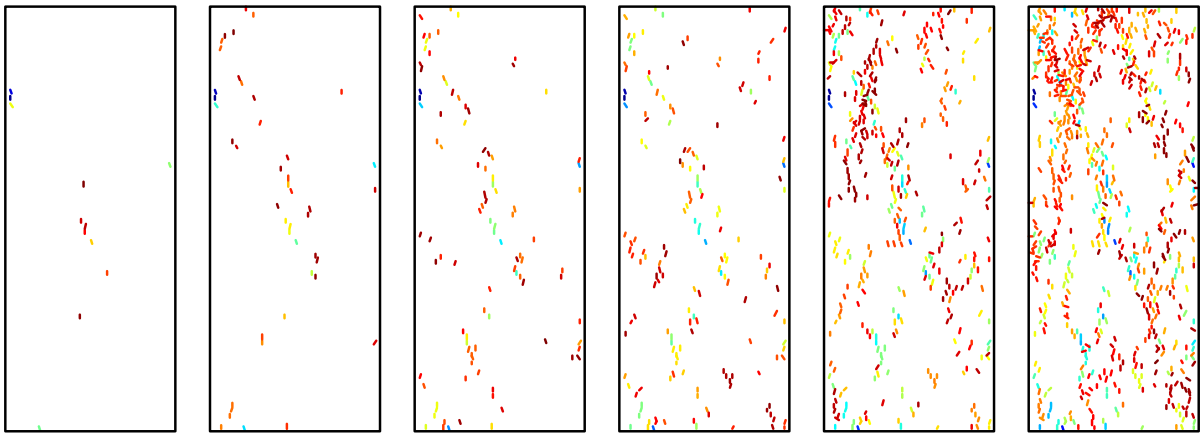

Figure 2.18: Evolution of micro-crack in uniaxial compression test in 2D; sample size $W \times H = 60 \times 150$ mm.

The distribution of micro-cracks in PFC shows the typical shear bands similar to experimental observations. Figure 2.18 shows the distribution of micro-cracks at different stages. The first few events of the micro-cracks are observed at about 60% of the loading level, mostly near the center of the sample, nearly perpendicular to the loading directions. As the load keeps increasing, more isolated micro-cracks are generated along the diagonal of the sample, where the shear band would eventually form. At the peak, the isolated micro-cracks coalesce and shear bands can be clearly identified. The shear band inclination is about 21° w.r.t. the direction of loading. Meanwhile, cracks developed along the loading direction are observed adjacent to the shear band surface. The final failure pattern observed in PFC2D is quite similar to that in experiments reported by [82], see Figure 2.19.

Evolution of the micro-cracks from the 3D simulation is similar to those from 2D and is not shown here for brevity.

Table 2.9: Calibrated micro-scale parameters for Berea sandstone

	3D
Softening coefficient β	0.15
Normal bond strength $\bar{\sigma}_c$ (MPa)	15±1.5
Shear bond strength $\bar{\tau}_c$ (MPa)	320±32
Point contact modulus E_c (GPa)	20.0
Parallel bond modulus $\bar{E}_c$ (GPa)	20.0
Elastic modulus E_c (GPa)	17.98
Uniaxial compressive strength σ_c (MPa)	108.35
Uniaxial tensile strength σ_t (MPa)	6.80
Strength ratio σ_c/σ_t	15.88

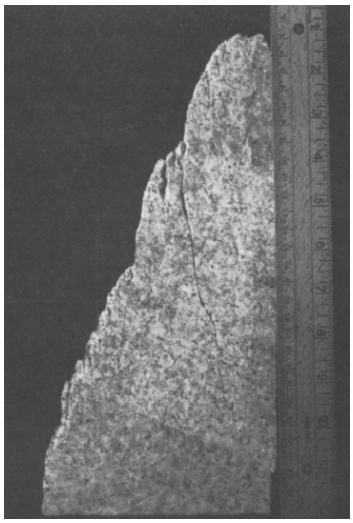

Figure 2.19: Failure pattern from an unconfined compression experiment on LdB granite[82], the failure surface is inclined at 23° with respect to the loading direction.

2.4.2 Berea Sandstone

The unconfined and confined three dimensional numerical simulations are performed on Berea sandstone samples with $D \times H = 40 \times 80$ mm. The macro-scale material properties of Berea sandstone are listed in Table 2.6 [18]. We assume the Berea sandstone samples used in experiments are intact. So $s = 1$ is applied for the Hoek-Brown Criterion as shown in Eq. 12.

The agreement of PFC3D and experimental results is excellent from the complete failure envelope standpoint. More importantly, the agreement of the tensile and compressive

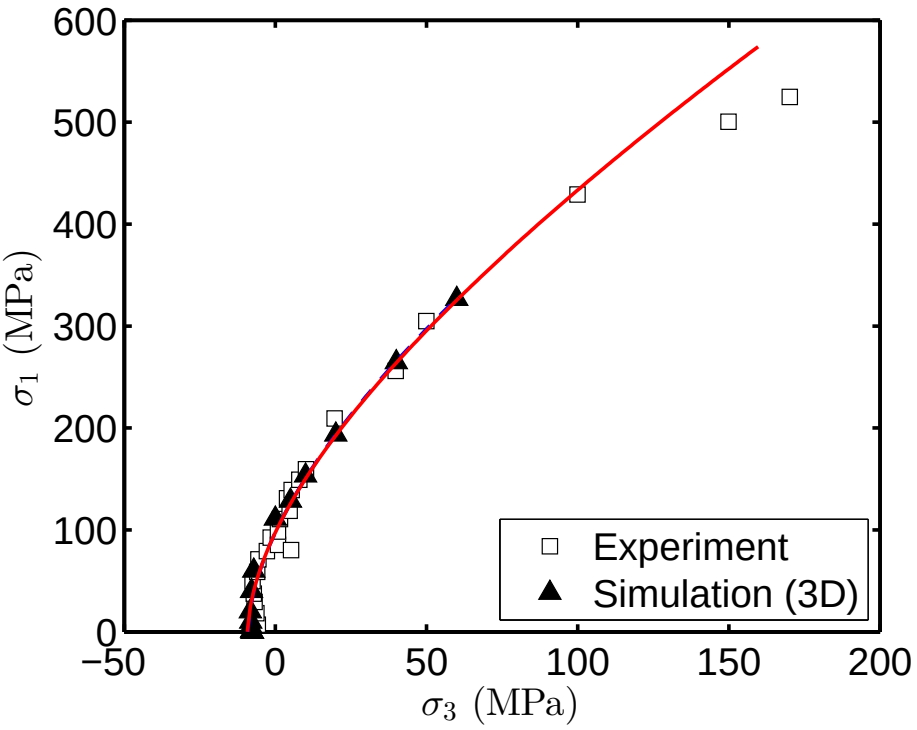

Figure 2.20: Failure envelopes of Berea sandstone vs. simulations. Experimental data is reported in [18]. Red solid line represents the regression curves of simulations and experiments based on Eq. 12. The parameters are summarized in Table 2.10.

strength is also satisfactory. In laboratory tests, the friction angle measured is $\phi = 38.55°$ while in PFC3D, $\phi = 37.36°$. The comparison of the failure envelope between experiments and simulations is presented in Figure 2.20.

The complete stress-strain curves obtained from unconfined tests are shown in Figure 2.21. The critical strain at peak in unconfined compression test is $\epsilon_c = 0.0069$ while the peak stress is σ_c =108.35 MPa. In direct tension test, the stress-strain curve shows an instant drop in post-peak stage indicating the numerical model is rather brittle. The critical strain at peak is $\epsilon_c = 0.0013$ while the peak stress is $\sigma_t = 6.80$ MPa. As such, the strength ratio $\sigma_c/\sigma_t = 10.65$ is consistent with experimental results.

Meanwhile, the failure pattern under various confining pressure shows localized shear bands along the diagonals of the sample, see Figure 2.22. When the confining pressure is low, a strong localization can be seen inclining about 29 degree w.r.t. the loading direction. The higher the confining pressure is, the more localized micro-cracks along the diagonals. In

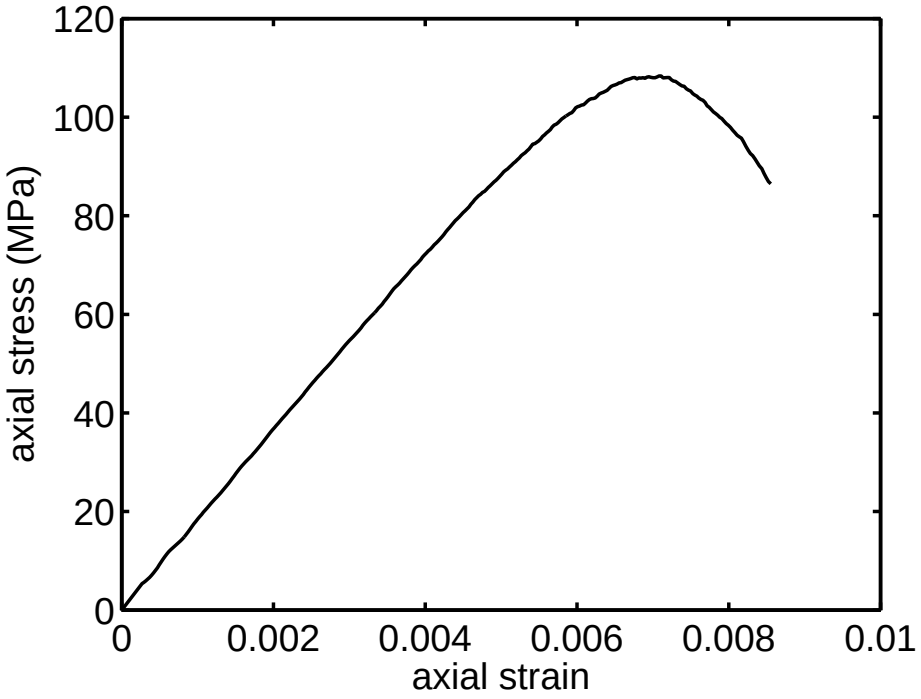

(a) unconfined compression test

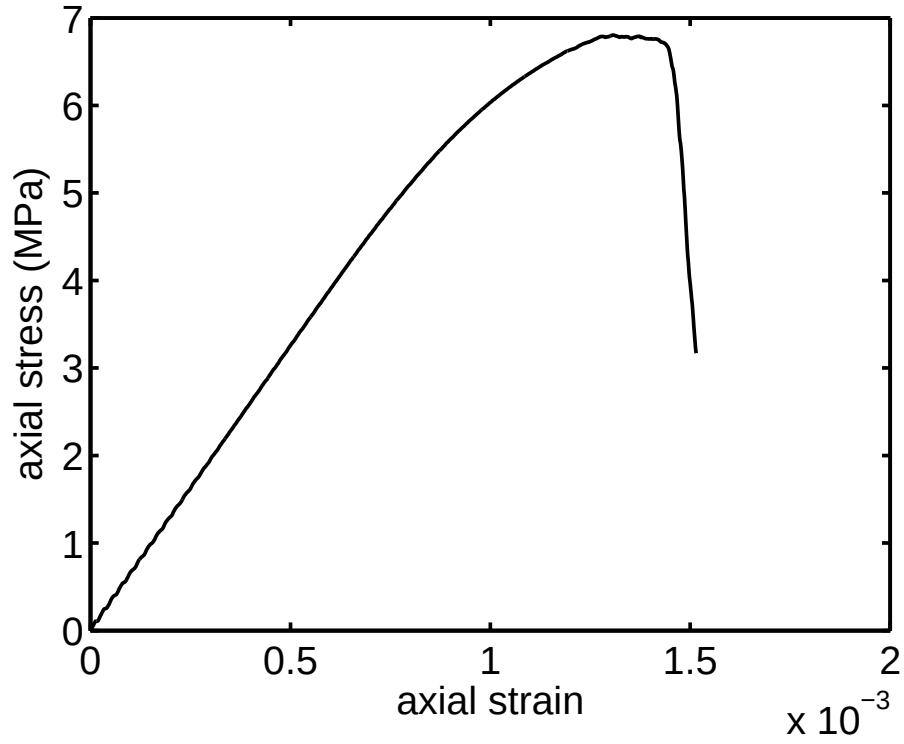

(b) direct tension test

Figure 2.21: Stress-strain curves for unconfined tests in 3D; sample size $D \times H = 40 \times 80$ mm.

Table 2.10: Hoek-Brown criterion parameters and results for Berea sandstone and PFC models.

Parameters	Berea sandstone	3D
m	10.40	10.56
s	1	1
σ_c (MPa)	97.63	97.67
ϕ (degree)	38.55	37.36
σ_t (MPa)	9.30	9.17
Strength ratio σ_c/σ_t	10.5	10.65

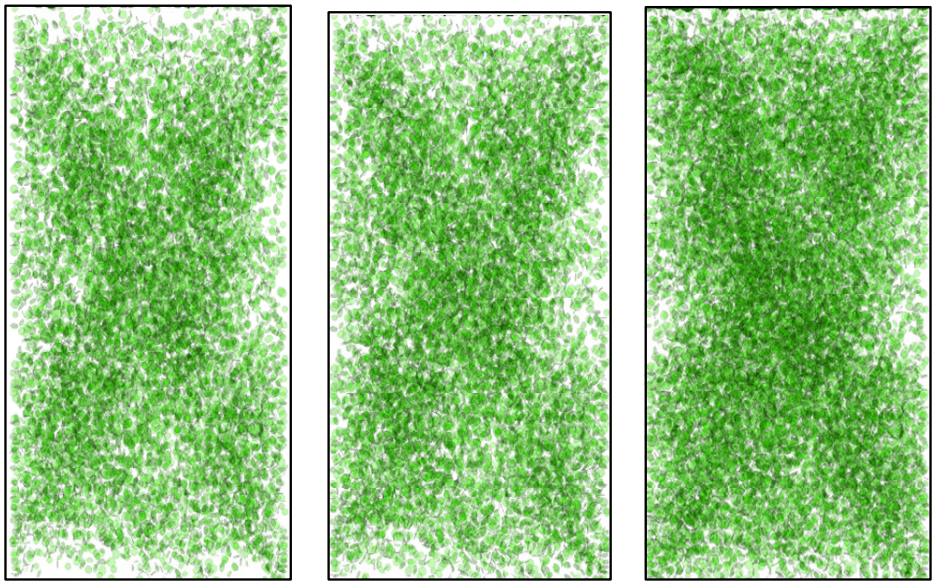

$\sigma_3 = 5$ MPa $\sigma_3 = 10$ MPa $\sigma_3 = 40$ MPa

Figure 2.22: Distribution of the micro-cracks at peak in 3D confined compression tests; sample size $D \times H = 40 \times 80$ mm.

confined tension tests, the failure of the sample is caused by the development of the tensile cracks, as shown in Figure 2.23. As can be seen, not only the complete failure envelope, but also the localized shear bands and tensile cracks can be captured by implementing the softening contact law introduced in this chapter.

2.5 Conclusions

The discrete element method has been widely used to investigate the failure of quasi-brittle materials. However, conventional modeling techniques suffer from a low compressive to tensile strength ratio σ_c/σ_t. Besides, the nonlinear failure envelope at low confinement

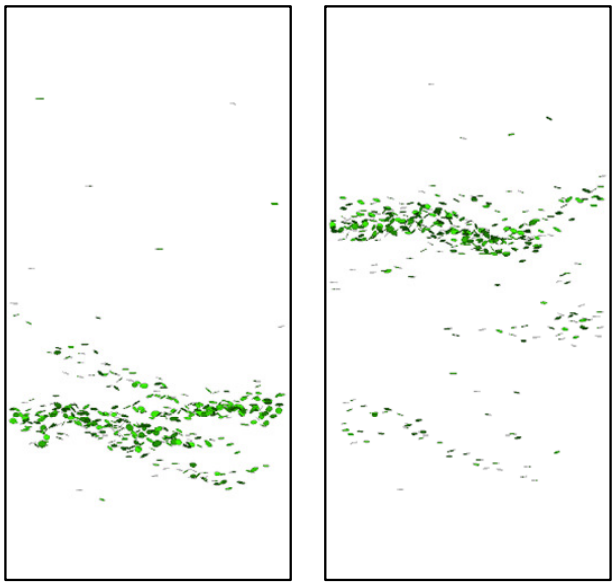

$\sigma_1 = 5$ MPa $\sigma_1 = 10$ MPa

Figure 2.23: Distribution of micro-cracks at 90% post-peak in 3D confined tension tests; sample size $D \times H = 40 \times 80$ mm.

cannot be properly captured. In this study, both two and three dimensional simulations are conducted to investigate the effectiveness of a displacement-softening contact law in improving the behavior of the numerical model. Implementation of the softening contact model allows us to explore materials with realistic properties, such as the compressive to tensile strength ratio σ_c/σ_t. We show that the softening coefficient β could only be effective in influencing the strength ratio if β is below a threshold value. As β decreases from the threshold value, the strength ratio increases, i.e., $\sigma_c/\sigma_t \in [4, 30]$, which covers the strength ratio range for most common rocks.

As consistent with experimental observations, the nonlinear failure envelope under confined tension is properly captured by applying the softening model. The numerical model is calibrated to compare with two different types of rocks: Lac du Bonnet granite and Berea sandstone. The numerical results from PFC2D successfully captured the characteristic failure pattern, as well as the mechanical properties of hard rock, including the high shear band angle, axial cracks near the shear plane, high friction angle, and reasonable σ_c/σ_t ratio. The friction angle predicted from PFC3D for hard rock is slightly lower than laboratory tests, it is nevertheless reasonable because granite usually consists of angular grains that lead to

high degree of interlocking. However, given a material consists of round grains, e.g., Berea sandstone, the PFC3D simulation results show that the complete nonlinear failure envelope could be matched, in addition to the high compressive to tensile strength ratio σ_c/σ_t.

CHAPTER III

FAILURE MECHANISMS AND SIZE EFFECT IN INTACT BRAZILIAN TEST

3.1 Introduction

Uniaxial tensile strength of quasi-brittle materials such as rocks and concretes is often measured indirectly by the Brazilian test. In the test, a circular disk-shaped specimen is loaded to fail in a splitting pattern under diametrical compression. Essential to the justification for the Brazilian test is that the elastic solution [56] predicts that the tensile stress perpendicular to the loading axis is nearly constant in a large portion of the central loading plane. Meanwhile, experimental observations [20, 88, 54, 100, 53] suggest that failure in confined extension still occurs according to the uniaxial tensile strength, if the magnitude of the compressive principal stress in a biaxial stress state is no more than a few times of the tensile stress. The Brazilian tensile strength (BTS) is therefore considered a good measure of the uniaxial tensile strength (UTS) with the premise that tensile failure initiates from the center of the specimen and propagates unstably towards the two loading platens. Given the specimen diameter D and thickness t, the nominal strength based on the peak load P can be written as,

$$\sigma_{\mathrm{BTS}} = \frac{2P}{\pi D t} \tag{13}$$

Compared to the direct tension test, the Brazilian test is relatively robust to perform. Nevertheless, since the location of crack initiation is difficult to be unambiguously discerned from visual inspection after routine testing, validity of the results has often been questioned (see review in [5, 6, 72]). Much of the discussion in the earlier literature focuses on how the loading platens and the contact condition/area affect the failure mechanisms. As pointed out by Fairhurst [40], small angles of loading contact area with materials of low compressive over tensile strength ratios could result in failure occurring away from the center and the tensile strength being underestimated. In other words, there is an alternative indentation-type of

failure scenario where the splitting failure pattern forms as a result of cracks emanating from the crushed zones beneath the loading areas.

Existence of both failure scenarios has been verified through a variety of experimental techniques, e.g., high speed photography of the photoelastic patterns [27], loading/unloading process controlled by lateral displacement [63, 86], strain gages [123], acoustic emission [69] and digital image correlation [113]. Similar evidences were also obtained based on the images from a high-speed camera in the dynamic Brazilian tests [130, 129]. These experimental findings were corroborated by numerical analyses [71, 72], though we should recognize that the failure mechanisms in numerical analyses are largely dictated by the constitutive models assumed a *priori*.

The difference between BTS and UTS obtained from laboratory experiments is well recognized. Depending on the rock types, BTS has been found to both overestimate and underestimate the UTS. The ratio, $\sigma_{\mathrm{BTS}}/\sigma_{\mathrm{UTS}}$, was found in [94] to scatter in between 0.56 for trachyte and 1.86 for sandstone. Rock type specific correlations were suggested [94]: $\sigma_{\mathrm{UTS}} = f\sigma_{\mathrm{BTS}}$, $f = 0.9$ for metamorphic, $f = 0.8$ for igneous and $f = 0.7$ for sedimentary rocks. Meanwhile, in some studies [69, 78], Brazilian test has been reported to exhibit size effect, namely, the dependence of the Brazilian tensile strength on the test sample size. When the effect of sample shape is excluded (constant t/D), BTS was found to decrease monotonically with $D \in [19, 56.5]$ mm in [78]. But the size effect is concluded statistically insignificant in [86] when $D \gtrsim 50$ mm (2 in.) and in [115] when $D \in [45, 80]$ mm. Using perhaps the largest Brazilian test sizes, $D \in [0.1, 3]$ m and $t = 0.5$ m, Hasegawa *et al.* [47] showed that BTS of concrete decreases with the diameter, but becomes nearly constant when the diameter is large enough. However, a possible weak reversal of the decreasing trend was suggested in [13], namely, as the diameter becomes large, BTS seems to increase instead of decreasing before reaching the asymptote. Table 3.1 and Figure 3.1 summarizes the aforementioned studies as well as the work in [121] on the size effect in the point load and direct tension tests. At least 15 specimens were tested for each diameter in [121]. Since the point load test, where a pair of concentrated loads is applied diametrically in a cylindrical sample, is similar to the Brazilian test, the results from [121] serve as a valuable reference.

Excluding the results with small sample diameters ($D < 1$ in.), the experimental evidences seem to collectively suggest a general size effect trend where BTS decreases as the diameter increases and becomes nearly constant as the diameter becomes sufficiently large.

Size effect in the strength of quasi-brittle materials has been attributed to the statistical distribution of weakness in the materials [120], fractal characteristics of cracks and/or flaws [23], or stress redistribution and growth of a process zone near the crack tip [10, 11, 12]. Lundborg [78] invoked Weibull theory to explain the decreasing trend in the BTS. Bažant [10, 11, 12] however argued that since failure of quasi-brittle materials is primarily governed by energy dissipation in the process zone ahead of the crack tip instead of crack initiation or formation of the crack surfaces, neither Weibull theory nor the crack fractality argument is the most appropriate explanation. Existence of a process zone near the crack tip has been strongly supported by experimental evidences from acoustic emission monitoring [69, 24] and digital image correlation [76].

The size effect laws of Bažant [10, 11, 12] have been developed based on asymptotic analysis of two limiting cases, namely, the "strength-of-material" type of failure criterion and the linear elastic fracture mechanics (LEFM) theory. The underlying arguments are that in the limit when the characteristic sample size l is small and comparable to that of the process zone, failure is governed by the strength of material; and when the sample size is much larger than the size of the process zone, the effect of the process zone becomes negligible and failure can be described by LEFM. A nominal strength σ_N is therefore constant for small l and decreases asymptotically according to $l^{-1/2}$ when l becomes large. Note that this deterministic or non-statistical size effect argument assumes that the samples obey geometrical similarity, where the size of material defect, a, scales according to the sample size $a \propto l$. This may not necessarily be valid at the scale of laboratory tests on intact samples. Though this size effect law reasonably describes results from tests such as notched three-point bending [12], it is inadequate to explain the observation that the size effect vanishes at large D in the Brazilian test. Instead, shear failure or the wedging effect at the loading ends [13] was suggested as a possible mechanism to overcome the weakening effect of $D^{-1/2}$ as D increases.

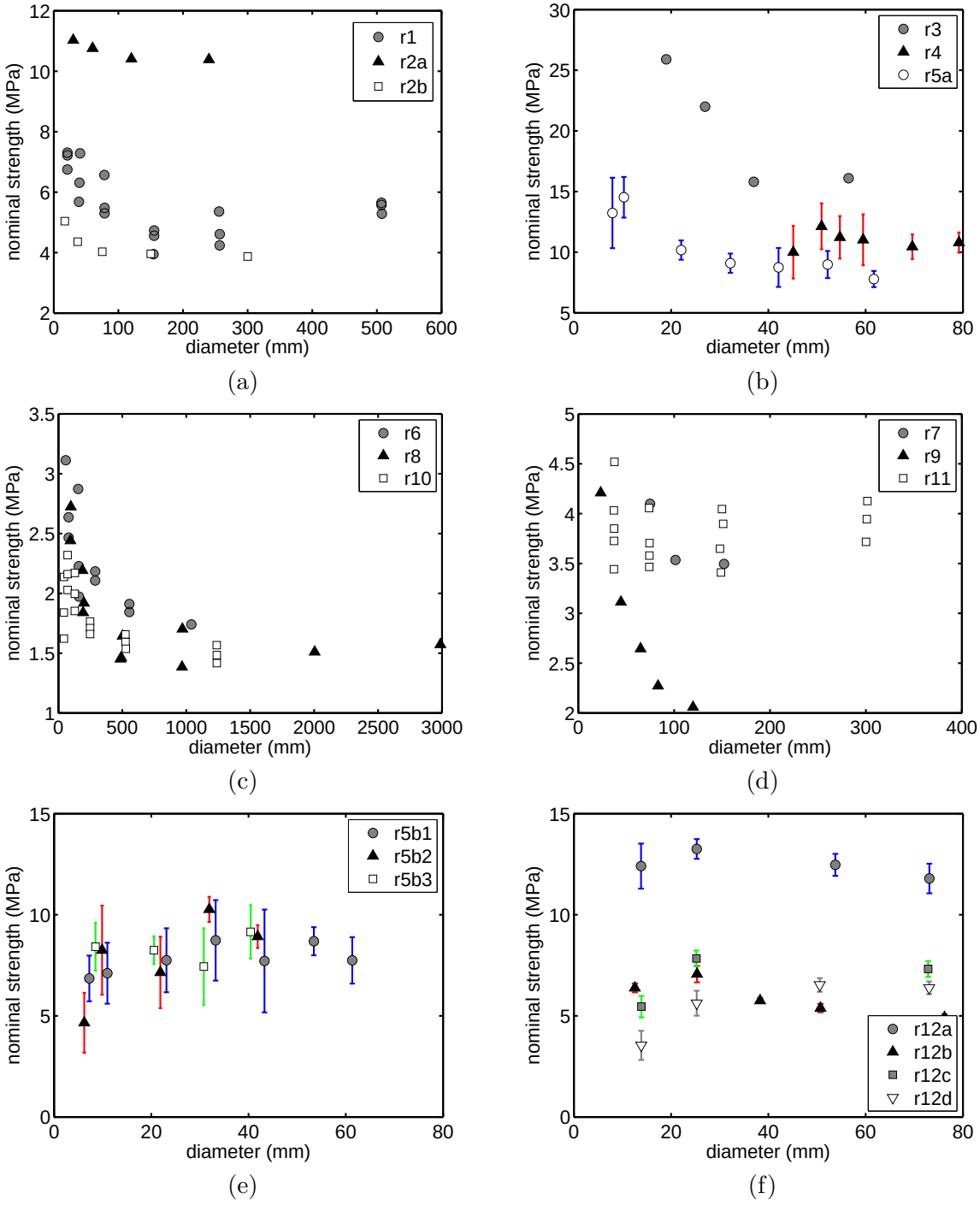

Figure 3.1: Experimental evidences of size effect. Details about the experimental data can be found in Table 3.1.

Over the last few decades, discrete element method (DEM) [32] has become an indispensable numerical tool to model the progressive failure in quasi-brittle materials. DEM models solid as a collection of particles, where failure mechanisms at the macro-scale emerge as a generic consequence of particle sliding and separation at the micro-scale. A prerequisite in DEM modeling is to calibrate the material properties by identifying a set of micro-scale parameters for the particles and the contacts so as to yield desirable properties at the macro-scale. We notice that in DEM modeling with a randomly packed spherical particle assembly, while BTS is often reported in the literature as the tensile strength for the purpose of material properties calibration, to the best of our knowledge, there is no indication that the failure mechanism in those studies is indeed in form of tensile crack initiation from the center.

In order to better understand how the failure mechanisms and the sample size in the Brazilian test affect BTS and how BTS compares with UTS, we conduct a comprehensive numerical study using the discrete element method (DEM) to model the intact Brazilian test. First, failure mechanisms in the Brazilian test and their dependence on the material properties and sample size are examined. Second, we focus on the connection between the failure mechanisms and BTS as well as the size effect and the comparison between BTS and UTS. A novel aspect of this study is that we implement a new contact model accounting for softening in the contact bond strength. As such, not only realistic rock properties, especially, the uniaxial compressive over tensile strength ratio σ_c/σ_t, can be obtained, dependence of the failure mechanisms on the macro-scale material properties as well as the sample size, as consistent with experimental evidences from the Brazilian test, can also be reproduced in the numerical simulations. In particular, the diametrical splitting failure pattern resulted from a tensile crack initiation and propagation from the center can now be simulated numerically in a randomly packed spherical particle assembly.

Intact Brazilian test is then modeled in both 2D and 3D to explore how the failure scenarios are affected by the material properties as well as the sample size. Implications of this numerical analysis to laboratory testing, and more importantly, to the calibration of material properties in DEM modeling in general are also discussed.

Table 3.1: Summary of experimental results (Unit: mm).

Ref.	Index	Shape	Testing Method	Material	Diameter D	Thickness t	Trend	No. of tests/size
[13]	r1	cylinder	Brazilian	concrete	19 - 508	$t = 51$	$[A]$	3
[107]	r2a	cylinder	Brazilian	granite	30 - 240	$t = 30$	$[B]$	≥ 3
	r2b	prism	Brazilian	mortar	17 - 300	$t = 50$	$[B]$	≥ 3
[78]	r3	cylinder	Brazilian	granite	19 - 56.5	$t/D = 1$	$[A]$	5
[115]	r4	cylinder	Brazilian	limestone	45 - 80	$t/D = 1$	$[C]$	4
[121]	r5a	cylinder	point load	granite	8 - 62	$t/D \geqq 2$	$[C]$	15-20
	r5b1	cylinder	direct tension	granite	7 - 56	$t/D = 4$	$[C]$	$\geq$15
	r5b2	cylinder	direct tension	granite	6 - 42	$t/D = 2$	$[C]$	$\geq$15
	r5b3	cylinder	direct tension	granite	8 - 40	$t/D = 1$	$[C]$	$\geq$15
[67]	r6	cylinder	Brazilian	concrete	57 - 1000	-	$[A]$	-
[25]	r7	cylinder	double punch	concrete	75 - 150	-	$[C]$	-
[47]	r8	cylinder	Brazilian	concrete	100 - 3000	$t/D = 1$	$[A]$	1 - 3
[109]	r9	cylinder	Brazilian	concrete	23 - 140	-	$[A]$	-

[118]	r10	dog-bone	direct tension	concrete	50 - 1600	$t = 100$	$[A]$	3-5
[105]	r11	cylinder	Brazilian	concrete	50 - 300	-	$[C]$	3
[86]	r12a	cylinder	Brazilian	granite	13 - 76	$t/D = 0.5$	$[C]$	unknown
	r12b	cylinder	Brazilian	sandstone	13 - 76	$t/D = 0.5$		
	r12c	cylinder	Brazilian	limestone	13 - 76	$t/D = 0.5$		
	r12d	cylinder	Brazilian	sandstone	13 - 76	$t/D = 0.5$		

Trend classification:

$[A]$: strength decreases with increasing sample size;

$[B]$: strength increases first, then decreases with increasing samples size;

$[C]$: strength is independent of sample size;

3.2 Numerical Model Setup

Numerical test is performed with the contact law discussed in Chapter II with $\beta = [0.015, \infty)$ and $D = [40,\ 320]$ mm to investigate the failure mechanisms on the softening coefficient β and the sample diameter D. It should be mentioned that here we make no attempt to match the macro-properties of the model to those of specific rocks, since the primary focus of this work is to investigate the effect of the strength ratio σ_c/σ_t, as adjusted through the softening coefficient β, on the failure behaviors and size effect in the Brazilian test in general.

To understand how different strength ratios can impact the failure mechanisms, a series of simulations with $\beta = 0.015,\ 0.1$, and ∞ are carried out in detail. The micro-scale parameters for both 2D and 3D simulations are listed in Table 2.1. The resulted macro-scale material properties in 2D and 3D are listed in Table 2.2 & 2.3 , respectively.

A circular particle assembly consisting of bonded particles are compressed by two horizontal wall elements placed at the top and bottom of the circular specimen. Velocities of the walls are applied in a ramp-up fashion with the terminal velocities chosen to be much smaller than the compressional wave velocity of the particle assembly so that the loading process can be approximated as quasi-static. 2D simulations are first conducted and analyzed. Selective 3D simulations are then performed to verify the 2D analysis. To reduce the influences stemming from the random nature of the particle assemblies, at least three samples for each size are generated.

3.3 Two Dimensional Simulations

3.3.1 Macro-scale Failure Patterns

In order to investigate the dependence of the failure mechanisms in the Brazilian test on the macro-scale material properties and the sample diameter D, a series of numerical simulations are performed with $\beta = [0.015,\ \infty)$ and $D = [40,\ 320]$ mm. The smallest sample to mean particle size ratio is $D/d_p \sim 16$.

Evolution of the micro-scale failures from 12 selected cases of two dimensional simulations around the peak load is shown in Figure 3.2. The spatial and temporal coordinates

of a micro-crack are represented by the position and color of a line segment, drawn in the direction perpendicular to the contact axis of a pair of particles. Note that the length of the line segment is magnified for the purpose of easier visualization. The color of the line segment marks the bond breakage time normalized by the elapsed time of a simulation stage. The start of loading is 0 and the end of the simulation stage is 1. Sequence of the micro-crack development can therefore be inferred from the color of the line segments. Blue indicates early time while brown means late time. Unless otherwise noted, this jet colormap is followed in all other micro-crack plots in this work.

Two primary failure scenarios can be identified from this series of simulations. Scenario I in Figure 3.3 refers to the failure mechanism where micro-cracks appear first in the center of the sample and then coalesce to form a macro-scale tensile crack, propagating towards the loading walls. There is no significant growth of a damaged zone beneath the loading walls during the initiation and propagation of the tensile crack. The cases in Figure 3.2 with $\beta = 0.015$, $D = 40$, 80, 200 mm, $\beta = 0.05$, $D = 40$ mm and $\beta = 0.1$, $D = 40$ mm fail according to Scenario I. Notice that locations of the micro-cracks at the early time are affected by both the randomness and the discrete nature of the specimens. As a result, the tensile crack in the cases with $\beta = 0.015$ and 0.1 and $D = 40$ mm initiates slightly off the central loading axis. Scenario II corresponds to the mechanism where the micro-crack events occur first adjacent to the loading walls. The micro-cracks then accumulate to form two distinct clusters, which resembles the formation of damaged zones. Growth of the micro-crack clusters eventually leads to initiation and propagation of tensile cracks either from both ends towards the center of the specimen ($\beta = 0.1$, $D = 280$ mm; $\beta = \infty$, $D = 320$ mm) or from one loading end to the other ($\beta = \infty$, $D = 80$ and 160 mm). There are also transition cases where growth of the tensile crack at the center and formation of the damaged zones near the ends occur more or less simultaneously and the two mechanisms do not appear to have a cause and effect relationship ($\beta = 0.05$, $D = 160$ and 280 mm; $\beta = 0.1$, $D = 160$ mm). Scenario I corresponds to the conventional center crack failure mechanism we generally assume for the Brazilian test, while Scenario II resembles indentation induced fracturing, which has also been observed in laboratory experiments. We have purposely

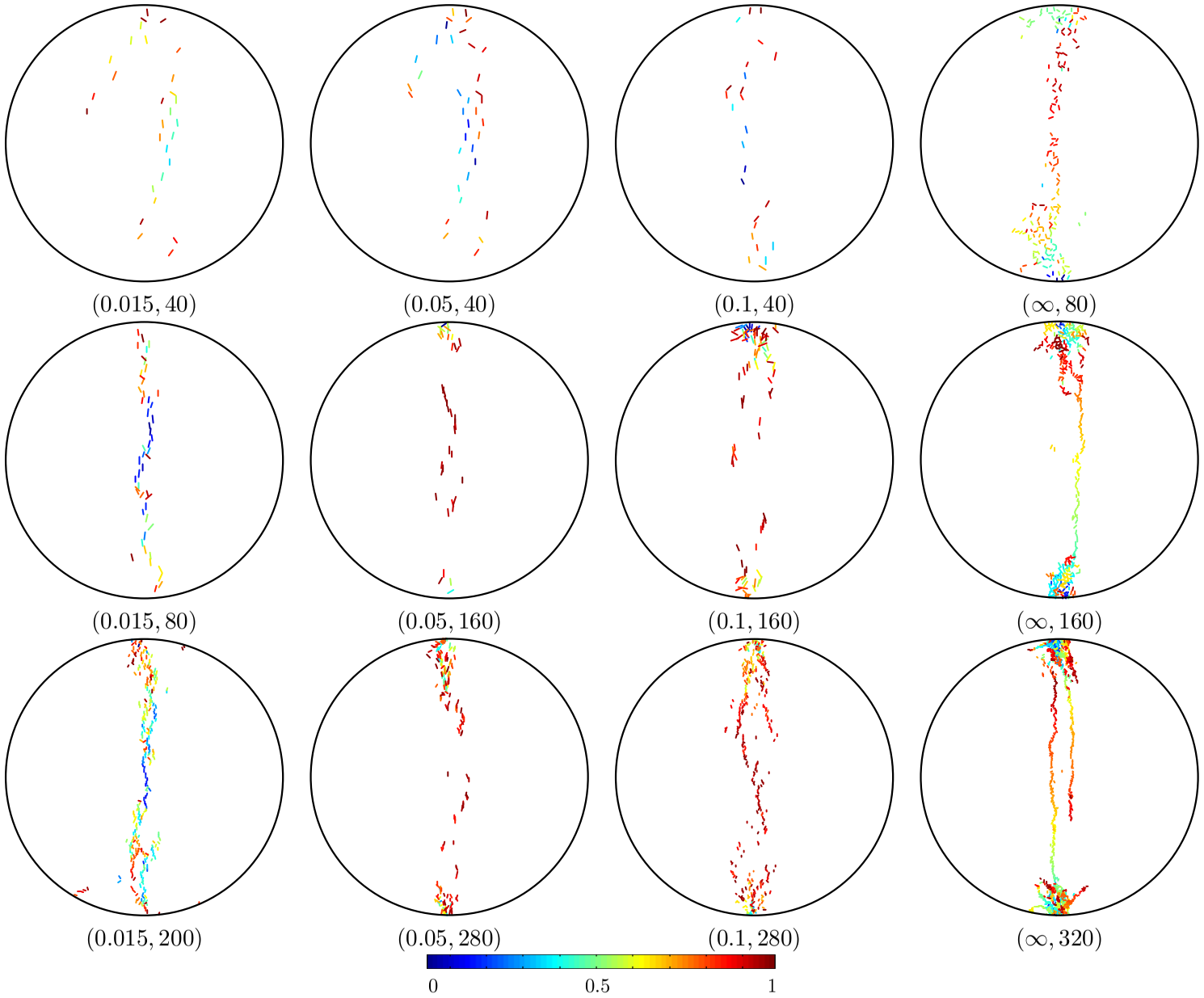

Figure 3.2: Dependence of the micro-scale failure mechanisms on the softening coefficient β and the sample diameter D (2D); the color bar represents the bond breakage time relative to the elapsed time of the simulation stage; crack lengths are magnified for easier visualization; the simulation cases are indexed by (β, D); unit of D in mm.

avoided using terms such as “brittle” or “ductile” in describing the macro-scale failure mechanisms in order to be clear of any ambiguity.

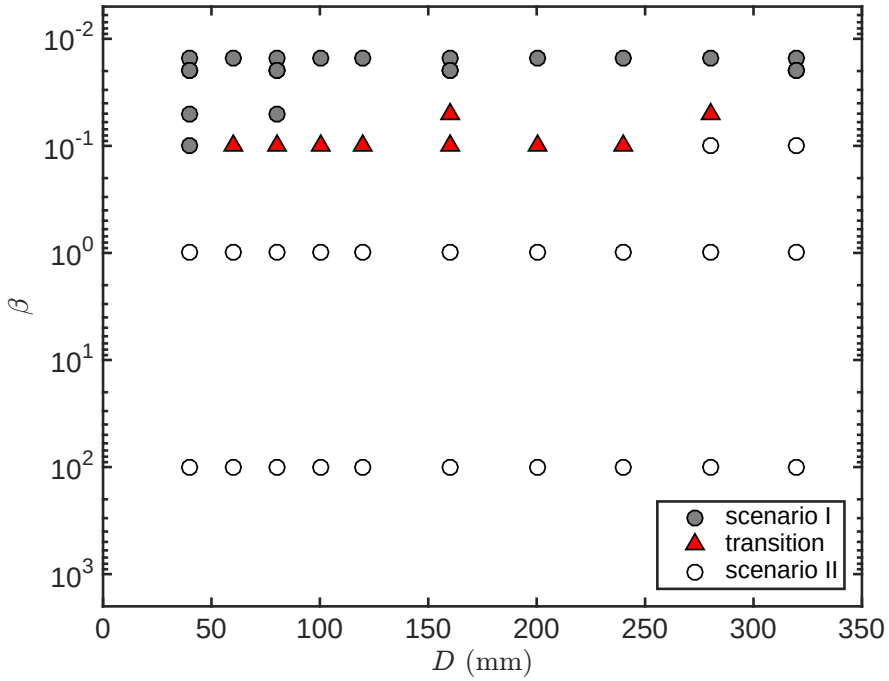

Figure 3.3: Dependence of the macro-scale failure mechanisms on the softening coefficient β and the diameter of the specimen D (2D).

Additional simulations are performed to populate a failure mechanisms map in Figure 3.3. This summary of the failure scenarios from all the simulations suggests that transition of the failure modes from Scenario I to Scenario II occurs when either β or D increases. At $\beta = 0.015$ and 0.02 ($\sigma_c/\sigma_t = 28.8$), all the simulations cases with the diameter D ranging from 40 mm to 320 mm fail according to Scenario I. Meanwhile, at $\beta = 1$ ($\sigma_c/\sigma_t \simeq 5.4$), 100 and ∞, all the cases fail according to Scenario II. At $\beta = 0.1$, failure with $D = 40$ mm can be clearly identified as Scenario I. As the diameter increases, the failure mechanisms appear to be in the transition, where both the damaged zones and the tensile crack in the center develop in parallel. At $D \geq 280$ mm, the failure mechanism follows Scenario II. Compared to the cases with $\beta = 0.05$, the transition from Scenario I to Scenario II occurs at a smaller D as β increases.

3.3.2 Micro-Scale Failure Evolution

Further insight into the effect of the material properties on the failure mechanisms may be derived from a detailed examination of the micro-scale failures at different loading levels in the simulations with $\beta = 0.015$, 0.1, and ∞ and $D = 280$ mm. The force-displacement relationships for the simulations with $\beta = 0.1$ and ∞ display distinct peaks, see Figure 3.4, while at $\beta = 0.015$, the curve seems to show a plateau before the loss of stability. One may note that in these three cases, as β decreases, the peak forces and consequently the nominal BTS increases. This is in contrast to the decreasing trend in UTS (see Table 2.2). The BTS based on the peak forces are $\sigma_{\mathrm{BTS}} = 13.13$, 10.42, and 6.45 MPa for $\beta = 0.015$, 0.1 and ∞, respectively. The ratios of $\sigma_{\mathrm{BTS}}/\sigma_{\mathrm{UTS}}$ are about 2.76, 1.19 and 0.39 for $\beta = 0.015$, 0.1 and ∞. If the load level corresponding to center crack initiation is used for $\beta = 0.015$, the BTS reduces to $\sigma_{\mathrm{BTS}} = 6.64$ MPa and $\sigma_{\mathrm{BTS}}/\sigma_{\mathrm{UTS}} = 1.40$. The underlying reason for the opposite trends in the variations of BTS and UTS with β is that the failure mechanisms in the three cases are not the same. Effect of the failure mechanisms on BTS and the comparison between BTS and UTS will be discussed in the following sections. In this part, we focus our discussion on the dependence of the failure mechanisms on the material properties and the sample size only.

At $\beta \to \infty$, micro-cracks start to appear near the loading walls around 35% of the peak load. When the loading level reaches about 50% (stage D_1 in Figure 3.4), a small damaged zone can already be identified at each end of the sample, see Figure 3.5. As the micro-cracks aggregate, the damaged zone grows in size. At 75% of loading (stage C_1), there are evidences of micro-cracks coalescence into forming thin, slit-like features. This may be considered as equivalent to the initiation stage of the macro-scale cracks. Size of the damaged zones and length of the cracks both grow stably as the loading level increases to 90% (stage B_1). Eventually, extension of the two primary cracks in the preferential subvertical directions leads to the collapse of the sample. The two primary cracks, however, do not become directly linked, instead they create an overlapping pattern, commonly observed in en-echelon dilating fractures [96]. Since the contact model is perfectly brittle in this case, the crack trajectories are well-defined and strongly localized.

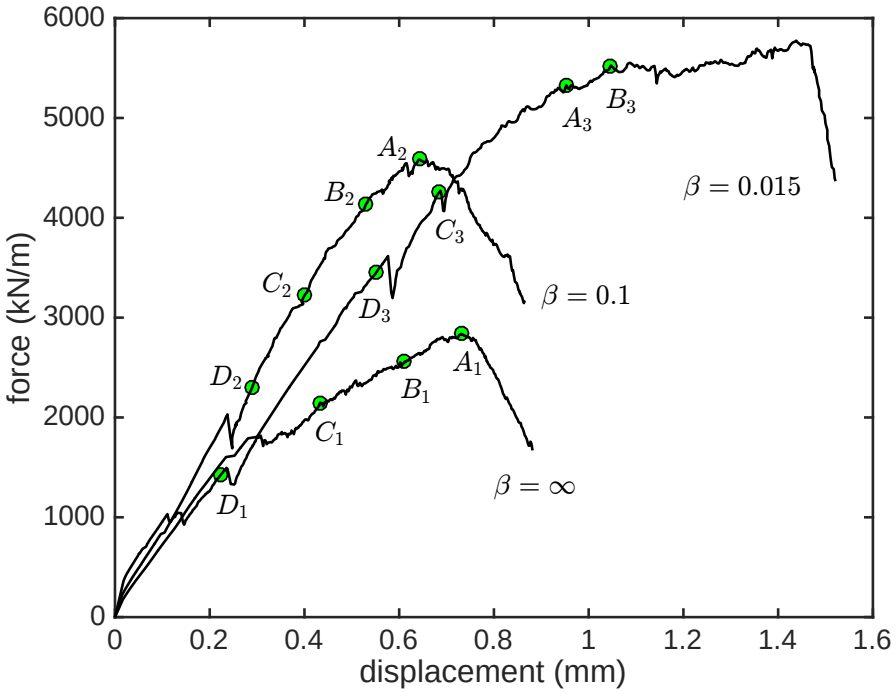

Figure 3.4: Force-displacement relationships for the 2D Brazilian tests with $\beta = 0.015$, 0.1, ∞ and $D = 280$ mm.

At $\beta = 0.1$, the failure mechanism is similar to that of $\beta \to \infty$, where formation of the damaged zones precedes any macro-scale crack growth (see Figure 3.6). However, at $\beta = 0.1$, the micro-cracks, which will later coalesce to form macro-scale cracks, appear earlier. At 90% of loading (stage B_2 in Figure 3.4), the primary cracks are already partially developed across the whole sample, whereas at $\beta \to \infty$, no micro-crack appears in the center region of the sample at the same loading level. This could be explained by the fact that the strength ratio σ_c/σ_t is higher at $\beta = 0.1$ and at the macro-scale, the material is more likely to fail in tension. Consequently, the transition from the shear failure, responsible for the formation of the damaged zones, to tensile failure occurs earlier at a relatively lower loading level. In addition, it is interesting to note that crack growth at $\beta = 0.1$ appears to have mixed-mode characteristics, reminiscent of a wing crack [41], albeit the growth is in a reversed order.

At $\beta = 0.015$, the micro-cracks first appear in the center of the sample around 55% of the loading level (w.r.t stage A_3). At 80% of loading (stage C_3), a center crack has formed

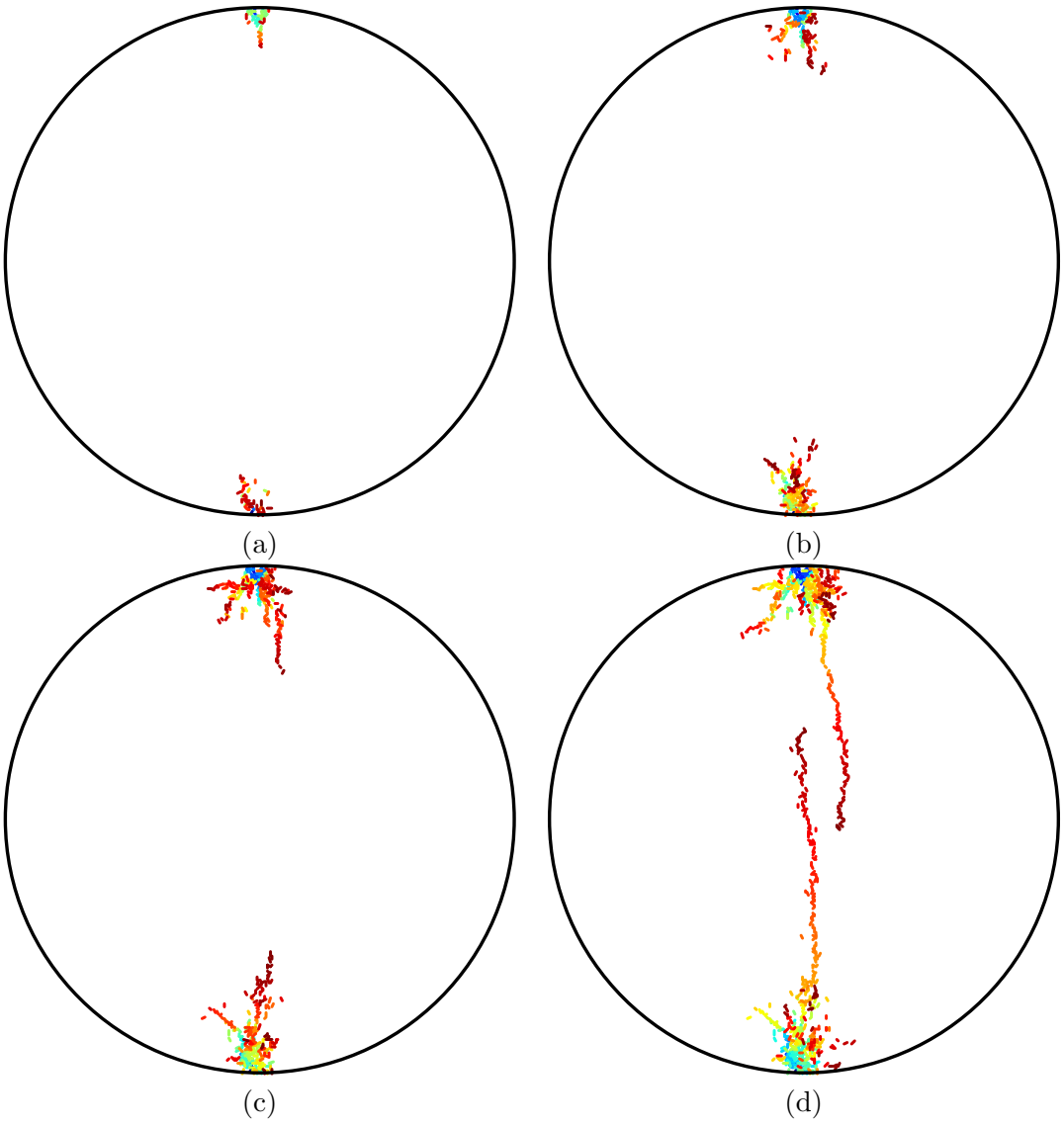

Figure 3.5: Evolution of the micro-scale failure mechanisms with $\beta \to \infty$ and $D = 280$ mm (2D); (a) 50% of loading level-stage D_1, (b) 75%-stage C_1, (c) 90%-stage B_1, (d) peak-stage A_1.

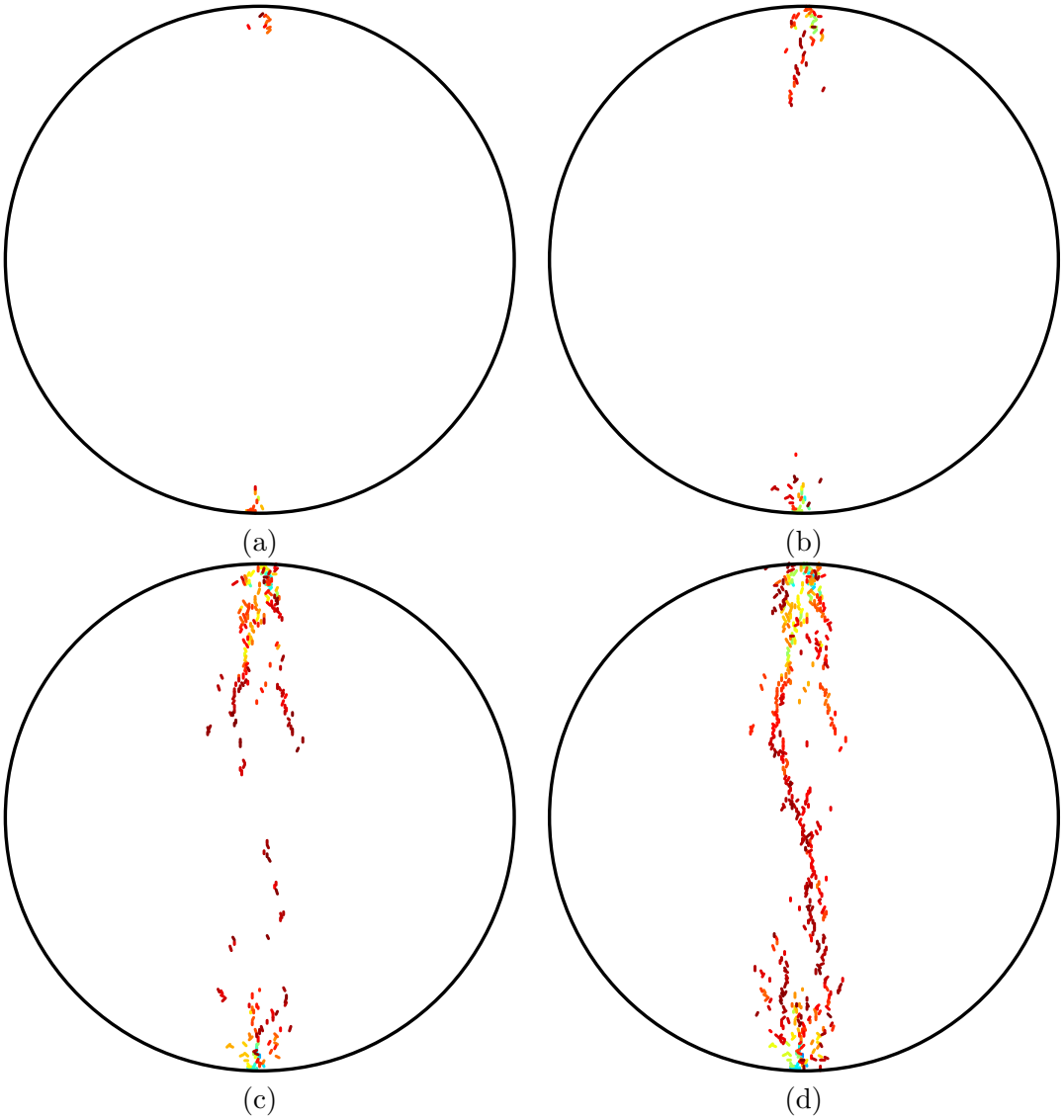

Figure 3.6: Evolution of the micro-scale failure mechanisms with $\beta = 0.1$ and $D = 280$ mm (2D); (a) 50% of loading level-stage D_2, (b) 70%-stage C_2, (c) 90%-stage B_2, (d) peak-stage A_2.

and grown to about $D/3$ in length (see Figure 3.7). From stage C_3 to A_3, micro-cracks accumulate within two bands bridging the regions between the center crack and the two ends. It can be discerned from the micro-crack pattern at stage A_3 that the center crack extends downwards in the lower half of the sample. However, in the upper half of the sample, the sense of crack propagation direction is relatively weak, indicating that the tensile stress gradient along the loading axis is relatively small. The presence of strong compression near the ends seems to promote tortuosity in the crack trajectories and formation of the sizable crack bands. From stage A_3 to B_3, the force increases slightly by about 3.5% and the band of the micro-cracks in the center expands laterally. Meanwhile, additional micro-cracks occur near the two loading walls and secondary cracks start to grow radially inwards from the perimeter. After stage B_3, continuous growth of the secondary cracks eventually causes the sample to collapse.

Since the failure mechanism after stage A_3 is mostly associated the growth of secondary cracks, the load level at stage A_3 can be taken as what is required to split the sample into two halves by a diametric tensile crack. As similarly observed in laboratory experiments [106], the two halves of the disk are able to sustain slight increase in the load as the edges of these two halves are being crushed and secondary cracks emanate from the perimeter. The difference in the failure mechanisms before and after stage A_3 is also reflected in the force-displacement curve (see Figure 3.4), where after stage A_3, the tangent slope of the curve becomes much smaller. Note that though the failure scenario here is distinct from the cases with $\beta = 0.1$ and ∞, the post peak failure morphology in these three cases in fact shares similarities. They also show evidences of crushed zones near the loading walls and the overall failure is in form of diametric splitting. As far as laboratory testing is concerned, the numerical results from this particular case imply that the peak force in the force-displacement curve does not necessarily correspond to the moment of center crack initiation. Furthermore, identifying the failure mechanism simply by post-mortem visual inspection could be misleading.

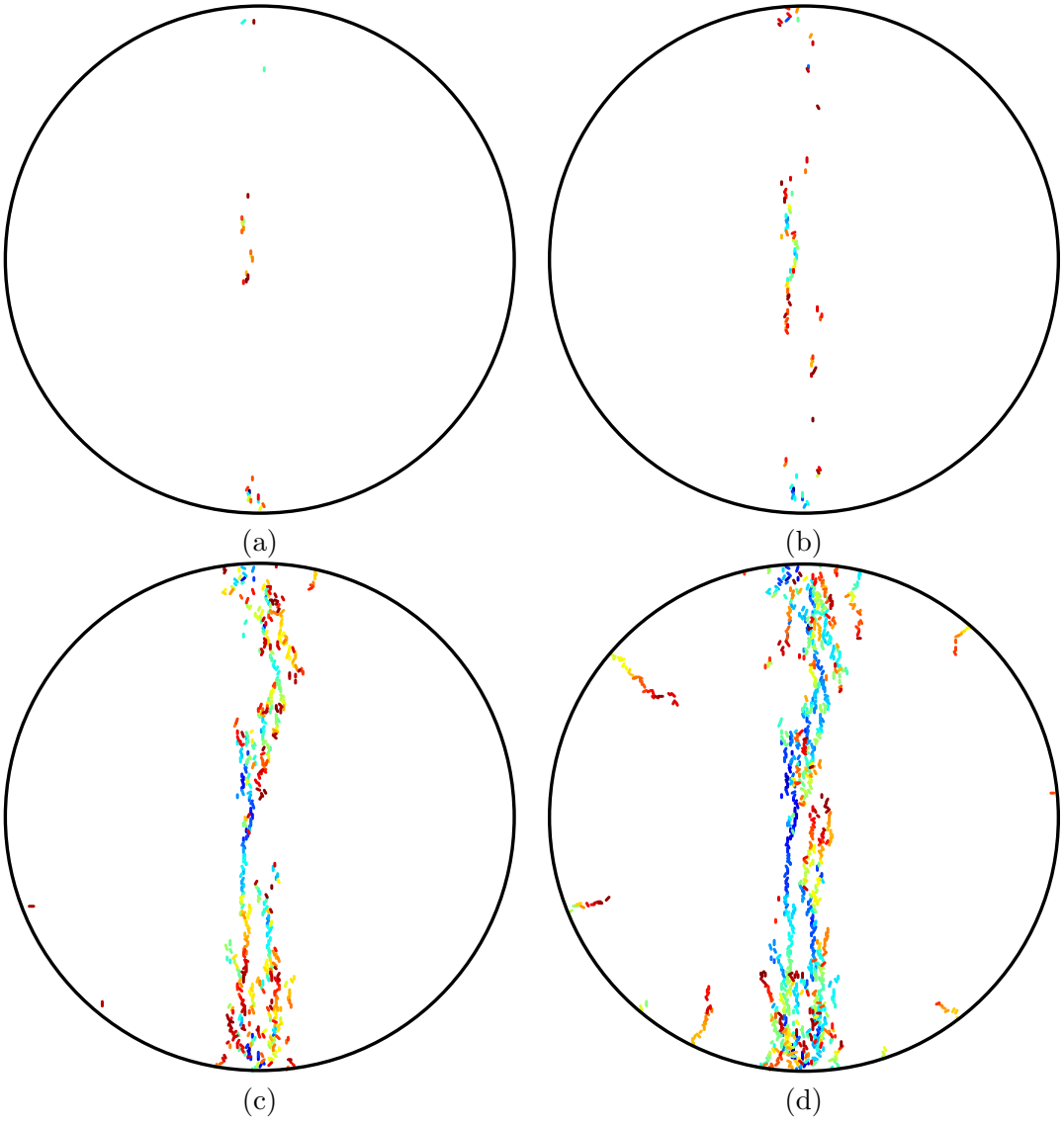

Figure 3.7: Evolution of the micro-scale failure mechanisms with $\beta = 0.015$ and $D = 280$ mm (2D); (a) 65% of loading w.r.t stage A_3-stage D_3, (b) 80%-stage C_3, (c) stage A_3, (d) 103.5%-stage B_3.

3.3.3 Damage Evolution

Fracturing in quasi-brittle materials has often been associated with the concept of a process zone. The so-called process zone may be described as the region where the material undergoes micro-cracking prior to extension of the fracture and has been experimentally identified based on the locations of acoustic emission (AE) events [68, 69]. Existence of a process zone has implications on the stability of fracture propagation and size effect in material strengths [12]. In order to assess the influence of the process zone development on the failure mechanisms (and on the BTS), evolution of contact bond softening in the two representative cases with $\beta = 0.015$ and 0.1 and $D = 280$ mm is analyzed.

Arguably, there is no one-to-one rigorous correspondence between the micro-scale bond softening and breakage in DEM and the AE events measured based on the transient elastic wave or the elastic energy released due to micro-cracking. The process zone is therefore loosely defined here as the region containing contact bonds where the degree of softening, ξ, has exceeded a certain threshold,

$$\xi = \frac{\overline{\delta}_n - \overline{\delta}_1}{\overline{\delta}_2 - \overline{\delta}_1} \tag{14}$$

The degree of softening ξ may be considered as an index measuring the elastic energy released due to bond softening. Small ξ corresponds to low energy release. Note that since the criterion for bond breakage includes the rotational contribution, at the moment when a bond breaks, $\xi \leq 1$.

In DEM modeling, given the same loading and geometrical configurations, characteristics of the process zone are primarily dictated by the prescribed contact model. For the perfectly brittle contact model ($\beta \to \infty$), bond breakage occurs once the contact forces reach the bond strengths. Therefore, there is no bond in softening at $\beta \to \infty$. Meanwhile, at $\beta = 0.015$ and 0.1, differences in the failure scenarios are reflected not only in the locations of the softening bonds, but also in the distributions of the degree of softening. Figures 3.8 and 3.9 show locations of all softening bonds and broken bonds at various stages of loading for $\beta = 0.015$ and 0.1. In both cases, the softening bonds appear first adjacent to the loading walls. Onset

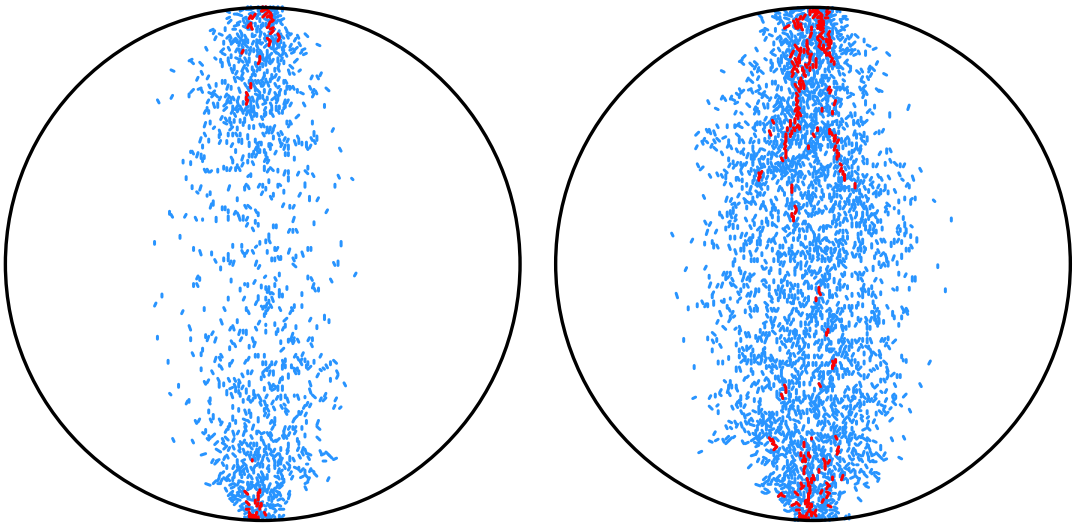

(a) 65% (b) 90%

Figure 3.8: Locations of all the softening bonds (blue) and broken bonds (red) at (a) 65% and (b) 90% of the loading levels; $\beta = 0.1$, $D = 280$ mm (2D).

of softening is caused by the large compressive forces in response to the highly concentrated loading from the two walls. In laboratory testing, since the stress concentration at the ends tends to promote failure according to Scenario II, it is common to use curved loading jaws or add cushion in between a specimen and the loading platens as remedies to lessen the stress concentration. As far as DEM modeling of the Brazilian test is concerned, the implication of these numerical results is that if the loading process is realized through two flat walls and the contact model is perfectly brittle ($\beta \to \infty$), stress concentration and micro-scale failures near the walls are inevitable. Failure according to Scenario II is therefore highly likely.

At $\beta = 0.1$, the softening bonds remain more concentrated near the walls at both 50% and 65% of loading, suggesting there is a relatively large stress gradient across the zones with different concentrations of softening bonds. Between 65% and 90% of loading, the softening bonds gradually fill into the middle region of the specimen, see Figure 3.10. In this region, softening bonds with $\xi \geq 0.5$ as well as isolated broken bonds, which will eventually coalesce to form the primary crack, appear in a more or less evenly distributed fashion as the loading level increases, without showing a strong directional sense of crack propagation. This is consistent with the nearly uniform color of the primary crack in Figure

3.6(d). Excluding the damaged zones near the walls, if we consider the central region with softening bonds at $\xi \geq 0.5$ as the process zone associated with the primary crack growth, the length of the process zone in this particular case is in fact relatively large and comparable to the sample diameter D.

At $\beta = 0.015$, as the loading level increases to about 30%, the softening bonds are already more or less evenly distributed across the loading axis. At 65% of loading, a center crack has initiated. However, the softening bonds are still evenly distributed in a narrower band across the diameter if the threshold for the degree of softening is set to $\xi \geq 0.4$. Only when $\xi \geq 0.5$, locations of the softening bonds show the central band associated with center crack growth is detached from the two strips at the ends, see Figure 3.11, indicating that the tensile stress gradient along the loading axis is rather weak. At 80% of loading, the tensile crack has extended to about $D/3$ in length. Softening bonds with $\xi \geq 0.5$ are now clustered in the two strips, connecting the tensile crack in the center with the loading ends. Differences in the locations of the softening bond clusters with $\xi \geq 0.5$ between 65% and 80% of loading reflect the change in the crack tip positions and hence growth of the center crack.

Between the two cases, damage associated with $\beta = 0.1$ (Scenario II) seems to be relatively more severe. Histograms of the softening bonds at 65% of loading show that at $\beta = 0.015$, the largest percentage of the softening bonds is within $0 \leq \xi \leq 0.05$, whereas at $\beta = 0.1$, it is within $0.05 \leq \xi \leq 0.15$, see Figures 3.12 and 3.13. Such a contrast in the distribution of ξ persists prior to the peaks. Though the total number of softening bonds at $\beta = 0.015$ is higher, most of them are in lower degrees of softening or being associated with low energy release.

Softening bonds are the precursors of micro-scale failure. At $\beta = 0.1$, the micro-scale failures originate in the same regions where bonds softening first occurs. However, at $\beta = 0.015$, the location of the initial micro-scale failures differs from that of onset of softening. The differences between the two cases (and also the case with $\beta \to \infty$) can be attributed to the fact that in the softening contact model, while the softening criterion is based on the normal bond strength, the micro-scale failure is controlled by the maximum

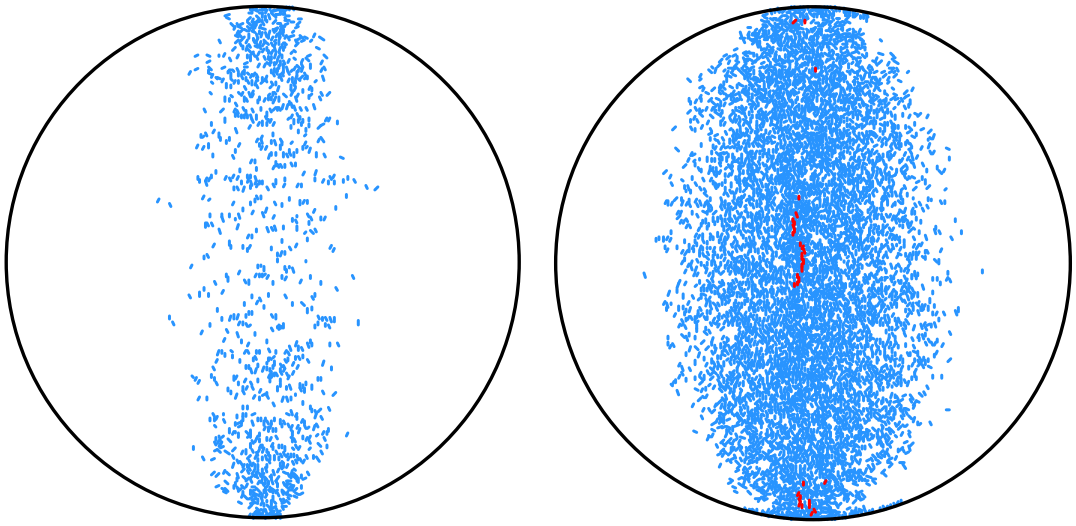

(a) 20% (b) 65%

Figure 3.9: Locations of all the softening bonds (blue) and broken bonds (red) at (a) 20% and (d) 65% of the loading levels; $\beta = 0.015$, $D = 280$ mm (2D); the loading level is w.r.t stage A_3.

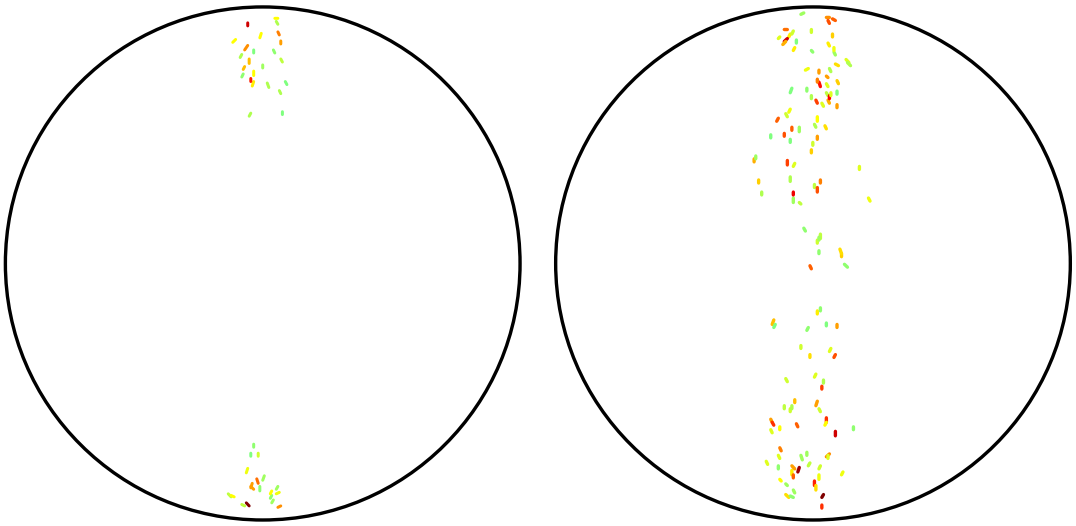

(a) $\xi \geq 0.5$ (65% of loading) (b) $\xi \geq 0.5$ (90% of loading)

Figure 3.10: Locations of the softening bonds with $\xi \geq 0.5$ at (a) 65% and (b) 90% of loading levels w.r.t stage A_2; $\beta = 0.1$, $D = 280$ mm (2D); the same jet colormap now marks the magnitude of ξ.

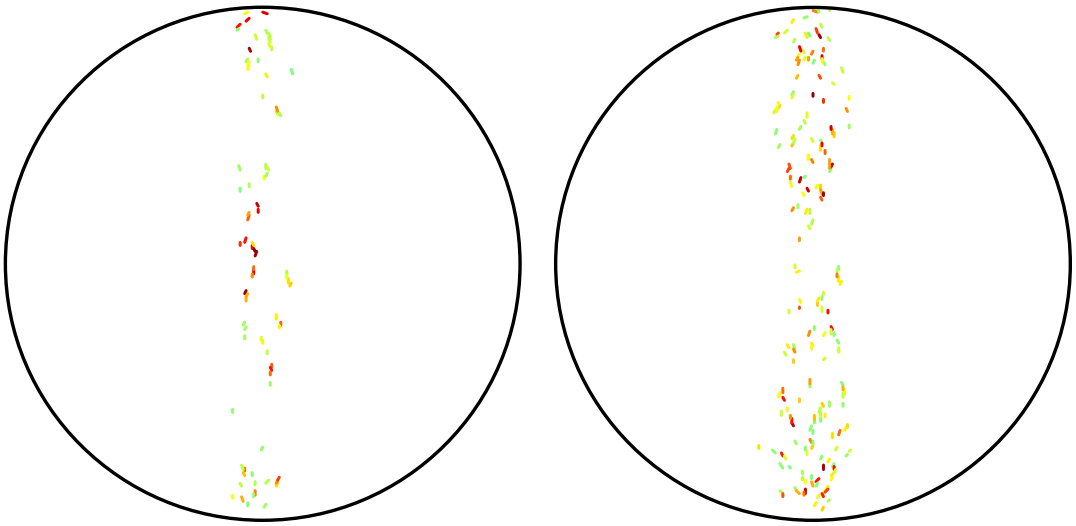

(a) $\xi \geq 0.5$ (65% of loading) (b) $\xi \geq 0.5$ (80% of loading)

Figure 3.11: Locations of the softening bonds with $\xi \geq 0.5$ at (a) 65% and (b) 80% of loading levels w.r.t stage A_3; $\beta = 0.015$, $D = 280$ mm (2D); the same jet colormap now marks the magnitude of ξ.

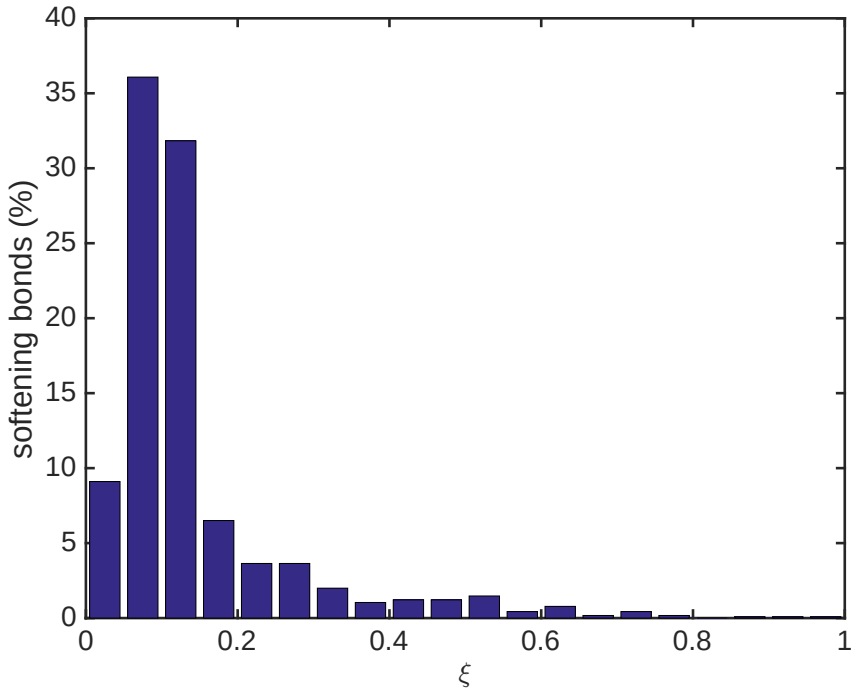

Figure 3.12: Histogram of the parallel bonds in softening, 65% of loading w.r.t stage A_2; $\beta = 0.1$, $D = 280$ mm (2D).

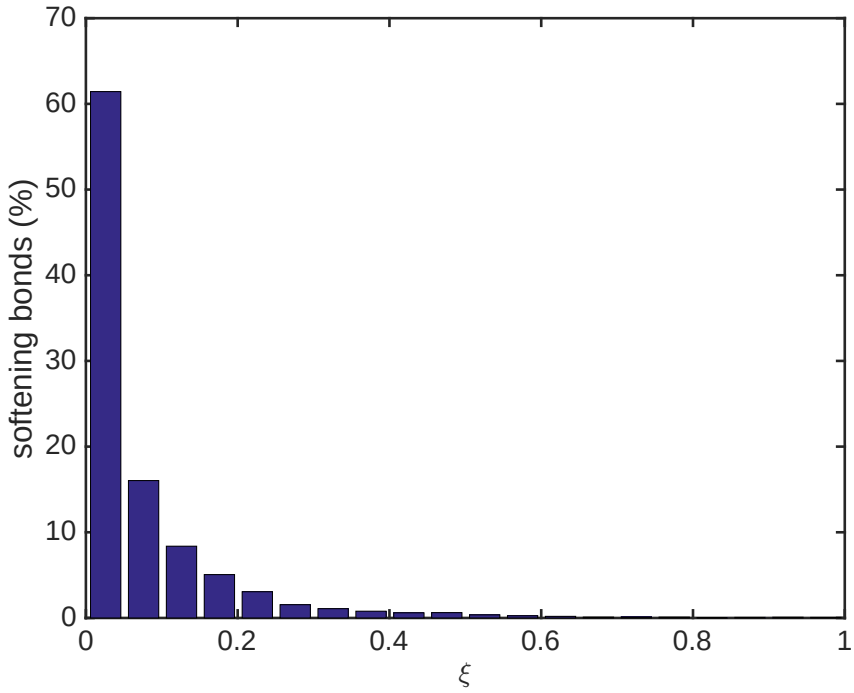

Figure 3.13: Histogram of the parallel bonds in softening at stage D_3 (65% of loading level w.r.t stage A_3); $\beta = 0.015$, $D = 280$ mm (2D).

bond stretch $\overline{\delta}_c$. To a certain degree, this is somewhat equivalent to state that in these numerical simulations, failure according to Scenario I is related to a maximum tensile strain criterion, while failure according to Scenario II is a result of a stress-based criterion.

Overall, the softening contact model is able to produce the characteristics of the process zone associated with crack growth and the results are qualitatively similar to the AE measurements from the experiments [69]. In these two cases, the lengths of the process zone at the peak loads are comparable to the sample diameter. The BTS determined from the peak load is therefore not expected to exhibit size effect in this diameter range. Though the softening bonds are not exactly equivalent to the AE events, the numerical results do seem to suggest that determination of the process zone geometry may be affected by the sensitivity of the AE measurements.

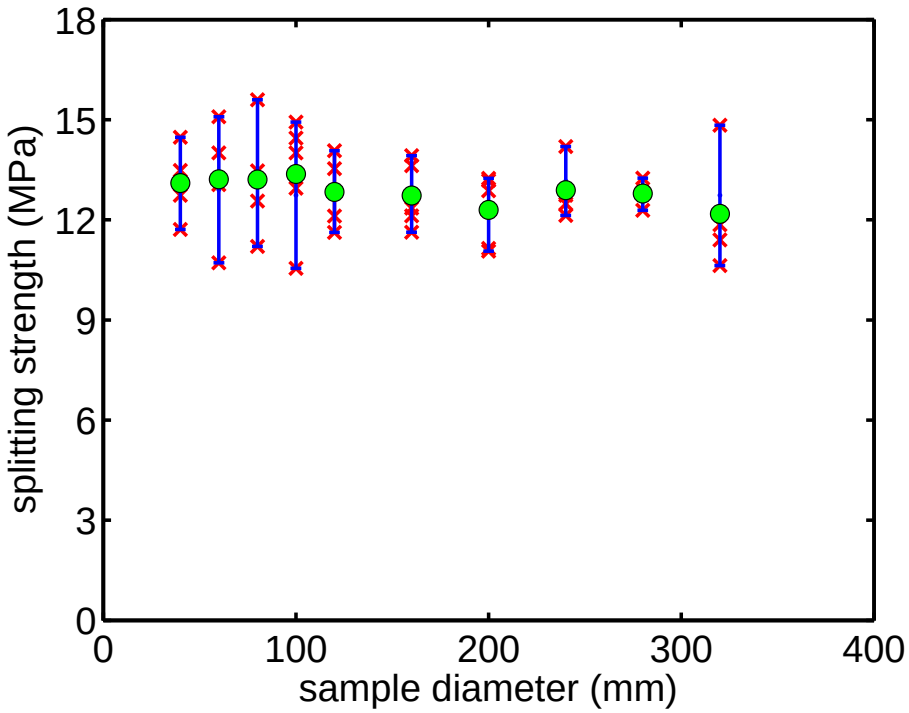

Figure 3.14: 2D BTS vs. sample size, $\beta = 0.015$.

3.3.4 Size Effect

Next we examine how the differences in the failure scenarios and the sample size affect the nominal Brazilian tensile strength as determined from Eq. 13. The results from these series of simulations suggest that when $\beta = 0.015$, BTS is nearly constant and independent of sample size, see Figure 3.14. However, when $\beta = 0.1$ and ∞, BTS decreases with the sample size, but reaches a plateau as $D/\bar{d}_p \gtrsim 100$, where $\bar{d}_p$ is the mean particle diameter, see Figures 3.15 and 3.16. In other words, if the sample fails according to Scenario II, the size effect can only be observed when sample is small. Moreover, the size effect vanishes for large samples. Therefore, regardless of the failure mechanism that dominates the Brazilian test, size effect cannot be captured if the sample size exceeds a threshold value. If we assume the nominal tensile strength from Braziliant tests σ_t^B is the value at the asymptote when sample size is large, and then normalize BTS w.r.t. σ_t^B, we can see a clear size effect transition as shown in Figure 3.17.

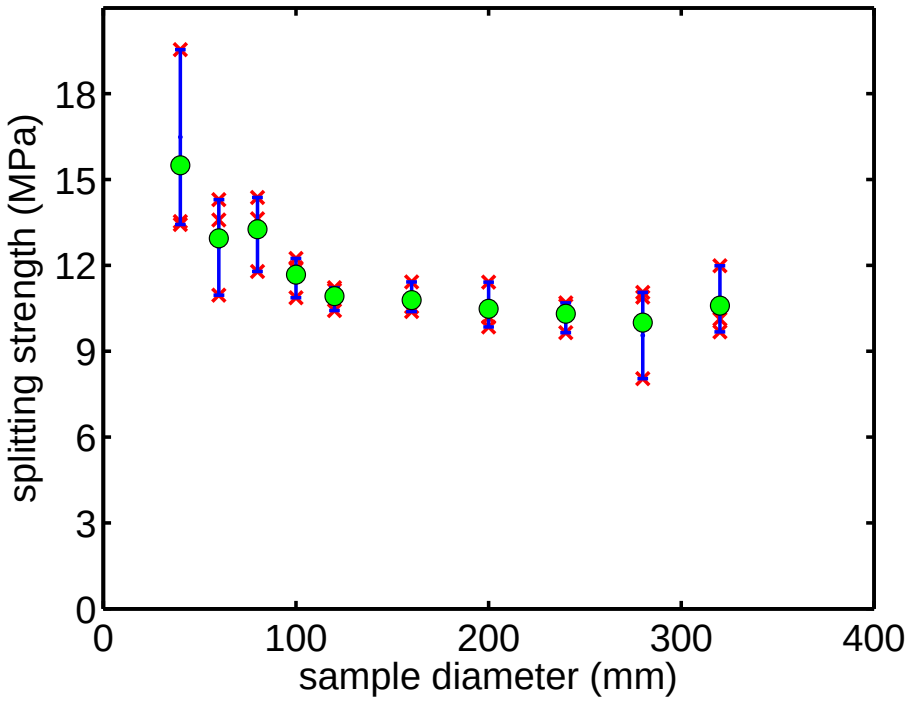

Figure 3.15: 2D BTS vs. sample size, $\beta = 0.1$.

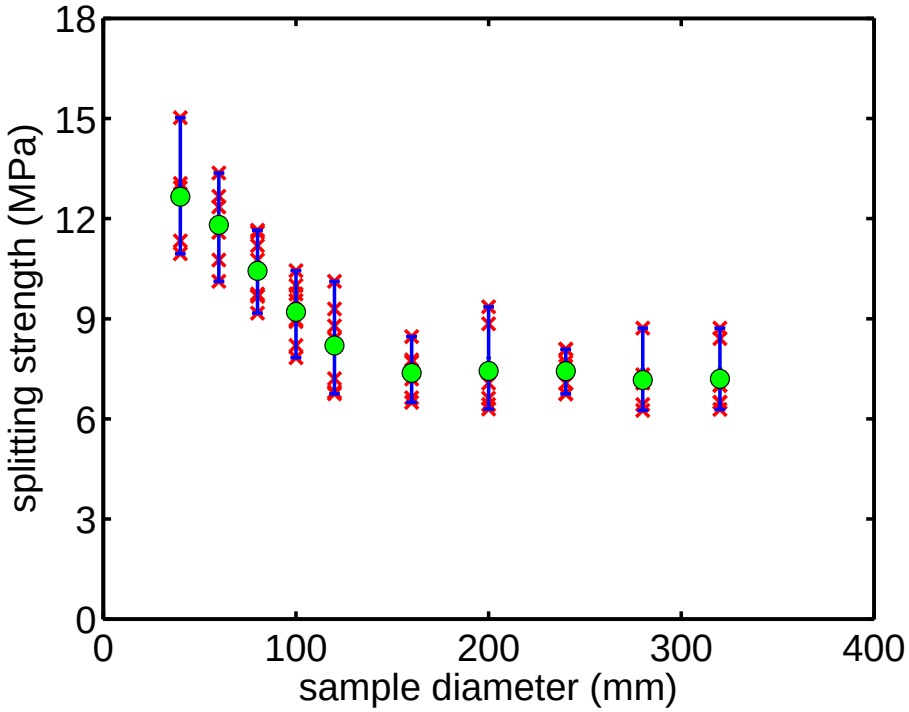

Figure 3.16: 2D BTS vs. sample size, $\beta \to \infty$.

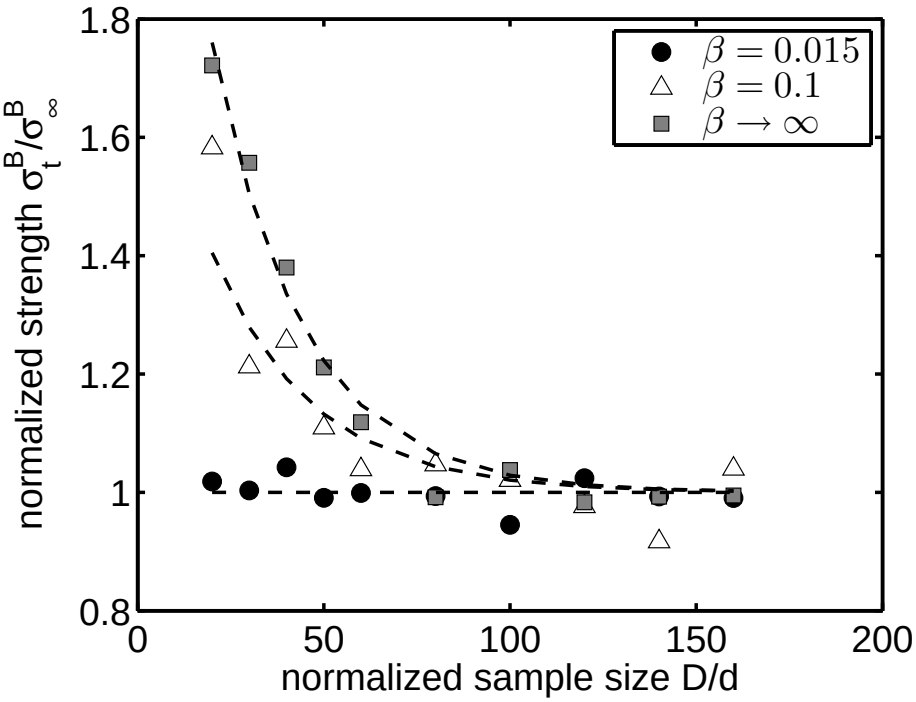

Figure 3.17: Variation of the normalized splitting strength with the sample size in 2D.

3.4 Three Dimensional Simulations

3.4.1 Macro-scale Failure Patterns

Three dimensional simulations are performed with the same micro-scale baseline parameters as those in 2D, see Tables 2.1 and 2.3. The macro-scale properties in 3D, obtained from the unconfined tests on a cylindrical sample of diameter 40 mm and height 80 mm, are not drastically different from those in 2D. Compared with the 2D results, the strength ratios are only slightly changed. At $\beta = 0.1$, the strength ratio $\sigma_c/\sigma_t = 14.7$ is comparable with common rocks.

The Brazilian test is performed with numerical samples of thickness $t = 10$ mm. A total of 12 simulations are conducted with $\beta = 0.015$, 0.1 and ∞ and $D = 40$, 120, 200 and 280 mm. Plane strain condition is imposed by using two vertical walls to constrain the out-of-plane displacements in the front and back of the particle assembly. A micro-crack in 3D is now illustrated by projecting a circle on the contact plane onto a vertical plane. Radii of the circles are magnified from the contact radius $\overline{R}$ for easier visualization. A line segment means the micro-crack is perpendicular to the vertical projection plane while a full

circle means that it is parallel.

Summary of the failure patterns around the peak loading level from the 3D simulations is presented in Figure 3.18. The overall trend from the 3D simulations agrees with that of 2D simulations on the dependence of the failure scenarios on β and D. Among these 12 cases, two cases with $\beta = 0.015$ and 0.1 and $D = 40$ mm show an unambiguous pattern of Scenario I, where initiation and propagation of a tensile crack from the center of the specimen causes the sample to split into two halves. The failure scenario with $\beta = 0.015$ and $D = 120$ mm seems to be in the transition. There are very few micro-cracks accumulating near the loading walls. Across the diameter, the micro-cracks appear nearly simultaneously and gradually coalesce to cause the diametrical failure. Unlike the 2D case with $\beta = 0.015$ and $D = 280$ mm, there is no evidence of secondary crack growth from the perimeter in 3D. Meanwhile, the failure patterns in all the other cases seem to follow Scenario II. The cases with $\beta \to \infty$ show the clearest evidence of tensile cracks emanating from the damaged zones and the crack paths being strongly localized. In contrast, the splitting failures with $\beta = 0.1$ and 0.015 ($D > 40$ mm) involve tortuous and less well-defined crack trajectories, bearing resemblance to the growth of en-echelon cracks. As consistent with the 2D results, at a given sample size D, the loading level at which initiation of the primary crack occurs increases with β. At $\beta \to \infty$ and $D = 120$ mm, the primary crack starts to grow around 90% of loading. However, at $\beta = 0.1$, micro-cracks associated with early development of the primary crack are evident at about 80% of loading. At $\beta = 0.015$, there are already considerable micro-cracks accumulation across the sample diameter at 80% of loading, see Figure 3.19.

In general, the 3D simulation results substantiate the conclusions drawn from the 2D analysis that there are two primary failure scenarios in the Brazilian tests depending on the sample size as well as material properties with the softening coefficient β serving as the proxy. Compared with the 2D simulations, Scenario I is observed in narrower parameter ranges of β and D in 3D. A possible reason is that the 3D nature of the simulations has likely promoted micro-scale failures adjacent to the loading walls. The fact that micro-cracks in nearly full circles can be observed near the walls means that the out-of-plane response also

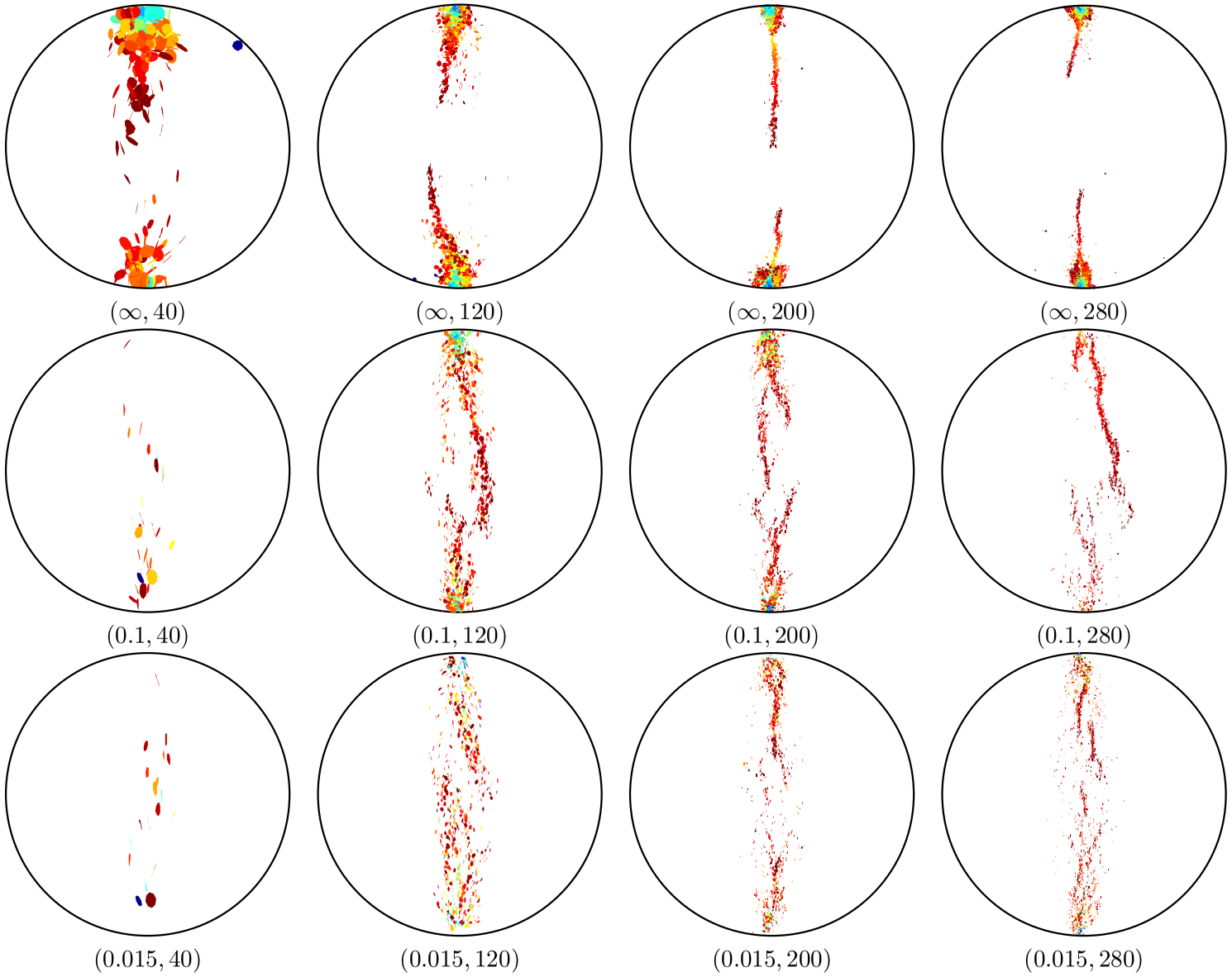

Figure 3.18: Dependence of the micro-scale failure mechanisms on the softening coefficient β and the diameter of the specimen D from 3D simulations; the simulation cases are indexed by $(\beta,\ D)$; unit of D in mm.

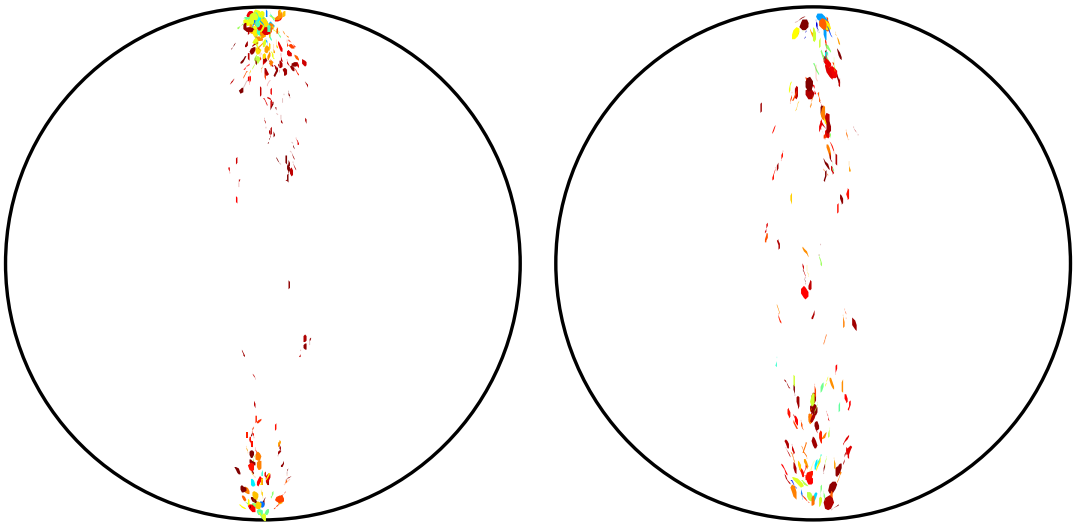

(a) $\beta = 0.1$ (b) $\beta = 0.015$

Figure 3.19: Micro-scale failures at 80% of loading at (a) $\beta = 0.1$ and (b) $\beta = 0.015$ with $D = 120$ mm from 3D simulations.

contributes to the bond breakage in the 3D simulations. Though the front and back of the specimen are constrained by the wall elements, the walls do not prevent out-of-plane displacements of individual particles within the bounds of the two walls, which is in contrast to the 2D simulations where the displacements are only in-plane. Consequently, Scenario II becomes more likely to occur in 3D. The 3D effect or the effect of sample shape in experiments has been reported in the literature [86, 115] and is indeed the primary reason for the thickness requirement of $t/D \geq 0.5$ for the ISRM suggested method [64].

3.4.2 Micro-scale Failure Evolution

The force-displacement relationships for the simulations with $\beta = 0.015$, 0.1, and ∞ and $D = 120$ mm are summarized in Figure 3.20. When $\beta = 0.015$, we do not observe a clear plateau in the pre-peak stage. After carefully examining the numerical model and comparing with 2D simulations, it seems that three dimensional model tends to split into two halves after the diametrical fracture is fully developed. Moreover, the sample losses its stability that cannot resist the load with the presence of the diametrical fracture. We can still observe some secondary fractures near the perimeter of the sample. Nevertheless, they are not dominant mechanism in the post-peak stage. Surprisingly, the force-displacement curve when $\beta \to \infty$ exhibits a plateau in pre- and post-peak stages. However, the evolution

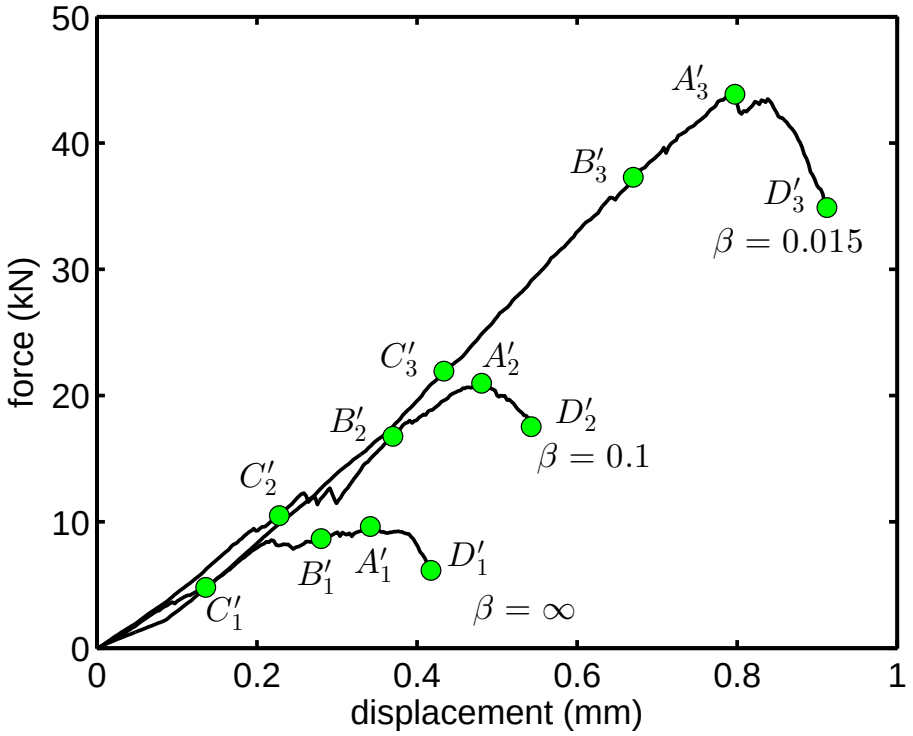

Figure 3.20: Force-displacement relationships for the 3D Brazilian tests with $\beta = 0.015$, 0.1, ∞ and $D = 120$ mm.

of the number of damaged bonds indicates no other mechanisms more significant than the indentation-type failure. To clarify the difference between 2D and 3D simulation results, more tests are performed with the same set of micro-scale parameters, except the random number that controls the random nature of the particle assembly. The results show that the plateau is a random behavior for that particular sample, instead of an intrinsic material property.

At $\beta \to \infty$, a shear zone is initiated and developed during the loading process. At approximately 50% load ratio, the size of the shear zone is clearly identifiable. At the bottom of the shear zone, a main crack is growing towards the center of the sample. When the load is increased to 90%, the main fracture keeps growing, as well as some secondary micro-cracks on the perimeter of the shear zone. The whole sample fails when the main fracture is formed along the diametric center of the sample, see stage $A_1^{'}$. Afterwards, the stress-strain curve starts to drop, behaving like a brittle material. The material fails when the two main fractures are connected, see Figure 3.21(d).

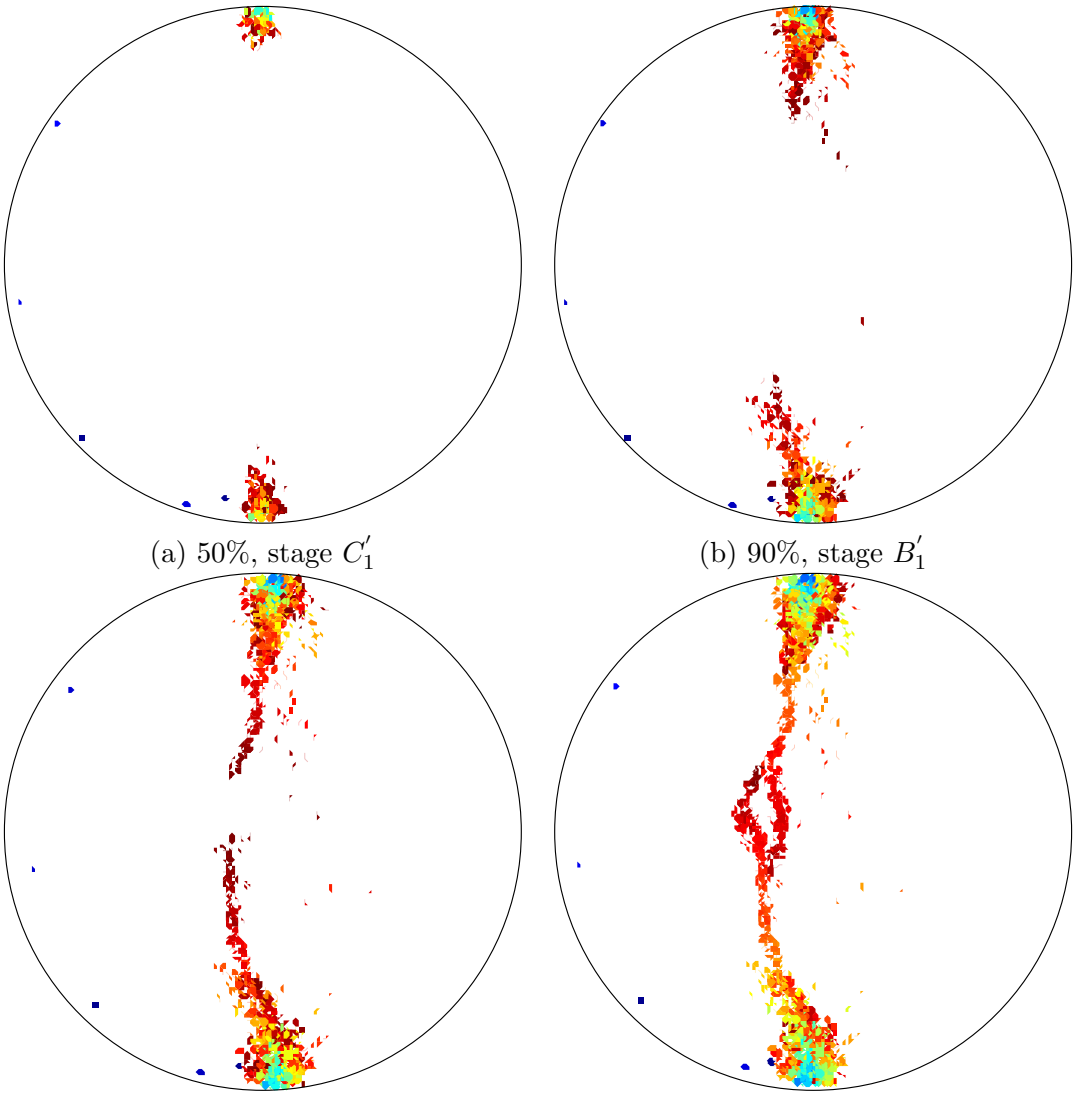

(a) 50%, stage $C_1^{'}$ (b) 90%, stage $B_1^{'}$

(c) peak, stage $A_1^{'}$ (d) post-peak, stage $D_1^{'}$

Figure 3.21: failure process in 3D, $\beta = \infty$ and $D = 120$ mm

At $\beta = 0.1$, the failure mechanism is similar to that of $\beta \to \infty$, except the presence of micro-cracks near the center of the sample. See Figure 3.22(b). When the load level reaches the peak, both the shear zones near the loading walls and the diametrical fracture are fully developed. As the load keeps increasing, the sample fails immediately after the peak. Even though the primary failure mechanism is similar to that of $\beta \to \infty$, the diametrical fracture is not always growing from the loading point towards the center. Instead, some of the micro-cracks are initiated near the center and coalesced together to form the main fracture. Therefore, the overall pattern appears to have a mixed-mode characteristics.

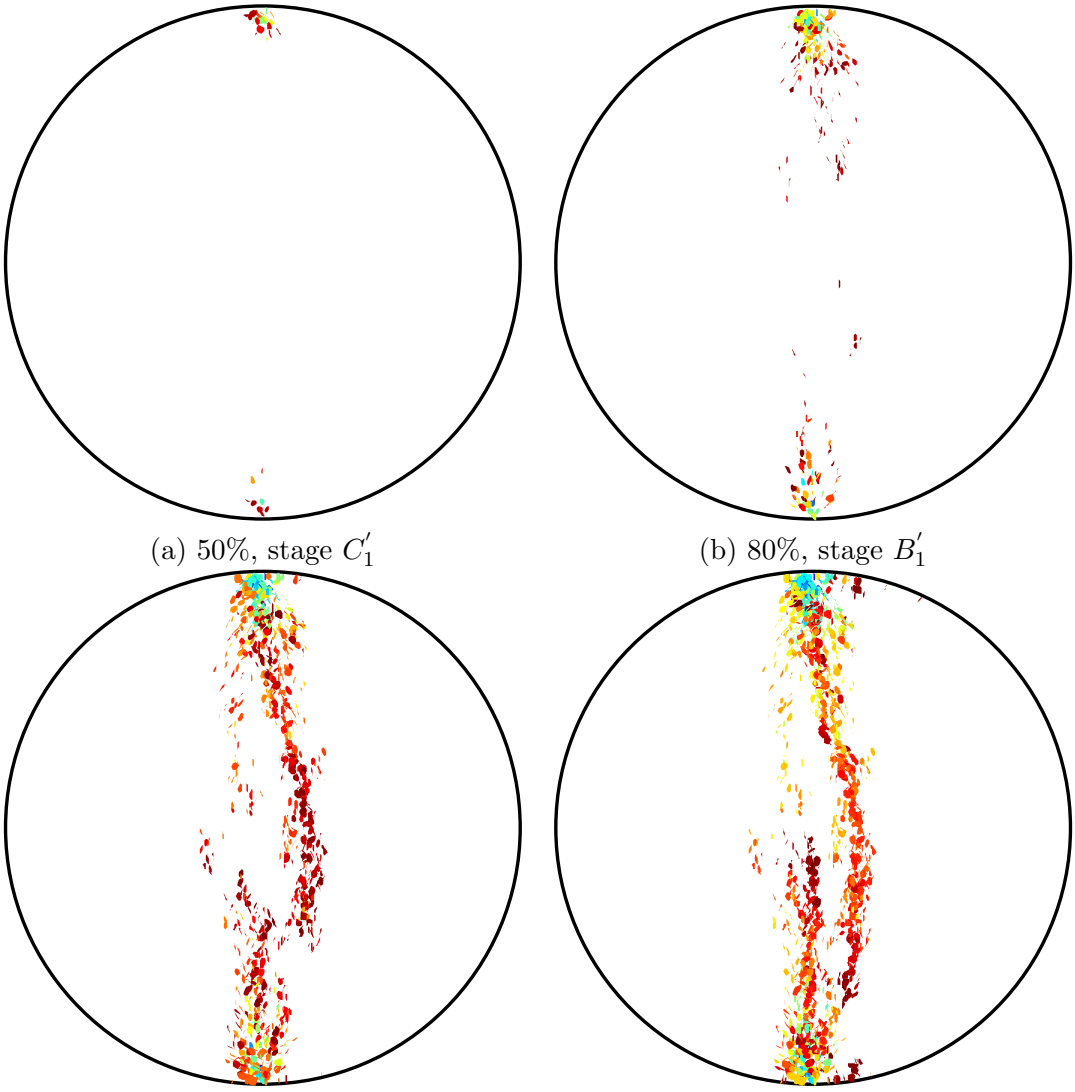

(a) 50%, stage C_1'

(b) 80%, stage B_1'

(c) peak, stage A_1'

(d) post-peak, stage D_1'

Figure 3.22: failure process in 3D, $\beta = 0.1$ and $D = 120$ mm

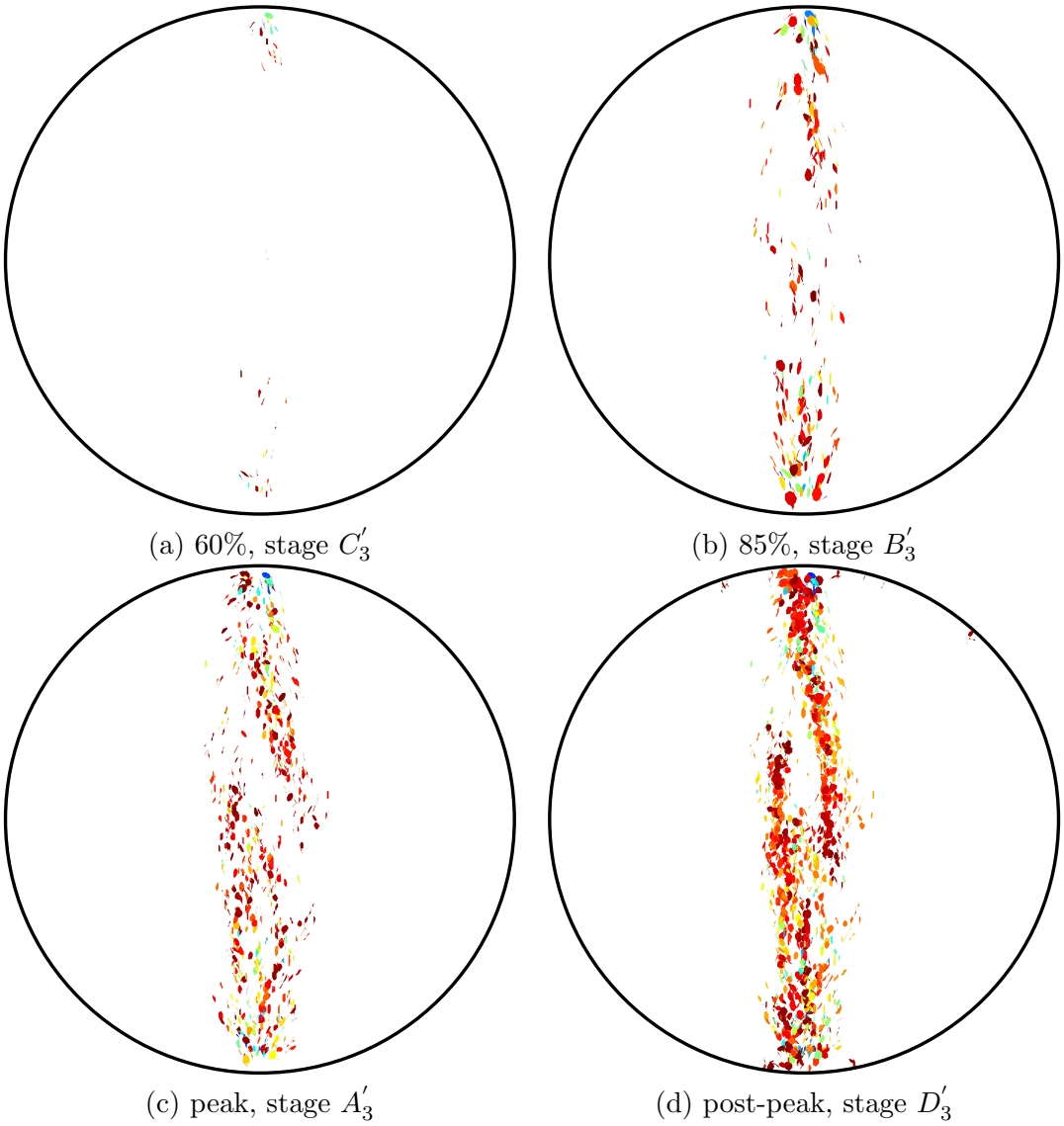

(a) 60%, stage C_3'

(b) 85%, stage B_3'

(c) peak, stage A_3'

(d) post-peak, stage D_3'

Figure 3.23: failure process in 3D, $\beta = 0.015$ and $D = 120$ mm

At $\beta = 0.015$, the sample allows stress redistribution by forming a football-shaped damage zone along the center of the sample. No micro-cracks can be identified before the load increased to 60%, stage $C_3^{'}$, in Figure 3.23(a). As the load increases, more and more micro-cracks appears and some of them started to coalesce together to form a macro-fracture. When the load reaches the peak, then the main fracture is clearly seen from the center of the sample. The failure process is basically the same as observed in 2D simulations with $\beta = 0.015$. Note that the fracture is formed through coalescence of micro-cracks and the main fracture is formed almost simultaneously along the diametric direction of the sample. After the main fractures along the center diameter are connected, the sample fails and generates more micro-cracks near the perimeter of the disk. More importantly, no clear evidence of shear zones under the loading walls can be observed through the whole failure process.

3.4.3 Size Effect

In 3D models, an additional ductility is added to the samples by introducing a finite softening coefficient. Thus the sample allows more deformation than that of $\beta \to \infty$ before it breaks. Therefore, the stress field along the diametric center is more uniform. The failure mechanisms are similar to 2D simulations. So in order to see if the size effect transition still can be observed in 3D models, Brazilian tests are conducted on various samples with different sizes. With $\beta \to \infty$, the sample size varies in the range from D =40 - 320 mm. The relationship between BTS and sample size is presented in Figure 3.26. It shows a clear strength decay with sample diameter up to $D = 120$ mm. When $D > 120$ mm, the strength is approaching a constant. With $\beta = 0.015$, samples with D =40 - 160 mm are used to investigate the size effect, because the size effect is usually more obvious for small sample size. Figure 3.24 shows that no clear sign of size effect can be seen in the tested sample size range. Similarly, we also performed tests with $\beta = 0.1$ to explore if the same size effect transition trend can be captured in 3D simulations, as shown in Figure 3.22. Strength decay happens when sample size is within a threshold $D < 120$ mm. Then we normalize BTS w.r.t. the value at asymptote as we did in 2D simulations. The results are summarized in

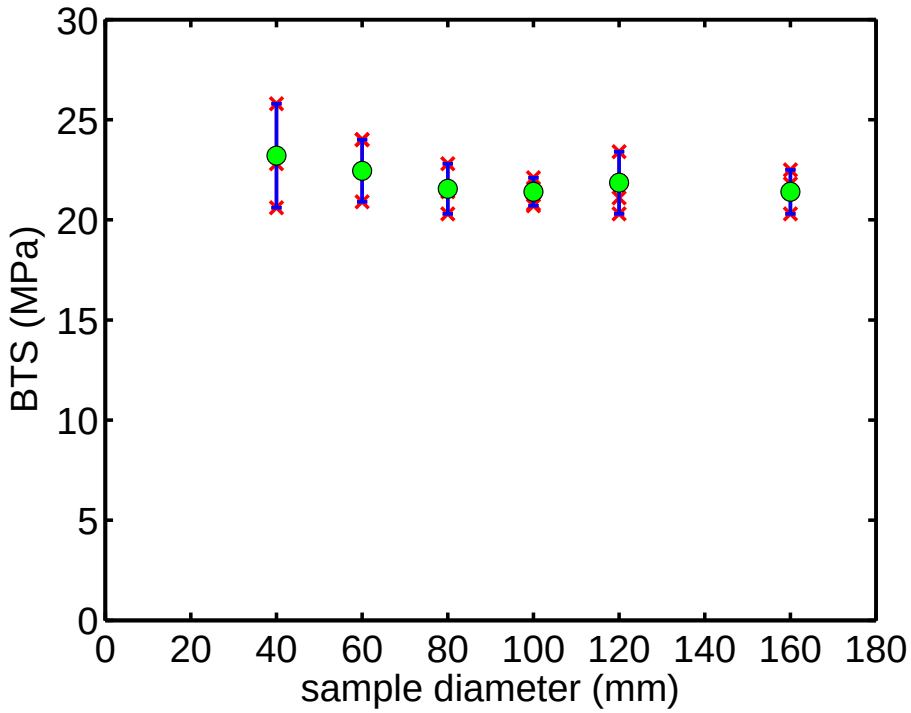

Figure 3.24: 3D BTS vs. sample size, $\beta = 0.015$.

Figure 3.27, indicating that the size effect transition exists in 3D simulations, too.

3.5 Limit Analysis

Clearly, the size effect transition with different softening coefficient β is associated with failure mechanisms. At $\beta \to \infty$, the energy is mainly dissipated from the wedge-shaped shear zone near the loading walls, as well as the tensile crack beneath it. The final failure pattern, as consistent with experimental observations, is schematically shown in Figure 3.28. Based on this failure pattern, we can simply assume a final fracture pattern with two identical wedge-shaped shear zones below the loading walls that are connected by a tensile crack located along the diametrical center line of the sample, as shown in Figure 3.29(a). The size of the wedge is represented by length l [L], the angle between the wedge and horizontal axis is assumed to be θ, which is related to internal friction angle ϕ of the material that can be determined from experiments. Because of the symmetric nature of the problem, we can assume cohesion c [F/L] on the contacting surfaces of block 1 and 3, as well as block 1 and 2. Note that c is also a material constant. Since the main fracture in

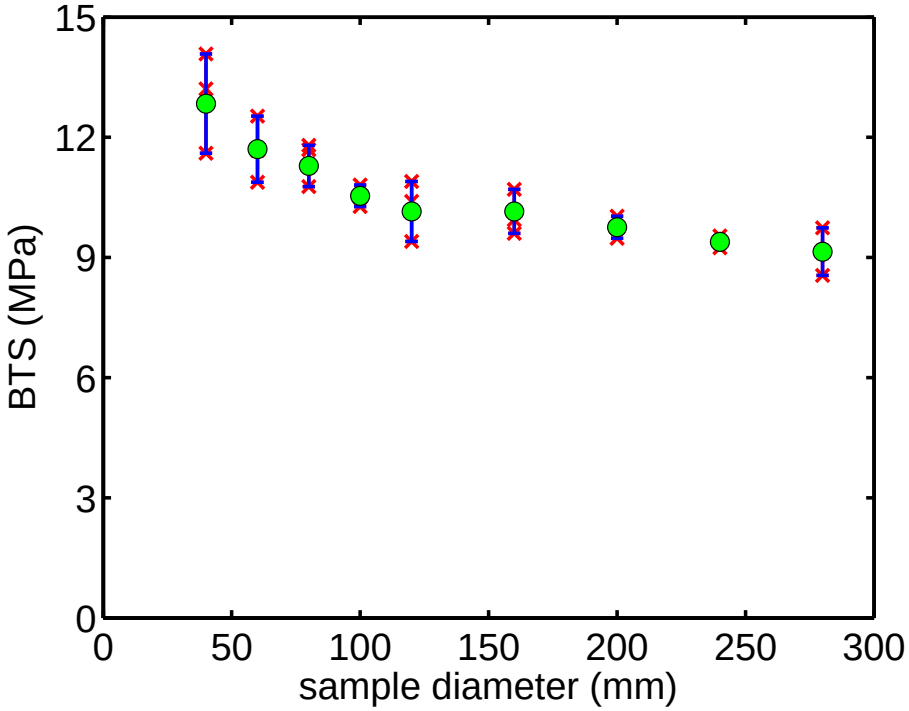

Figure 3.25: 3D BTS vs. sample size, $\beta = 0.1$.

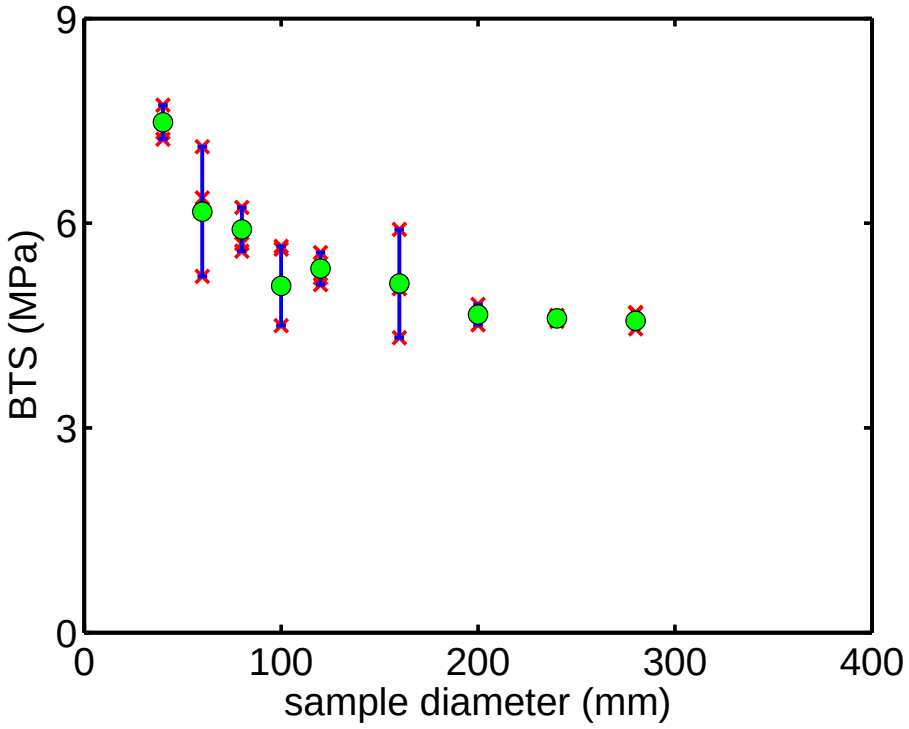

Figure 3.26: 3D BTS vs. sample size, $\beta \to \infty$.

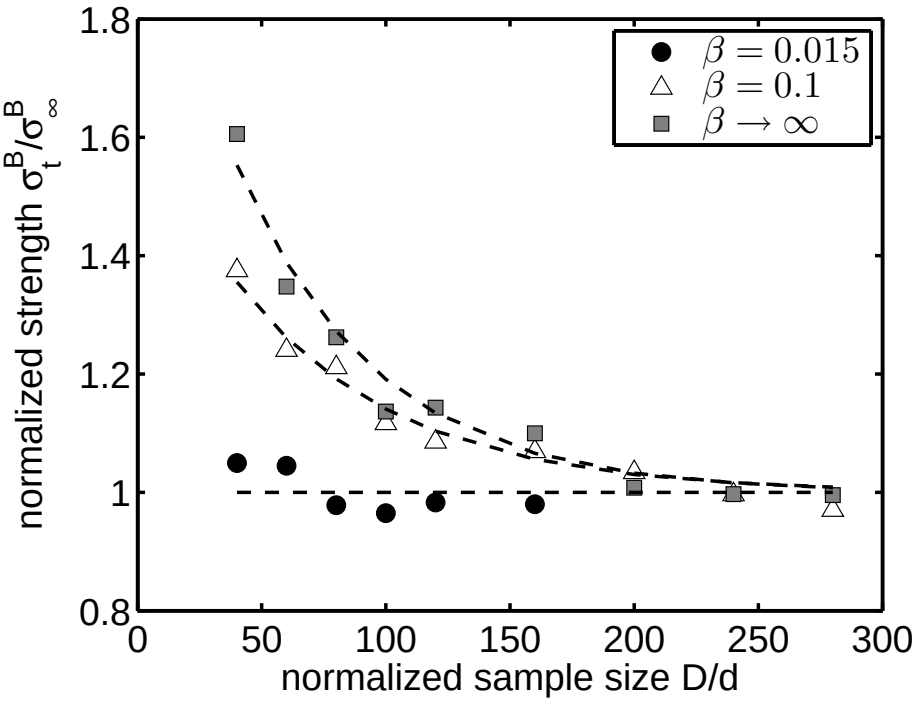

Figure 3.27: Variation of the normalized splitting strength with the sample size in 3D.

the center of the sample is assumed to be a tensile crack, the friction force on the fracture surface is zero (smooth surface). Meanwhile, the tensile and compressive strength of the material are assumed to be $\bar{\sigma}_t$ and $\bar{\sigma}_c$ [F/L], respectively. It has been shown in Chapter II that the unconfined strengths are material constants determined by the micro-scale normal bond strength and softening coefficient. For simplicity, we further assume dilatancy angle $\psi = \phi$. In this study, the yield criterion is dominated by Mohr-Coulomb criterion with a cut-off in tensile regime at $\sigma = \bar{\sigma}_t$. Thus, we have:

$$\bar{\sigma}_c = \frac{2c\cos\phi}{1-\sin\phi} \tag{15}$$

The hodograph of the velocity vector can be easily determined in terms of the velocity v_{01} by using any kinematically admissible velocity field, as shown in Figure 3.29(b), we have,

$$v_{12} = v_{13} = v_{01}/\sin(\theta-\phi) \tag{16}$$

$$v_{02} = v_{03} = v_{01}\cot(\theta-\phi) \tag{17}$$

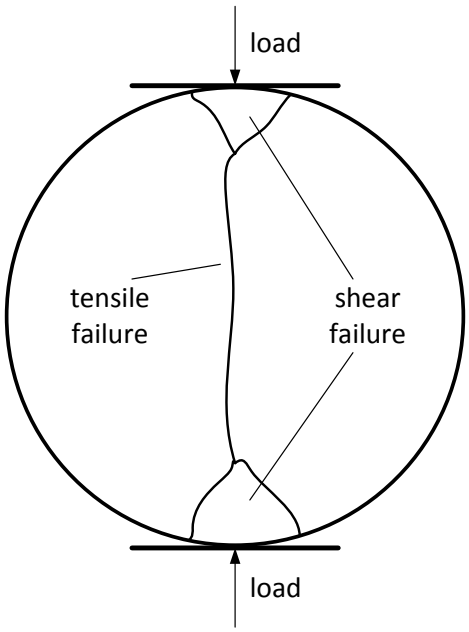

Figure 3.28: Schematic of a shear failure mechanism in the Brazilian test [52, 124].

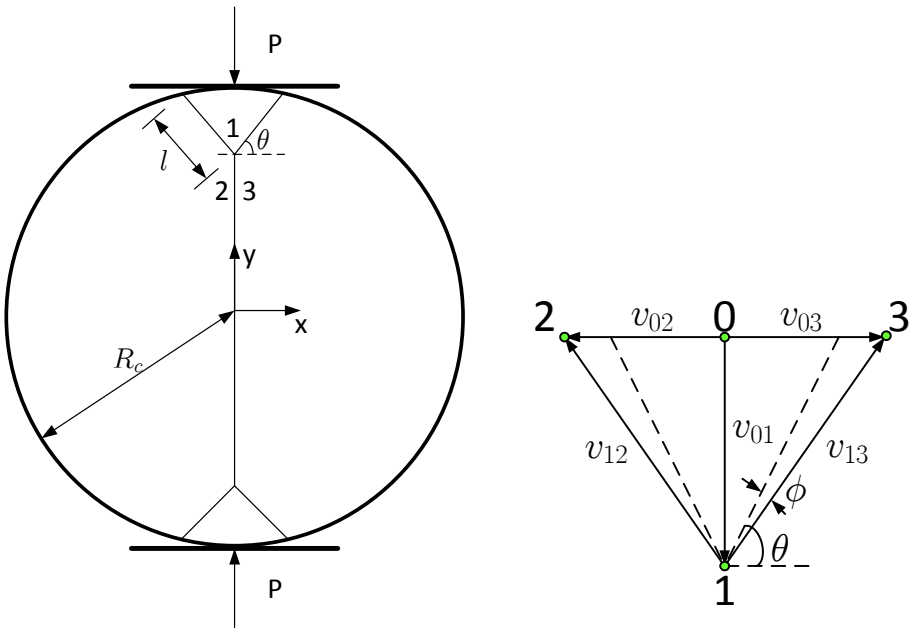

(a) failure mechanism model (b) velocity hodograph

Figure 3.29: Upper bound analysis.

$$v_{23} = 2v_{01}\cot(\theta - \phi) \tag{18}$$

Therefore, the internal energy dissipation rate will be the sum of the energy dissipation occurring on each slip surface and the tensile crack in the center. Because of symmetry we find:

$$\mathbb{D} = 4lcv_{12} + [2R_c - 2l\sin\theta]\bar{\sigma}_t v_{23} \tag{19}$$

where $\mathbb{D}$ is the total internal energy dissipation rate. To find the upper bound we equate $\mathbb{D}$ to the power of the external forces. The only external load is the applied force P. Therefore,

$$\mathbb{R} = 2Pv_{01} \tag{20}$$

where $\mathbb{R}$ is the total external input energy rate. Now substitute Eq. 16-18 into Eq. 19, and apply the energy conservation law, we have:

$$P = l \cdot \frac{2c\cos\phi - 2\bar{\sigma}_t \sin\theta\cos(\theta - \phi)}{\sin(\theta - \phi)} + 2R_c\bar{\sigma}_t\cot(\theta - \phi) \tag{21}$$

Substitute Eq. 13 into Eq. 21, then we have:

$$\sigma_t^B = \frac{l}{D} \cdot \frac{2[2c\cos\phi - 2\bar{\sigma}_t \sin\theta\cos(\theta - \phi)]}{\pi\sin(\theta - \phi)} + \frac{2\bar{\sigma}_t}{\pi}\cot(\theta - \phi) \tag{22}$$

Plug Eq. 15 into Eq. 22 yields:

$$\sigma_t^B = \frac{l}{D} \cdot \frac{2[\bar{\sigma}_c(1 - \sin\phi) - 2\bar{\sigma}_t \sin\theta\cos(\theta - \phi)]}{\pi\sin(\theta - \phi)} + \frac{2\bar{\sigma}_t}{\pi}\cot(\theta - \phi) \tag{23}$$

Eq. 23 can be further simplified as:

$$\sigma_t^B = \frac{l}{D}A + B \tag{24}$$

where $A = \dfrac{2[\bar{\sigma}_c(1 - \sin\phi) - 2\bar{\sigma}_t \sin\theta\cos(\theta - \phi)]}{\pi\sin(\theta - \phi)}$ and $B = \dfrac{2\bar{\sigma}_t}{\pi}\cot(\theta - \phi)$ are material constants. The load P increases with sample size D as shown in Eq. 13. The plastic zone size l also increases with sample size when D is within a threshold value. When sample size is large enough, l remains that same and thus l/D ratio becomes negligible. Moreover,

when l/D is negligible, the size effect vanishes and BTS is dominated by constant B which is proportional to $\bar{\sigma}_t$. Thus, for large enough samples, the Brazilian tests could only be used to approximate the tensile strength of the material up to a constant, even though the material fails in a mechanism governed by indentation-type cracks. Based on the passive failure mode, θ is estimated as $\theta = \frac{\pi}{4} + \frac{\phi}{2}$. If we assume the friction angle $\phi = 0$ or $40°$, then we have,

$$B = \frac{2}{\pi}\bar{\sigma}_t \cot(\theta - \phi) \approx \frac{2}{\pi}\bar{\sigma}_t \quad \text{or} \quad \frac{2}{\pi}\cot(\frac{\pi}{4} - \frac{\phi}{2})\bar{\sigma}_t \tag{25}$$

Eq. 25 suggests that $\sigma_t^B/\bar{\sigma}_t \simeq B/\bar{\sigma}_t \in [2/\pi, \frac{2}{\pi}\cot(\frac{\pi}{4} - \frac{\phi}{2})] = [0.64, 1.36]$. The ratio of BTS to UTS predicted by this analysis is consistent with the experimental data reported in [94]. Hence Eq. 25 gives a good estimation of the BTS/UTS ratio for indentation type of failure. In other words, when the sample is large enough, the splitting strength obtained from Brazilian test under indentation-type failure could be only about half of the uniaxial tensile strength of the material.

At $\beta = 0.015$, the energy is mainly dissipated through damaged bonds, or in other words, the development of the fracture process zone along the diametrical center of the sample. Before micro-crack initiates, a football-shaped damage zone is observed in the center part of the disk along its diameter. The shape of the zone remains roughly the same regardless of the sample size, as demonstrated in Figure 3.30. As the load increases, a macro-crack is formed in the center of the FPZ. When the load reaches the "peak", the two halves of the disk started to resist the load and softening bonds start to appear near the perimeter of the disk.

The total amount of energy associated with bond damage and breakage in the central portion of the sample is determined and illustrated in Figure 3.31. The density of nominal energy release is defined as the total energy E normalized by D^2. At each sample size, at least three samples are used to calculate the total dissipated energy. The data shows roughly a constant trend which means at the final stage, the energy dissipated in the football-shaped region is a constant when the sample size is normalized to one unit. As a matter of fact, the sample fails at roughly the same critical strain in Brazilian tests. Here we assume the

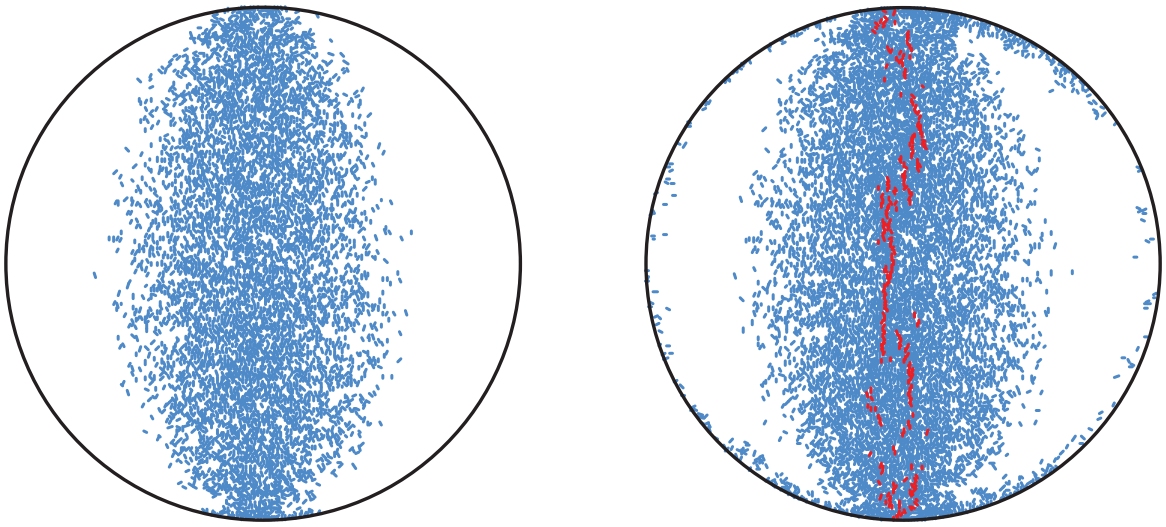

(a) FPZ in the center (b) FPZ and center crack

Figure 3.30: Energy dissipation in FPZ, $\beta = 0.015$.

vertical strain at peak is ϵ_c. Then the total input energy at the final stage can be expressed as:

$$\mathbb{E}_{in} = P \cdot \epsilon_c D/2 \tag{26}$$

where $\mathbb{E}_{in}$ is the total input energy. Meanwhile, the total energy dissipated can be approximated as:

$$\mathbb{E}_{out} = \mathbb{E}_{FPZ} \cdot D^2 \tag{27}$$

where $\mathbb{E}_{out}$ is the total energy dissipated, $\mathbb{E}_{FPZ}$ is the total energy dissipated in the football-shaped zone in a disk of unit size. Now substitute Eq. 13 into Eq. 26 - 27, we have:

$$\sigma_t^B = \frac{2P}{\pi D} = \frac{4\mathbb{E}_{FPZ}}{\pi \epsilon_c} = const. \tag{28}$$

As consistent with the theory of elasticity, Eq. 28 indicates that BTS obtained from Brazilian test when $\beta = 0.015$ is a constant that independent of the sample size.

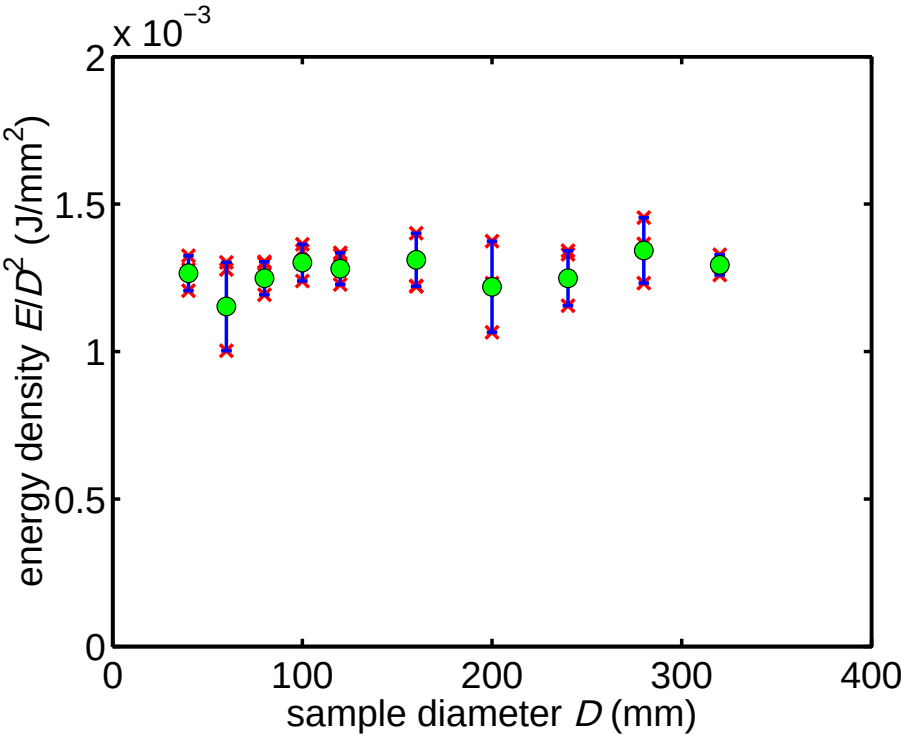

Figure 3.31: Energy dissipation in unit area of FPZ.

In this study, we assume UTS represent the intrinsic tensile strength of the material. Indeed, direct tension tests have showed that the tensile strength when $\beta = 0.015$ is 4.75 MPa, which is much lower than that from Brazilian test. That's because in Brazilian test, the loading walls restrain the splitting movement of the two halves of the Brazilian disc. Therefore, the strength won't decrease immediately after the main crack is formed. This boundary effect has been widely observed in experiments. However, in direction tension tests, the stress-strain curve would drop right after the mode I crack appears. Generally, the crack initiation stress is about 90%-95% of the peak. In numerical simulations, however, the crack initiation strength is only about 50% of the peak as shown in Figure 3.4. So if we consider the crack initiation stress as a representative of the intrinsic tensile strength of the material, then BTS is about 6.43 MPa, which is comparable to the uniaxial tensile strength of the material. In the next section, we will compare BTS with UTS in detail.

3.6 BTS vs. UTS

3.6.1 2D Results

The relationship between BTS and UTS has been under discussion for many decades. It has been conclude based on theoretical and experimental studies that BTS may under estimate the tensile strength with low uniaxial compressive to tensile strength ratio σ_c/σ_t [40, 29]. Meanwhile, some researchers believe that BTS gives a good approximation of tensile strength based on experimental evidences [5, 6, 46, 65]. On the other hand, a significant number of researchers show that BTS may overestimate UTS of rocks [38, 91, 43, 86]. As a result, some researchers argue that BTS should not be considered as a measure of UTS [63].

In this section, the relationship between BTS and UTS is discussed based on numerical simulation results. We use 2D simulation results as an example for this analysis. As suggested by the numerical simulation results, the continuous development of micro-cracks in Scenario I occurs at about 90% of peak stress. While in Scenario II, the crack initiation happens earlier at about 80% of peak stress. The crack initiation stress is usually at 90%–95% of peak stress in experiments [123]. Hence, we use both the peak and crack initiation stress to determine BTS.

A prerequisite in identifying crack initiation stress in Brazilian tests is to distinguish different failure mechanisms by analyzing the evolution of micro-events, including bond damage and breaking. To achieve such a goal, we monitor the number of micro-events during the whole failure process and analyze the ratio of broken to damage bonds number.

At $\beta = 0.015$ and $D = 280$ mm, history of the micro-crack number is shown in Figure 3.32. The number of damaged bonds N_d is consistently one order higher than that of the broken bond N_b. Note that this ratio reflects the contact behavior and can be adjusted by tuning softening coefficient β. The first micro-crack does not appear until the number of damaged bonds accumulated to about 5500, which indicates a nearly uniform stress state along the diametrical center of the sample. History of the ratio N_d/N_b is shown in Figure 3.33. From this figure, we can clearly identify two linear segments divided by the point A_3, note that A_3 is associated with the stage marked on the force-displacement curve shown in

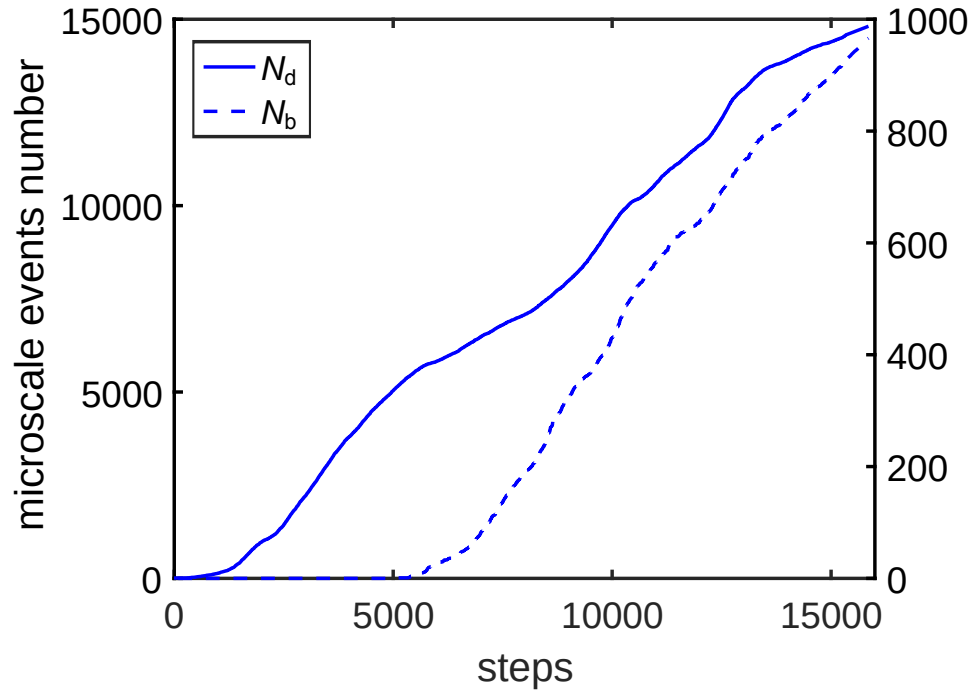

Figure 3.32: Histories of the number of micro-cracks N_b and the number of softening bonds N_d, when $\beta = 0.015$ and $D = 280$ mm.

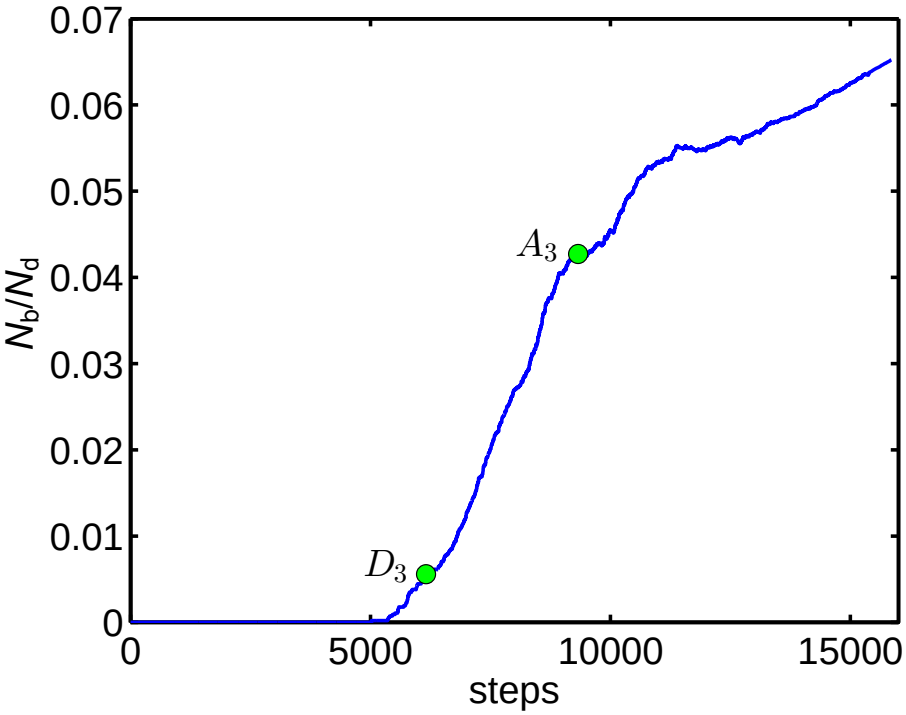

Figure 3.33: History of the ratio of N_b/N_d, when $\beta = 0.015$ and $D = 280$ mm.

Figure 3.4. Here we define A_3 represents the nominal peak of BTS, because the different slopes of these two linear segments indicates two different failure mechanisms in Brazilian test. First, the linear part from D_3 to A_3 corresponds to the growth of the main center crack. At A_3, the crack is fully developed and the sample is separated into two halves. The second linear segment from $A_3$to the end represents a secondary mechanism that the two halves work together to resist the load as two "columns". As a result, the load keeps increasing until the two halves are crushed, which gives the peak at $\sigma = 13$ MPa. The micro-crack events prior to stage D_3 are randomly distributed in the sample. Initiation of the center crack starts at stage D_3. Thus the crack initiation stress, as well as the nominal peak stress can be determined according to the loading steps, as shown in Figure 3.34. At D_3, the crack initiation stress is 6.4 MPa at step 5500. Meanwhile, the nominal peak stress at A_3 is 12.0 MPa. If we use the crack initiation stress at D_3 to represent the BTS, thus the ratio $\sigma_{\mathrm{BTS}}/\sigma_{\mathrm{UTS}} = 6.4/4.75 = 1.35$ is in a reasonable agreement with [72, 94].

At $\beta \to \infty$, the history of the number of broken bonds is shown in Figure 3.35. At C_1, the cumulative broken bond number is approaching 200, the curve shows a clear turning point that divides the whole curve into a nonlinear and a linear segment. As shown in Figure 3.5, the nonlinear increasing segment is associated with the development of micro-cracks near the loading walls. When the shear zone is fully developed, a crack beneath it appears and grows towards the center of the sample. As the crack grows, the evolution of the broken bond number exhibits a linear pattern. As a result, we could assume C_1 is the stage when the tensile crack initiates. From Figure 3.36, the nominal BTS determined at stage C_1 is about 4.9 MPa. Note that the oscillation observed on the stress curve stems from the limited number of particle-wall contacts. Before C_1, the primary energy dissipation mechanism is governed by the development of the shear zone beneath the loading walls. During the loading process, only limited number of particles have contact with the wall. The total contact force is significantly impacted when individual bond breaks.

Evolution of micro-cracks at $\beta = 0.1$ is also summarized to demonstrate the effect of failure mechanisms on the BTS. The failure mechanism in this case exhibits a combined scenarios of "center splitting mode" and "indentation-type". We can observe both the

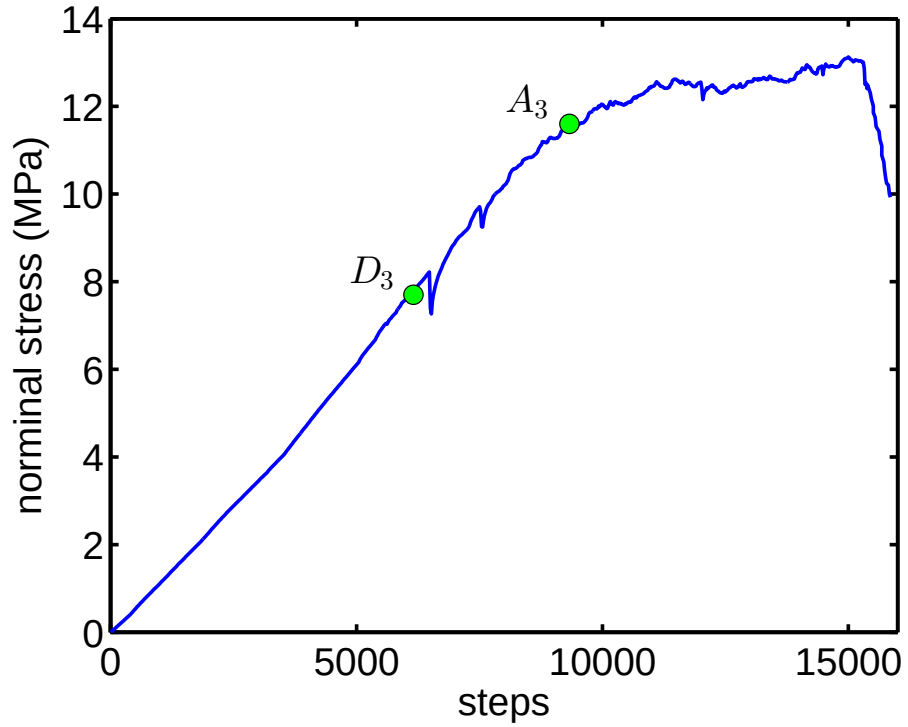

Figure 3.34: History of the nominal stress when $\beta = 0.015$ and $D = 280$ mm.

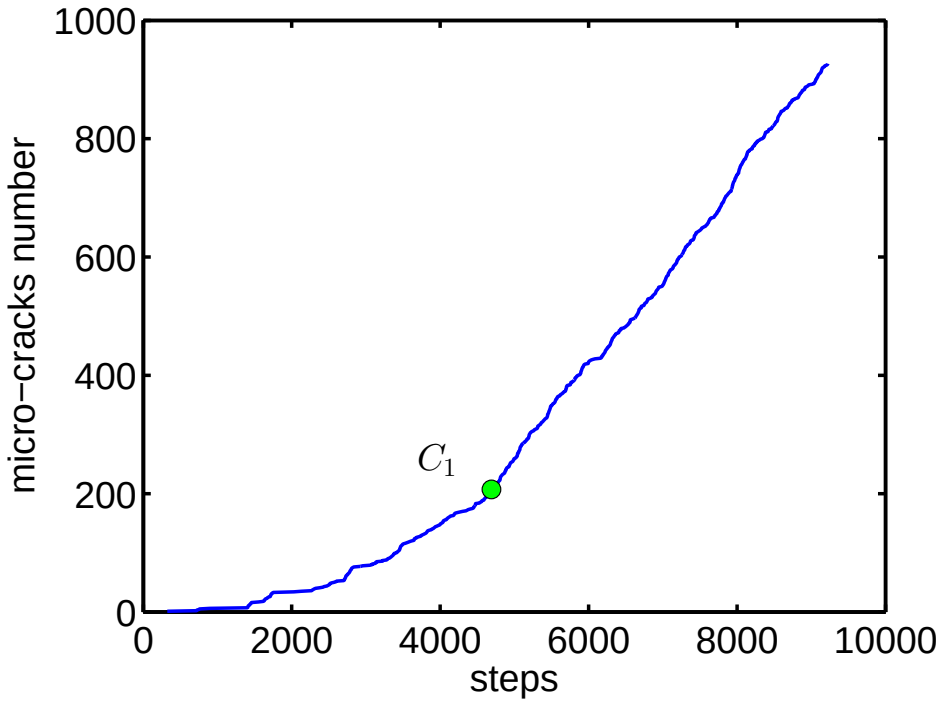

Figure 3.35: History of the number of micro-cracks when $\beta \to \infty$ and $D = 280$ mm.

damage zone under the loading wall and the crack growth near the center of the sample. The total micro-crack number shows a similar pattern to that of $\beta = 0.015$. However, the magnitude of N_d is lower while N_b remains approximately the same compared to those of $\beta = 0.015$. Figure 3.38 shows three segments: nonlinear segment before B_2, linear segment between B_2 and A_2, and nonlinear segment after A_2. These three different characteristics indicate that the failure of the Brazilian test is governed by three different mechanisms. The initial nonlinear segment before B_2 corresponds to the development of the micro-cracks beneath the loading walls. The significant oscillation before $D_2$is associated with random micro-cracks distributed throughout the sample. When the damage zone starts to grow, the curve is stabilized and increases nonlinearly from D_2 to B_2. Note that this pattern is similar to that of $\beta \to \infty$, namely, indentation-type failure. As the load keeps increasing, the tensile crack growth near the center becomes the dominant mechanism and thus the curve exhibits a linear characteristic. As discussed in the other two cases, the linear segment could be attributed to two sources: growth of the tensile cracks from the center and beneath the damage zone. In the case of $\beta = 0.1$, it is hard to distinguish the source because the growth of the tensile crack from the center and beneath the damage zone is simutaneous. Nevertheless, the curve in Figure 3.38 still shows a linear segment. Regardless of the type of the tensile crack, the sample loses its stability as the crack grows. Thus we define stage B_2 as being associated with the crack initiation. Compared to the peak at stage A_2, Figure 3.39 shows that the crack initiation stress is about 90% of the peak, which is realistic compared to experimental observations. Indeed, crack initiation stress at B_2 is 9.4 MPa while UTS is 8.37 MPa. In the post-peak stage, the ratio N_b/N_d shows a shallower slope that is related to the crushing mechanism. Indeed, multiple types of failure are all reflected in the history of micro-events ratio N_b/N_d.

We use the method discussed above to identify the crack initiation and peak stress in other simulations of the Brazilian tests. The results are summarized in Figures 3.40–3.42. At $\beta \to \infty$, the crack initiation stress decreases slightly as the sample size increases; however, it then approaches an asymptote when $D > 120$ mm. The BTS is about half of UTS. Thus UTS is underestimated if measured using the Brazilian test. On the other hand, the crack

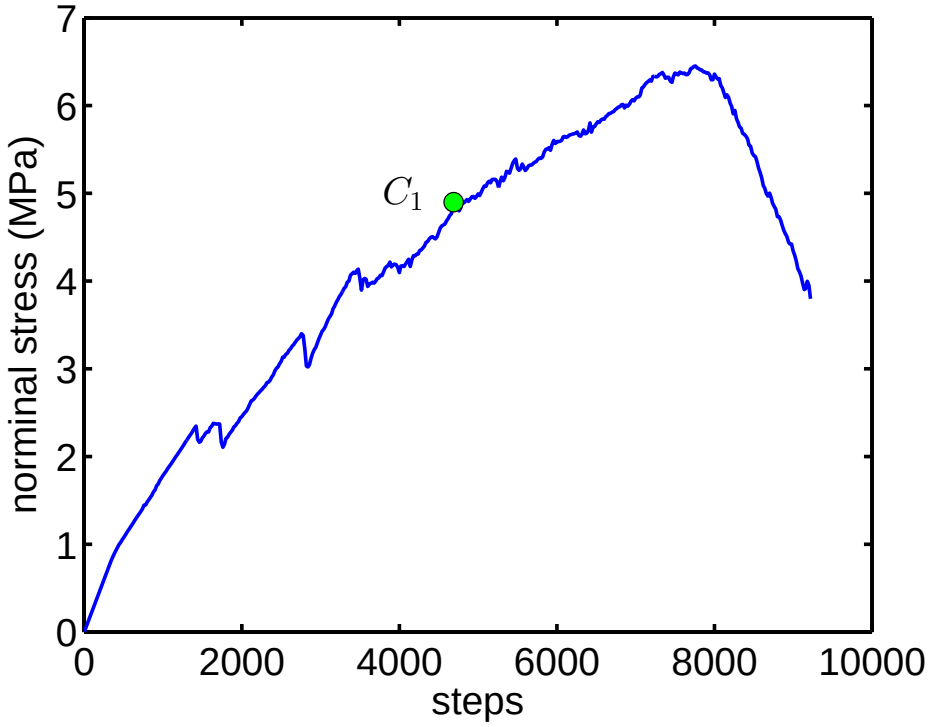

Figure 3.36: History of the nominal stress when $\beta \to \infty$ and $D = 280$ mm.

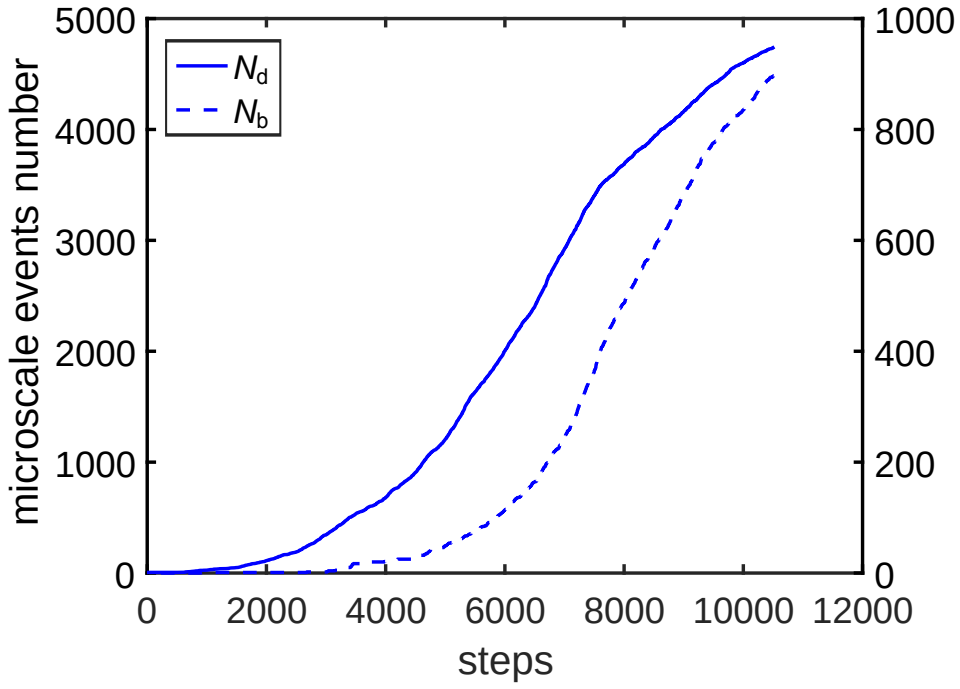

Figure 3.37: History of the number of micro-cracks numbers when $\beta = 0.1$ and $D = 280$ mm.

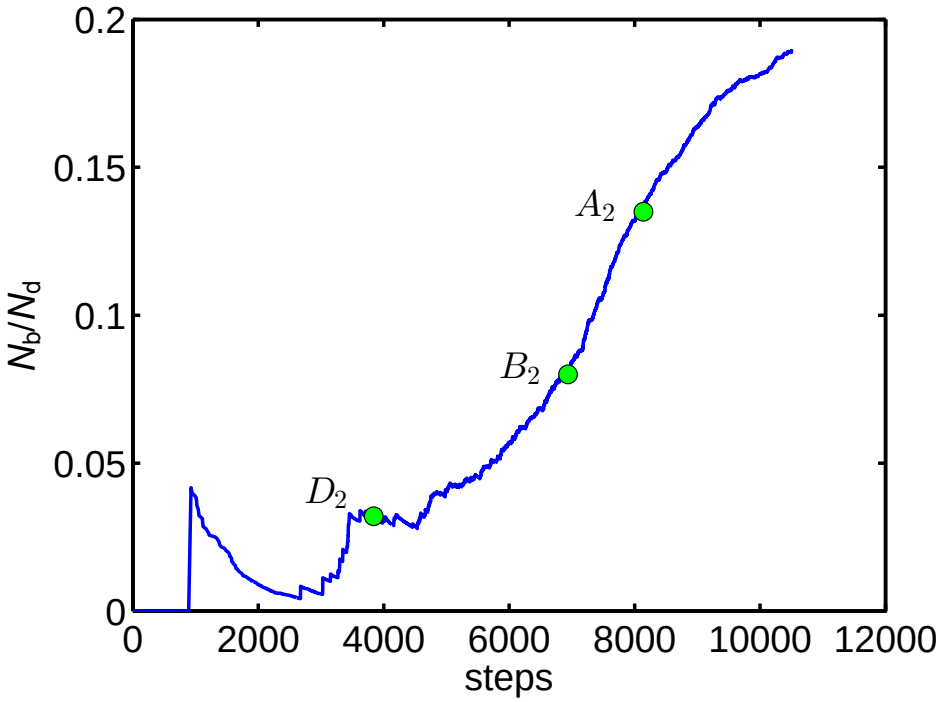

Figure 3.38: Ratio of micro-event numbers when $\beta = 0.1$ and $D = 280$ mm.

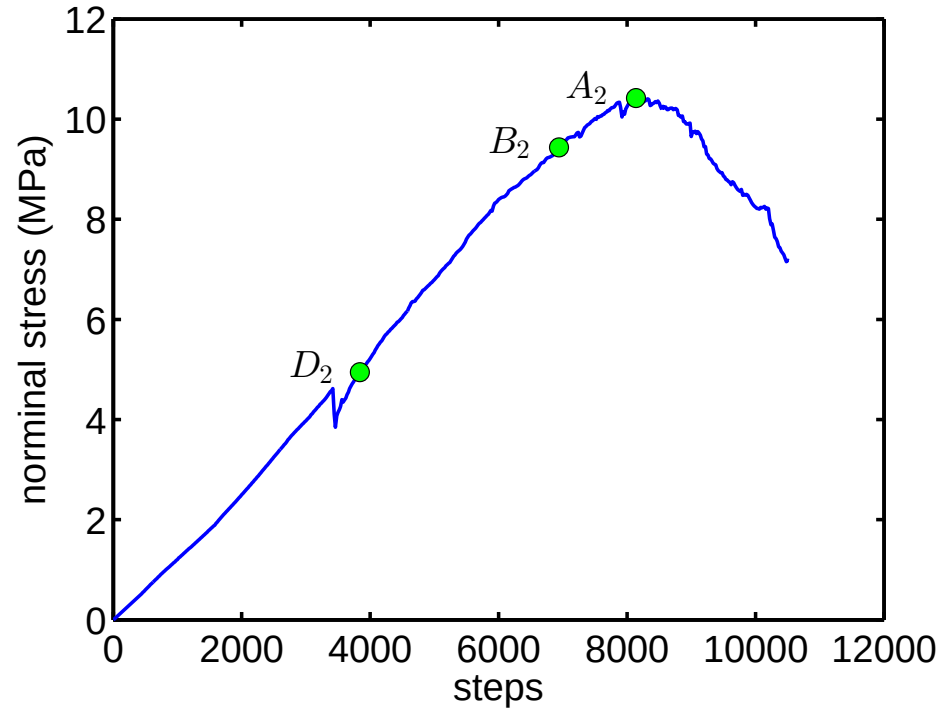

Figure 3.39: Peak and crack initiation stress when $\beta = 0.1$ and $D = 280$ mm.

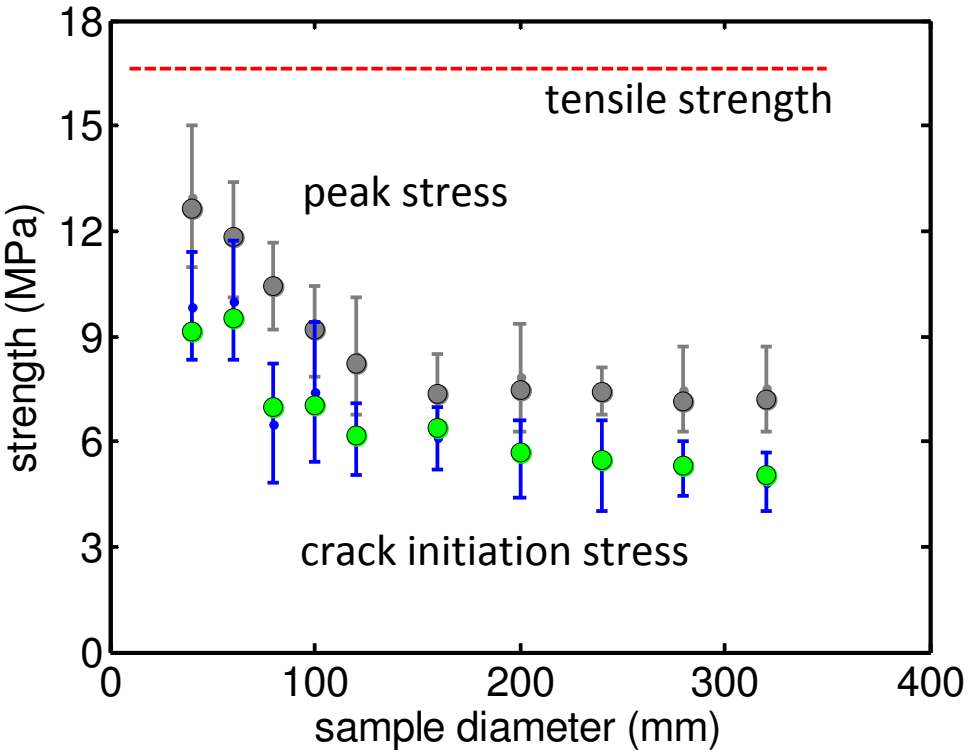

Figure 3.40: Comparison of crack initiation stress, peak strength, and UTS, $\beta \to \infty$.

initiation stress of $\beta = 0.015$ is independent of sample size. The average is about 6.8 MPa while the tensile strength is 4.75 MPa. As a result, UTS will be overestimated by BTS by a ratio of 1.43. At $\beta = 0.1$, the crack initiation stress decreases with sample size. Then it approaches an asymptote nearly the same as UTS. Note that the ratio of $\sigma_{\text{BTS}}/\sigma_{\text{UTS}}$ is in the range from 0.5 to 1.43, which is consistent with the results reported in literature [94] and the references therein.

While the failure mechanism changes w.r.t. softening coefficient β, the ratio of BTS to UTS also varies with β, as shown in Figure 3.43. When β is large, the peak stress from Brazilian test is about 1.4 times of the crack initiation stress. This ratio is roughly a constant if the sample fails under Scenario II (indentation-type). However, if β decreases to as low as 0.015, the failure mechanism is in the form of tensile crack initiated from the center. And the ratio increases to about 2.2. Note that, in some cases, the crushed zone and the center crack may be developing simultaneously in near peak stages, which makes it difficult to distinguish one from the other. Overall, the numerical results show that the difference

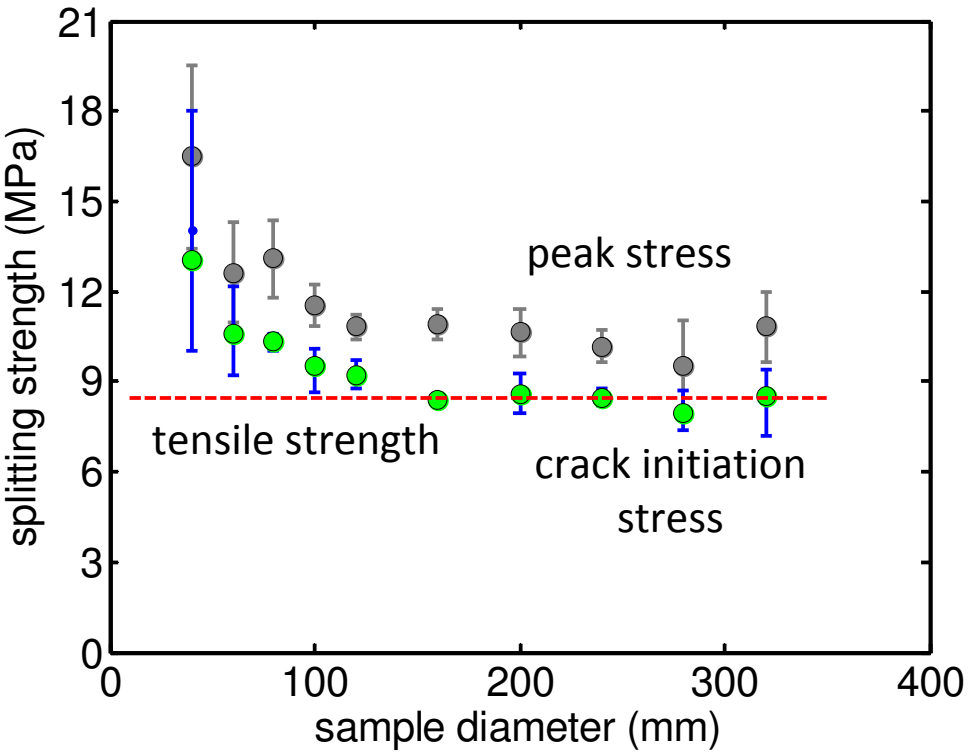

Figure 3.41: Comparison of crack initiation stress, peak strength, and UTS, $\beta = 0.1$.

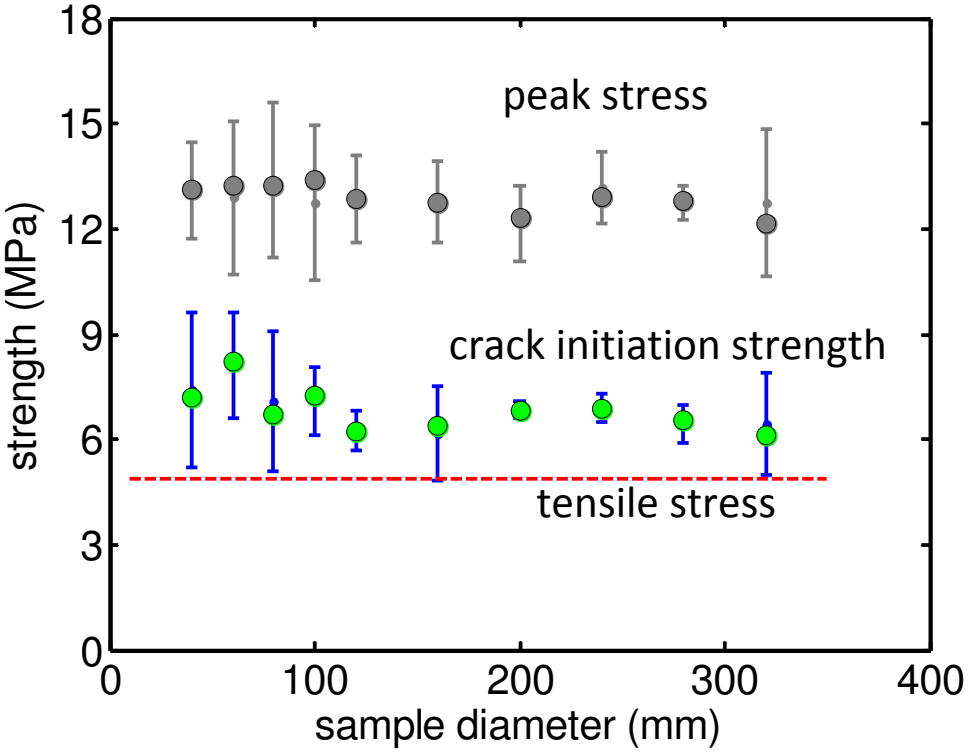

Figure 3.42: Comparison of crack initiation stress, peak strength, and UTS, $\beta = 0.015$.

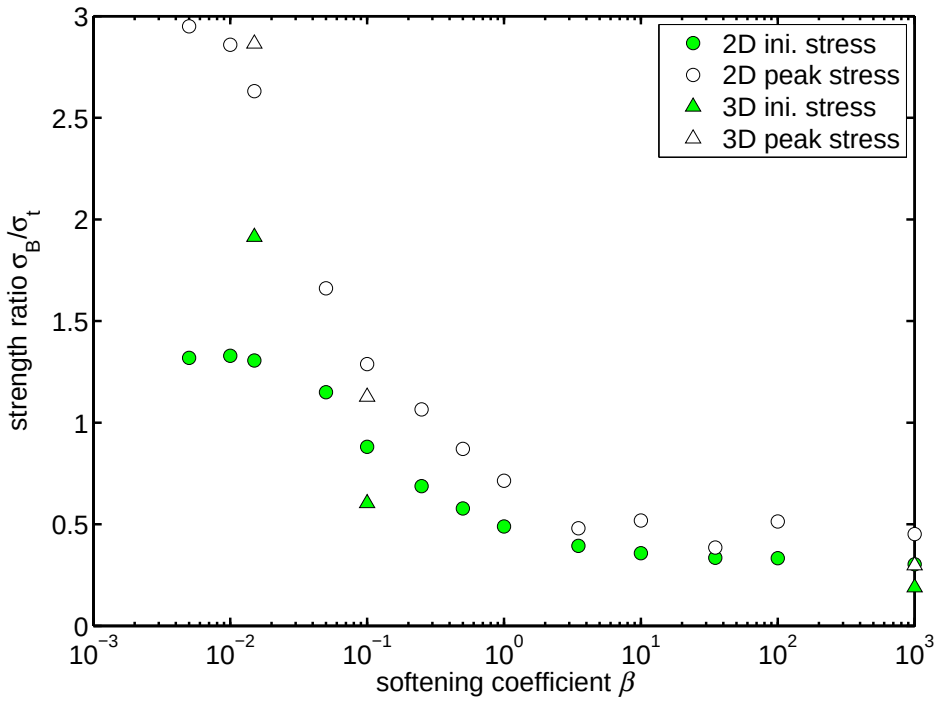

Figure 3.43: BTS/UTS ratio vs. β.

between the peak and crack initiation stress in Brazilian tests is another important factor to put into consideration when using this method to calibrate tensile strength of the numerical model, as well as in obtaining the tensile strength from the laboratory. Variation of the ratio $\sigma_{\text{BTS, ini}}/\sigma_{\text{BTS, peak}}$ as a function of β is shown in Figure 3.44.

3.6.2 3D Results

In order to justify the conclusions made from two dimensional simulations, three dimensional simulations are carried out in this study. At $\beta = 0.015$, the total number of micro-cracks N_d is roughly one order higher than N_b, as shown in Figure 3.45. Compared to 2D results, the curve of N_d vs. steps shows a convex pattern before number of micro-cracks start to increase. One of the possible reasons is secondary cracks are developing near the loading walls prior to the center cracks although the softening coefficient is already as low as $\beta = 0.015$. Nevertheless, the ratio N_b/N_d exhibits a linear segment indicating the existence of a tensile crack that eventually leads to the complete failure of the sample. The nonlinear segment before B_3' is similar to the case when "indentation-type" failure mechanism occurs. Since

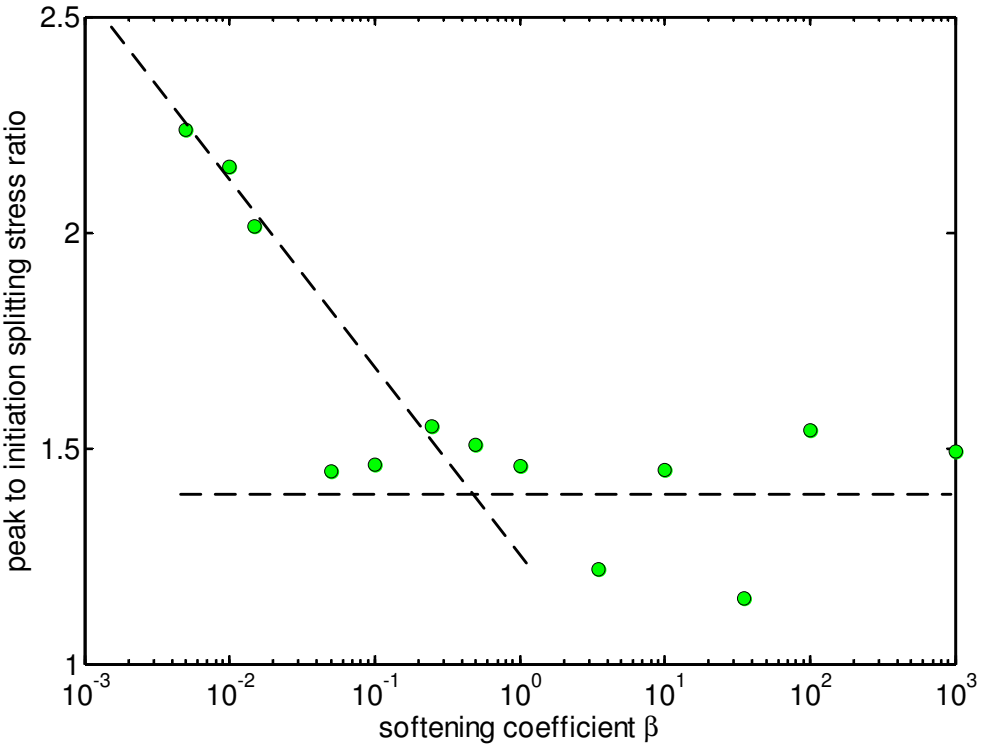

Figure 3.44: Ratio of peak to initiation stress vs. β in 2D.

B_3' is the starting point of the linear segment, we assume the stress at that point is the crack initiation stress.

At $\beta \to \infty$, the stress curve shows a plateau prior to the peak. Note that the plateau shown in Figure 3.48 is not associated with plasticity of the sample; instead, it seems to stem from the limited number of contacts between the wall and the sample. Indeed, this type of plateau is not reproduced in other tests with the same set of micro-parameters, except the random seed number. Figure 3.49 shows the same pattern including an initial nonlinear part corresponding to the development of the shear failure near loading walls, and a linear segment results from the growth of tensile crack.

At $\beta = 0.1$, as expected, the total number of micro-cracks is approximately the same as that of $\beta = 0.015$, see Figure 3.50. Because the shear zone size in both cases are not significant compare to the tensile crack. Indeed, the sample fails when it is split into two halves by the tensile crack. Thus, the propagation of the tensile crack is the primary mechanism leading to the failure, as shown in Figure 3.51.

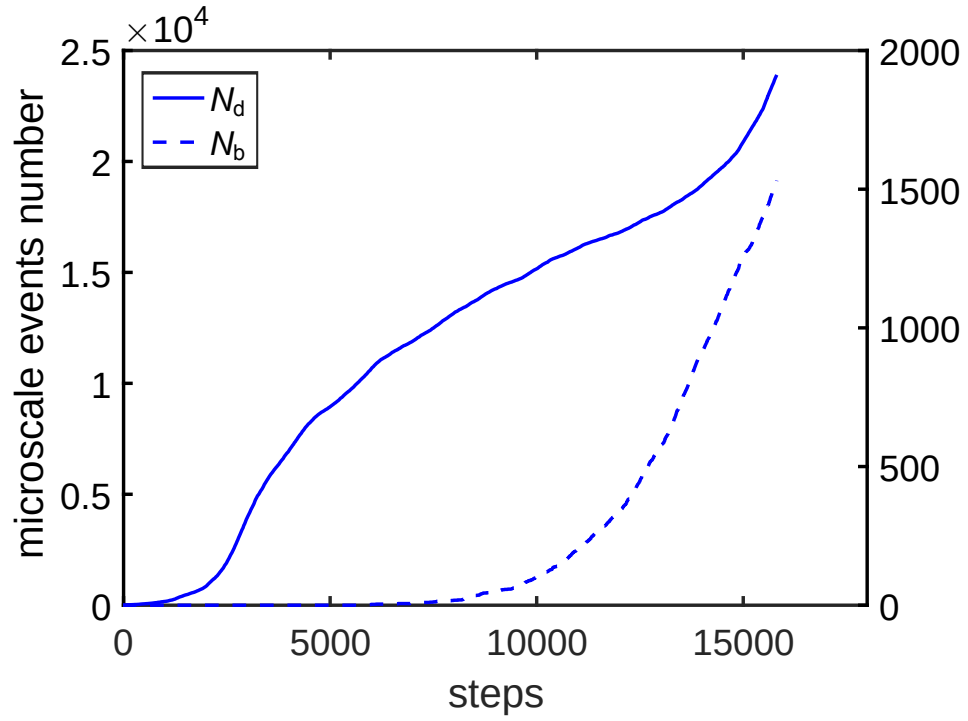

Figure 3.45: Micro-event numbers when $\beta = 0.015$ and $D = 120$ mm.

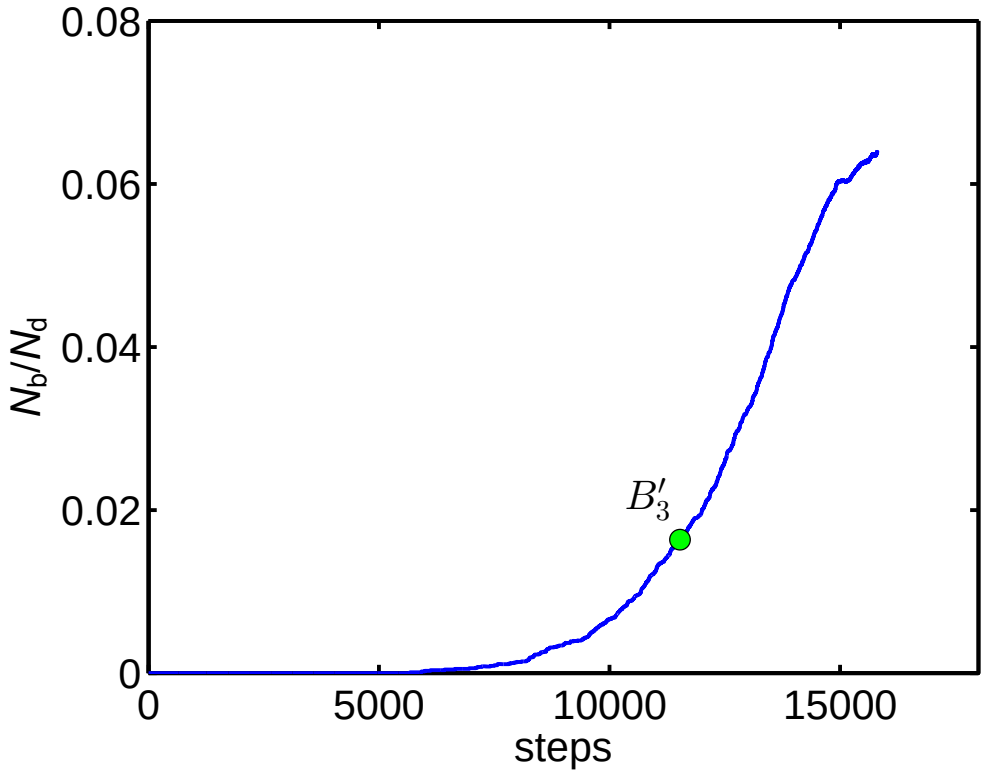

Figure 3.46: Ratio of micro-event numbers when $\beta = 0.015$ and $D = 120$ mm.

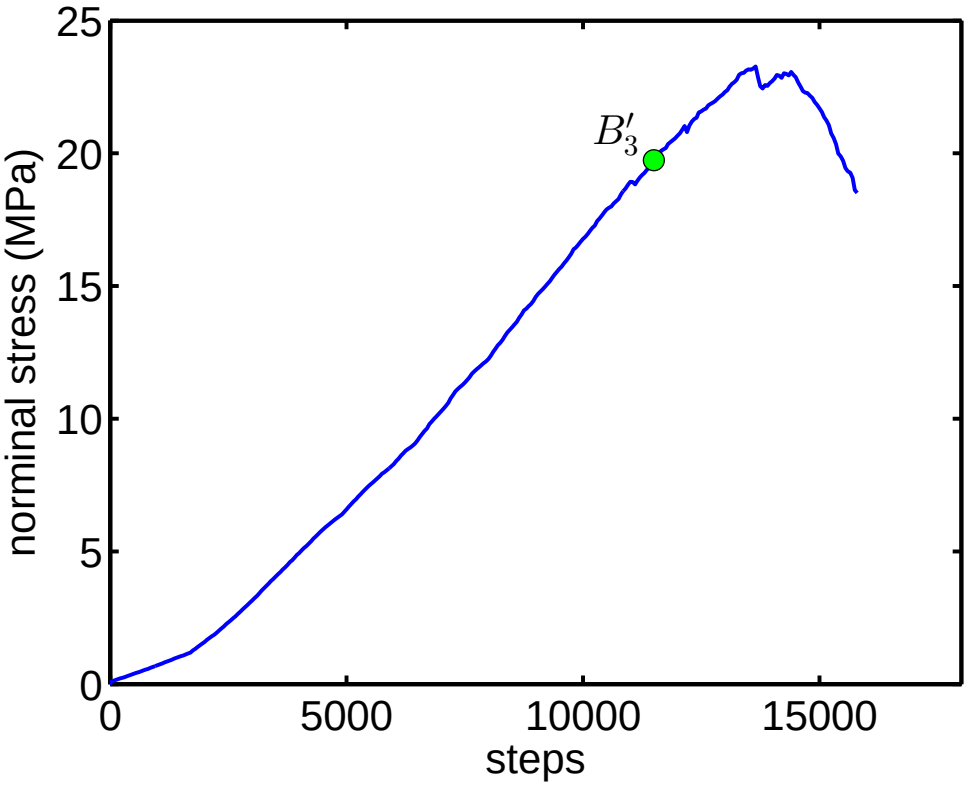

Figure 3.47: Peak and crack initiation stress when $\beta = 0.015$ and $D = 120$ mm.

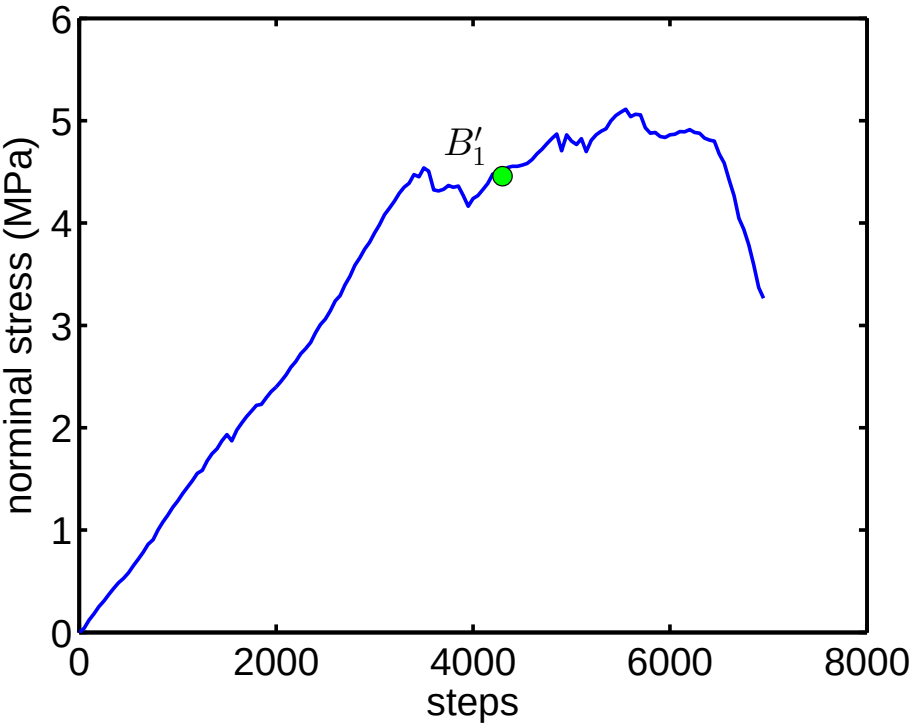

Figure 3.48: Number of broken bonds when $\beta \to \infty$ and $D = 120$ mm.

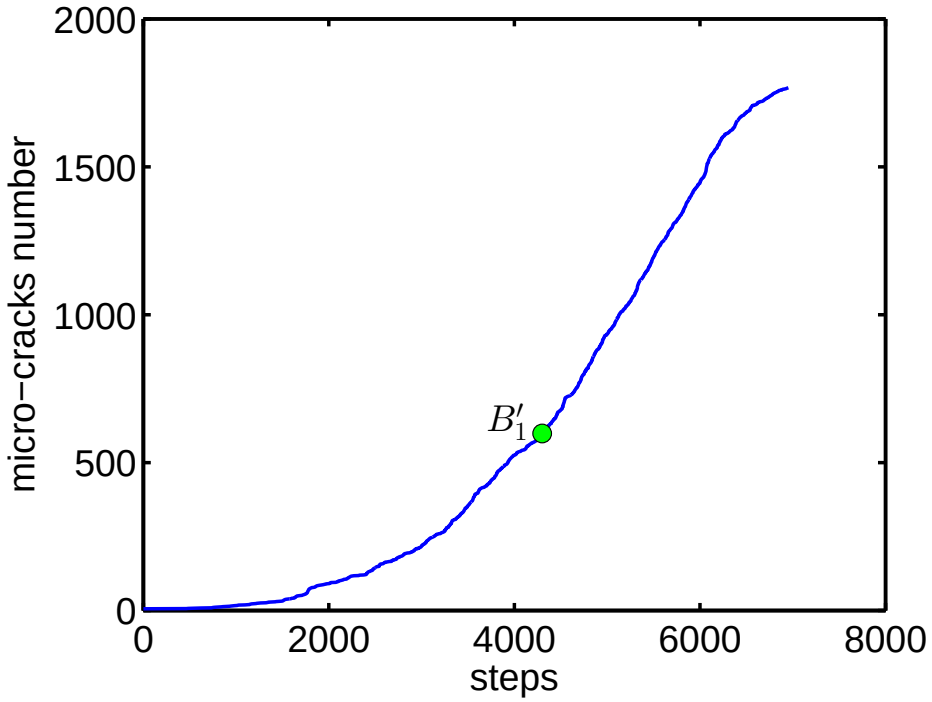

Figure 3.49: Crack initiation stress when $\beta \to \infty$ and $D = 120$ mm.

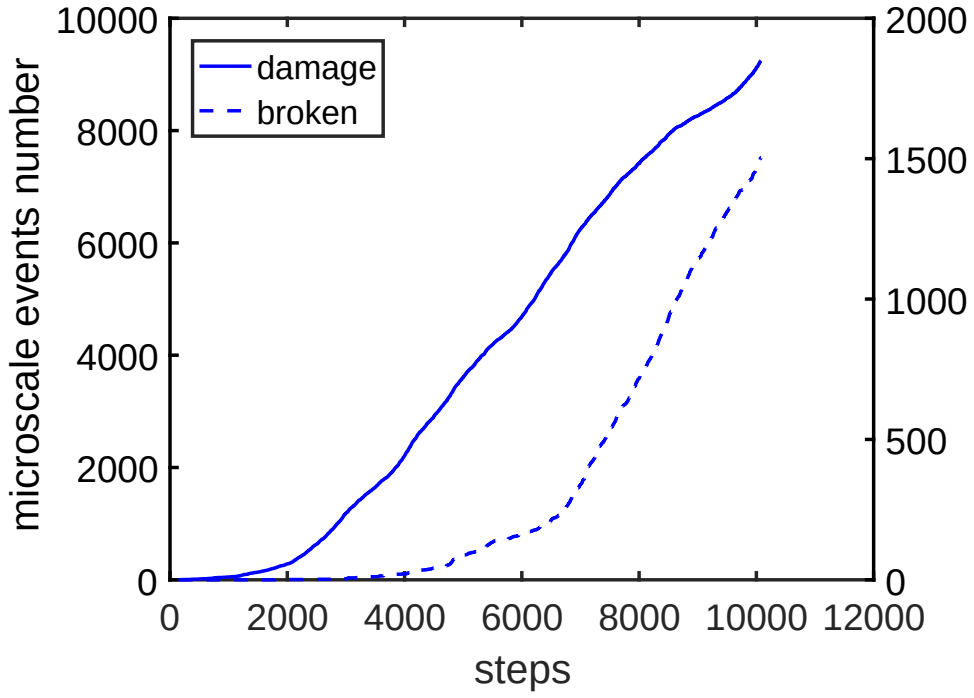

Figure 3.50: Micro-event numbers when $\beta = 0.1$ and $D = 120$ mm.

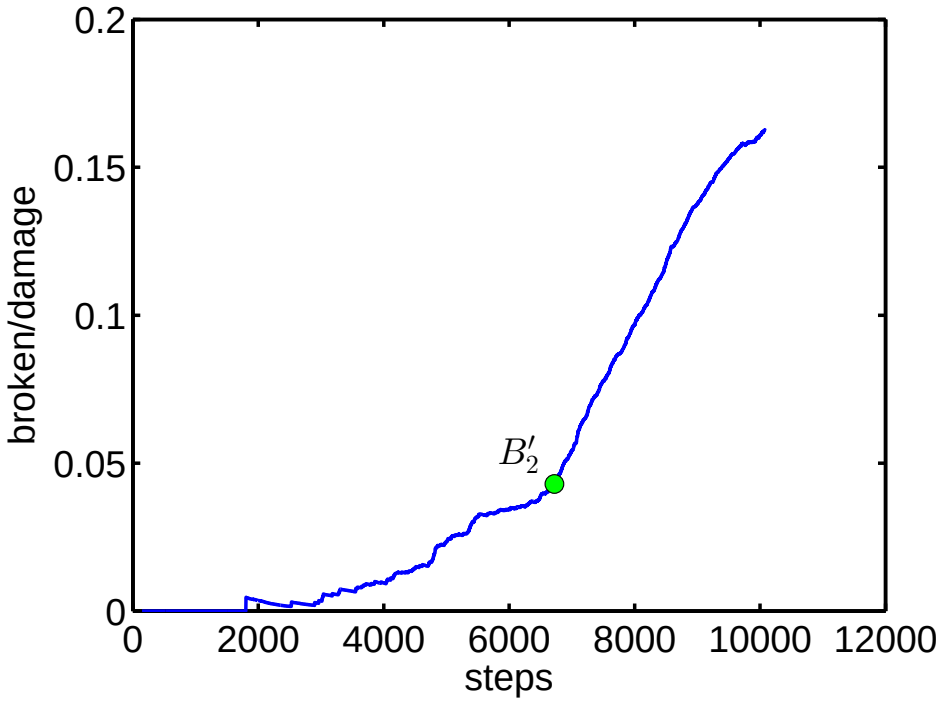

Figure 3.51: Ratio of micro-event numbers when $\beta = 0.1$ and $D = 120$ mm.

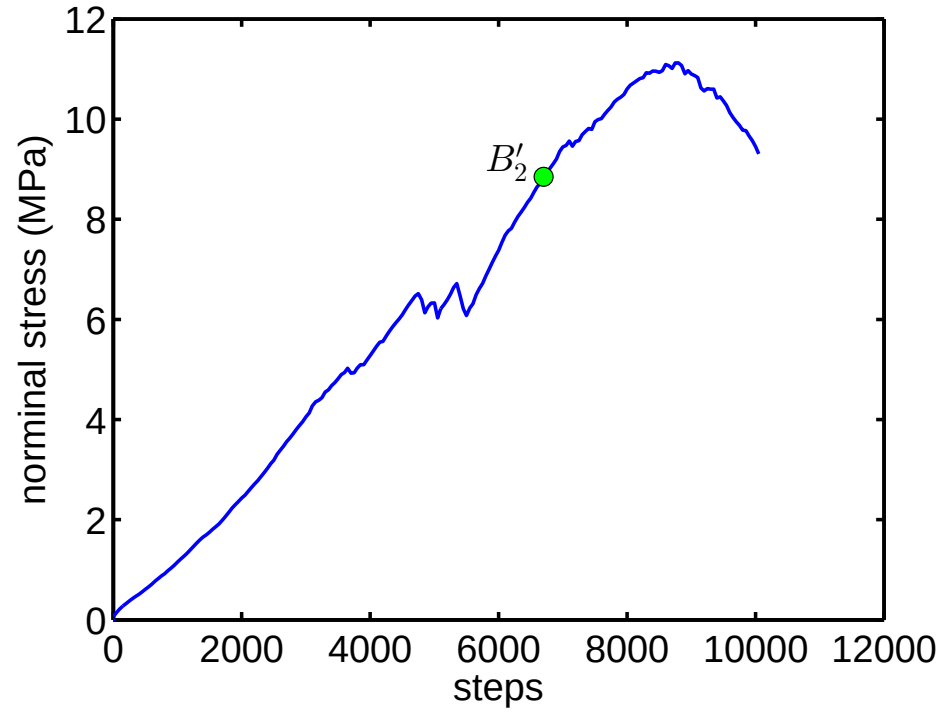

Figure 3.52: Peak and crack initiation stress when $\beta = 0.1$ and $D = 120$ mm.

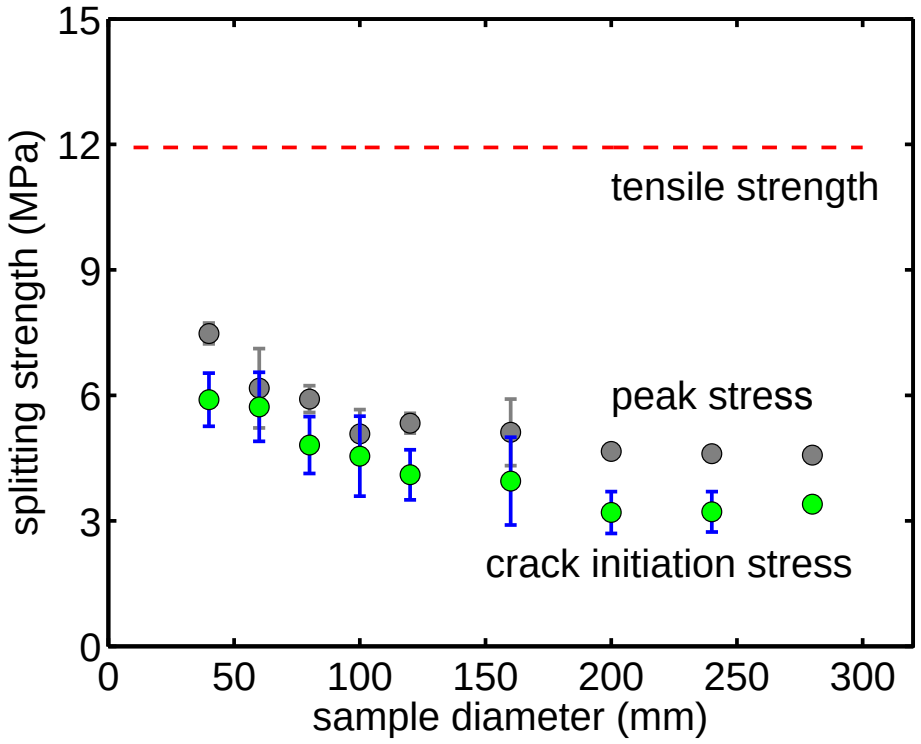

Figure 3.53: Comparison of crack initiation stress, peak strength, and UTS, $\beta \to \infty$.

Based on the discussion above, we can determine the crack initiation stress for all the simulations with different β. The results are summarized with the nominal peak stress and UTS in Figures 3.53–3.55. At $\beta \to \infty$, the scenario is similar to that in 2D. Both peak and crack initiation stress underestimate the tensile strength by a ratio of approximately $0.35 \sim 0.5$. Since when β is large, the failure mechanism is governed by the damage zone beneath the loading walls. In both two and three dimensional analyses, BTS is consistently lower than UTS. As β decreases, BTS becomes larger than UTS. When $\beta = 0.1$, the asymptote of BTS at crack initiation is slightly higher than UTS. The variation of $\sigma_{\text{BTS}}/\sigma_{\text{UTS}}$ with β is presented in Figure 3.43. The figure also suggests that $\sigma_{\text{BTS}}/\sigma_{\text{UTS}} \sim 1$ when $\beta \sim 0.05$.

3.7 Discussions

3.7.1 Effects of Strength Ratio and Sample Size

Observations of the two primary failure scenarios from the numerical analysis are consistent with prior experimental findings in the literature. Our numerical results validate the conclusions in [40] that failure in a material with a lower σ_c/σ_t ratio (equivalent to a larger

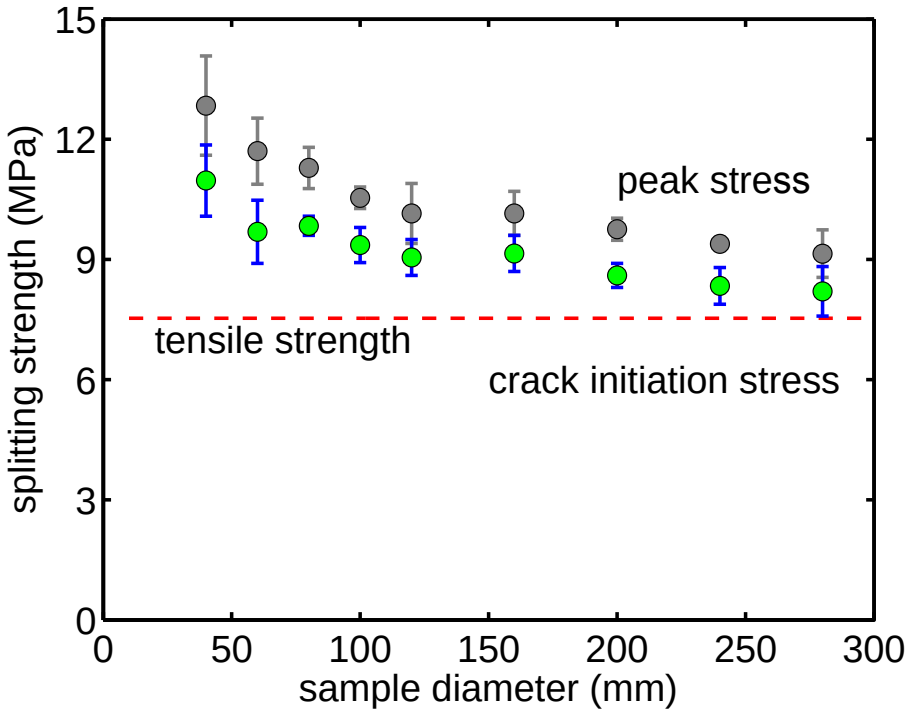

Figure 3.54: Comparison of crack initiation stress, peak strength, and UTS, $\beta = 0.1$.

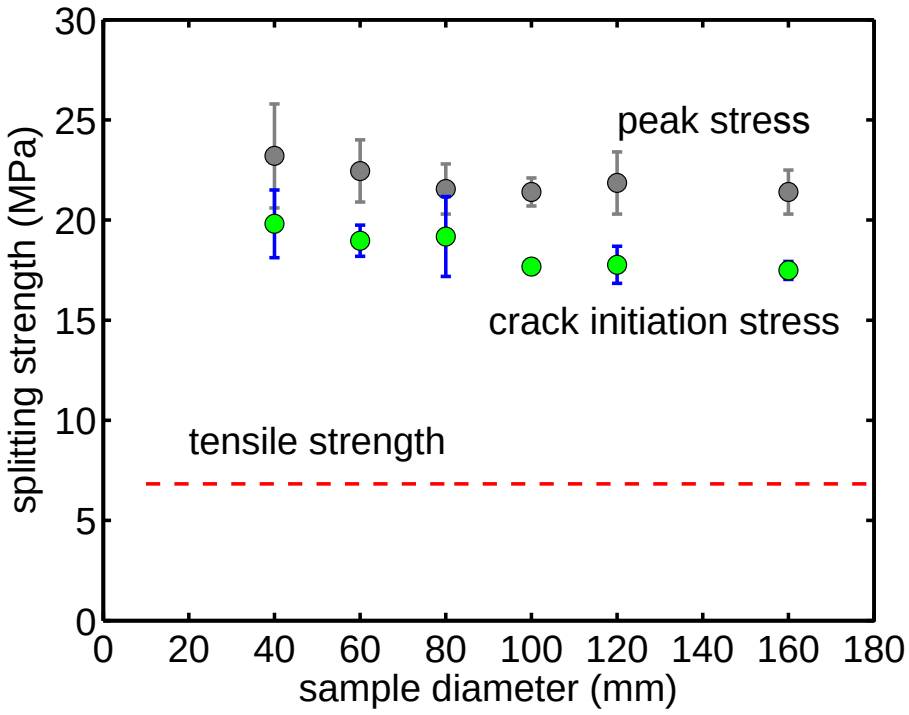

Figure 3.55: Comparison of crack initiation stress, peak strength, and UTS, $\beta = 0.015$.

β here) is likely to occur away from the center. By applying a generalized Griffith-type criterion to the elastic solution [56], Fairhurst [40] showed that for the case when the load is applied radially within an angle of $2\tan^{-1}(1/12)$ and $\sigma_c/\sigma_t = 8$, the force required for a point along the vertical axis to meet the shear failure criterion is only 70% of that required for tensile failure in the center. As the strength ratio increases to $\sigma_c/\sigma_t = 12$, the force required for tensile failure becomes the smaller one of the two. Though the analysis in [40] deals only with incipient failure, the predictions regarding the link between the failure scenarios and the strength ratio and that BTS could potentially be underestimated in Scenario II agree with our numerical results. In the 2D simulation with $\beta \to \infty$ ($\sigma_c/\sigma_t = 3.84$) and $D = 280$ mm, $\sigma_{\mathrm{BTS}}/\sigma_{\mathrm{UTS}} = 0.39$. If the Brazilian test is used for material property calibration in DEM modeling with a perfectly brittle contact model, the strength ratio becomes $\sigma_c/\sigma_{\mathrm{BTS}} = 9.85$, more than twice the strength ratio of σ_c/σ_t. Such a result is indeed rather misleading in describing the brittleness of a particle assembly.

The numerical results also show that the failure mechanisms in the intact Brazilian test depend on the sample size. While the size effect of BTS has been discussed in the literature, effect of the sample size on the failure mechanisms is rarely reported. Dependence of the failure mechanisms on the sample size as shown by the 2D cases with $\beta = 0.05$ and 0.1 and 3D cases with $\beta = 0.015$ and 0.1 could be explained by the fact that as D increases, the peak load required to initiate the tensile crack in the center also needs to increase, $P \propto D$ according to Eq. 13. It then becomes possible that plastic yielding occurs near the loading walls prior to the tensile failure in the center. Along the loading axis, there could be two local maximum tensile stresses, $\sigma_{t\max 1}$ at the center and $\sigma_{t\max 2}$ at the interface between the damaged zone and the intact material, generated by plastic yielding. Depending on the material properties and the sample size, tensile failure associated with $\sigma_{t\max 2}$ may occur first ($\beta = 0.1$ and $D = 280$ mm, 2D) or not ($\beta = 0.05$ and $D = 160$ and 280 mm, 2D). As β increases (or σ_c/σ_t decreases), the failure mode transition from Scenario I to Scenario II occurs at smaller D. In the limit when $D \to \infty$, $P \to \infty$ is needed to initiate tensile failure in the center. The problem becomes similar to that of a half space subjected to concentrated loading on the surface. Only Scenario II, namely, the indentation-type of

Table 3.2: Comparison between ASTM and ISRM.

	ASTM		ISRM	
	min	max	min	max
L/D	0.2	0.75	∼0.5	-
Test duration (min)	1	10	0.25	0.5
Stress rate (MPa/s)	0.05	0.35	-	-
Loading rate (N/s)	-	-	200	

failure, is possible. These numerical results mean that in laboratory testing, if a sample has already failed according to Scenario II at a given diameter, a proper strategy to achieve the center crack failure mechanism would be to decrease the sample size.

3.7.2 Other Factors Affecting Size Effect

Since Brazilian test has been considered as a reliable indirect testing method for tensile strength of the material for many years, it is essential to make sure that the splitting strength is not related with sample size. Also, the sample should fail in the same mechanism as predicted by the theory of elasticity. Therefore, both ASTM [8] and ISRM [64] have specific requirements for Brazilian tests, some of the differences are summarized in Table 3.2.

ISRM suggests to use a curved apparatus to hold the specimen, then apply the load by two half ball bearings. On the other hand, ASTM suggests using a cardboard or plywood between the platens and the specimen to reduce the stress concentration and maximize the possibility of the splitting failure mechanism to avoid size effect. They both require the sample diameter to be no less than ˜54 mm, which is at least 10 times greater than the largest mineral grain constituent. Sample thickness is approximately equal to the specimen radius to reduce the influence from the third dimension. It seems that both methods don't consider the size effect influence, instead, they require certain apparatus and loading conditions to make sure the sample fails as much as possible from the center instead of the loading points. Also, at least 10 samples are recommended for each test. After all, the test is only valid for materials fail in tension at their uniaxial tensile strength when one principal

stress is tensile and the other finite principal stress is compressive with a magnitude not exceeding three times that of the tensile principal stress [85, 21].

3.7.3 Direct Tension Test

In general, size effect in the tensile strength of quasi-brittle materials has been attributed to the statistical distribution of weakness in the material according to Weibull theory [120]. Statistical size effect was modeled in [125] by introducing initial flaws into the particle assembly, the size and number of which follow a predefined distribution. Unlike laboratory tests where the sample dimensions are typically standardized, from the point of view material strength calibration, we still need to ask what the appropriate sample size should be so that the material strengths obtained from the unconfined calibration tests could be representative. Here we examine how the strengths of a particle assembly in random dense packing vary with the sample size if the bond strengths follow Weibull's distribution,

$$\bar{\sigma}_c = \bar{\sigma}[-\ln(1-\alpha)]^{1/m} \tag{29}$$

where $\bar{\sigma}$ is a scale parameter; α is a random variable in [0, 1] and m is the shape factor. In this study, we set $\bar{\sigma} = 110$ MPa and $m = 1.5$. The histogram of the normal bond strength in a rectangular particle assembly of 200×400 mm is shown in Figure 3.56. This particle assembly serves as the original sample source. The individual test samples of various sizes and an aspect ratio of $H/W = 2$ are all cropped out of this original sample from random locations.

Variations of the uniaxial compressive and tensile strengths with the sample width are shown in Figures 3.57–3.58. The simulations are performed with the same set of micro-scale parameters listed in Table 2.1 and $\beta \to \infty$. Though only limited statistical realizations are run, the overall trends do not seem to suggest a statistically significant size effect within the sample size range explored.

This may be explained by the fact that in both unconfined tests, micro-scale failures occur across the whole sample width. In direct tension, the micro-cracks appear across the width nearly simultaneously right around the peak, while in the uniaxial compression

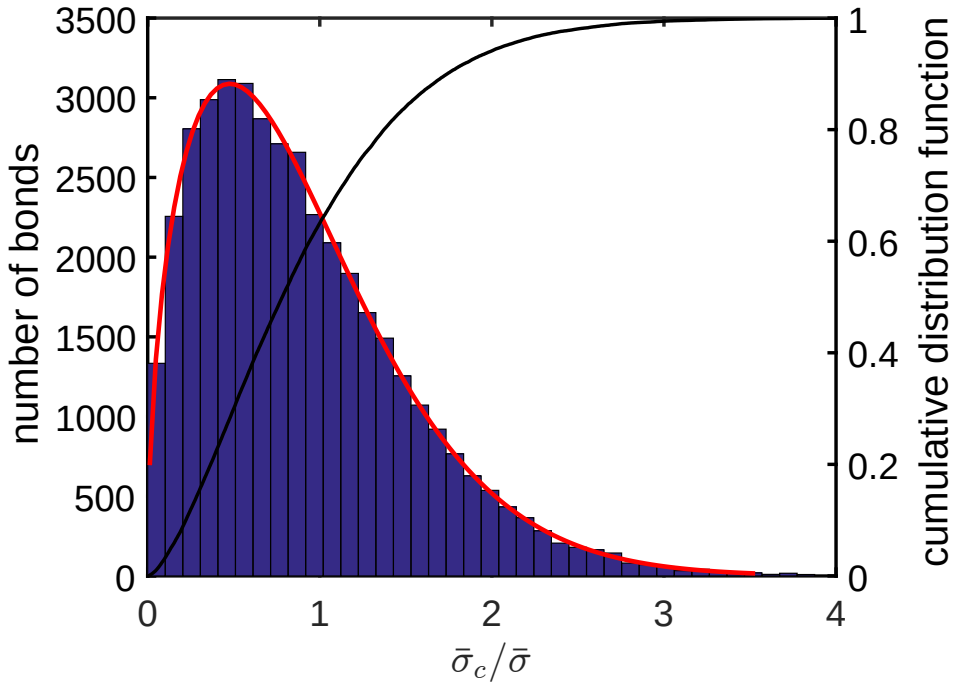

Figure 3.56: Histogram of the normal bond strength in a rectangular particle assembly of 200×400 mm.

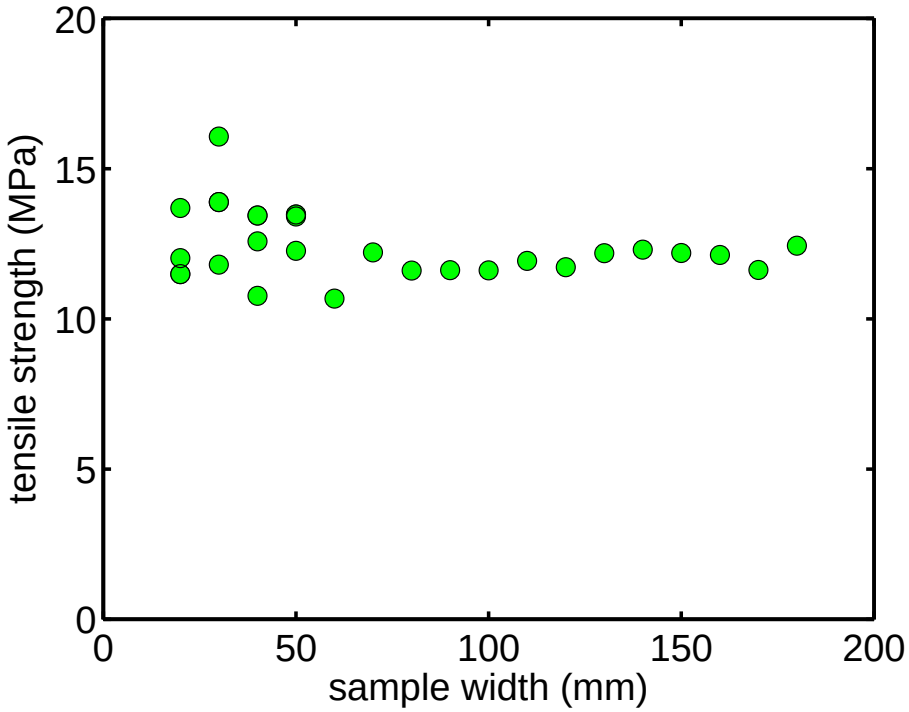

Figure 3.57: Variation of the unconfined tensile strength as a function of the sample size.

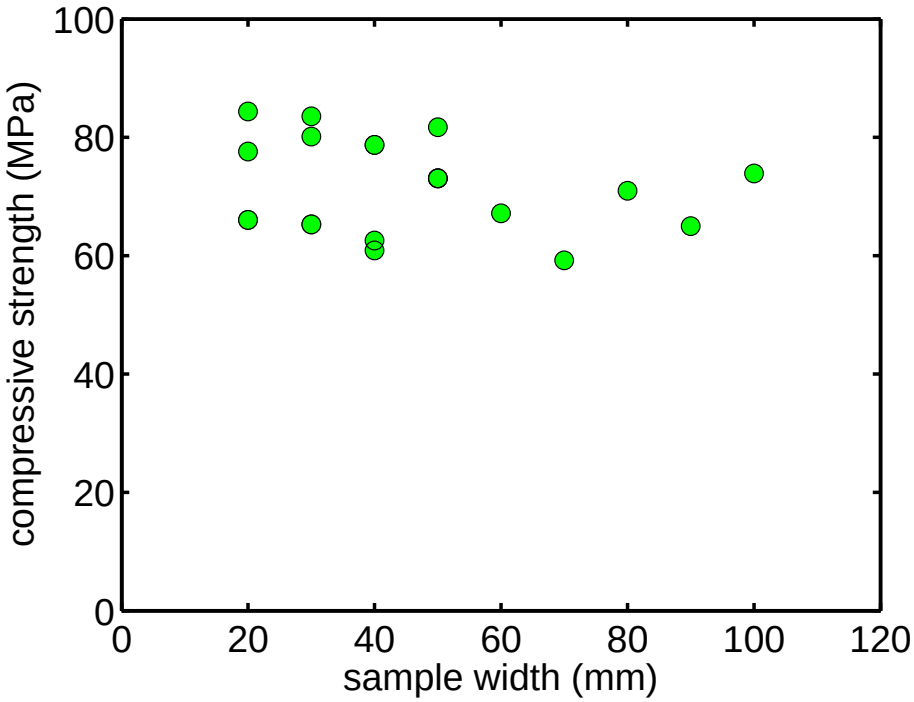

Figure 3.58: Variation of the unconfined compressive strength as a function of the sample size.

test, the micro-cracks accumulate more or less uniformly to form shear bands across the width. In other words, if we assume the weakest bond in the domain to be the initial flaw, the process zone size associated with this flaw is larger than the sample width. Therefore, while the statistical distribution contributes to the scatter in the strength at a given width, strengths of the particle assembly are statistically insensitive to the sample width as long as the discretization is sufficiently fine. The fact that micro-cracks appear simultaneously across the sample width also means that the statistical size effect is negligible.

Similar observation is found for the other two β cases and also if the normal bond strength follows a Gaussian distribution. A group of rectangular samples with different sizes are generated for direct tension tests to compare with the experimental results in [121], at least three samples are used for each size. The aspect ratio is chosen to be $H/W = 2.0$ while W is in the range from 40 mm to 180 mm. Simulation results are summarized in Figure 3.59. These numerical results are consistent with [121] where the size effect in direct tension is observed to be statistically insignificant.

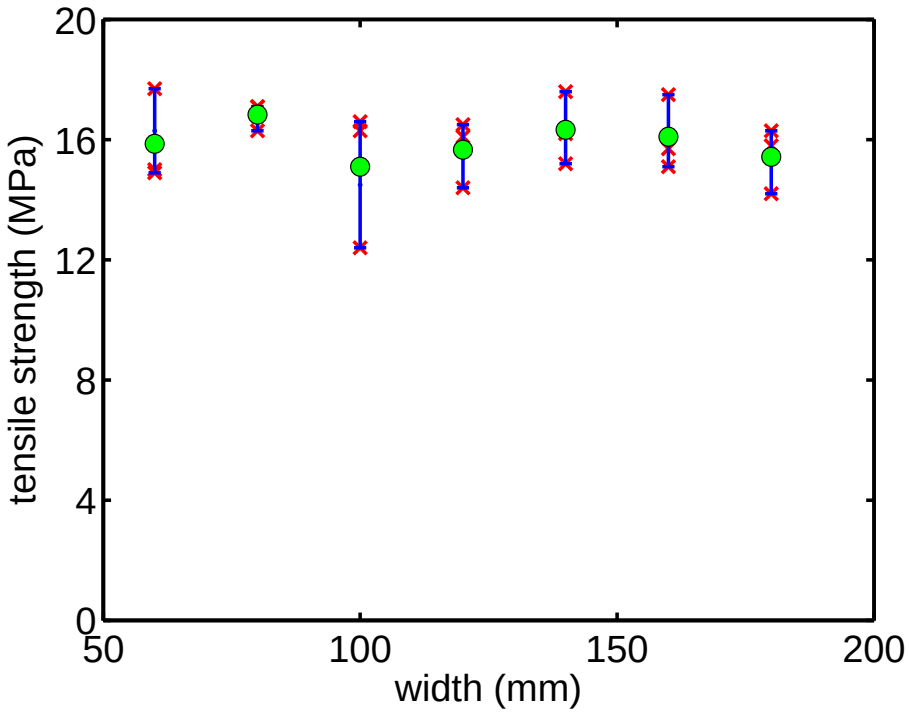

Figure 3.59: Tensile strength of rectangular samples in 2D; $\beta \to \infty$.

3.8 Conclusion

As consistent with experimental observations, evolution of the micro-scale failures from the DEM simulations reveals that there are two distinct failure scenarios in the Brazilian test. Diametrical splitting could be a result of either Scenario I where a tensile crack initiates from the center and then propagates towards the two loading ends, or Scenario II, similar to the indentation-type of failure, where plastic yielding occurs first near the loading points and drives to initiate tensile cracks to propagate towards the center of the specimen. Given a material with a low strength ratio, Scenario II is more likely to occur. In DEM simulations with a randomly packed assembly consisting of circular/spherical particles, if the contact model is perfectly brittle ($\beta \to \infty$ or above the threshold value), the highest strength ratio is typically around $\sigma_c/\sigma_t \sim 4$. As such, Scenario II is most likely the failure mechanism in the numerical Brazilian test with a perfectly brittle contact model. The simulation with $\beta \to \infty$ and $D = 280$ mm suggests that the nominal Brazilian tensile strength, determined based on the peak force, could potentially underestimate the intrinsic tensile strength. If

the Brazilian test is employed for tensile strength calibration, the strength ratio $\sigma_c/\sigma_{\mathrm{BTS}}$ could be much larger than $\sigma_c/\sigma_{\mathrm{UTS}}$. It is therefore not a good practice in DEM modeling to conduct material properties calibration using the Brazilian test.

The numerical results also suggest that failure behaviors in the Brazilian test vary with the sample size. The conventional scenario of tensile failure from the center is more likely to occur when the sample size is relatively small. As the sample size increases, the failure mechanisms could evolve to the indentation-type of failure. For a material with a low strength ratio, using a larger size specimen in laboratory testing does not necessarily yield a more accurate measure of the intrinsic tensile strength.

The limit analysis carried out in this study suggest that the size effect is related to the ratio of shear zone size over sample size l/D. Given a material with low strength ratio σ_c/σ_t ($\beta \to \infty$), BTS is governed by the ratio l/D for small sample size, namely $D < 120$ mm in this study. However, when D exceeds the threshold value, l/D becomes negligible and BTS approaches a constant and thus the size effect vanishes. In the other failure scenario, $\beta \leq 0.1$, the evolution of the tensile crack governs the failure mechanism. As predicted by the theory of elasticity, BTS shows no correlation with sample size.

Based on the simulation results, crack initiation stress is proposed to represent tensile strength from Brazilian test to account for the inefficiency that crack generation and propagation in PFC is a stable process which requires increased deviatoric stress to initiate new cracks. As such, intrinsic tensile strength is exaggerated if measured by the peak Brazilian tensile strength. We monitor the evolution of micro-events, including the number of broken bonds and damaged bonds, to determine the crack initiation and peak stress. The results indicate that the apparent peak stress usually represents multiple failure mechanisms. As a matter of fact, intrinsic BTS is associated with the splitting-type of failure. So we use the nominal peak to compare with uniaxial tensile strength. As consistent with experimental data, the ratio of $\sigma_{\mathrm{BTS}}/\sigma_{\mathrm{UTS}}$ is in a range from 0.5 to 1.35. At $\beta \to \infty$, UTS is underestimated by BTS. Meanwhile, at $\beta \leq 0.1$, UTS is overestimated. Nevertheless, if $\beta = 0.1$, the asymptote give a good approximation of the intrinsic tensile strength of the material. Hence, properly conducted Brazilian test is still a reliable way to estimate uniaxial tensile

strength.

In general, the failure mechanisms are also related to other factors such as the effect of thickness, the loading platen configuration, the contact conditions and the loading rate. Future work is needed to address these issues and to model specific rocks and testing conditions.

CHAPTER IV

FAILURE MECHANISMS AND SIZE EFFECT IN SHEAR FAILURE

4.1 Introduction

In Brazilian tests, the results show that the variation of the BTS is associated with the brittle-ductile failure mechanism transition. To be more specific, the nominal strength is independent of the sample size if the failure is governed only by the brittle mode. If the dual failure modes are observed, then the nominal strength decreases with the sample size up to a threshold value and then remains constant. Therefore, we expect to see similar relationship between a nominal shear strength and the sample size if the shear strength test involves both brittle and ductile failure mechanisms.

The three-point bending test with the tensile failure mode at the mid-span suppressed and the four-point bending test are investigated in this study. Dependence of the uniaxial compressive strength from the unconfined test on the sample size is first analyzed. On the one hand, from the point of view of material strength calibration in DEM, we need to address the question whether the UCS obtained from a certain size of particle assembly is representative of the intrinsic strength. On the other hand, if the UCS can be shown to be independent of the particle assembly size, we can then argue the size effect in the nominal strength from the three-point bending and four-point bending tests can be attributed to factors other than the size effect in UCS.

4.2 Numerical model

In this section, a synthetic rock is generated using the parameters listed in Tables 4.1. The macro-scale properties are summarized in Table 4.2. Then three different loading configurations, namely, uniaxial compression tests, three point bending, and four point bending tests, are considered. We first examine the behavior of the material with $\beta \to \infty$ to show the different failure patterns in various loading conditions. In addition, the failure mechanism transition is investigated using four-point bending test on intact samples with

Table 4.2: Micro-scale parameters for the sample.

Softening coefficient β	$\beta \to \infty$
Compressive strength σ_c (MPa)	42.40
Tensile strength σ_t (MPa)	15.00
Elastic modulus E (GPa)	23.24
Poisson's ratio ν	0.38

$\beta = 0.1$ and normal bond strength $\bar{\sigma}_c = 15 \pm 1.5$ MPa. Micro-scale parameters and macro-scale properties for this modification are listed in Table 2.1 and Table 2.2, respectively.

Table 4.1: Micro-scale parameters for the sample.

Particle radii (mm)	0.8-1.66
Density ρ (kg/m^3)	2630
Point contact modulus E_c (GPa)	50
Stiffness ratio k_n/k_s	4.0
Friction coefficient μ	0.5
Parallel bond modulus $\bar{E}_c$ (GPa)	50
Bond stiffness ratio $\bar{k}_n/\bar{k}_s$	1.0
Radius multiplier $\bar{\lambda}$	1
Normal bond strength $\bar{\sigma}_c$ (MPa)	50±5
Shear bond strength $\bar{\tau}_c$ (MPa)	20±2
Softening coefficient β	$\beta \to \infty$

4.3 Uniaxial Compression Test

Uniaxial compression test is the most widely used method to evaluate rock strength. Generally, cylindrical or cubic samples are used for the test. In this study, we use rectangular samples in 2D to perform the tests. The aspect ratio of the sample is fixed to be $H/W = 2.0$ while the width W varies in the range from 20 mm to 180 mm. The compressive strength

is defined as:

$$\sigma_c = P/W \tag{30}$$

where P is the load applied to the sample.

The complete stress-strain curve is shown in Figure 4.1. A sample with $W = 120$ mm and $H = 240$ mm is used as an example to demonstrate the analysis. Since the shear bond strength is relatively low than the normal bond strength, we have both tensile and shear micro-cracks, represented using green and blue colors, respectively, in this chapter. Four critical stages are marked on the curve. No micro-crack is recorded until the stress reaches about 80% of peak, namely, stage A. All the micro-cracks at this stage are shown in Figure 4.2(a). Then, continuous micro-cracks are observed as the load increases. Clearly, the micro-cracks are randomly distributed along the shear band directions, as shown in Figure 4.2(b). Note that, all the micro-cracks are distributed randomly through the sample. No macro-crack can be identified at this stage. As a result, the overall stress is still increasing; however, the stiffness slightly decreases because of damages. When the load increases to peak, more micro-cracks are initiated near the center of the sample. Meanwhile, some of the micro-cracks coalesce together and a shear band is formed along the diagonal of the sample, as shown in Figure 4.2(c). As the shear band is formed, the stress drops immediately after peak, indicating the sample is crushed, as shown in Figure 4.2(d).

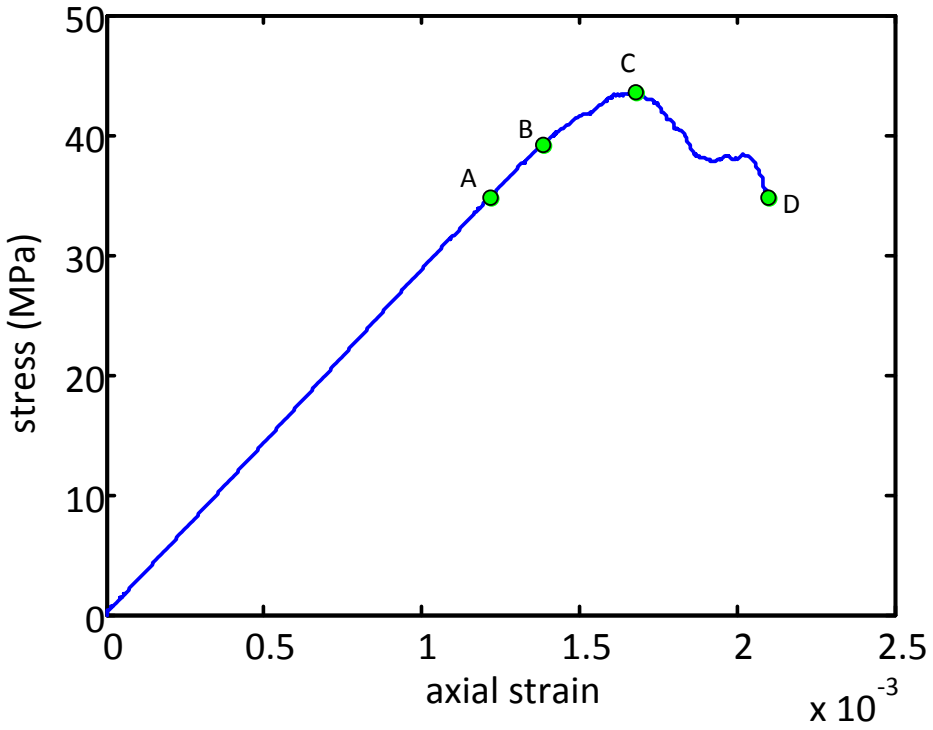

Figure 4.1: Stress-strain curve; sample size $W \times H = 120 \times 240$ mm and $\beta \to \infty$.

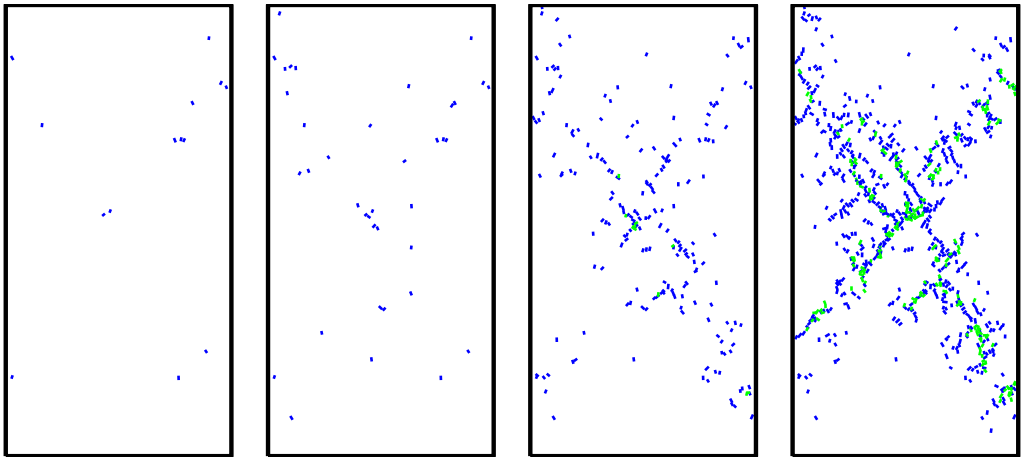

(a) stage A (b) stage B (c) stage C (d) stage D

Figure 4.2: Cumulative micro-cracks; sample size $W \times H = 120 \times 240$ mm and $\beta \to \infty$.

In order to show the evolution and distribution of micro-cracks , their locations and types are recorded in specific time intervals. We divide the whole test into six stages to monitor the development of micro-cracks in each time interval. Figure 4.3(a) reveals that

up to 90% of peak, only random micro-cracks are recorded. The overall stiffness of the sample is not reduced. Meanwhile, no obvious fracture is observed. In addition, all the micro-cracks are mostly distributed along the diagonals of the sample, where the potential shear band lies. When the load reaches peak, some of the micro-cracks start to coalesce together. In other words, a macro-scale shear band is formed, see Figure 4.3(b). As a result, the stress-strain curve shows a clear softening behavior. When the load continues increasing, more and more micro-cracks are observed. We can clearly see from Figure 4.3(c) that the shear band becomes the dominant failure mode. Besides, some of the micro-cracks indicate the existence of axial fractures near the shear band plane. As a result, the sample loses its load bearing ability, and the stress reaches the peak. Note that, the evolution of the micro-events shows no sign of fracture tip. All the micro-cracks are more or less simultaneously generated and uniformly distributed along the two diagonals. Besides, the number of micro-events during the post-peak regime are more significant than that in pre-peak regime. Figure 4.3(d) shows a second shear band from top-right to bottom-left. Still, there is no evidence where the fracture tip is. After two diagonal shear bands are fully developed, the sample is crushed and failed in ductile shear mode.

In the whole failure process, the micro-cracks are generated almost simultaneously and distributed uniformly along the two diagonals of the sample. Then the uniaxial compressive strength of all the samples are recorded and shown in Figure 4.4, we can see that there is no clear size effect. The UCS is basically a constant, especially when the sample size exceeds 100 mm. On the other hand, the standard deviation is larger when the sample size is relatively small. This may be caused by the DEM model resolution and boundary effect. Taking the smallest sample as an example, $W = 20$ mm and $H = 40$ mm, the average grain diameter is about 2 mm, which means the total number of particles along the horizontal cross-section is about 10. Even though this condition satisfies the requirement in ASTM [112] that the sample size must be 10 times greater than the largest grain diameter, the uneven contact between the loading wall and particles may still introduce a large stress gradient near the boundary.

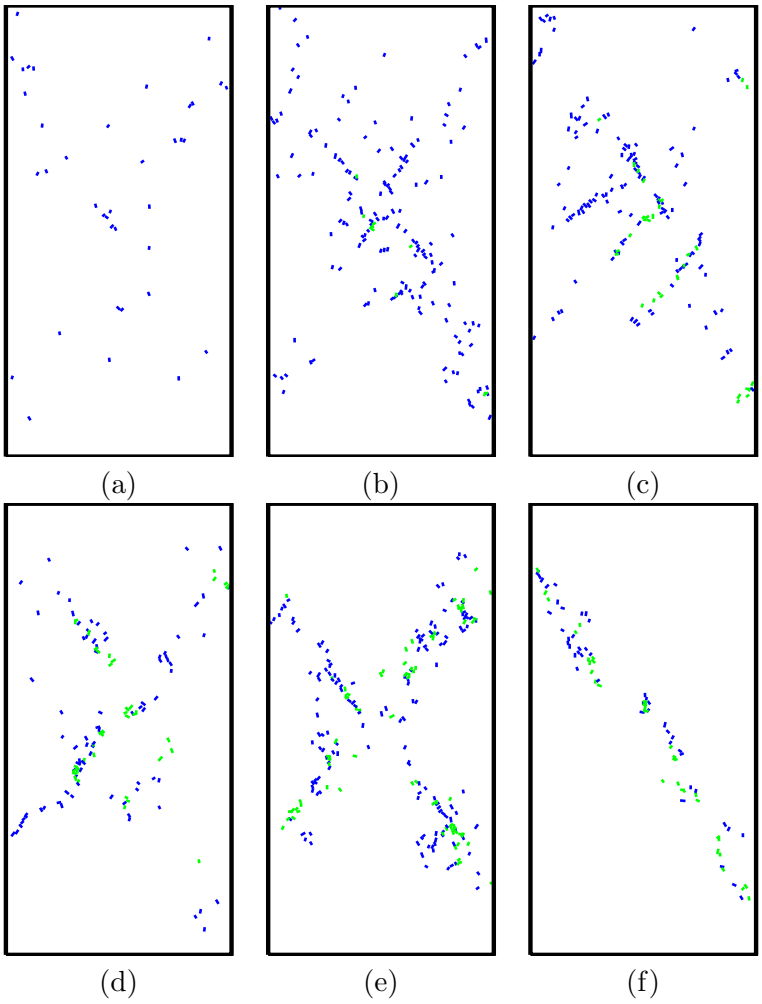

Figure 4.3: Evolution of micro-cracks; sample size $W \times H = 120 \times 240$ mm and $\beta \to \infty$. (a) 0–90% pre-peak; (b) 90% pre-peak–peak; (c) peak–95% post-peak; (d) 95% post-peak–90% post-peak; (e) 90% post-peak–85% post-peak; (f) 85% post-peak–80% post-peak.

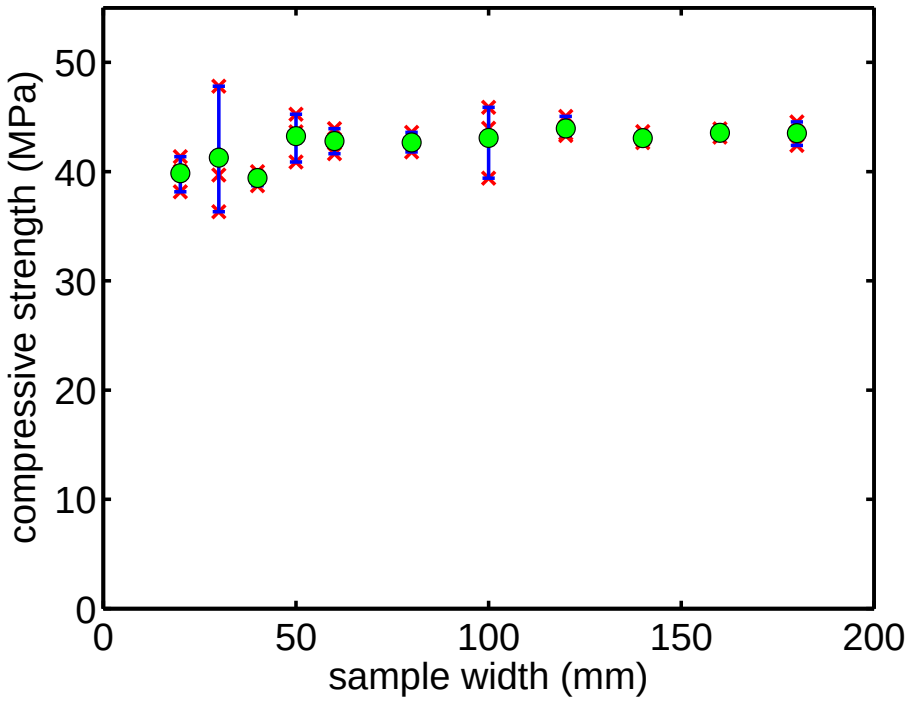

Figure 4.4: Compressive strength vs. sample width.

4.4 Three-point Bending Test

According to different loading configurations, the sample is subject to mode I tensile or mode II shear failure in three-point bending tests. Since the main objective in this section is to investigate the shear strength of the material, we implement a longitudinal rebar at the bottom of the sample to restrain the mode I tensile failure, as shown in Figure 4.5. Within the framework of shear failure, sample could fail in two different types of mechanism, including ductile and brittle modes, controlled by span depth ratio $\lambda = S/2D$. We introduce two sets of λ, $\lambda = 0.8$ and $\lambda = 1.6$, to simulate different failure modes. As such, the nominal shear strength is defined as:

$$\sigma_n = \frac{P_u}{2BD} \tag{31}$$

where P_u is the ultimate load, B is the sample thickness, $B = 1.0$ in this study, D is the depth. For the tests with $\lambda = 0.8$, the sample span varies from 60 mm to 160 mm by 20 mm. For the tests with $\lambda = 1.6$, the sample span varies from 160 mm to 300 mm by 20 mm. At least three specimens are tested for each sample size to account for the randomness of

DEM models.

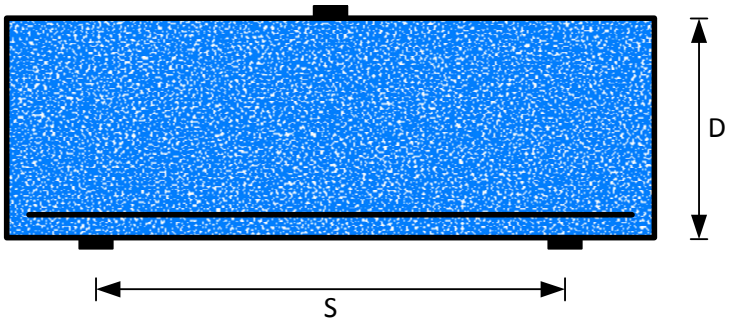

Figure 4.5: Three-point bending test model setup.

The force-displacement curve is shown in Figure 4.6. Without loss of generality, the samples with $D = 60$ mm, $S = 96$ mm and $\lambda = 0.8$, and $D = 50$ mm, $S = 160$ mm and $\lambda = 1.6$, are used to present the analysis. For the case when $\lambda = 0.8$, the whole failure process is divided into four stages. At about 65% of peak , see Figure 4.7(a), the shear zones are first observed near the loading locations. A plateau is observed on the force-displacement curve, right after the shear zones are initiated. Then the force continues to increase with a reduced stiffness until the force reaches about 90% of peak. At this stage, see Figure 4.7(b), the shear zones are almost fully developed. From Figure 4.7(b), we can see three shear zones near the loading locations. In this case, the load is imparted by a rigid load bearing stripe with a relatively small width, so the stress is more concentrated, leading to a larger stress gradient near the loading points. When the load reaches the peak, we can see from Figure 4.7(c) that the size of the shear zone is stable and more micro-cracks are developed near the perimeter. When the load continues increasing, the sample eventually fails as the micro-cracks outside of shear zone coalesce together from beneath both the top and bottom load bearing stripes, as shown in Figure 4.7(d).

The micro-crack evolution process is demonstrated in Figure 4.8. Before the load reaches the peak, the micro-cracks are mostly distributed under the load bearing stripes. Figure 4.8 indicates that there is no clear sign of shear crack initiation. Instead, the energy is mostly dissipated through the development of the shear zones. However, when the shear zone is fully developed, the force starts to decrease because of the initiation and propagation of

shear cracks between the two shear zones. In Figures 4.8(c)-(f), we can clearly identify the fracture tip growing from the bottom shear zone towards the top. This pattern is very different from previous simulations, where no clear evidence of fracture tip is captured. We define this type of failure that shows shear zones and shear crack in macro-scale as ductile to brittle failure mechanism transition.

In the other group of simulations with $\lambda = 1.6$, the force-displacement curve is shown in Figure 4.6(b). Compared to the case when $\lambda = 0.8$, the curve shows more kinks in the whole loading process. The first continuous micro-event is not captured until the force is about 90% of peak, as shown in Figure 4.9(a). Meanwhile, we can also observe development of micro-cracks near the mid-bottom of the beam, which is the main reason of the kinks on the force-displacement curve. What's more, those tensile cracks do not lead to the final failure of the sample, because the rebar at the bottom of the beam can still transmit forces even though the sample is fractured with tensile cracks. In other words, the mode I tensile failure is restrained in this case. When the force reaches the peak, the shear zones are fully developed and tensile micro-cracks are observed. Similarly, we can observe some initiations of micro-cracks near the bottom of the shear zone, and these eventually develop into a macro-crack as shown in Figures 4.9(c)-(d), leading to the collapse of the sample.

The evolution of the fracture is mainly in the post-peak regime, as shown in Figures 4.9(c)-(d). Since the evolution process is very fast, the post-peak stage is refined into several time intervals. Figure 4.10(b) shows that after the shear zones are fully developed, some micro-cracks are initiated at the perimeter of the shear zones. In this case, the bottom shear fracture propagates to the top load bearing stripe really fast, as shown in Figure 4.10(c). As the load increases, the tip of the fracture grows. Meanwhile, in other part of the sample, hardly any micro-events are observed. The propagation of the shear fracture causes the load to drop significantly in the post-peak regime. The failure pattern observed in this case is similar to that of the case when $\lambda = 0.8$.

Experimental results reported in [14] show that the shear strength is decreasing with sample size. In these simulations, consistent results are observed. For the case when $\lambda = 0.8$, sample size increases from 60 mm to 160 mm, and the average shear strength decreases about

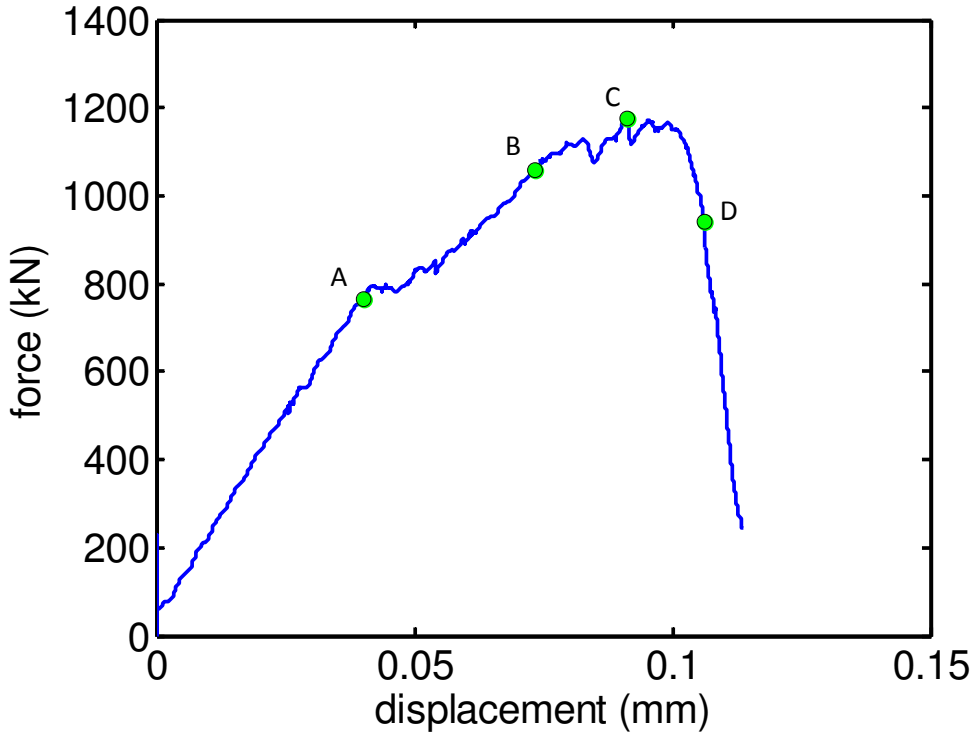

(a) $D = 60$ mm and $S = 96$ mm, λ= 0.8

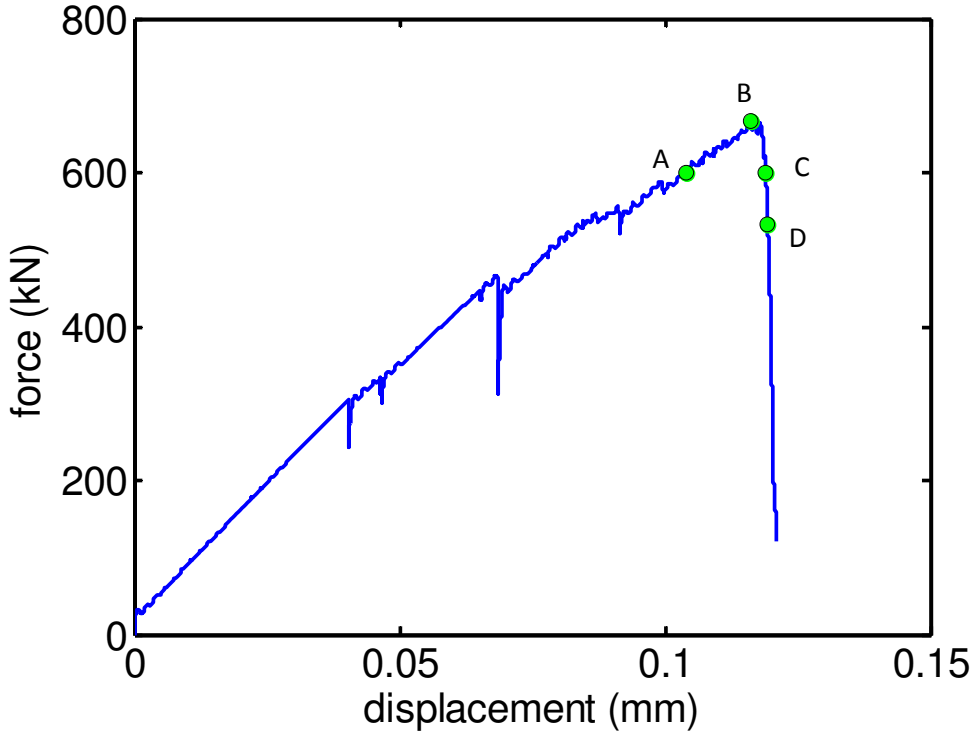

(b) $D = 50$ mm and $S = 160$ mm, λ= 1.6

Figure 4.6: Force-displacement curve in three-point bending test with $\beta \to \infty$.

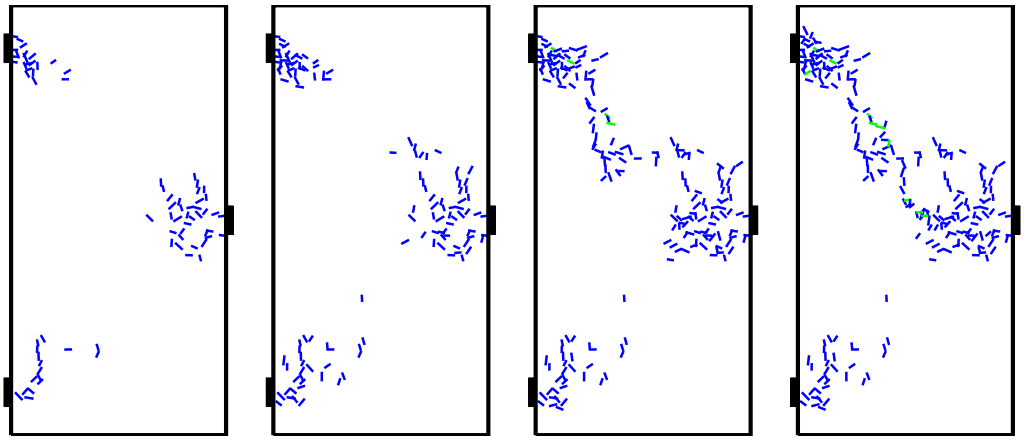

(a) stage A (b) stage B (c) stage C (d) stage D

Figure 4.7: Cumulative micro-cracks with $D = 60$ mm and $S = 96$ mm, $\lambda = 0.8$ and $\beta \to \infty$.

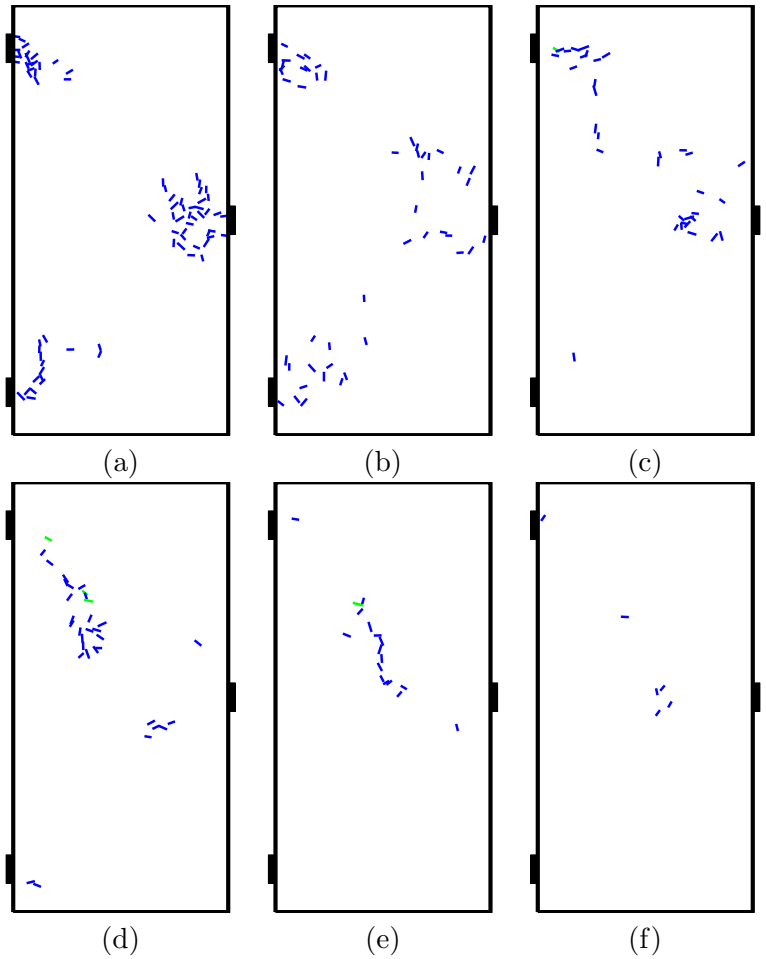

(a) (b) (c)

(d) (e) (f)

Figure 4.8: Evolution of micro-cracks with $D = 60$ mm and $S = 96$ mm, $\lambda = 0.8$ and $\beta \to \infty$. (a) 0–90% pre-peak; (b) 90% pre-peak–peak; (c) peak–99% post-peak; (d) 99% post-peak–92% post-peak; (e) 92% post-peak–85% post-peak; (f) 85% post-peak–70% post-peak.

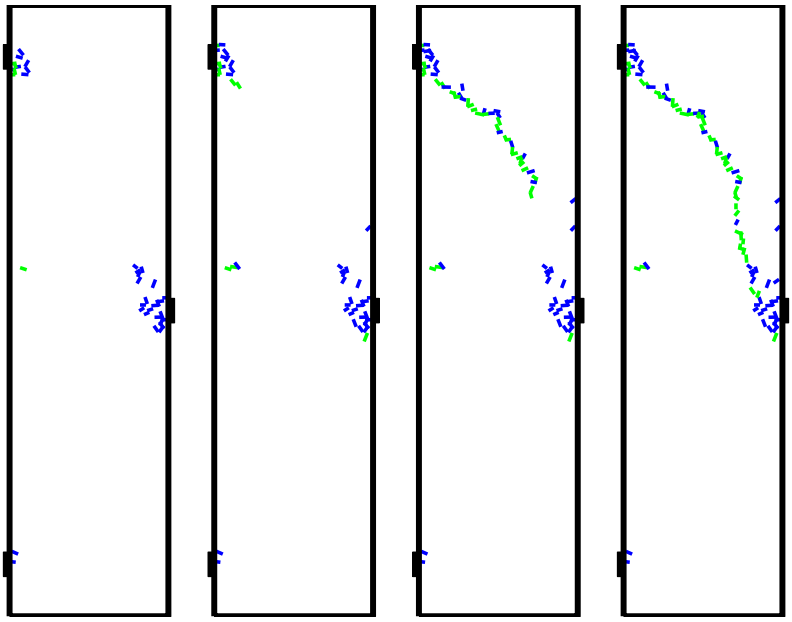

(a) stage A (b) stage B (c) stage C (d) stage D

Figure 4.9: Cumulative micro-cracks with $D = 50$ mm and $S = 160$ mm, $\lambda = 1.6$ and $\beta \to \infty$.

50%. When $\lambda = 1.6$, the shear strength decreases about 25% when the sample size increases from 160 mm to 300 mm. Though the range of sample sizes in this study is relatively small than that of experiments, it still indicates a decreasing trend. What's more, the magnitude of the strength decay is related to the relative size of shear zone to the overall sample size. When $\lambda = 0.8$, the shear zone size as shown in Figure 4.7 is larger than that of $\lambda = 1.6$ as shown in Figure 4.9. The total amount of energy dissipated through cracks determines the strength of the material, so the mechanism of cracks initiation and propagation plays a crucial role in the size effect phenomenon. In three point bending tests, regardless of λ, the input energy is mainly dissipated in two different forms: shear zone beneath load bearing stripe and shear crack between two shear zones. Since shear crack is formed mainly by bond breaking in micro-scale, the amount of energy dissipated is related to bond strength and bond stiffness. In the case when $\lambda = 0.8$, the shear zone size to the shear crack size ratio is large, so the size effect is more obvious compare to that when $\lambda = 1.6$.

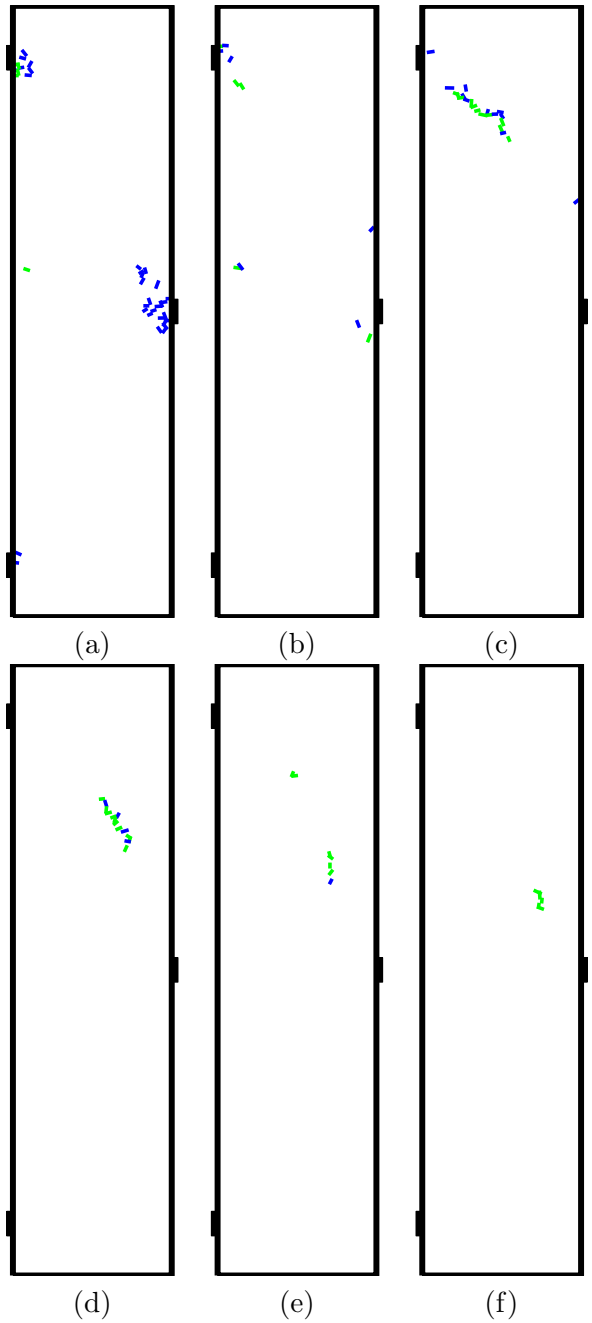

Figure 4.10: Evolution of micro-cracks with $D = 50$ mm and $S = 160$ mm, $\lambda = 1.6$ and $\beta \to \infty$. (a) 0–90% pre-peak; (b) 90% pre-peak–peak; (c) peak–99% post-peak; (d) 99% post-peak–92% post-peak; (e) 92% post-peak–85% post-peak; (f) 85% post-peak–70% post-peak.

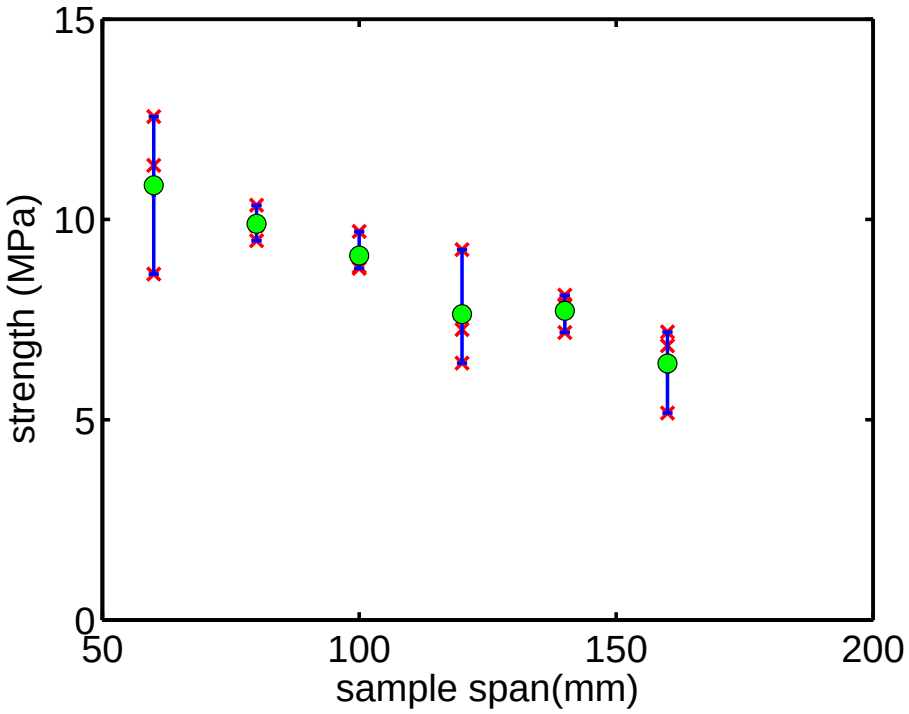

(a) $\lambda = 0.8$

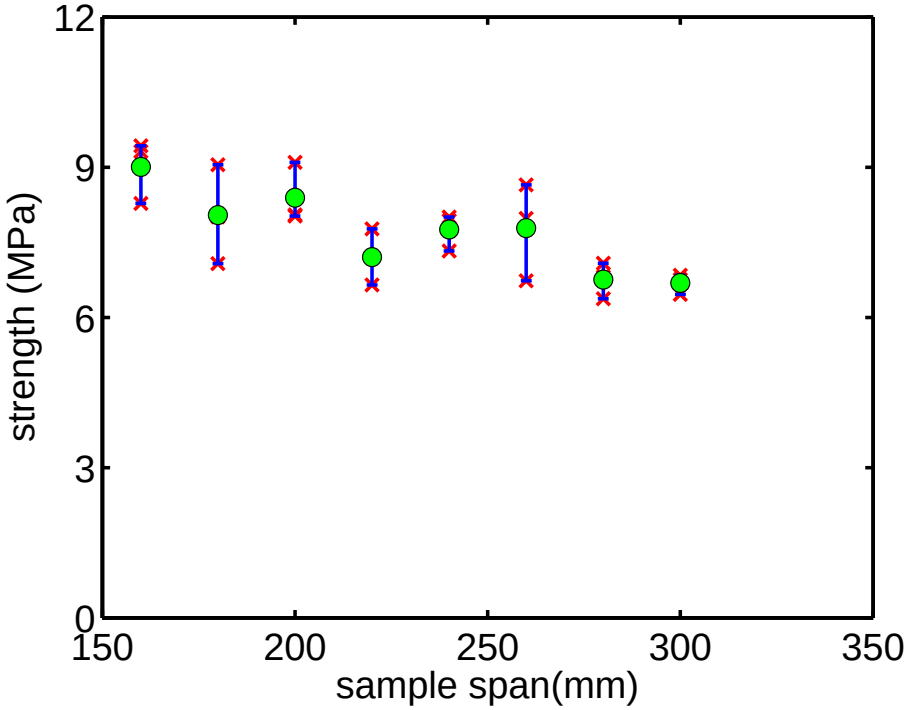

(a) $\lambda = 1.6$

Figure 4.11: Strength vs. sample width in three point bending with $\beta \to \infty$.

4.5 Four-point Bending Test

4.5.1 Failure Mechanism

Four-point bending test has been used to study mode II shear fracture of concrete [15]. In this study, a numerical model as shown in Figure 4.12 is implemented to perform the test. The symmetric notched sample is loaded by concentrated forces near the notches. The fracture developed in a direction dominated by the shear stress is considered a pure mode II shear band. Experimental evidence shows that the sample may fail in two different patterns: one, as mentioned above, is dominated by mode II shear fracture; two, a mode I fracture propagates sideways from the notch tip first then quickly run into a low stress zone of the material. In order to prevent the sample from failing in the second scenario, the distance between the load bearing stripes near the notch is carefully chosen to guarantee the presence of a narrow shear stress zone in the center. All the dimensions are labeled in Figure 4.12. The nominal shear strength obtained from the test can be defined as:

$$\sigma_{\mathrm{FPB}} = P/(D - 2a) \tag{32}$$

where P is the load and a is the notch length. In order to capture the size effect, a series of samples with depth changes from 20 mm to 300 mm are tested. To minimize the influence of the random nature of the samples, at least three samples are tested for each size. Since in DEM, the sample resolution (grain size to the sample or load bearing stripe size) plays a very important role in determining the stress field. In order to prevent local shear failure beneath the load bearing stripes near the notch, the bonds near that region are set to be elastic. Thus, the fracture initiation locations are restrained to be at the notch tip.

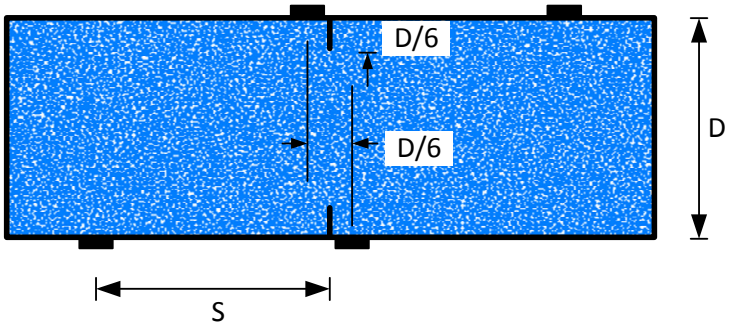

Figure 4.12: Schematics of four-point bending test.

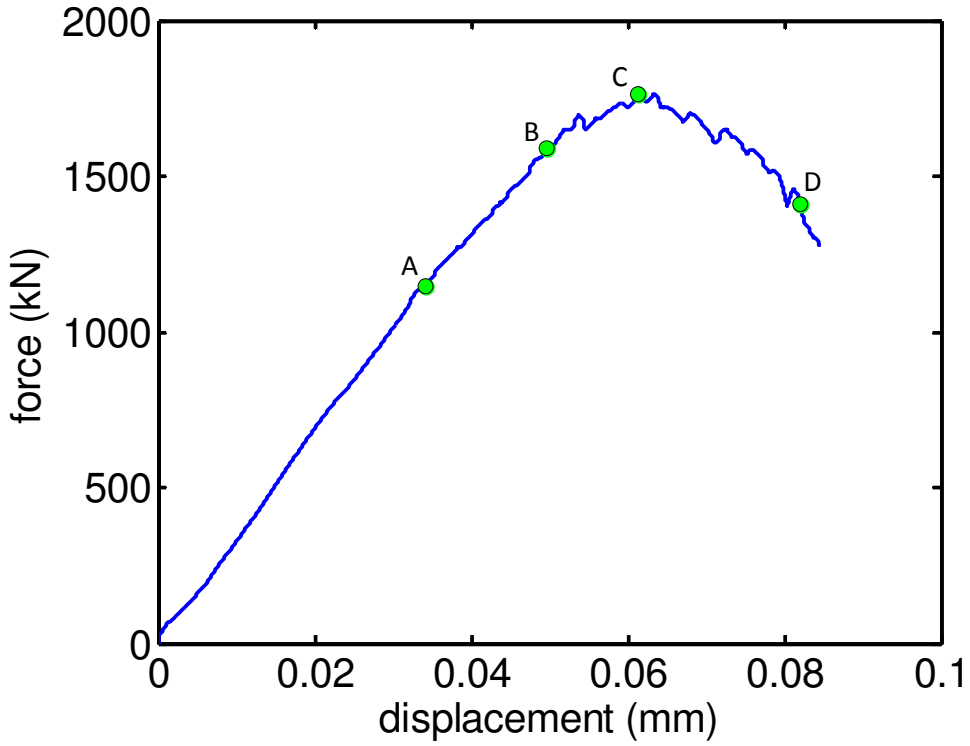

Figure 4.13: Force-displacement curve in four-point bending test with $\beta \to \infty$, S =60 mm and D =160 mm.

We choose the sample with $S = 60$ mm and $D = 160$ mm as an example to show the analysis. Figure 4.13 shows the force-displacement curve. The first micro-cracks are captured near the notch tip when the load is about 65% of peak, see Figure 4.14(a). Then when the load keeps increasing up to the peak, more and more micro-cracks are observed near the notch tip region and coalesced together to form a shear zone, as shown in Figures 4.14(b)-(c). The force starts to drop when a macro-fracture propagates between the two shear zones, see Figure 4.14(d). This failure pattern is similar to the one observed in three-point bending test, which is defined as shear brittle failure.

The whole failure mechanism can be further demonstrated by analyzing the micro-crack evolutions in different time intervals, as shown in Figure 4.15. First of all, two shear zones can be clearly seen in Figure 4.15(b) near the two notch tips. Besides, when the load reaches the peak, the two shear zones are more or less fully developed. As the load continues, two groups of micro-events are nucleated near the notch tips: one near the bottom shear zone and the other is beneath top shear zone. Figure 4.15(d) shows that both of the two groups of

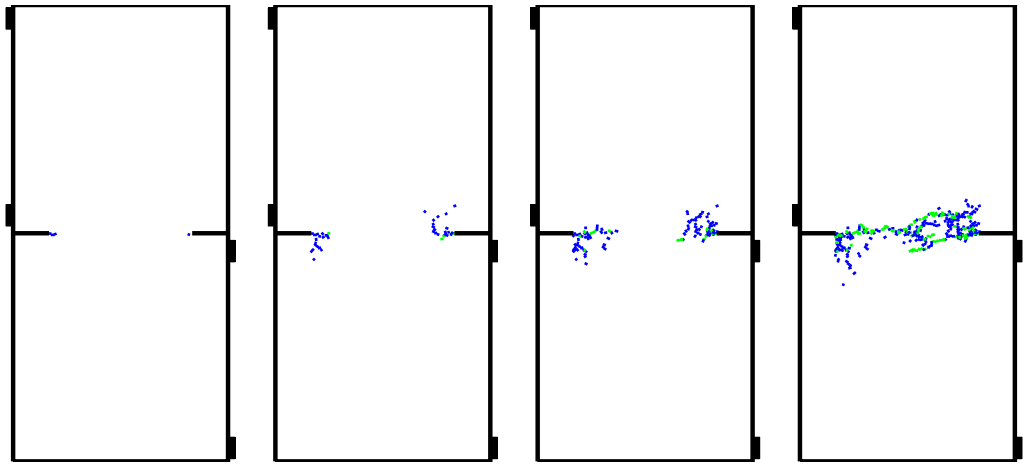

(a) stage A (b) stage B (c) stage C (d) stage D

Figure 4.14: Cumulative micro-cracks with $\beta \to \infty$, and S =60 mm and D =160 mm.

micro-cracks coalesce together and propagate towards each other. When they form a macro shear fracture together in the center of the beam, the sample fails. Figures 4.15(e)-(f) demonstrate where the fracture tip is.

The variation of nominal strength with sample size is shown in Figure 4.16. When the sample size is relatively small, the nominal strength is increasing with sample size up to about $D = 80$ mm. Then the strength starts to decrease with sample size up to $D = 180$ mm. After that, the strength is more or less a constant irrelevant to sample size. This trend, though contradicts with traditional size effect, satisfies the conclusion drawn from results of brittle shear failure. For small samples, the size is not large enough for the shear zones to be fully developed. As a result of that, the strength would be increasing with sample size. When the sample size exceeds a critical value, the two shear zones have enough space to grow and a shear crack is observed connecting them. At this stage, the strength of the sample decreases with sample size. As mentioned before, the shear zone sizes are a material constant if sample size is relatively large than the grain size. So if the sample size keeps increasing, the ratio between the shear zone size to the sample size is vanishing. Thus the size effect phenomenon would become weaker and eventually negligible.

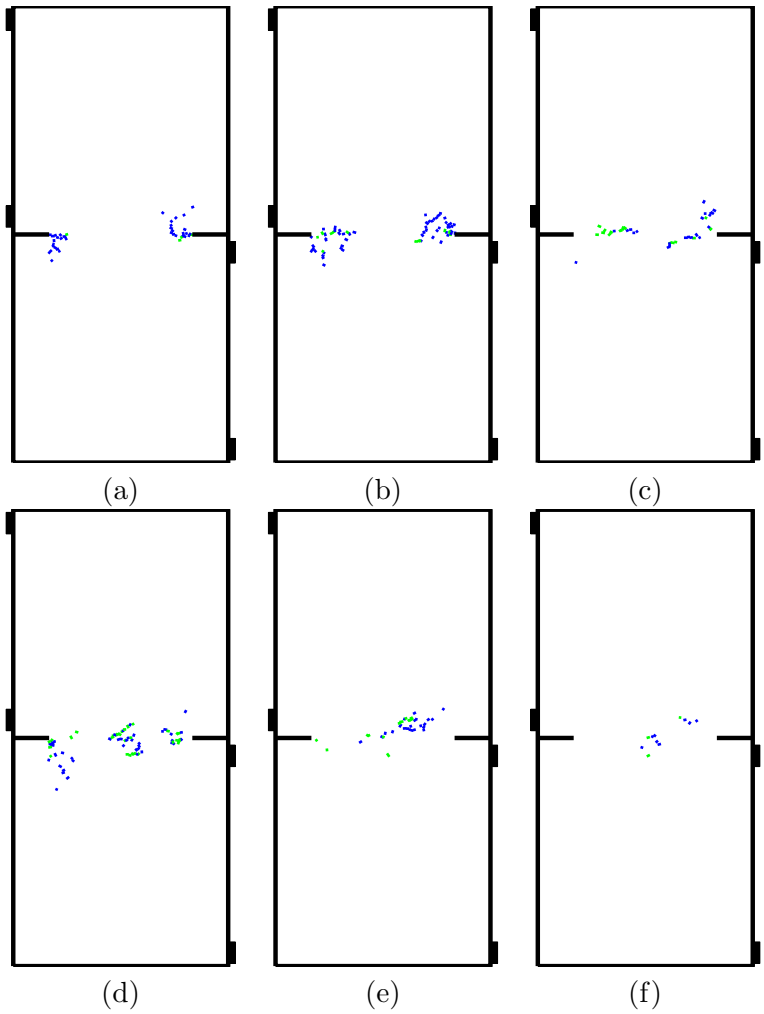

Figure 4.15: Evolution of micro-cracks with $\beta \to \infty$, and S =60 mm and D =160 mm. (a) 0–90% pre-peak; (b) 90% pre-peak–peak; (c) peak–99% post-peak; (d) 99% post-peak–92% post-peak; (e) 92% post-peak–85% post-peak; (f) 85% post-peak–80% post-peak.

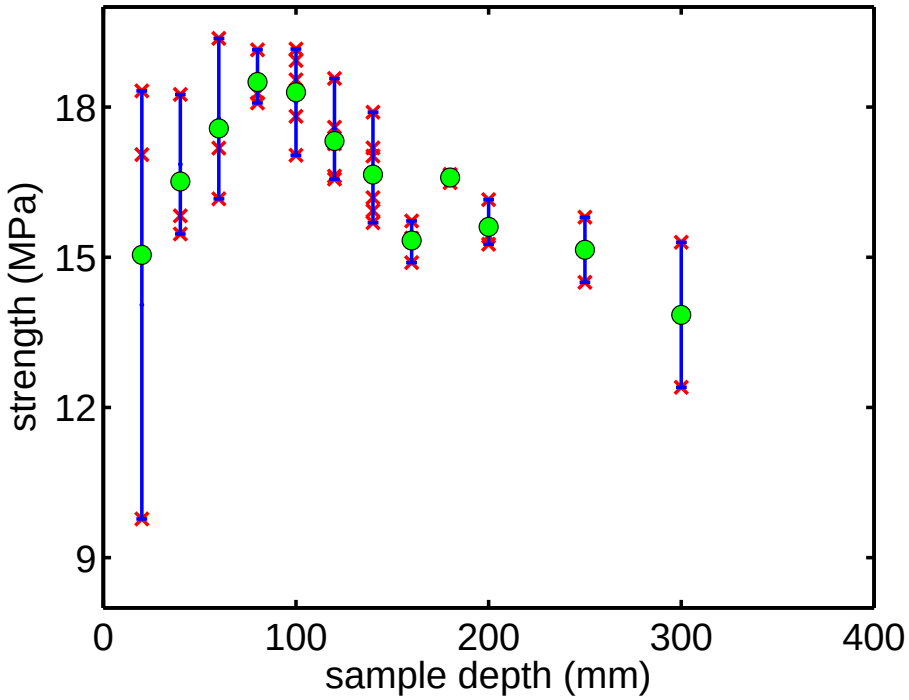

Figure 4.16: Shear strength vs. sample width with $\beta \to \infty$.

4.5.2 Size Effect

In this section, we primarily focus on the issue of failure transitioning from shear crack to shear band and its impact to the size effect by investigating two factors: softening coefficient β and uniformity of the load. Since the preexisting notch may have contributions to the overall size effect, we will perform the four-point bending tests with intact samples. The configuration for the tests is summarized in Figure 4.17. The uniformity of the stress field along the center line is adjusted by revising the width of the loading wall, w. In this section, we set $w = 20$ mm and 70 mm and $D/S = 1$.

At $\beta \to \infty$ and $w = 20$ mm, D varies in a range from 120 mm to 200 mm, the failure mechanism is governed by a localized shear zone beneath the loading wall. In addition, we can observe a fracture along the center of the sample when the sample collapses, see Figure 4.19. Each micro-crack is represented using a line indicating the location, while the time sequence of the micro-cracks is indicated by the color. The blue micro-cracks near the loading wall suggests that the shear zone develops earlier than the center fracture. This failure mode is similar to what we have identified in Brazilian test, namely, indentation-type

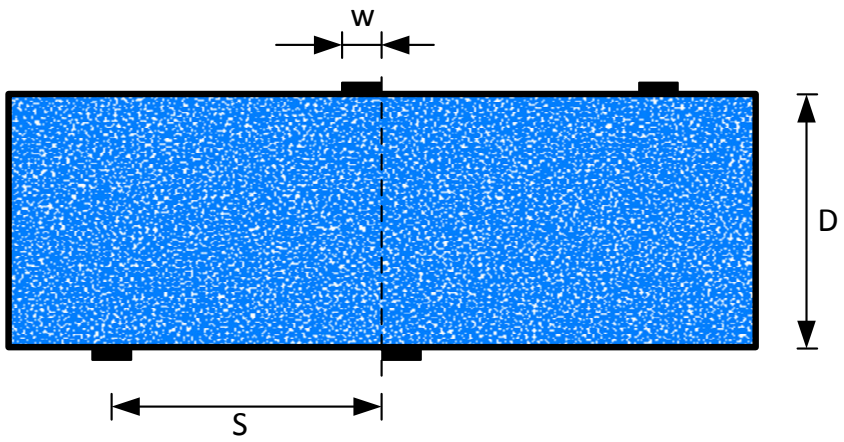

Figure 4.17: Four-point bending test model setup.

failure. This failure mode remains the same as $D \in [120, 200]$ mm. As such, the nominal shear strength defined as in Eq. 32 can be calculated and analyzed to show the size effect. The results are summarized in Figure 4.18. As expected, the shear strength decreases with sample size.

Then we increase the width of the loading walls near the center line of the sample to $w = 70$ mm. The stress field along the center line is thus more uniform. The distribution of the micro-cracks are demonstrated in Figure 4.21. The color represents the initiation sequences of the micro-cracks at the specific stage. The results show no clear evidence of the shear zone beneath the loading walls. Instead, the failure mode is governed by the development of the rupture along the center line. Meanwhile, inclined shear cracks adjacent of the fracture plane are also observed. By the time the sample fails, the shear band along the center line split the sample into two halves. In addition, there is no apparent length scale can be identified through the failure process. Though the width of the center fracture seems like a factor influencing the size effect, careful examination suggests that the expansion of the center fracture in lateral direction only happens in post-peak regime. The shear strength is therefore only governed by the development of the center crack. As expected, the shear strength exhibits no size effect, see Figure 4.20.

To investigate the impact of the strength ratio σ_c/σ_t on the failure mechanism and size effect, the softening coefficient β is decreased to $\beta = 0.1$. At $w = 20$ mm, the distribution

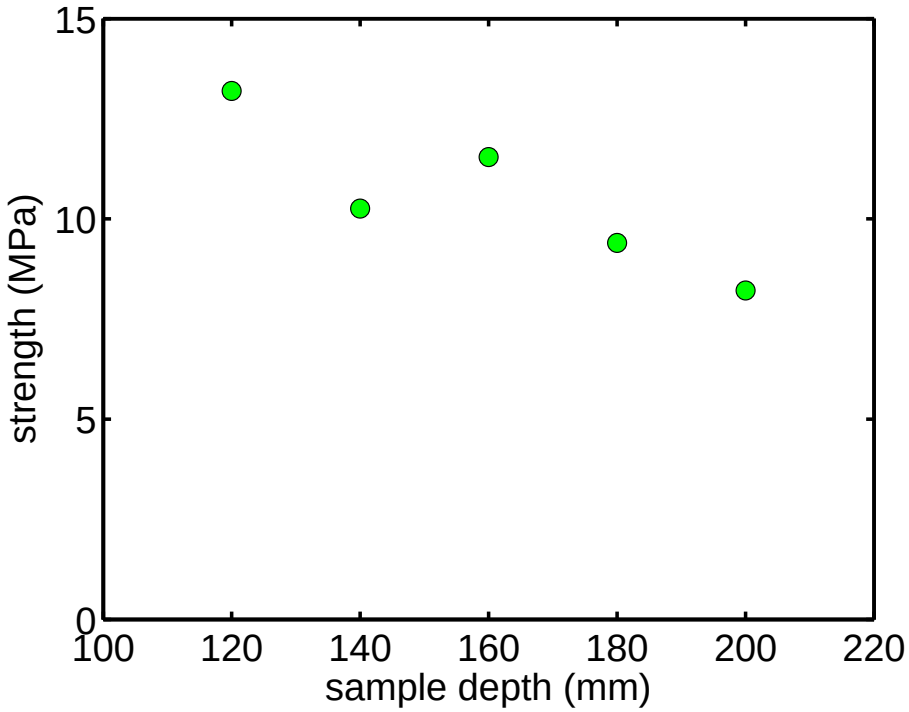

Figure 4.18: Shear strength vs. sample width, $\beta \to \infty$ and $w = 20$.

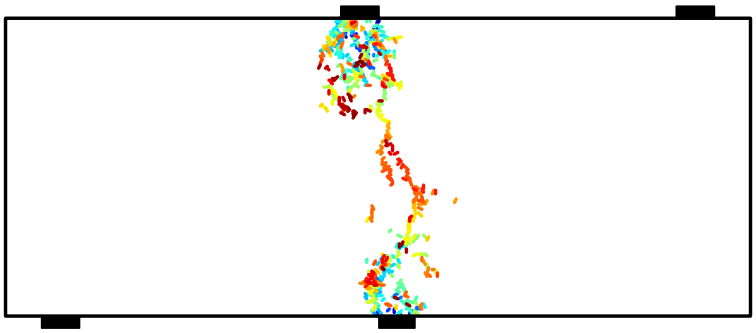

Figure 4.19: Distribution of micro-cracks at peak with $\beta \to \infty$, $w = 20$ mm, and $D = 160$ mm.

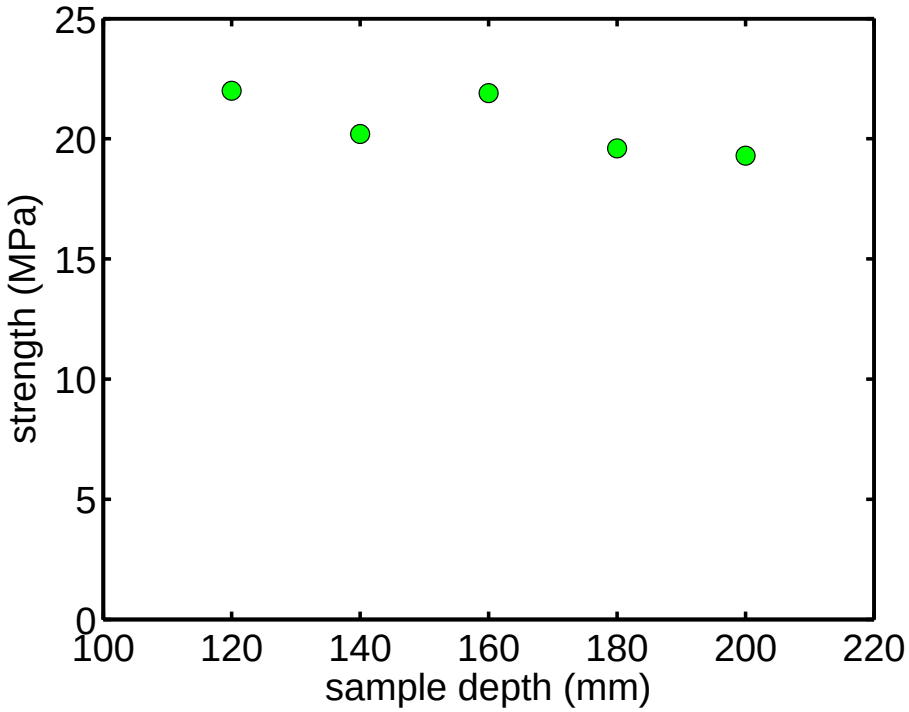

Figure 4.20: Shear strength vs. sample depth, $\beta \to \infty$ and $w = 70$ mm.

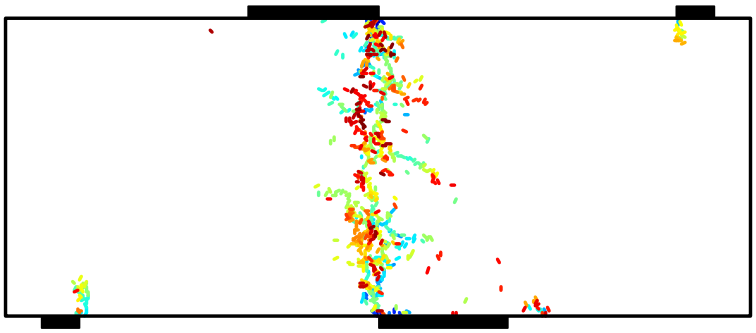

Figure 4.21: Distribution of micro-cracks at peak with $\beta \to \infty$, $w = 70$ mm, and $D = 160$ mm.

of the micro-cracks is illustrated in Figure 4.23. The color of the micro-cracks suggests that the failure is initiated from near the center. Though several tensile fractures are observed beneath the loading walls, they are not the dominant failure mechanism governing the strength. By the time the shear stress reaches the peak, the sample collapse because of the fracture along the center line. Meanwhile, there is no evidence to show the existence of shear zones near the loading point. As such, the shear strength at peak exhibits a constant trend w.r.t. sample size, see Figure 4.22.

At $\beta = 0.1$ and $w = 70$ mm, the micro-cracks exhibit a similar pattern governed by a rupture along the center line of the sample. In addition, inclined shear fractures are observed near the shear plane. In macro-scale, the shear band consists of multiple shear fractures, as seen in Figure 4.25. From this failure pattern, there is no clear evidence of existing an intrinsic length scale that controls the failure. The nominal shear strength thus should be a constant independent of the sample size. However, Figure 4.24 shows that the shear strength from four-point bending decreases with sample size. This observation contradicts with previous conclusion that ductile shear failure should not exhibit size effect. After carefully examine the fracture process zone during the failure process, it seems that the shear strength at small sample size is associated with multiple shear bands.

In Figure 4.26, the fracture process zone is represented using the cloud of micro-bonds in softening regime. The main shear band is located between the two loading walls. The inclination angle is associated with the size of the loading wall w and the depth of the sample D. Meanwhile, we can also observe a secondary shear band developed between the loading wall and the support, particularly for the case with small D. As such, the shear strengths are overestimated by samples with small D. We may also consider the size effect as a boundary effect.

It has been shown in Figures 4.24 & 4.26 that the boundary effect has a great impact to the shear strength measured from these tests. To justify the influence of the support to the shear strength, an additional series of simulations with modified configurations are used for the four-point bending test. Since the support located at the top right and bottom left of the sample is used to restrain the rotational movement of the sample during the test.

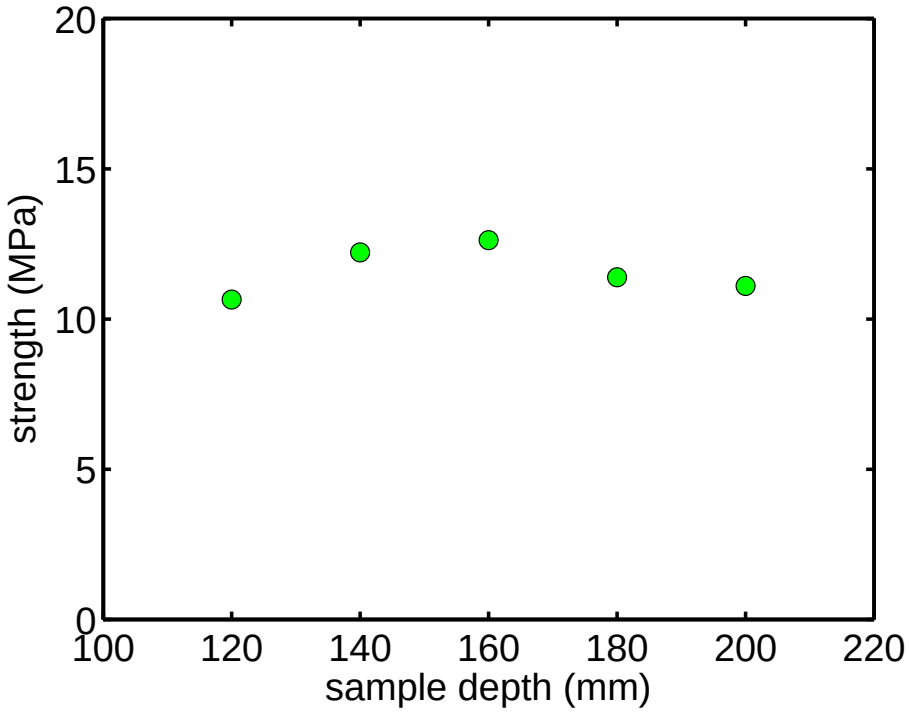

Figure 4.22: Shear strength vs. sample depth, $\beta = 0.1$ and $w = 20$ mm.

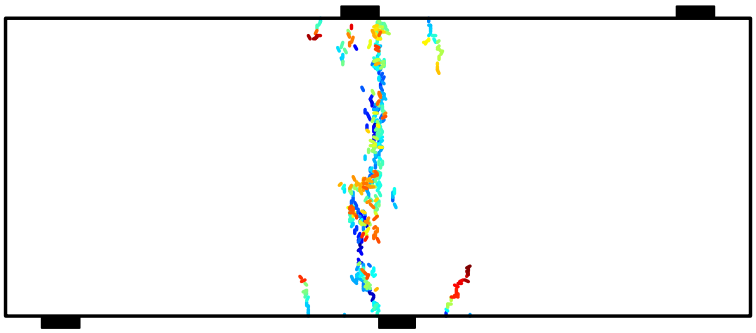

Figure 4.23: Distribution of micro-cracks at peak with $\beta = 0.1$, $w = 20$ mm, and $D = 160$ mm.

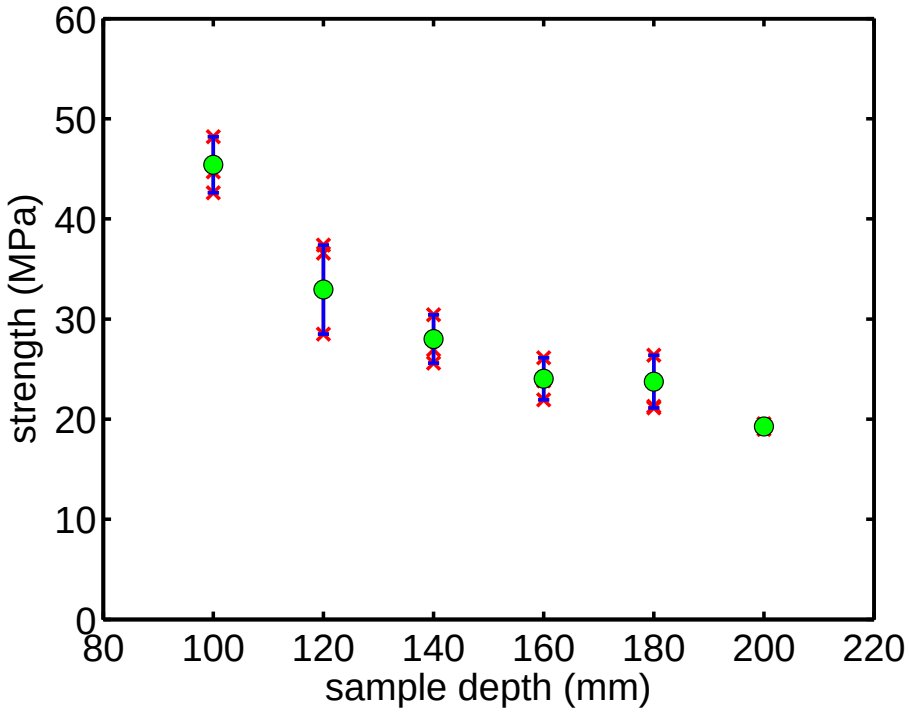

Figure 4.24: Shear strength vs. sample depth, $\beta = 0.1$ and $w = 70$ mm.

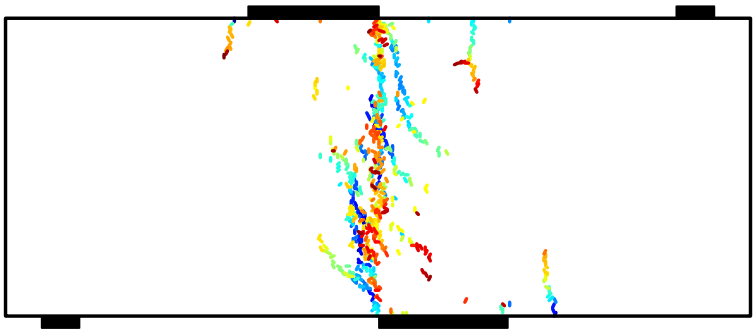

Figure 4.25: Distribution of micro-cracks at peak with $\beta = 0.1$, $w = 70$ mm, and $D = 160$ mm.

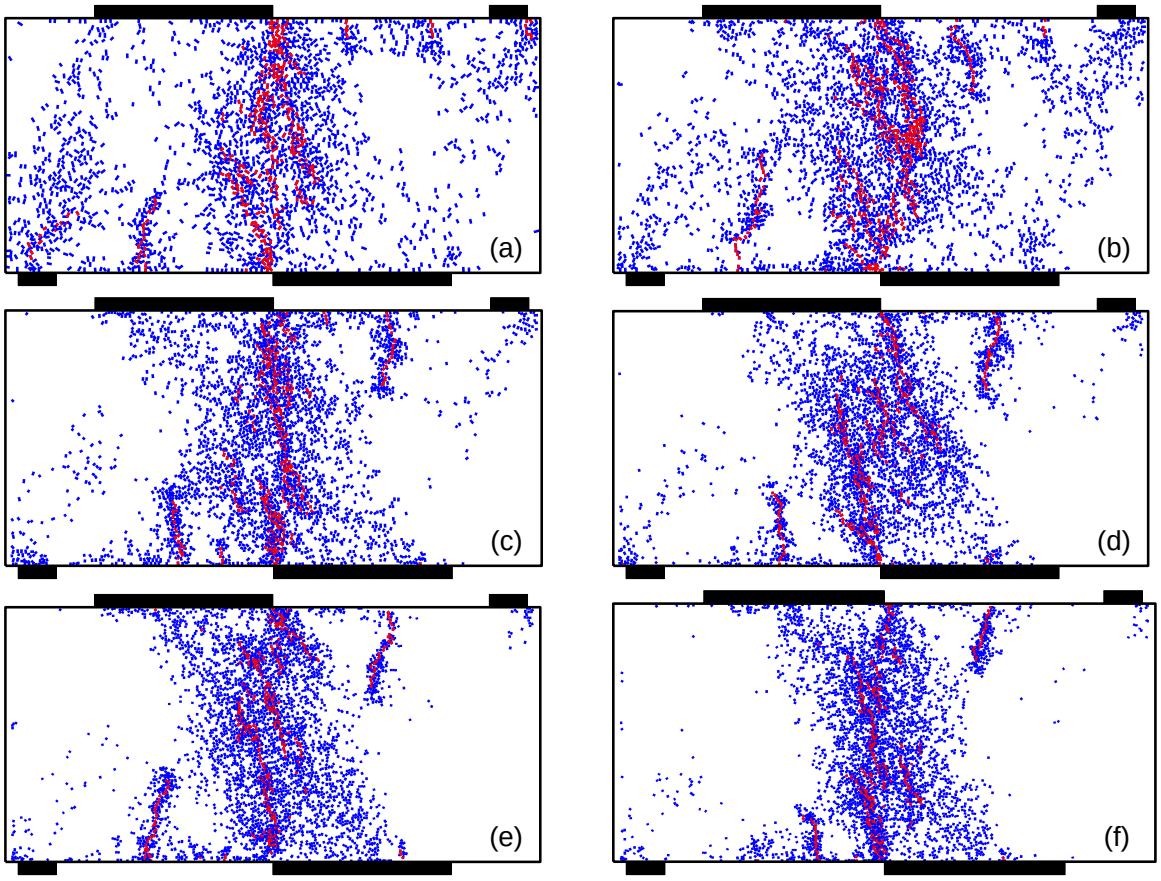

Figure 4.26: Evolution of the secondary shear band at peak. From (a) to (f), sample size increases from $D = 100$ mm to 200 mm by 20 mm. Blue dots are damaged bonds while red ones are micro-cracks. The sample sizes are normalized to 1. Blue and red dots represent softening bonds and bond breakage, respectively.

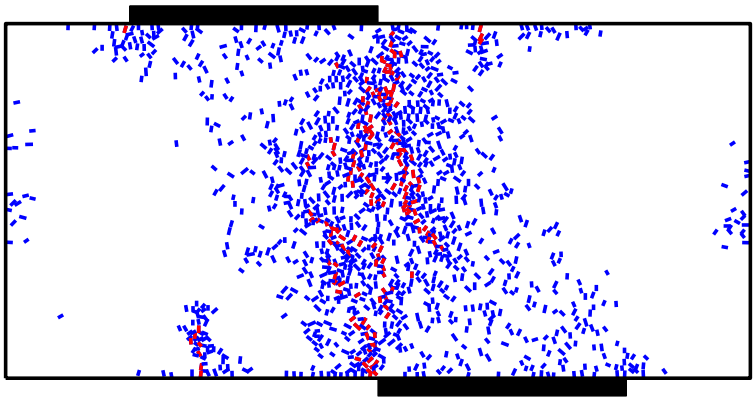

Figure 4.27: Distribution of micro-evens with $\beta = 0.1$, $w = 70$ mm, and $D = 100$ mm. Blue and red dots represent softening bonds and bond breakage, respectively.

They are necessary if the size of the loading wall is small, e.g., $w = 20$ mm. However, when $w = 70$ mm, the rotation of the sample under the loading wall is negligible in simulations. Therefore, we perform the four-point bending test using the same samples but without the top and bottom supports to remove the boundary impact to the shear strength. At $w = 70$ mm, $\beta = 0.1$ and $D = 100$ mm, the distribution of micro-events are demonstrated in Figure 4.27. Compared to that in the case with supports as shown in Figure 4.26(a), the secondary shear bands cannot be observed by removing top-right and bottom-left supports. As such, the size effect contributed from the boundary is removed from the nominal shear strength. The relationship between shear strength and sample depth D is summarized in Figure 4.28. Although the average strength decreases from approximately 25 MPa to 20 MPa with sample size, the amount of strength decay is negligible compared to that shown in Figure 4.26(a). Even though the size effect associated with boundary condition is removed, there are other factors that contribute to the size effect as well. In four-point bending test, the shear band consists of multiple shear cracks. As such, the contributions of the length scales, e.g., shear band width, shear crack spacing, center fracture length, etc, to the size effect require further investigation.

4.6 Discussion

To sum up, all the simulations in this study exhibit two failure patterns. First, if the sample fails with a shear band, showing no clear sign of fracture tip, the failure mechanism is defined

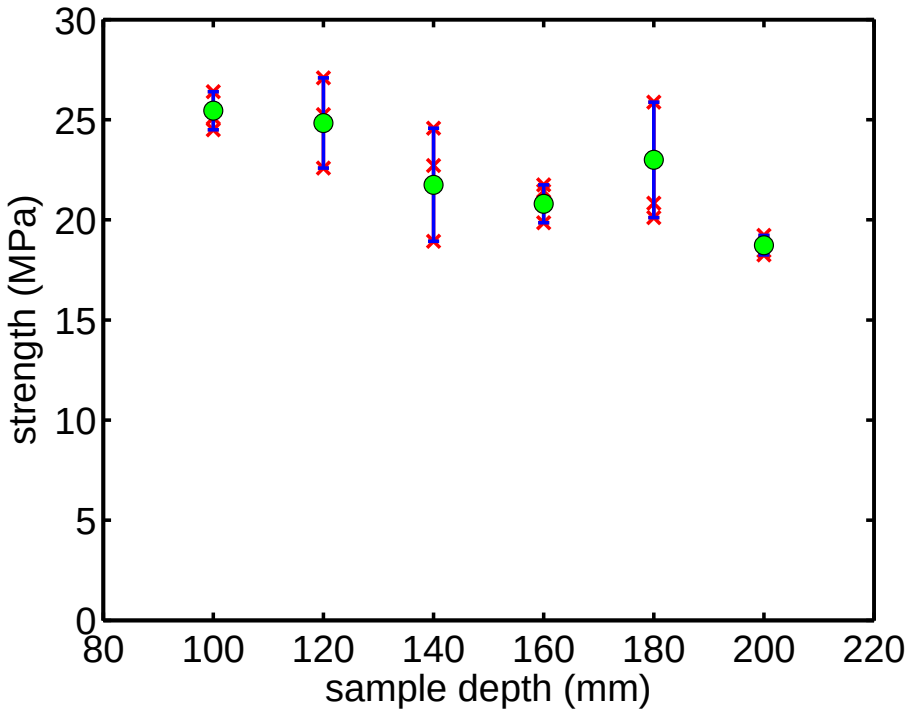

Figure 4.28: Shear strength vs. sample depth, $\beta = 0.1$ and $w = 70$ mm.

as ductile shear failure. Second, if the sample fails with shear zones and a clear shear fracture in macro-scale, this failure pattern is called brittle shear failure. The difference between shear zone and shear fracture can be visualized in Figure 4.29. Take the failure pattern shown in Figure 4.29(a) as an example, we can clearly see two shear zones near the notch tips, connected with an obvious shear fracture. We monitor the directions of all the micro-cracks in this failure pattern. Since this is a two dimensional problem, the angles are in the range from 0 to 180 degree. Then we divide this angle range into 20 buckets and count the number of micro-cracks in each bucket. The result is presented in Figures 4.29(b)-(c). It shows that micro-cracks in shear crack zone has a strong orientation, while the directions are distributed uniformly in shear zone.

In this study, ductile shear failure pattern is observed in uniaxial compression tests, as well as in mode II shear tests. The reason is the load is applied uniformly on the boundary, yielding a relatively uniform stress field in the sample. On the other hand, in three-point bending and four-point bending tests, the failure pattern is dominated by brittle shear failure. The load applied is more concentrated at a point, though a load bearing stripe is

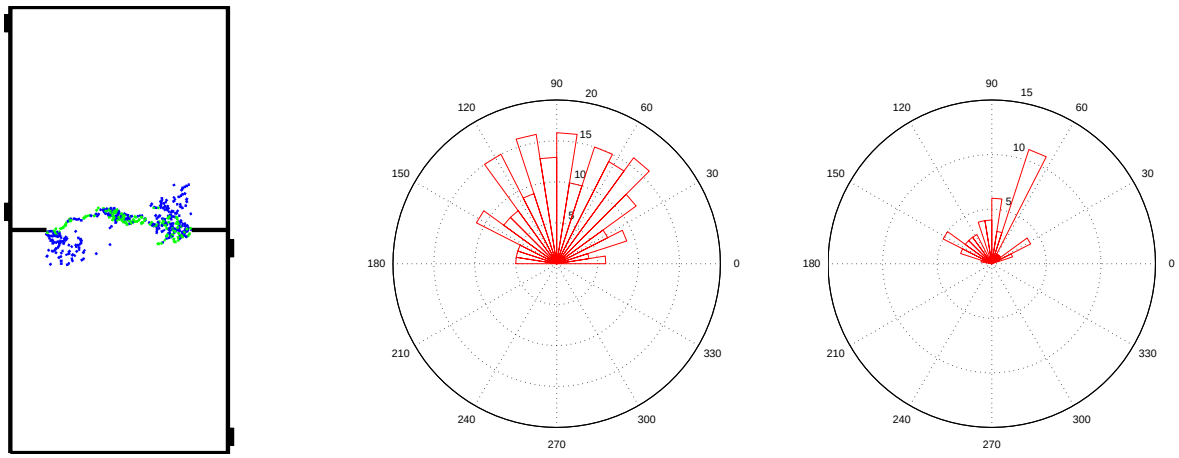

(a) micro-cracks (b) shear zone (c) crack zone

Figure 4.29: Shear band vs. shear crack.

used. Under such loading conditions, the gradient in the stress field is larger than former tests. As a result, a clear shear zone and shear fracture are observed. The simulation results also indicate that the nominal strength of quasi-brittle material is independent of sample size under the condition of uniform stress, or in other words, ductile shear failure pattern. The correlation between nominal strength and sample size is only observed under brittle failure pattern.

In the case of brittle shear failure, the amount of strength decay with sample size seems related with the relative size of the ductile shear zone to the brittle shear fracture. For small sample size, there is not enough space for the shear fracture to develop. In this case, the strength will be increase with sample size until the sample is large enough for ductile shear zones to be fully developed. Furthermore, if the sample size exceeds that limit, shear fracture is the dominant reason of the material losing its strength. Under such a scenario, the ratio of shear zone size to the fracture size is decreasing with increasing sample size. As a result, the strength will be decreasing with increasing sample size. When the ratio is negligible, the dependency of the strength on the sample size vanishes as well, thus it explains why the size effect cannot be observed for large enough samples, especially for the experimental evidences presented in the first section.

4.7 Conclusion

In this study, three different loading configurations are investigated with various sample sizes. Certain modifications are also applied to the sample to demonstrate different failure mechanisms. The simulation results presented show that the synthetic rock simulated using discrete element method is capable of reproducing many basic characteristics of different failure mechanisms of quasi-brittle material that have been widely observed in experiments. Then two different shear failure patterns are observed, namely ductile shear and brittle shear failure mode, respectively. The whole failure process in ductile shear failure mode shows that the micro-cracks are distributed along the maximum shear stress directions and the sample eventually fails because of the coalescence of those micro-cracks. During this process, no clear sign of progressive crack can be identified. On the other hand, the whole failure process in brittle shear failure mode shows that the micro-cracks are first observed near the high-gradient stress field region. Note that the development of the shear zone won't lead to the failure of the sample. Instead, a shear fracture is observed beneath the perimeter of the shear zone, which is the dominant reason for the strength decay.

On the basis of the two distinctive failure mechanisms, the simulation results suggest that the relationship between the nominal shear strength and sample size is governed by the development of the plastic zone. If the material fails in ductile shear mode, the strength shows no correlation with sample size. However, if the sample fails in brittle shear mode, the sample strength would decrease with sample size, as observed in experiments. The failure mechanisms of the sample are governed by loading conditions. If the sample is imparted with concentrated load, the sample would fail in brittle shear mode. Meanwhile, if the load is uniformly distributed, the sample is likely to fail in ductile shear mode. Consequently, the size effect phenomenon can only be observed in brittle shear failure mode. Moreover, the amount of the strength decay is related to the ratio of ductile shear zone size to brittle shear fracture length. The theory proposed in this study offers another explanation to the divergence in experimental results of size effect phenomenon. However, further investigations are required to thoroughly identify the intrinsic mechanisms of shear band and shear fracture.

CHAPTER V

NUMERICAL SIMULATION OF ROCK CUTTING

5.1 Introduction

Utilizing the scratch test to measure material properties can be traced back to the treatise, On Stones, by Theophrastus (372 B.C.–288 B.C.) and the hardness test of Mohs (1773–1839) [22]. In the past decades, experimental observations [102, 103] from the scratch test or the rock cutting test in sedimentary rocks present compelling evidence that there exists a correlation between the uniaxial compressive strength σ_c and the specific energy ϵ determined from the slope of the mean cutting force versus the cross sectional area of the cut, i.e., the input energy per unit volume of cut, when the test is conducted in a ductile-dominant mode of failure. The ductile mode, which occurs when the depth of cut is smaller than a critical threshold, is associated with continuous decohesion and plastic flow of pulverized materials ahead of the cutter face. With the benefits of the test being non-destructive and can yield continuous results along the length of cut, the scratch test has been employed in evaluating rock heterogeneity [104, 103]. For a relatively homogeneous rock, the cutting force signals in the ductile mode exhibit characteristics of white noise [93]. Variations in the pattern of the force signals may therefore be inferred as a reflection of the changes in the rock strength along the length of cut.

One of the characteristics of the cutting process is that it involves not only the ductile mode, but also a brittle mode associated with rock chipping and fragmentation, when the depth of cut increases. The issue that whether rock scratch test results represent strength or fracture properties of the material has been under debate for many years. Previously in the literature, the cutting process is generally modeled with the objectives to establish the scratch test as a laboratory testing technique and/or to improve drilling efficiency [59]. It has been proposed that the cutting force reflects the material toughness if it fails in brittle mode. Many researchers believe that scratch test is an alternative way of measuring the

fracture toughness of the material [117, 9, 2, 3, 4], rather than the strength. The key to settle this long-lasting argument is to clearly explain the failure mechanism transition in scratch test.

Failure mechanism is often characterized by apparent observations of macro-scale cracks and influenced by numerous micro-scale factors that cloud the researcher's view of the underlying causality. Thus the failure mechanisms that dominate different failure modes in scratch tests are still mystery. It has been shown that the failure process of rock cutting involves both ductile and brittle fractures by FEM simulations [128]. In addition, the authors interpret the results from failure mechanism transition point of view by showing the size effect in brittle failure mode. As pointed out in [11] and the literature cited therein, the apparent strength of quasi-brittle material is known to be a direct reflection of different failure mechanisms.

It has been shown that the failure mechanism of rock cutting is closely related to the cutter depth [102] . If cutter depth d is within a threshold value d^*, then the failure process is dominated by ductile failure mode; on the other hand, if $d > d^*$, then the failure process is dominated by brittle mode. Besides, experimental evidence has showed that the specific energy determined from ductile failure mode is linearly related to uniaxial compressive strength.

In this work, the scratch test is modeled numerically using the three-dimensional distinct element method (DEM) [32]. DEM has been shown to be uniquely suited to model the cutting process in rocks [60, 59]. Particularly, the DEM code particle flow code (PFC3D) is employed in this analysis. Since PFC3D uses an explicit central difference time integration scheme, simulations with different cutting velocities are carried out with a homogeneous model to investigate whether the numerical analysis has a rate effect. Then the failure mechanisms transition with softening coefficient β is reproduced to explore the critical cutting depth. Because of the limitation of experimental apparatus, cutter width cannot be changed during the cutting tests. Therefore, a series of numerical models are used in this study to investigate the three dimensional effect to the cutting process, including cutting force and specific energy. Scratch test simulations with numerical samples consisting of

multiple layers with contrasts in material properties are then performed to investigate the effect of rock heterogeneity.

5.2 Model Setup

Numerical simulations of the scratch test are conducted with a rectangular prism shaped numerical sample with length $L = 100$ mm, height $H = 50$ mm and width $W = 25$ or 50 mm, see Figure 5.1. The numerical domain is densely packed with 16,102 randomly generated spheres (when $W = 25$ mm) with the radii uniformly distributed in the range of $0.8 \leq \bar{R} \leq 1.33$ mm. Normal displacements on four sides, ABCD, A'B'C'D', BB'C'C, and ABB'A' are set to zero while sides AA'D'D and DCC'D' are traction-free. A cutter, modeled by the wall elements in PFC3D, is inclined by a rake angle $\theta = 15^{\circ}$. The numerical simulations are conducted at four cutter depth, $d = 5$, 10, 15 and 20 mm; for each cutter depth, the cutter width varies from $w = 5$ mm to 50 mm by 5 mm. Note that the case of $d = 20$ mm will not be discussed here because the damage zone is so large that it reaches the bottom boundary of the domain, implying that the effect of the bottom boundary can no longer be ignored. The cutting process is modeled by imparting a constant horizontal velocity V_x to the cutter. The cases with $w = 50$ mm correspond to the slab cut while the others are the grove cut.

In this chapter, materials with softening coefficient $\beta \to \infty$ and $\beta = 0.1$ are both modeled to investigate various issues in rock cutting process. When the cutter moves, the forces applied to the cutter is recorded. The total cutting force F_c is decomposed into two components, namely, horizontal force F_h^c and vertical force F_v^c, as shown in Figure 5.1.

The micro-scale parameters for the homogeneous particle assembly are listed in Table 5.1. Unless otherwise noted, the rest of the parameters are chosen as follows: the radius multiplier, $\bar{\lambda}$=1; the stiffness ratios, k_n/k_s=1 and $\bar{k}_n/\bar{k}_s$ =1; the interparticle friction coefficient, μ=0.5; the particle density, ρ=2630 kg/m^3; and the standard deviation of both the normal and shear bond strengths is chosen to be 1% of the mean value. The macro-scale material properties obtained from the uniaxial compression and the direct tension tests are given in Table 5.2. These index tests are performed with a loading velocity $V = 0.05$ m/s achieved by ramping up at an increment $\Delta V = 0.005$ m/s. The frictional angle ϕ of

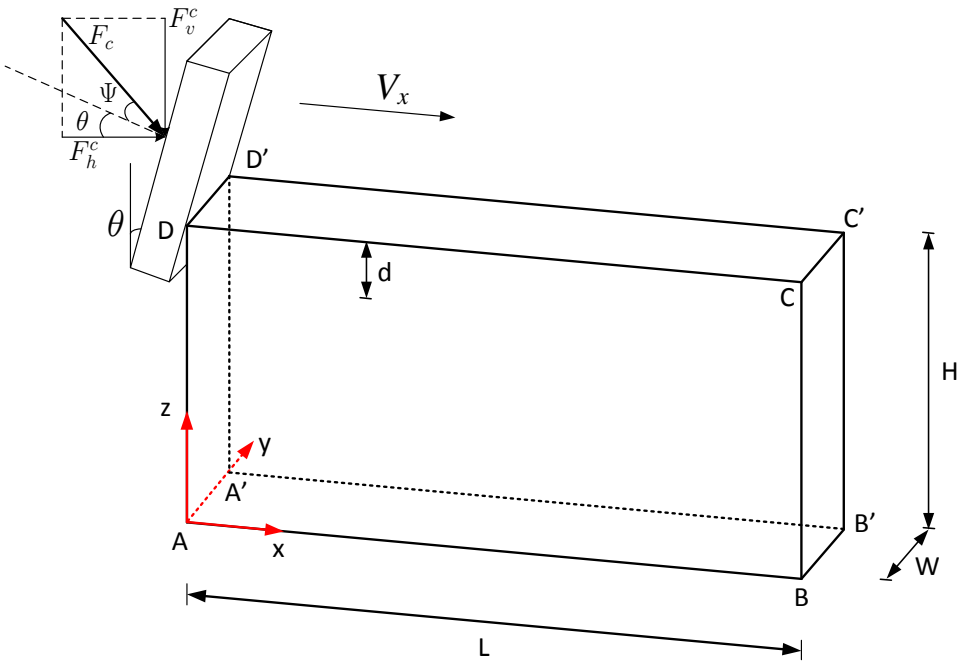

Figure 5.1: Schematic of the cutting models.

the particle assembly is obtained by linearly fitting the failure envelope obtained from the triaxial tests, see Appendix C. In addition, the stiffnesses of the cutter are chosen to be two orders of magnitude higher than those of the particles and the interface friction coefficient between the walls and the particles is also μ_w =0.5.

For the purpose of thoroughly examining the cutting process, two different materials are tested, M1 and M2, respectively. For M1, two different types of cutters are used. In one group of the samples, a box cutter is used as shown in Figure 5.1(a); while in the other group, the side and back walls of the cutter are removed, so L-shaped cutter is used. In order to investigate how the particles with broken bonds can impact the cutting force, or in other words, the effect of the lose grains, the simulations with L-shaped cutters automatically remove all particles out side of the domain that have broken bonds. Meanwhile, simulations with M1 and M2 using box cutters keeps all the particles with broken bonds. Thus the particles will pile-up in front of the cutter affecting vertical and horizontal forces.

Table 5.1: Micro-scale parameters of the particle assembly.

		Parallel Bond	
		M1	M2
Density $\rho\left(\mathrm{kg/m^3}\right)$	2630	-	-
Elastic Modulus E (GPa)	5	5	5
Stiffness Ratio k_n/k_s	1	1	1
Normal Bond Strength $\bar{\sigma}_c$ (MPa)		10 (STD=1)	100 (STD=1)
Shear Bond Strength $\bar{\tau}_c$ (MPa)		100 (STD=10)	1000 (STD=10)
Friction Coefficient μ	0.5	-	-
Radius Multiplier $\bar{\lambda}$	-	1.66	1.66

Table 5.2: Macro-scale material properties.

	UCS σ_c (MPa)	UTS σ_t (MPa)	σ_c/σ_t
M1	19.50	3.90	4.90
M2	231.06	47.46	4.87

5.3 Effect of Cutting Velocity

5.3.1 Failure Mechanism

A mechanical process may be approximated as quasi-static if the inertia effect is negligible. We may argue that if the cutter velocity is much smaller than the P-wave velocity of the particle assembly, namely, $V_x \gg V_P$, the scratch test can be considered as quasi-static [60]. The P-wave velocity in a homogeneous isotropic medium can be determined from $V_p = \sqrt{E(1-\nu)/\rho(1+\nu)(1-2\nu)}$, where ρ is the density of the medium. For porosity n≈35%, V_p ≈2120.8 m/s for the baseline Sample S1. Simulations with V_x=0.5, 1, 2.5 and 5 m/s (V_x/V_p $O(10^{-4}) - O(10^{-3})$), are performed with Sample S1. For each case, histories

of the reactions in the cutter as well as the time and location that a parallel bond is first broken are recorded. The x-component force on the front face of the cutter is referred to as the cutting force F_c. The micro-scale failure for the two simulations with $V_x = 0.5$ m/s and 5 m/s are shown in Figure 5.2. The numerical results are post-processed by illustrating a micro-crack, namely, a broken parallel bond, using a filled circle, drawn perpendicular to the contact axis with the size equal to the mean diameter of the two particles previously in contact. Figure 5.2 shows the micro-cracks projected onto the xz-plane at $y = 0$. Isolated micro-cracks outside of the range of $0 \leq y \leq 25$ mm are removed for better view of the events inside the domain. The color of a micro-crack represents the length of cut when the micro-crack is generated. Note that the length of cut s is proportional to the elapsed time through $t = s/V_x$. The blue color corresponds to the early time and the brown color to the late time. The sequence of the micro-crack events can therefore be inferred from the color of the circles. Since the shear bond strength $\bar{\tau}_c$ is much larger than the normal strength $\bar{\sigma}_c$, the micro-cracks here are mostly of tensile origin.

Clustering of the micro-cracks showing a diffuse mode of failure can be interpreted as development of a plastic zone, whereas a localized trajectory formed from micro-cracks coalescence can be considered a brittle crack. Figure 5.2 illustrates scratching of the tool induces debonding of particles along the length of cut and in front of the cutter face. The depth of damage along the length is close to the depth of cut d. A brittle mode of failure where a crack initiated from the plastic zone near the tip of the cutter and propagated to reach the free surface can be identified from Figure 2(a) for $V_x = 0.5$ m/s, while failure in Figure 5.2(b) for $V = 5$ m/s indicates a ductile-dominant mode involving a shock, i.e., an interface of velocity discontinuity between the damage zone and the intact material ahead of the cutter. The orientation of the shock is around 45° w.r.t. the x-axis at $s = 50$ mm. Orientation of the shock nevertheless fluctuates as the cutter advances. The failure mode remains brittle at $V_x = 1$ m/s, but becomes ductile at $V_x = 2.5$ and 5 m/s. Increase in the cutter velocity results in slight increase in the depth of damage and the thickness of the damage zone ahead of the cutter, in addition to a transition from a brittle-dominant mode to a ductile-dominant mode of failure.

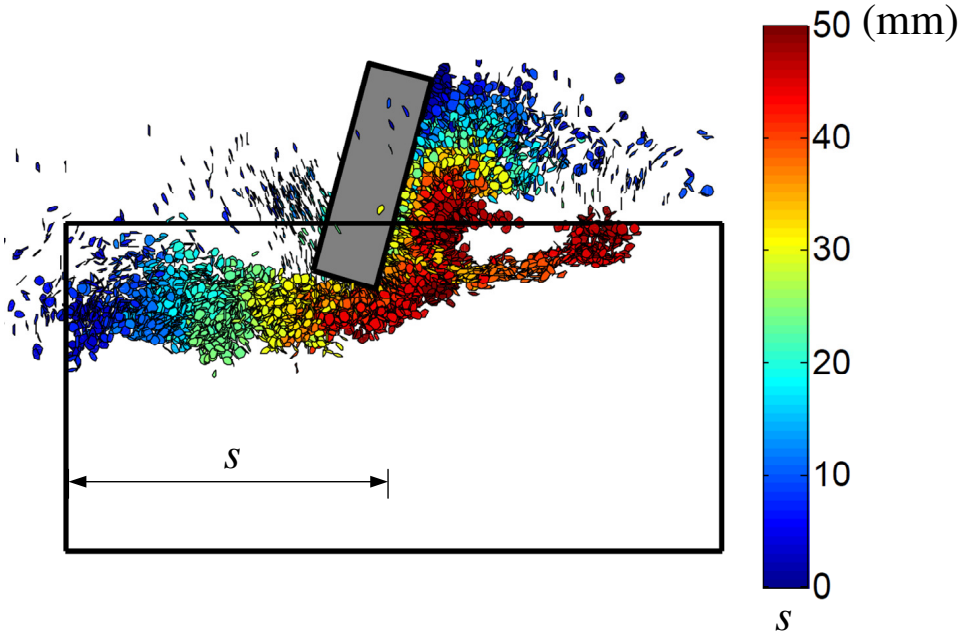

(a) $V_x = 0.5$ m/s

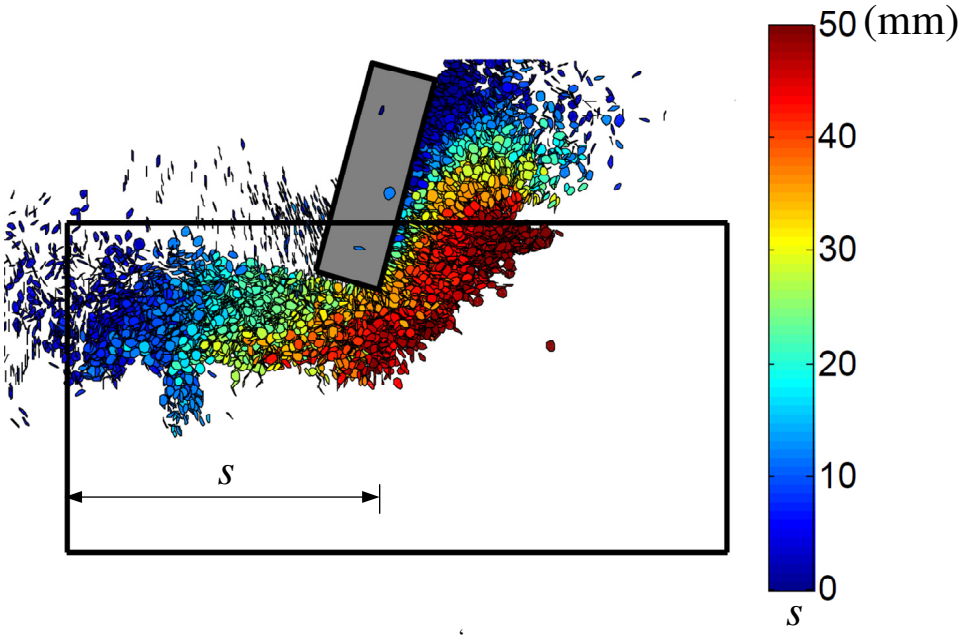

(b) $V_x = 5$ m/s

Figure 5.2: Micro-scale failure at length of cut $s = 50$ mm with Sample S1.

The effect of the loading rate on the failure mechanisms in these simulations is consistent with the experimental observations that when the loading rate is relatively large, the fracture toughness increases with the loading rate, since in order to produce equivalent main crack surfaces, extra energy is need to produce more branching cracks and more micro-cracks in the vicinity of the crack if the loading rate increases [127, 126]. Such a brittle-to-ductile transition as a result of the cutter velocity has nevertheless not been observed in laboratory scratch tests where the range of cutting velocity is relatively small, typically $O(1)$ mm/s (Detournay, personal communication). It is yet to be seen whether the rate effect observed here is a numerical artifact since the numerical results are affected by the damping scheme used to speed up convergence of the numerical calculation. A default value for the coefficient for frequency-independent damping, $\alpha = 0.7$, is used here. Hazzard *et al.* [49] suggested that the damping coefficient $\alpha = 0.7$ maybe relatively higher than realistic values for rocks. We may argue that though the cutter velocity used in the numerical simulation is relatively higher than typical experimental values, the severe numerical damping enables it to behave close to the quasi-static condition.

5.3.2 Force Signal Analysis

A comparison of the cutting force signals at $V_x = 0.5$ and 5 m/s is shown in Figure 5.3, dashed lines represent the mean values. Note that the force signals at the cutting distance (i.e., the length of cut) $s = 80$ mm, are not shown due to the boundary effect. The cutting force signal at $V_x = 0.5$ m/s appears to resemble the experimentally observed sawtooth pattern with the rise and drop reflecting the phases of crack development. Meanwhile, though the force signal at $V_x = 5$ m/s fluctuates more or less evenly around the mean value, it is far from looking like the white noise generally observed for the ductile mode in the laboratory experiments. Indeed, a power spectral analysis reveals that the force signals at $V_x = 5$ m/s possesses the characteristics similar to brown noise. The power vs. frequency relationship can be fitted by a power law with an exponent $N \approx 1.8$, instead of 0 for a white noise. At $V_x = 0.5$ m/s, $N \approx 1.9$ instead of -1 for a pink noise as observed in [93]. This discrepancy may be understood based on the fact that the particle size distribution in

the simulations is truncated. As a result, the force signals lack the high frequency content, which corresponds to events associated with small length scale. Interestingly, the histograms of the numerically obtained force signals nevertheless show similar characteristics to those obtained from the experiments on Mountain Gold sandstone [93]. Here the histograms are obtained by discretizing the range of the cutting force into $N = 50$ bins, counting the number of data points in each bin and then normalizing it with respect to the total number of data points. For the ductile mode ($V_x = 2.5$ and 5 m/s), the distribution of the normalized cutting force $F_h^c/\bar{F}_h^c$ is more or less symmetric and is mainly in the range of $0.5 < F_h^c/\bar{F}_h^c < 1.5$ (see Figure 5.4). For the brittle mode ($V_x = 0.5$ and 1 m/s), the distribution of the force is skewed to the right and is zero when $F_h^c/\bar{F}_h^c > 3$.

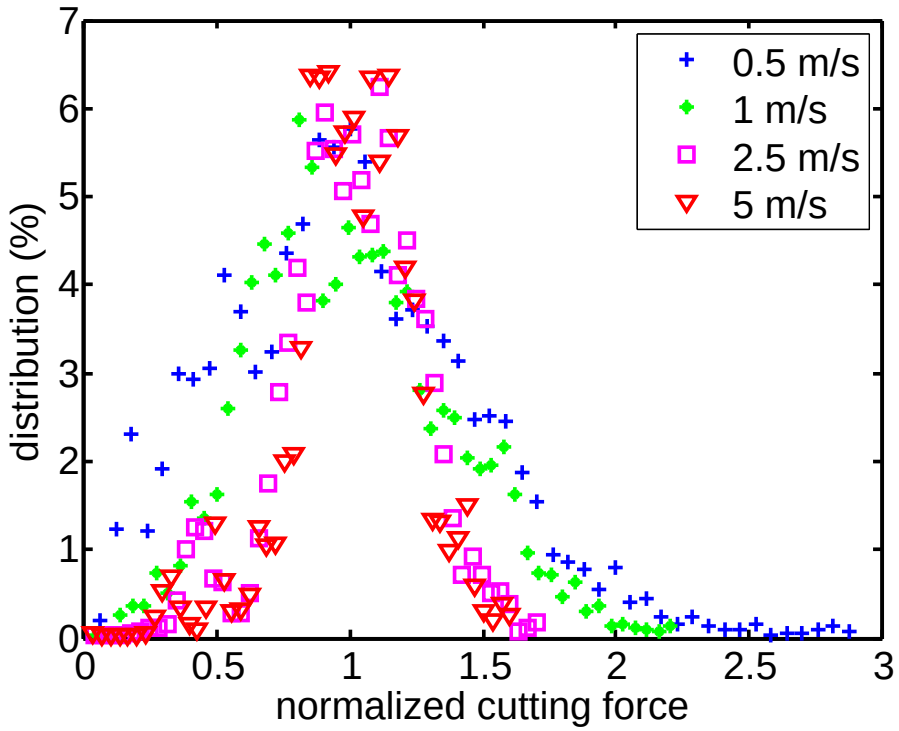

Figure 5.4: Histograms of the normalized cutting force at different cutting velocity.

The mean cutting force, averaged over the range of $10 \leq s \leq 70$ mm, are $\bar{F}_h^c$ =4.41 kN, 7.49 kN, 13.75 kN, and 21.12 kN as the velocity increases from $V_x = 0.5$ m/s to 5 m/s. As expected, the mean force is lower when fracturing is involved. The mean cutting force $\bar{F}_c^h$ at V_x=5 m/s yields a specific energy $\epsilon = F_h^c/wd$ =84.48 MPa. The ratio between the

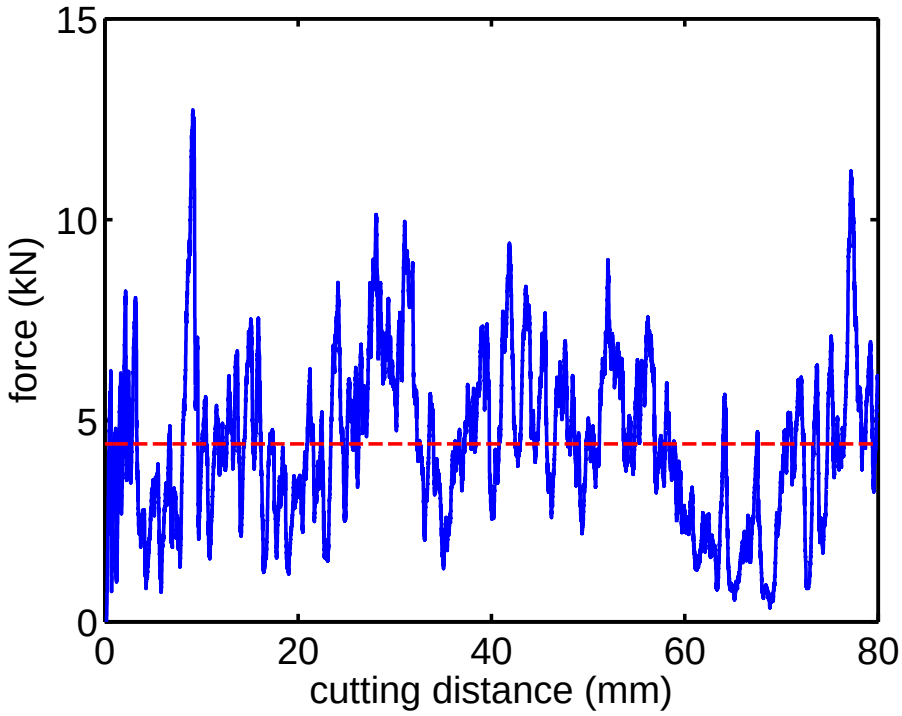

(a) $V_x = 0.5$ m/s

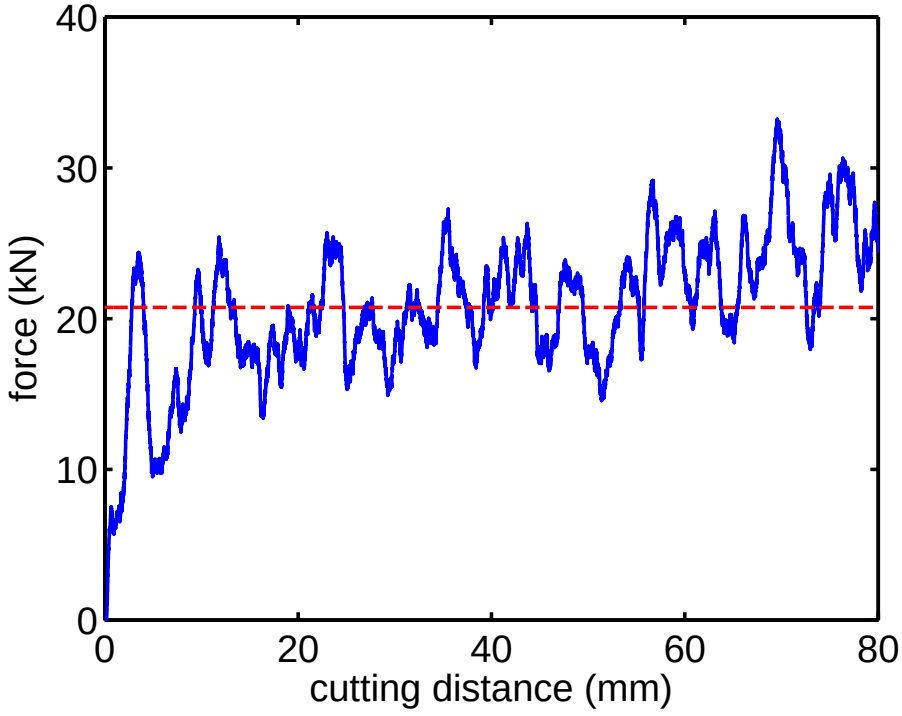

(b) $V_x = 5$ m/s

Figure 5.3: Cutting force signal from sample S1 at different cutting velocities.

specific energy and the uniaxial compressive strength from the triaxial test is ϵ/σ_c =1.35, higher than $\epsilon/\sigma_c \approx 1$ from the experiments [103]. In addition to the possible rate effect in the numerical simulations, another reason for the higher specific energy maybe because in the simulations, the displacements in the y direction are set to zero for sides ABCD and A'B'C'D', whereas the correlation of $\epsilon/\sigma_c \approx 1$ is obtained experimentally by cutting in a grove in rock cores where the lateral confinement is relatively weaker. With the constraint of the computational cost in mind and considering the fact that the connection between the strength and the specific energy is only applicable in the ductile mode, we set $V_x = 5$ m/s for all subsequent simulations.

5.4 Effect of Softening Coefficient β

Since the brittle failure mode cannot be achieved at high cutting velocities. Thus in this section, the cutter moves at a constant velocity from the left to the right of the sample at $V_x = 0.5$ m/s. Both the horizontal and vertical forces applied to the cutter are recorded and analyzed. The friction force on the side of the cutter/rock interface is negligible compared to the horizontal and vertical forces based on the simulation results. When the cutter moves close to the boundary of the sample, the cutting force is significantly elevated because of the boundary effect. As such, the data recorded in these range is considered as misleading and not included in the calculations. Meanwhile, brittle failure that involves chipping formation on the side of the sample are observed during the scratch process. Hence the cutting force doesn't represent the grinding process under such conditions. We will also exclude those simulations when analyzing the data.

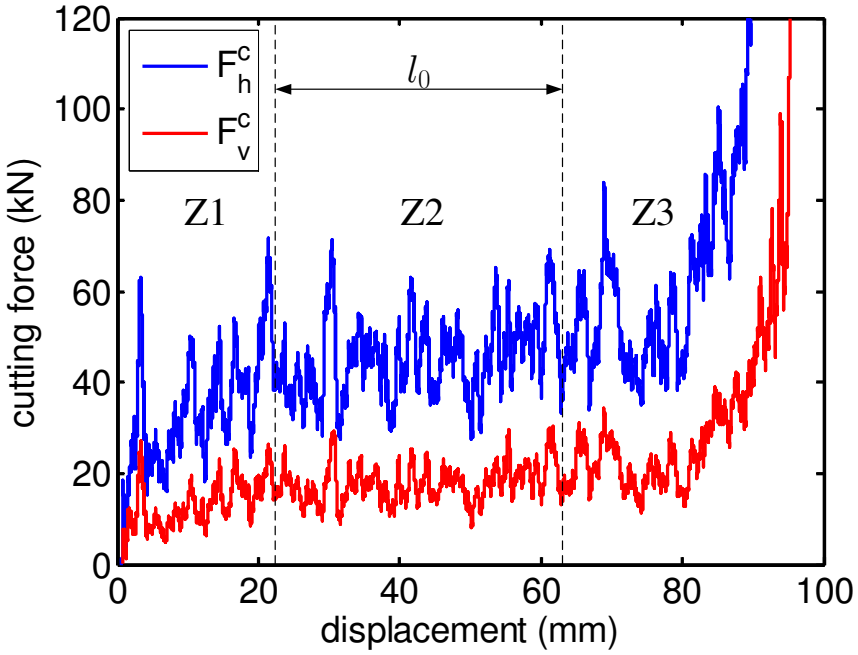

Figure 5.5: Cutting force vs. displacement for M2, $d = 10$ mm and $w = 25$ mm.

In the case when $d = 15$ mm and $w = 40$ mm, the cutting force signal shows a sudden drop when cutting distance exceeds 60 mm. That phenomenon is related to the rock chip formation, as shown in Figure 5.6(b), in which the green particles represents the fixed lower boundary, the bonded particles are colored in yellow, and particles with broken bonds are colored in red. When the cutter width is large, the rock tends to fail side ways, which results in a brittle failure mode in lateral directions. This phenomenon is usually observed when the cutter is approaching the end of the sample.

Other then previously described lateral brittle failure, most of the samples are dominated by ductile failure mode, as shown in Figure 5.7. The failure mechanism is shown by a section view at $y = 5$ mm. We can see that all the particles ahead of the cutter are debonded from its surrounding particles. Besides, no clear sign of localized fracture can be see in the whole failure process. Thus the failures are all dominated by ductile mechanism. It has been shown by Huang [60] that the critical cutting depth d^* governing the ductile-to-brittle mode transition satisfies the following correlation:

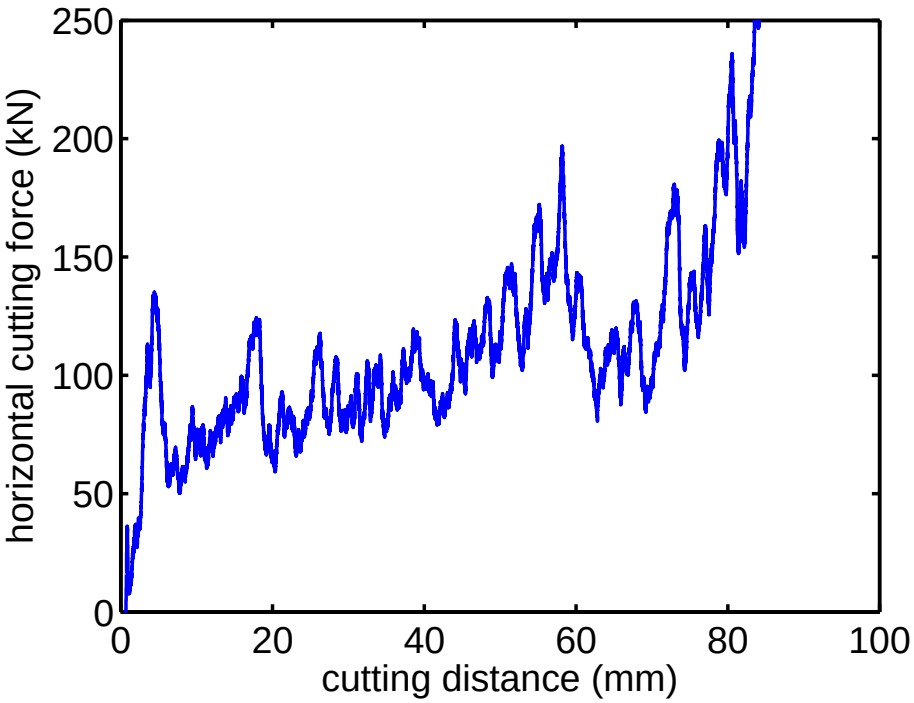

(a) horizontal cutting force

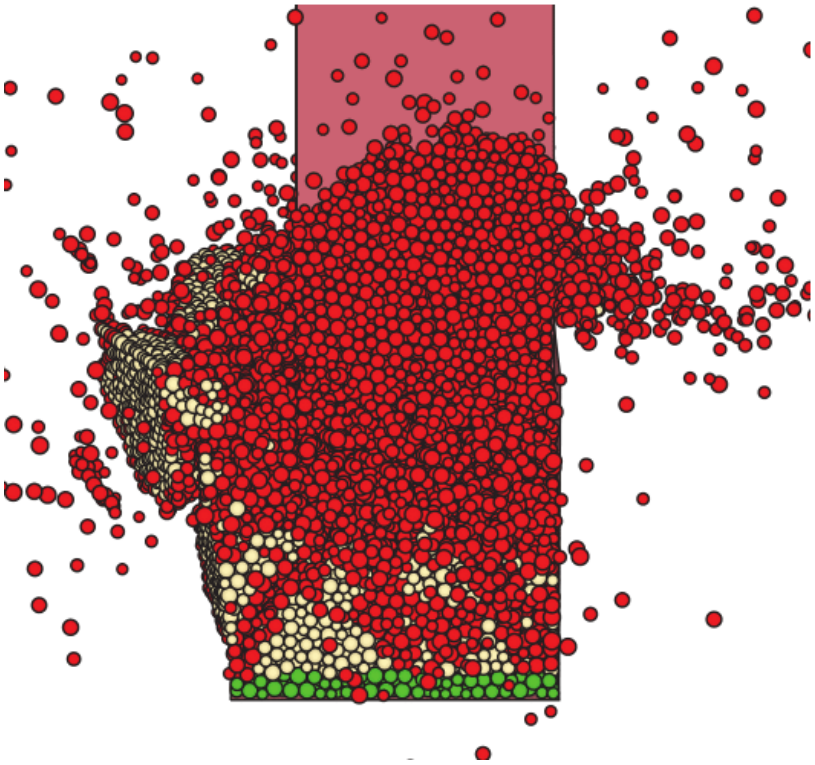

(b) chip formation

Figure 5.6: Cutting force history and failure mode at $d = 15$ mm and $w = 40$ mm. Red circles represent particles with broken bonds. Yellow ones represent particles that are still bonded.

$$d^* \sim (K_{IC}/\sigma_c)^2 \sim \bar{R}(\sigma_t/\sigma_c)^2 \tag{33}$$

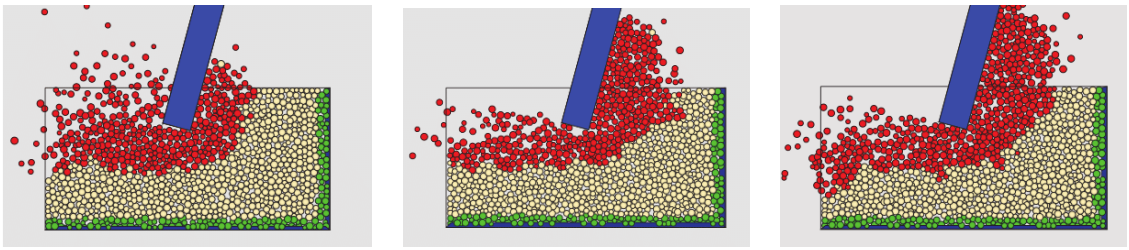

(a) $w = 5$ mm (b) $w = 20$ mm (c) $w = 50$ mm

Figure 5.7: Failure mechanism when $d = 15$ mm.

In this study, the ratio of σ_c/σ_t is relatively small at $\beta \to \infty$ compared to that of a real rock; thus d^* is much larger that the numerical sample is not large enough to exhibit brittle failure mode. As such, we reduce softening coefficient β in the numerical model from ∞ to 0.1 to investigate the failure mechanism transition in rock cutting tests.

We use the micro-parameters listed in Table 5.7 for sample S1 as a baseline, and then implement $\beta = 0.1$ and modify the normal bond strength according to Eq. 10 to compare the simulation results. Note that we apply the loading velocity $v = 0.5$ m/s (from left to right) to simulate a quasi-static loading condition (brittle failure mode cannot be captured under high loading velocities.). The following simulations are performed on samples with $L = 100$ mm $W = 25$ mm and $H = 50$ mm. The cutter width is kept a constant $w = 25$ mm.

At $\beta \to \infty$, $d = 10$ mm, the numerical model exhibits a mixed failure mechanism that involves both the ductile crushing failure and brittle failure. At cutting distance $s = 90$ mm, the initiation locations of all micro-cracks are demonstrated in Figure 5.8(b). The color represent the time sequence when the cracks are generated. Two arrows in the figure point out two lateral fractures. When the cutter moves to $s = 27.5$ mm and $s = 57.5$ mm, brittle fractures are observed ahead of the cutter. To better demonstrate the development of the brittle fractures, the distribution of micro-cracks when $s = 27.5$ mm and $s = 57.5$ mm are also summarized in Figure 5.9. At these critical cutting distances, the horizontal cutting

force also exhibits a sudden drop associated with the development of the brittle fracture, see Figure 5.8(a). Nevertheless, the complete cutting force signal still shows the characteristics of a White noise, which represents the ductile failure mode. Considering the evolution of the brittle fractures, we conclude that this is a mixed failure mode involves both ductile and brittle fractures. Although brittle fractures are observed during the cutting process, they are not connected to the free surface. As such, the brittle failure does not impact the average cutting force in the horizontal direction.

As suggested in Eq. 33, the failure mechanism transition in cutting test is controlled by d^*, which is a material constant. Thus for the specific numerical sample, brittle failure mode can be obtained by increase the cutting depth d. In this study, we increase d from 10 mm to 15 mm to justify the failure mechanism transition in numerical simulations. The complete failure process is shown in Figure 5.10(b). Compared to the case when $d = 10$ mm, the failure is governed by brittle failures. We can see several white regions on the path of the cutter, representing the materials excavated. Meanwhile, the cutter force signal exhibits distinctive patterns that involves more pikes and valleys, see Figure 5.10(a). The first brittle fracture is initiated at $s = 15$ mm, see Figure 5.11(a). As a result of the first brittle fracture, the cutting force drops immediately from about 12 kN to 3 kN. Then the cutting force increase again to about 12 kN until another brittle fracture is formed, see Figure 5.11(b). Since the development of this brittle fracture leads to the excavation of the materials in the cutting depth, the cutting force becomes almost negligible afterward. In brittle failure mode, all the brittle fractures are connected to the free surface, thus the materials are removed. As such, the cutting force is governed by the development of the brittle fractures.

It has been indicated that the critical cutting depth d^* is determined by the strength ratio of the material. Hence we keep the material particles at the same scale while reducing the softening coefficient β to reduce d^*. As such, we expect to see a similar failure mechanism transition in this new material. Note that, the normal bond strength is scaled based on β, so the absolute cutting force magnitude is not comparable to those of $\beta \to \infty$. Nevertheless, the cutting force signal patterns should exhibit the same characteristics.

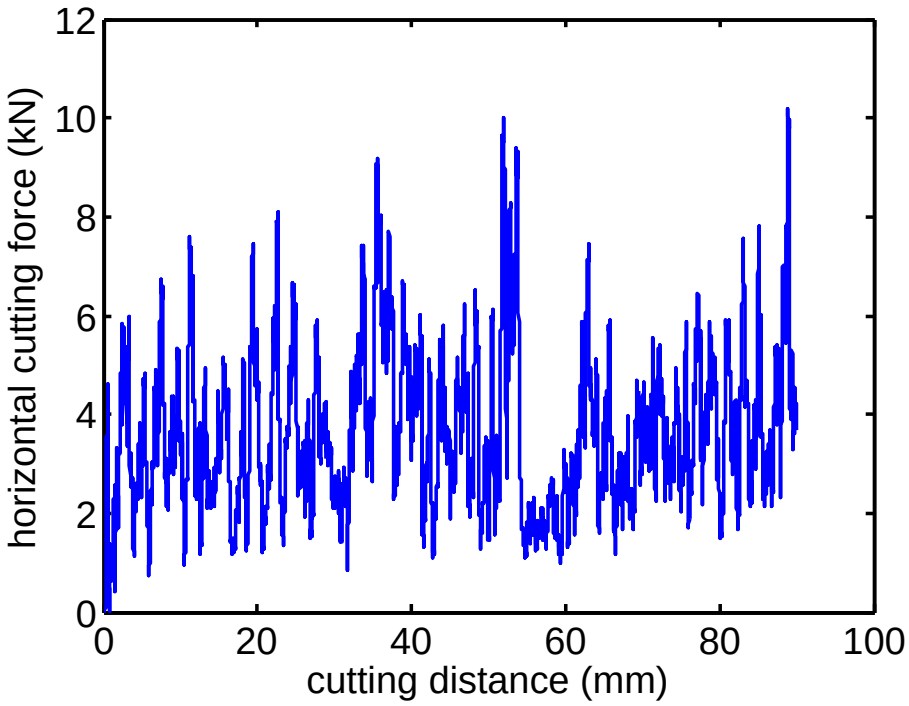

(a) horizontal cutting force

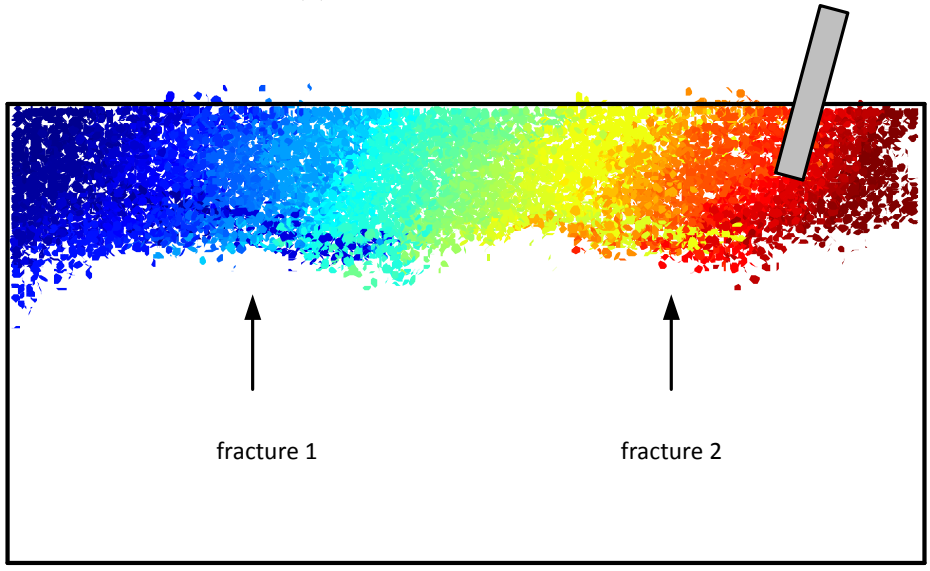

(b) micro-cracks at $s = 90$ mm

Figure 5.8: Cutting force and micro-cracks at $s = 90$ mm $d = 10$ mm and $\beta \to \infty$.

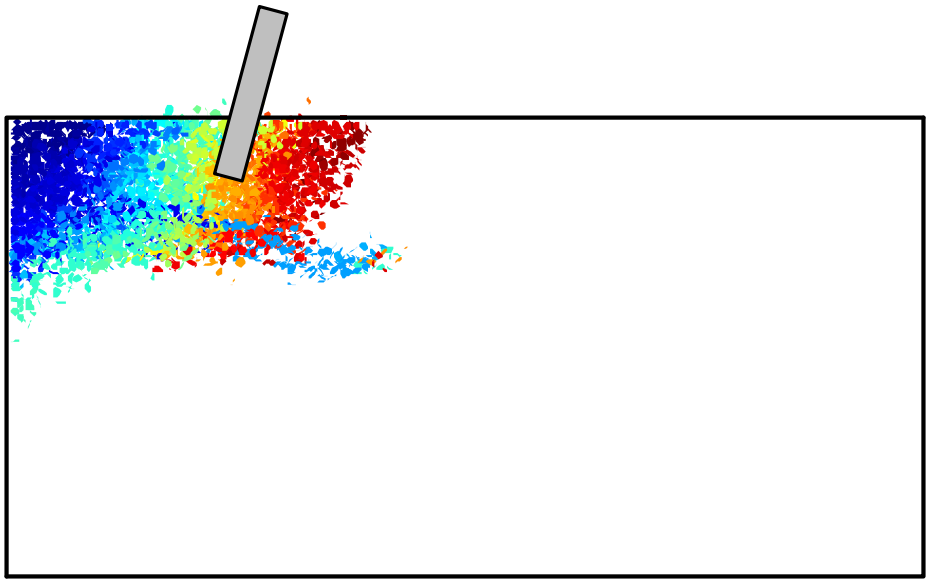

(a) micro-cracks at $s = 27.5$ mm

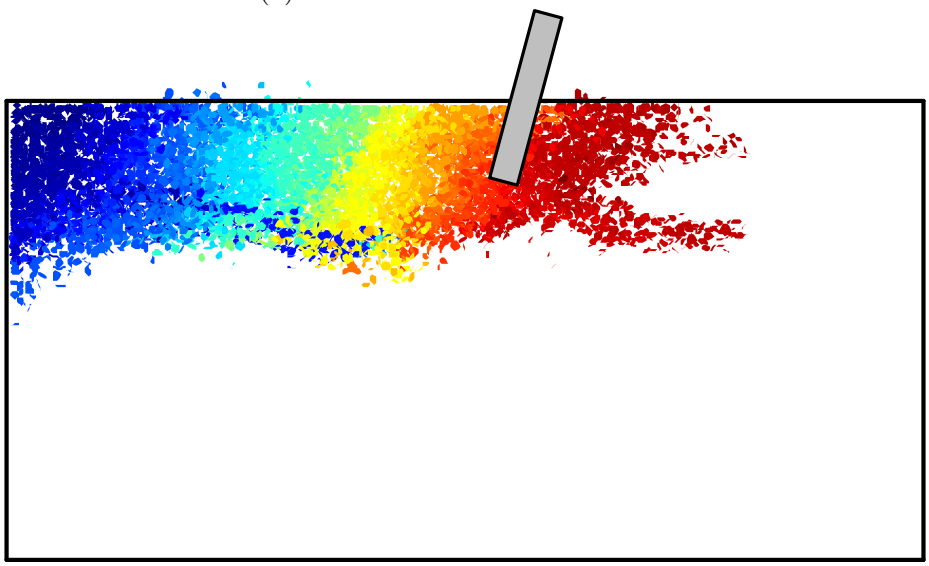

(b) micro-cracks at $s = 57.5$ mm

Figure 5.9: Distribution of micro-cracks at $s = 27.5$ and 57.5 mm, $d = 10$ mm and $\beta \to \infty$.

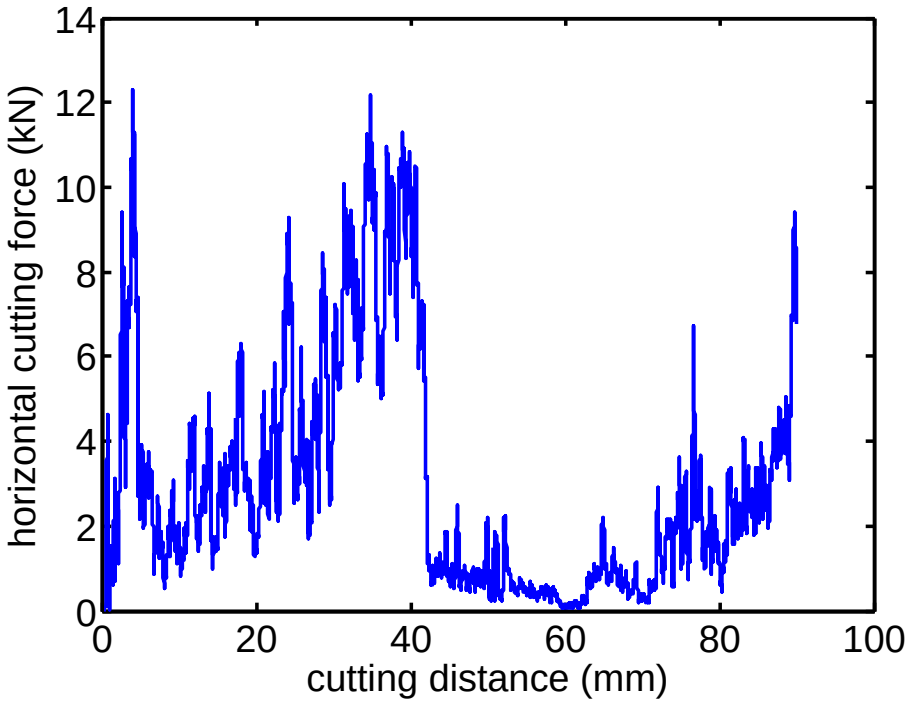

(a) horizontal cutting force

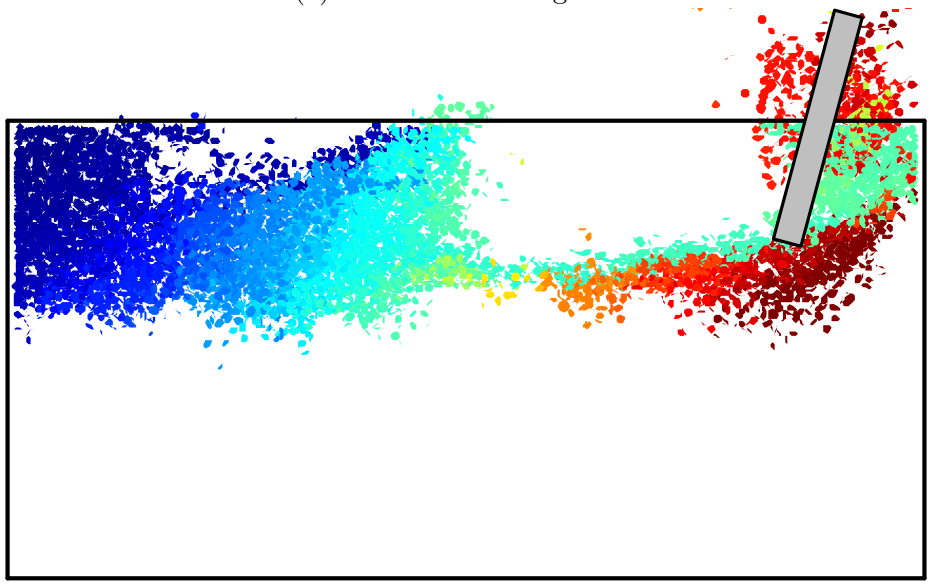

(b) micro-cracks at $s = 90$ mm

Figure 5.10: Cutting force and micro-cracks at $s = 90$ mm, $d = 15$ mm and $\beta \to \infty$.

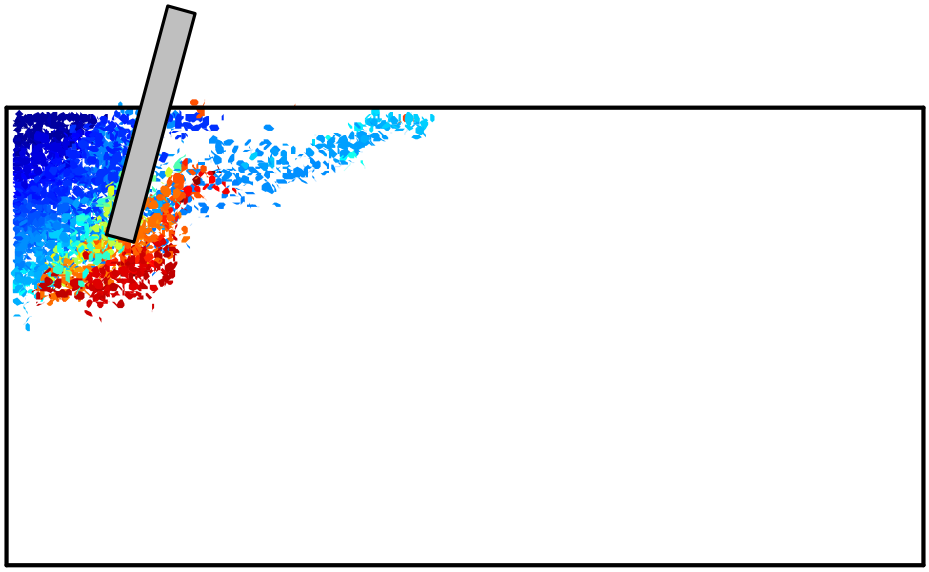

(a) micro-cracks at $s = 15$ mm

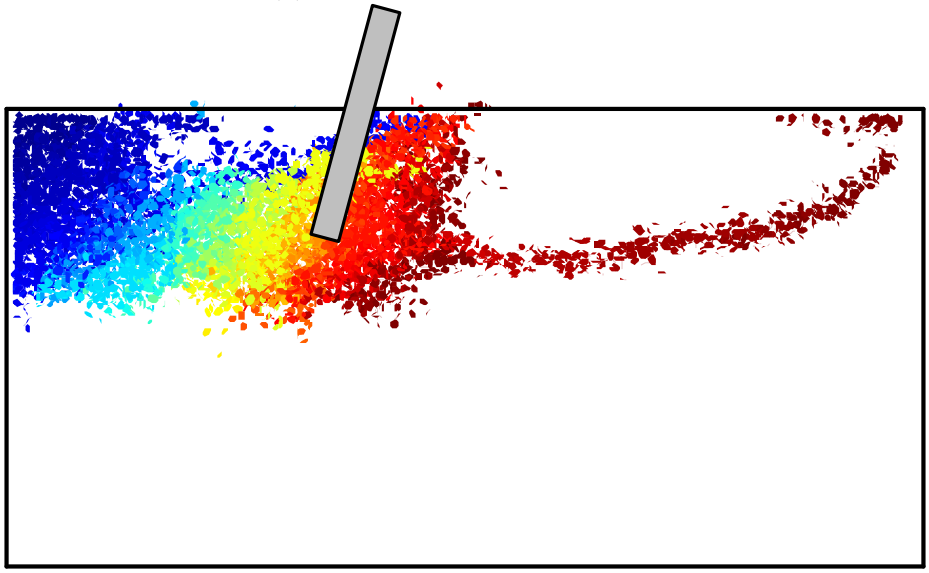

(b) micro-cracks at $s = 40$ mm

Figure 5.11: Distribution of micro-cracks at $s = 15$ and 40 mm, $d = 15$ mm and $\beta \to \infty$.

At $\beta = 0.1$, $d = 10$ mm, the cutting force signal and distribution of micro-cracks are illustrated in Figure 5.12(b). Given the condition that when $\beta = 0.1$, the strength ratio σ_c/σ_t is increased from ~ 4 to ~ 12, thus we expect to see at the same cutting depth $d = 10$ mm, the new material should exhibit brittle failure mode. Figure 5.12(b) suggests the existence of at least two brittle fractures during the cutting process, both are connected with the free surface. As such, the cutting force signal also shows two valleys with bottoms located at ~ 30 mm and ~ 80 mm. Since the development of the brittle fractures is always ahead of the cutting force decay, we examine the evolution of micro-cracks at $s = 15$ mm, see Figure 5.13(a). At the beginning of the cutting process, the failure is governed by ductile micro-cracks associated with particle grinding. A brittle fracture propagates in the lateral direction as the cutter proceeds. Then the fracture is connected with the free surface and the particles above the fracture are excavated causing the cutting force to drop. When the cutter proceeds to $s = 57.5$ mm, another brittle fracture is generated ahead of the cutter tip. Then the cutting force drops again because the materials at the cutting depth are already removed. Different to the failure mode when $\beta \to \infty$ and $d = 10$ mm, this failure mode is dominated by brittle fracture. Hence, the results suggest that the critical cutting depth d^* in the model with $\beta = 0.1$ is reduced than that of $\beta \to \infty$. The question is whether the ductile failure mode still exist in this numerical sample? To answer this question, we reduce the cutting depth to $d = 5$ mm and examine the evolution of micro-cracks to identify the possibility of brittle fractures.

At $\beta = 0.1$ and $d = 5$ mm, the distribution of micro-cracks shows no clear sign of brittle fracture, see Figure 5.14(b). Therefore, the cutting force signal is more or less uniformly distributed around the average. As suggested by the results, the failure mode is governed by ductile fractures. To sum up, when $\beta \to \infty$, the failure mechanism transition from ductile mode, despite the lateral brittle fractures, at $d = 10$ mm to brittle failure mode at $d = 15$ mm; while with $\beta = 0.1$,the failure mechanism transition from brittle mode at $d = 10$ mm to ductile mode at $d = 5$ mm.

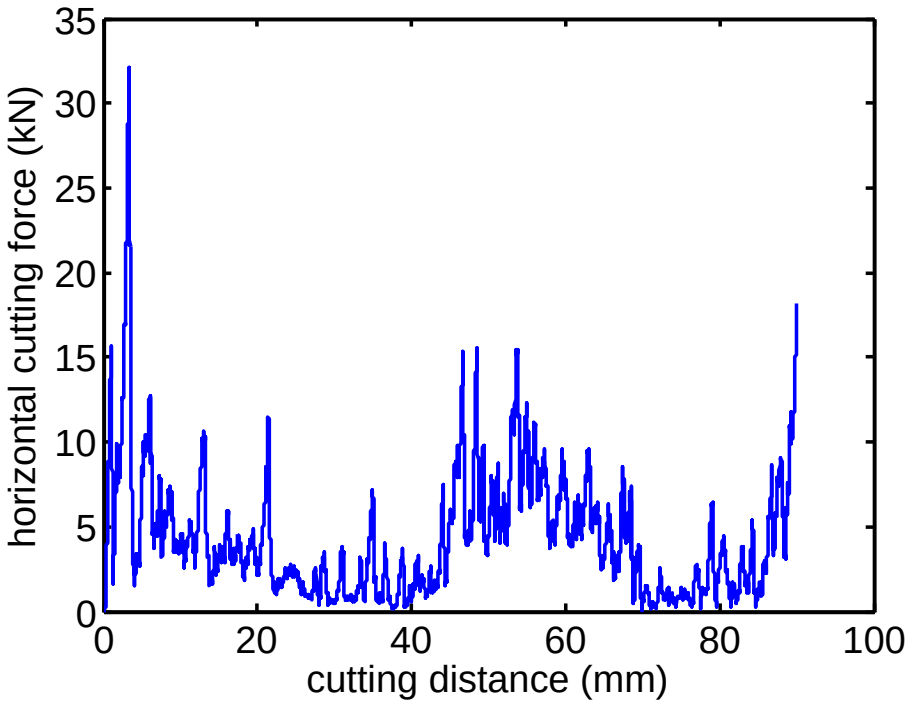

(a) horizontal cutting force

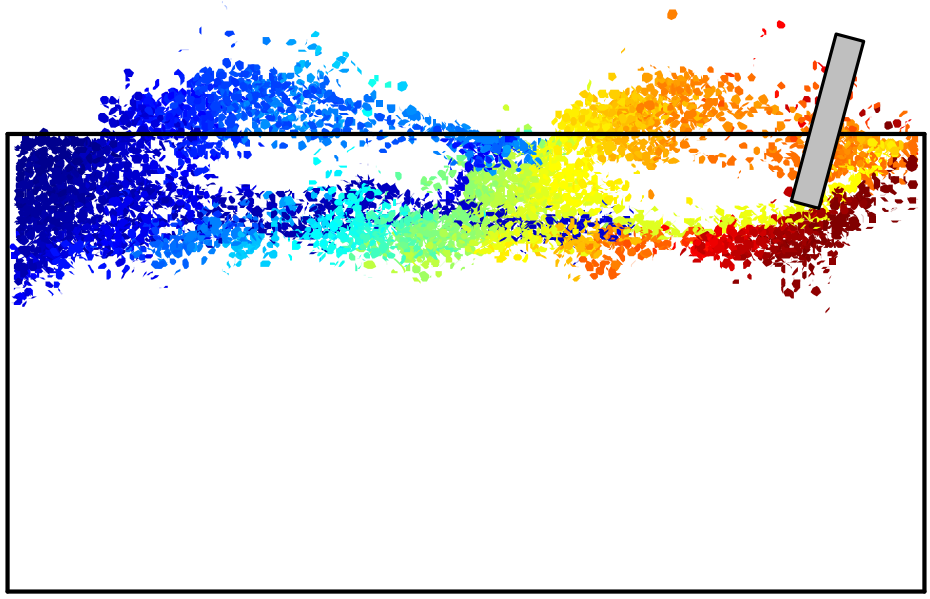

(b) micro-cracks at $s = 90$ mm

Figure 5.12: Cutting force and micro-cracks at $s = 90$ mm, $d = 10$ mm and $\beta = 0.1$.

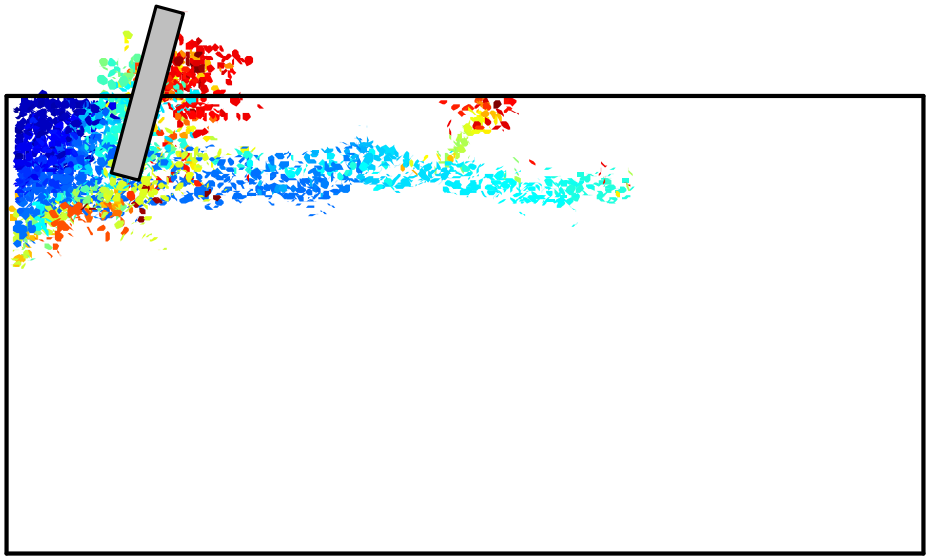

(a) micro-cracks at $s = 15$ mm

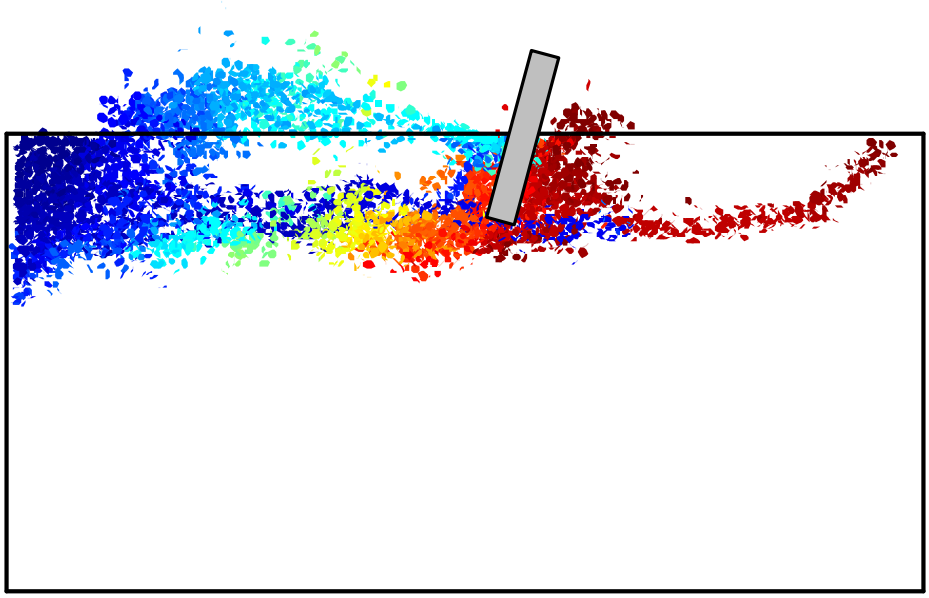

(b) micro-cracks at $s = 57.5$ mm

Figure 5.13: Distribution of micro-cracks at $s = 15$ and 57.5 mm, $d = 10$ mm and $\beta = 0.1$.

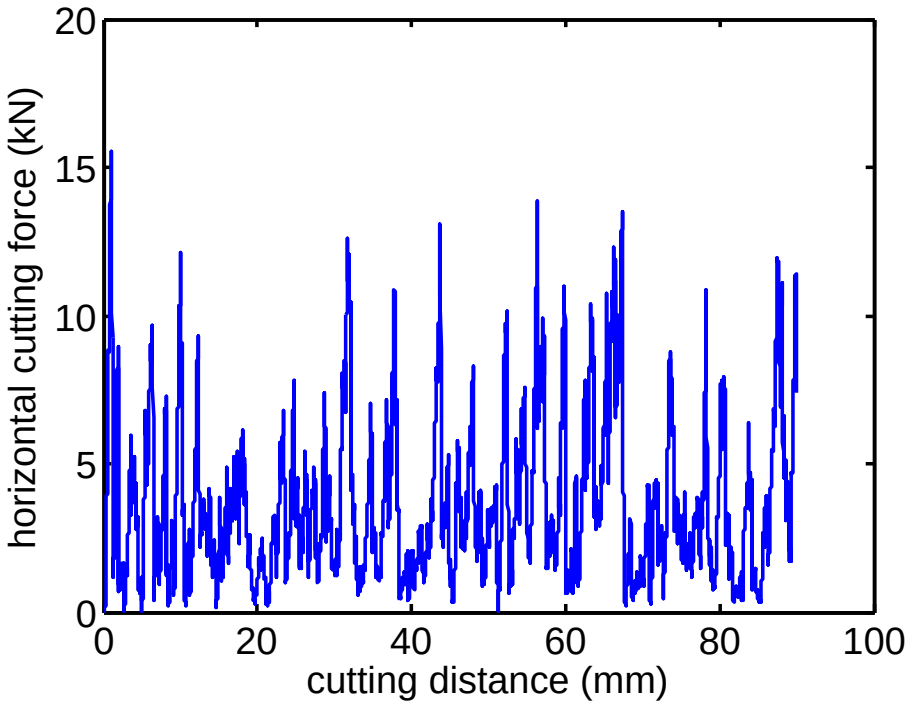

(a) horizontal cutting force

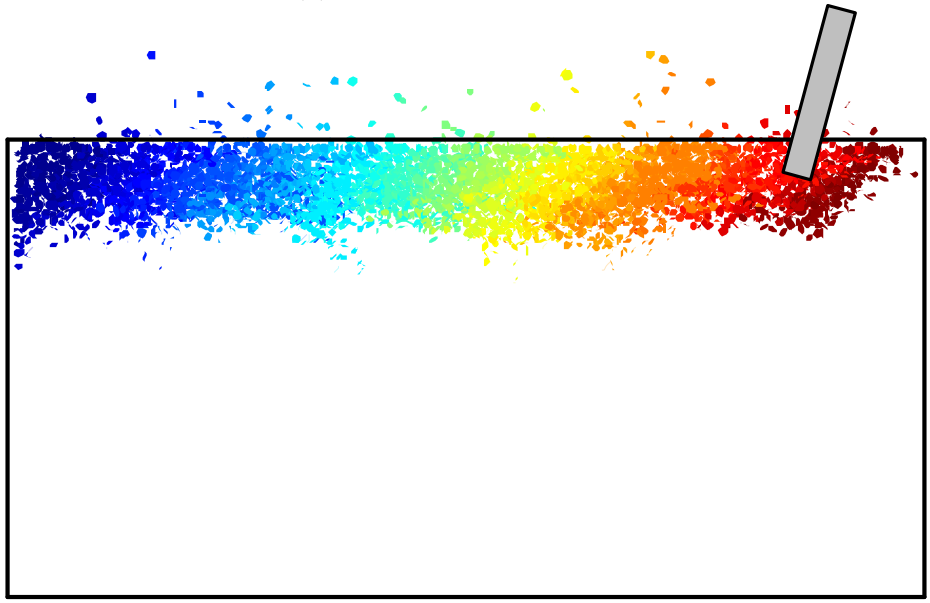

(b) micro-cracks at $s = 90$ mm

Figure 5.14: Cutting force and micro-cracks at $s = 90$ mm, $d = 5$ mm and $\beta = 0.1$.

Table 5.3: Cutter geometries and configurations.

	M1		M2
Cutter geometry	Box	L	Box
Pile-up effect	Yes	No	Yes

5.5 3D Effect of Cutter Geometry

In this section, three cutting geometries are examined. The cutter geometries and the configuration for each test is summarized in Table 5.3. Box cutter consists of six walls while L-shaped cutter consists of only two walls. The most significant difference during the cutting process is the effect of the friction on the side walls. Meanwhile, the pile-up effect is also considered by removing loose particles ahead of the cutter.

For each cutting test, the horizontal cutting force F_h^c and the vertical cutting force F_v^c are obtained by averaging the force signals within the length of cut $s \in [L/\lambda,\ (1-1/\lambda)L]$, where $\lambda$is a coefficient and defined by $\lambda = 2/(1-l_0/L)$; while L is the length of numerical sample, $L = 100$ mm for this study. Figure 5.5 shows the histories of the horizontal and vertical cutting forces for the case of $d = 10$ mm and $w = 25$ mm. The cutting force signal exhibits an early transient period (Z1), a pseudo steady state (Z2), and then the late cutting period (Z3) when the cutter becomes too close to the far right boundary.

In order to show the effect of λ to the average cutting force, we pick M2 and $d = 10$ mm as an example to show the analysis. By the definition of λ, we have $\lambda > 2$. So we choose $\lambda = 3$, 4, 5, and 6 to investigate the sensitivity of average cutting force. The results are summarized in Figure 5.15. It clearly shows that when the cutter width is small, the impact of λ to the average cutting force is negligible. When cutter width is large, then large pieces of chips are formed during the cutting process, which leads to large variation of the cutting force; thus the influence of λ is large. However, when $\lambda = 4$, the force is roughly the average. From Figure 5.5, we can see that when $\lambda = 4$, l_0 would cover most of the steady cutting process. Thus the average cutting force would be accurate enough to represent the whole cutting process. So for all the simulations, $\lambda = 4$ is used to determine the average cutting

force. Thus the average specific energy and drilling strength [35] respectively defined as:

$$E = F_h^c / A \tag{34}$$

$$S = F_v^c / A \tag{35}$$

where A is the cross sectional area of the cut. The results are summarized in Tables 5.4 - 5.6.

5.5.1 Influence of w on Specific Energy and Drilling Strength

The plane strain cutting model proposed in [35] shows that the specific energy is constant and linearly related to the uniaxial compressive strength. In this study, the average horizontal forces are plotted in Figure 5.16 - 5.18, which shows that all the horizontal cutting forces are linearly correlated with the cutting area; in other words, the specific energy for each synthetic material is a constant. However, for M1, two different cutters are used, and they yield different specific energy. The cutting tests with box cutter have larger frictions on the cutter sides. As a result of that, the energy required to excavate a unit volume of rocks is larger compared to using L-shaped cutter.

It has been shown that the cutting force would increase with cutter depth [33, 102, 103]. In this study, this phenomenon has been verified as well. What's more, the influence of cutter width is also investigated. At $d = 15$ mm, ϵ decreases with the cutter width for all three cases; while at $d = 5$ mm and $d = 10$ mm, ϵ first increases and then decreases with the width w when pile-up effect is considered. The maximum values occur when $w = 25$ mm. In the case of no pile-up effect, ϵ decreases constantly with cutter width when $d = 10$ mm and $d = 15$ mm. When $d = 5$ mm, ϵ is approximately a constant, which is independent of the width w.

On the other hand, drilling strength S shows an abnormal trend in the case when $d = 5$ mm for M2. When $d = 10$ mm and $d = 15$ mm, s is slightly increasing with w, then it decreases. However, the overall trend is roughly a constant. In the case of L-shaped cutter for M1, S shows a decreasing trend with cutter width. When $w = W$, the dependency is vanished. For M2, when cutter depth $d = 5$ mm and $d = 10$ mm, S increases with w up

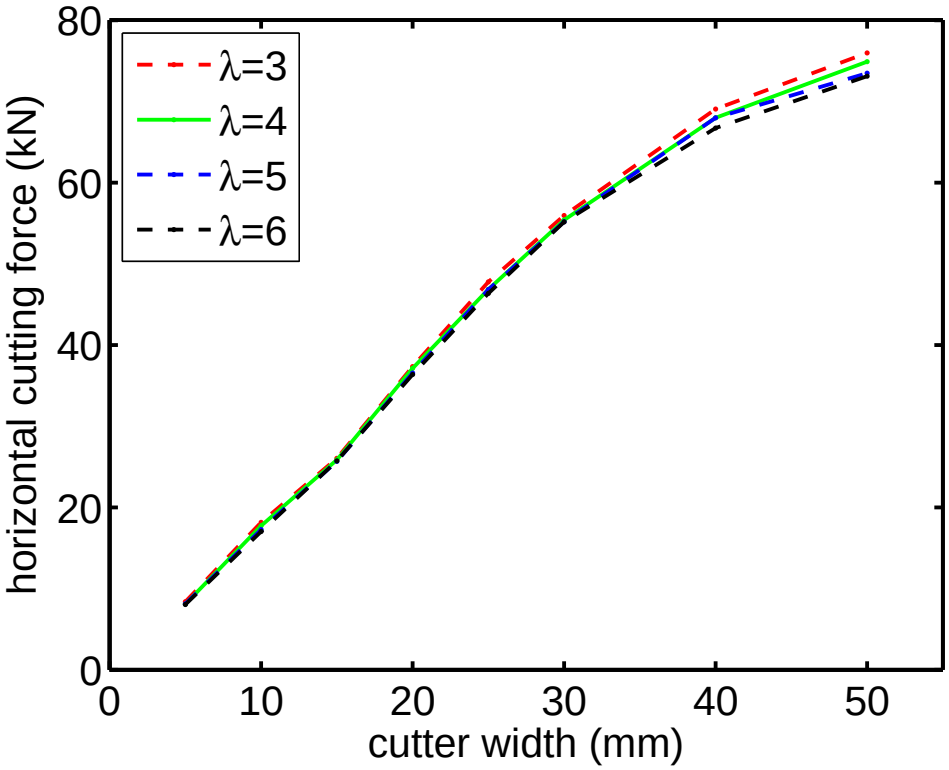

(a) horizontal force

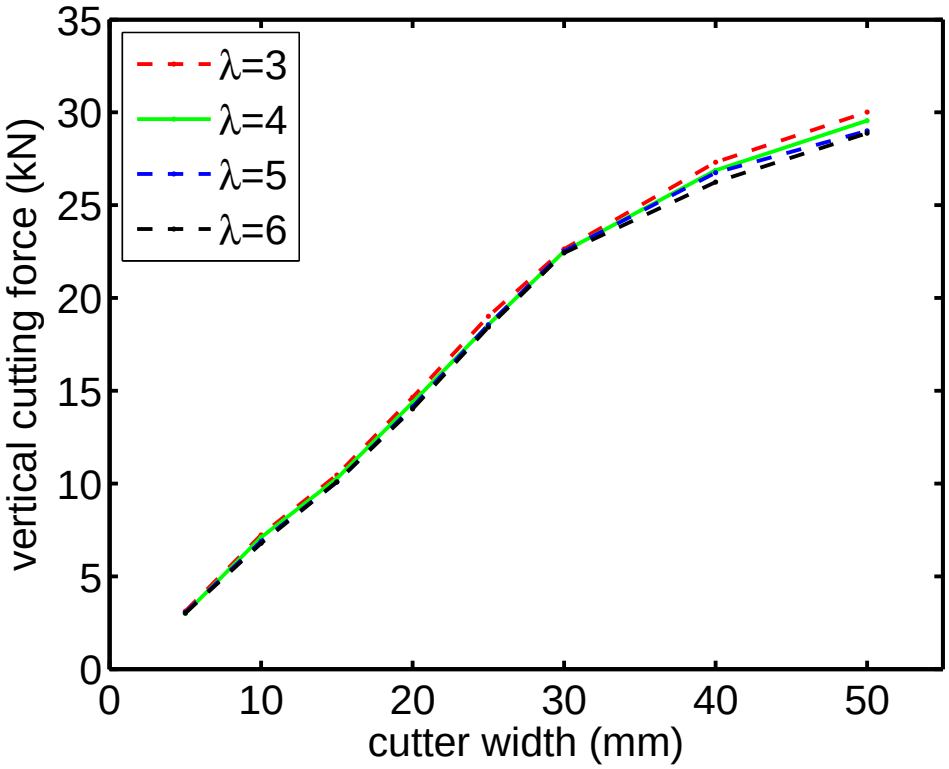

(b) vertical force

Figure 5.15: Influence of λ to average cutting force for M2, $d = 10$ mm.

Table 5.4: Results of the cutting tests for M1, box cutter.

Index	d (mm)	w (mm)	L (mm)	AVG. F_h^c (kN)	AVG. F_v^c (kN)	E (MPa)	S (MPa)
1	5	5	100	0.96	0.56	36.8	21.8
2	5	10	100	2.09	1.28	43.5	26.7
3	5	15	100	3.38	1.99	45.0	27.2
4	5	20	100	4.72	2.89	48.4	29.2
5	5	25	100	6.19	3.84	51.3	31.9
6	5	30	100	7.31	4.40	50.2	30.2
7	5	40	100	9.54	5.82	48.6	29.8
8	5	50	100	10.91	6.59	43.7	26.3
9	10	5	100	2.07	0.77	41.7	16.3
10	10	10	100	4.32	1.69	45.2	17.5
11	10	15	100	6.72	2.57	46.9	18.0
12	10	20	100	9.06	3.56	48.1	18.8
13	10	25	100	11.05	4.23	44.0	17.9
14	10	30	100	12.92	5.15	42.8	18.5
15	10	40	100	16.30	6.31	40.8	17.0
16	10	50	100	17.98	6.97	36.0	14.9
17	15	5	100	3.68	1.05	49.6	13.9
18	15	10	100	7.06	2.08	47.1	14.2
19	15	15	100	10.52	3.08	47.5	15.1
20	15	20	100	13.90	4.26	47.6	15.2
21	15	25	100	15.73	4.65	41.1	12.8
22	15	30	100	19.72	5.97	45.1	13.3
23	15	40	100	24.24	7.71	42.2	13.6
24	15	50	100	27.82	8.59	38.5	12.1

Table 5.5: Results of the cutting tests for M1, L-shaped cutter.

Index	d (mm)	w (mm)	L (mm)	AVG. F_h^c (kN)	AVG. F_v^c (kN)	E (MPa)	S (MPa)
1	5	5	100	0.67	0.28	26.68	11.29
2	5	10	100	1.50	0.64	29.90	12.88
3	5	15	100	1.97	0.83	26.32	11.04
4	5	20	100	2.57	1.07	25.72	10.69
5	5	25	100	3.32	1.41	26.54	11.32
6	5	30	100	3.86	1.63	25.76	10.88
7	5	40	100	5.10	2.07	25.50	10.35
8	5	50	100	5.77	2.32	23.10	9.27
9	10	5	100	1.90	0.72	37.91	14.33
10	10	10	100	3.42	1.36	34.23	13.64
11	10	15	100	4.94	1.96	32.95	13.09
12	10	20	100	6.21	2.47	31.07	12.35
13	10	25	100	7.51	2.93	30.04	11.70
14	10	30	100	8.70	3.33	29.01	11.12
15	10	40	100	10.37	3.94	25.92	9.85
16	10	50	100	12.04	4.56	24.08	9.11
17	15	5	100	3.67	1.36	48.98	18.19
18	15	10	100	6.52	2.45	43.48	16.36
19	15	15	100	8.85	3.20	39.35	14.22
20	15	20	100	10.89	4.25	36.28	14.18
21	15	25	100	12.53	4.56	33.41	12.15
22	15	30	100	13.52	5.01	30.05	11.14
23	15	40	100	17.82	6.77	29.70	11.29
24	15	50	100	20.11	7.63	26.81	10.17

Table 5.6: Results of the cutting tests for M2, box cutter.

Index	d (mm)	w (mm)	L (mm)	AVG. F_h^c (kN)	AVG. F_v^c (kN)	E (MPa)	S (MPa)
1	5	5	100	2.6	1.33	103.49	53.12
2	5	10	100	6.1	2.80	122.28	56.01
3	5	15	100	10.5	4.68	140.06	62.44
4	5	20	100	14.7	6.43	147.39	64.33
5	5	25	100	19.2	8.40	153.68	67.19
6	5	30	100	22.9	10.12	152.79	67.47
7	5	40	100	30.1	13.28	150.49	66.38
8	5	50	100	34.2	14.50	136.88	58.01
9	10	5	100	8.1	2.99	161.55	59.81
10	10	10	100	17.7	7.10	177.15	70.96
11	10	15	100	25.8	10.27	172.28	68.49
12	10	20	100	37.1	14.36	185.67	71.82
13	10	25	100	46.9	18.55	187.40	74.20
14	10	30	100	55.4	22.51	184.61	75.02
15	10	40	100	68.0	26.88	169.93	67.20
16	10	50	100	74.9	29.56	149.80	59.12
17	15	5	100	16.6	6.08	221.57	81.10
18	15	10	100	32.4	12.17	215.71	81.16
19	15	15	100	41.2	15.49	183.20	68.86
20	15	20	100	63.7	23.27	212.32	77.55
21	15	25	100	65.2	25.36	173.81	67.63
22	15	30	100	74.3	29.21	165.13	64.92
23	15	40	100	106.9	41.31	178.08	68.85
24	15	50	100	112.3	42.94	149.75	57.26

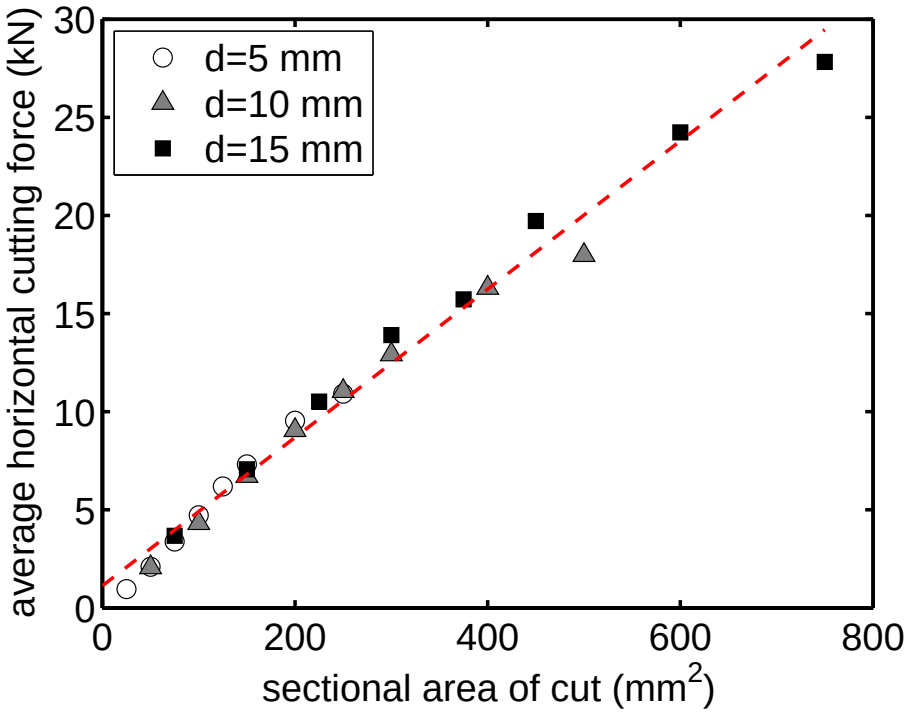

(a) horizontal cutting force

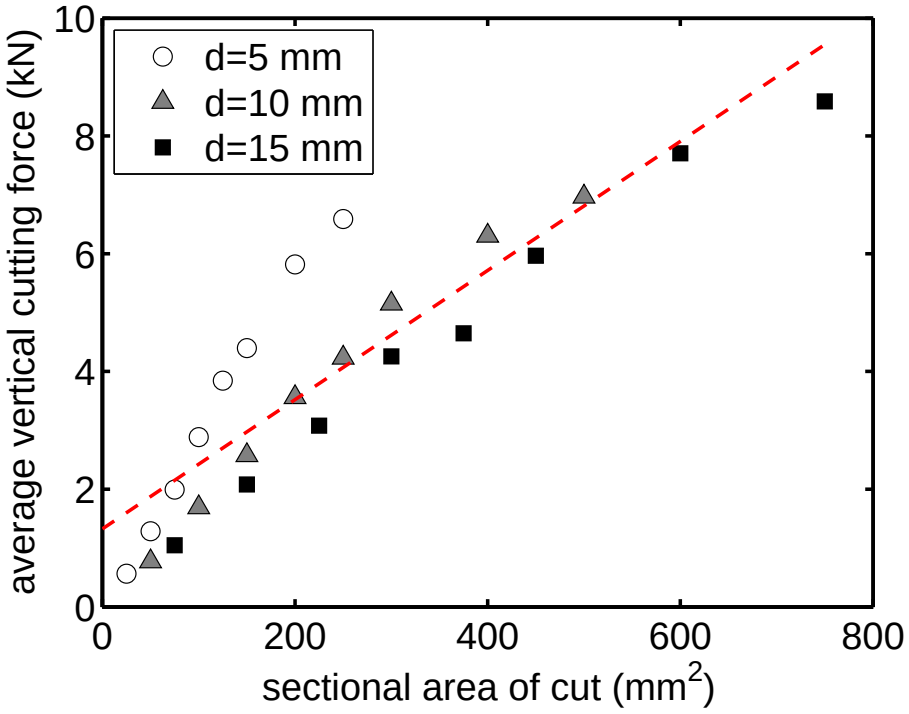

(b) vertical cutting force

Figure 5.16: Variation of cutting forces vs. cutting area for M1, box cutter.

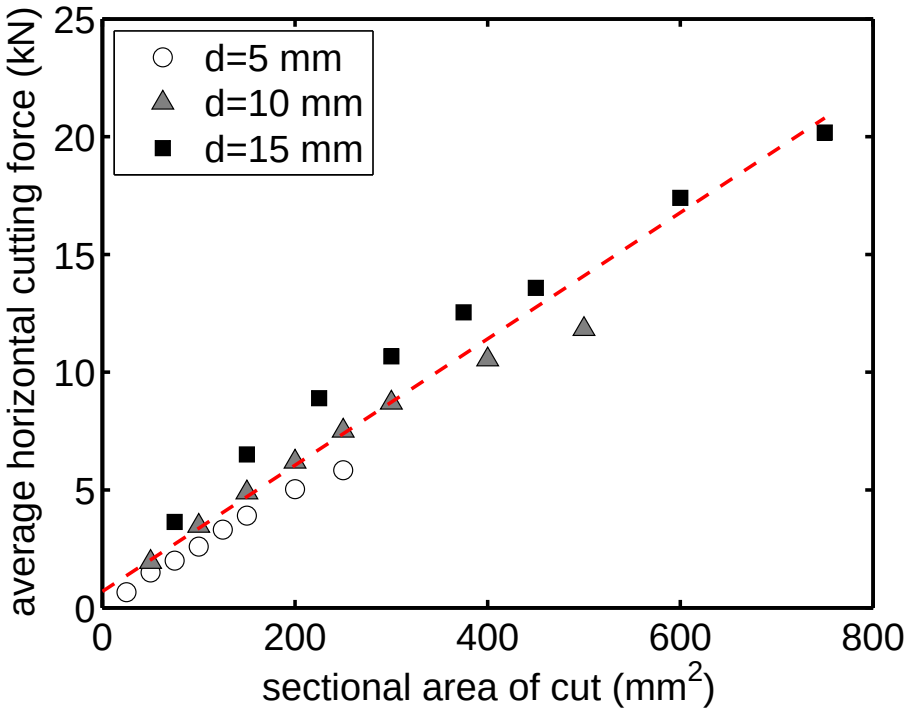

(a) horizontal cutting force

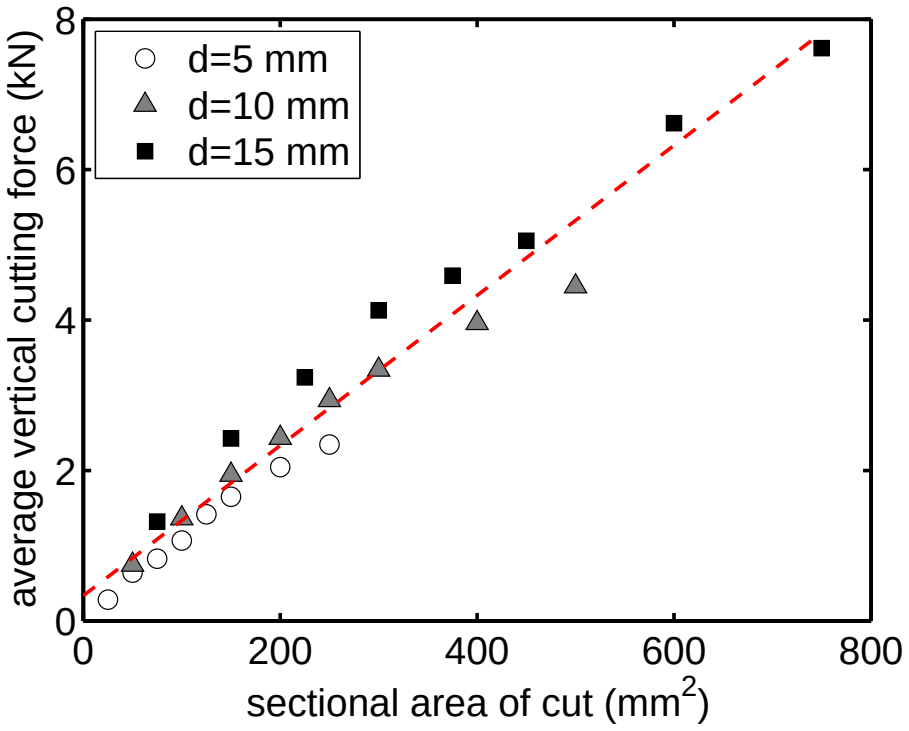

(b) vertical cutting force

Figure 5.17: Variation of cutting forces vs. cutting area for M1, L-shaped cutter.

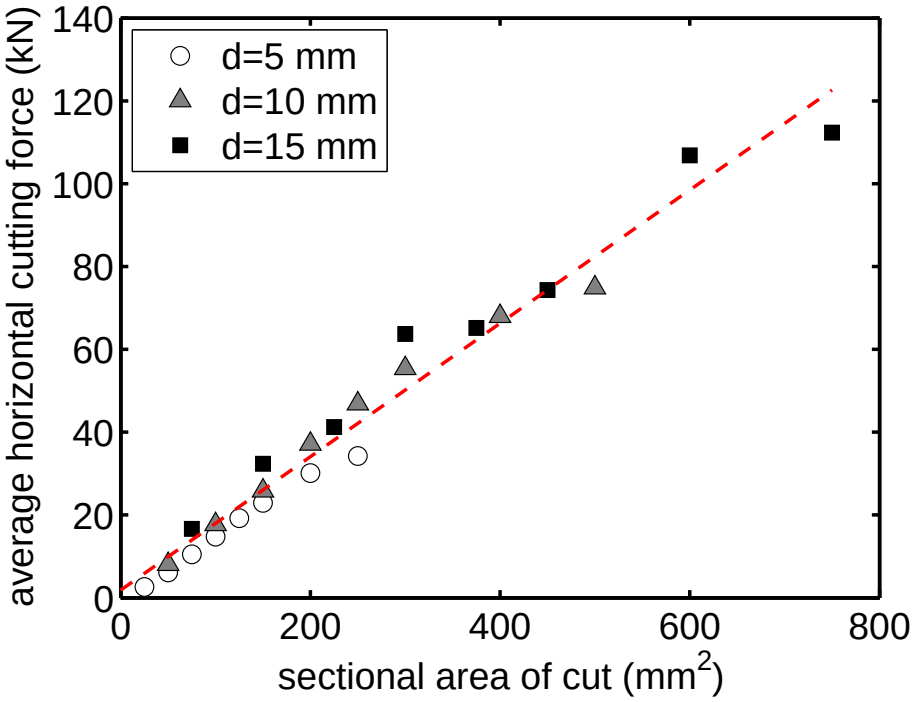

(a) horizontal cutting force

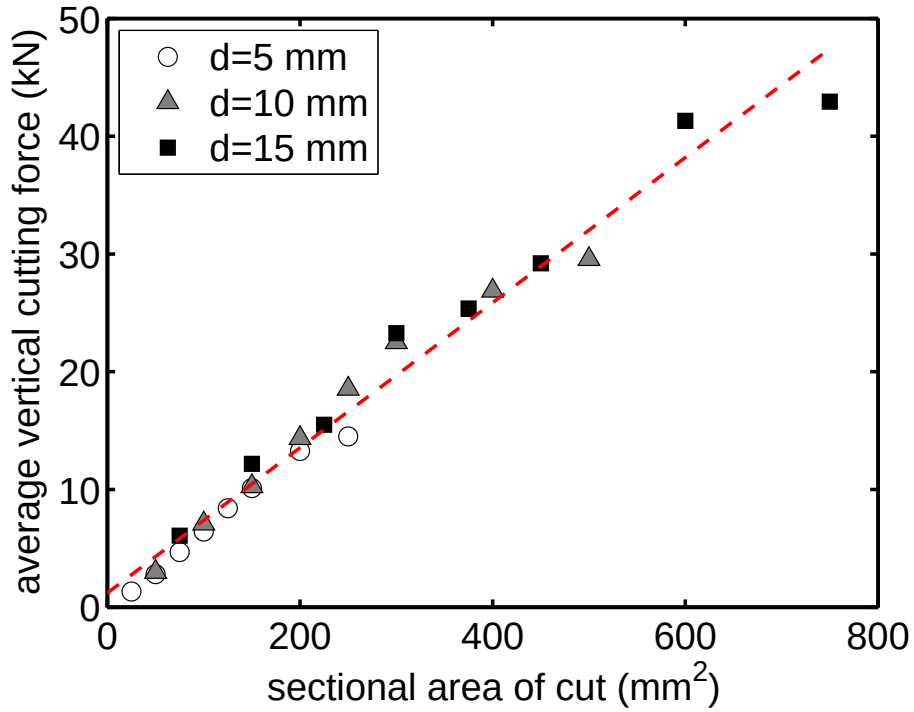

(b) vertical cutting force

Figure 5.18: Variation of cutting forces vs. cutting area for M2, box cutter.

to about 25 mm, then it starts to decrease. When $d = 15$ mm, S shows a decreasing trend with w.

5.5.2 E-S Diagrams

As predicted by D&D model [35], the theoretical E-S diagram is shown in Figure 5.22. If the cutter is sharp that no friction is considered in the whole cutting process, then the $E-S$ diagram converges to a point, namely the cutting point. On the other hand, if friction at the bottom of the cutter is considered, then $E - S$ data falls on the curve, namely friction line. In this study, the $E - S$ diagrams are shown in Figures 5.23-5.25.

In the case of cutting tests on M1 with box cutters, the data from different cutting depth mainly distributed on three different lines. Since the friction on the sides of the cutter are too significant to be neglected, so the horizontal force required to excavate the rock is increasing with cutting depth. However, the three friction lines intersect at a point as shown in Figure 5.23, which is defined as cutting point. Thus the specific energy obtained from these tests can be estimated as $\epsilon = 18.5$ MPa. For different cutter depth, the interactions between the cutter side walls and the rock is different, too. The mechanism is related to the confining pressure due to 3D effect in the lateral direction. Besides, under this tests, the particles with broken bonds are piling up in front of the cutter, results in more interactions to the cutter.

In order to minimize the influence from the cutter side walls, as well as the pile-up effect, L-shaped cutter is used to perform the rock cutting tests on M1. In this case, the $E - S$ diagram shows a better convergence of the friction line. When cutter depth $d = 10$ mm and $d = 15$ mm, the slope of the friction lines are more or less the same. However, when $d = 5$ mm, the slope of the friction line is slightly off the trend. But still all the simulation results intersect at the cutting point. The specific energy determined from this series of cutting tests is approximately $\epsilon = 21.5$ MPa. Since both groups of tests on M1 are using the same material, only the cutter geometry is different, thus the specific energy are very close to uniaxial compressive strength, $\sigma_c = 19.5$ MPa. Since in experiments, the friction interaction between the cutter and the sample is mainly concentrated at the bottom of the

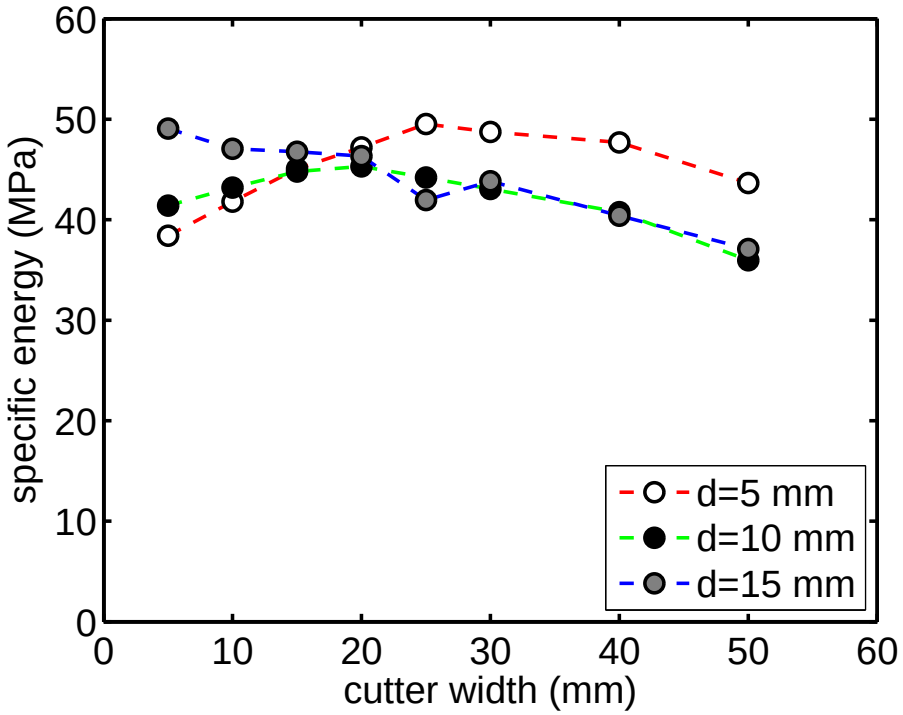

(a) specific energy

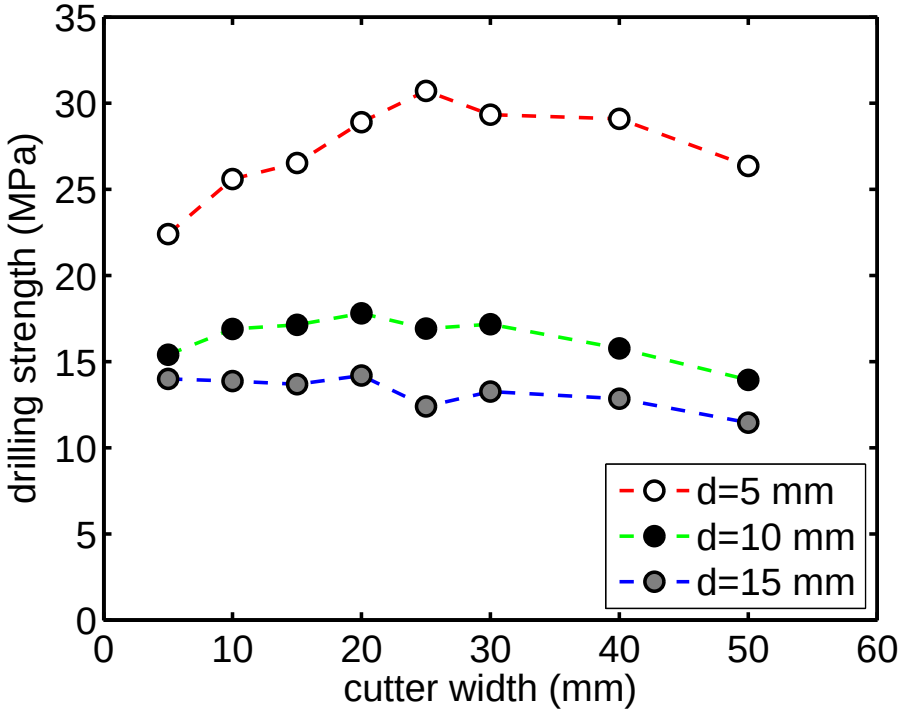

(b) drilling strength

Figure 5.19: Specific energy and drilling strength vs. cutter width for M1 box cutter.

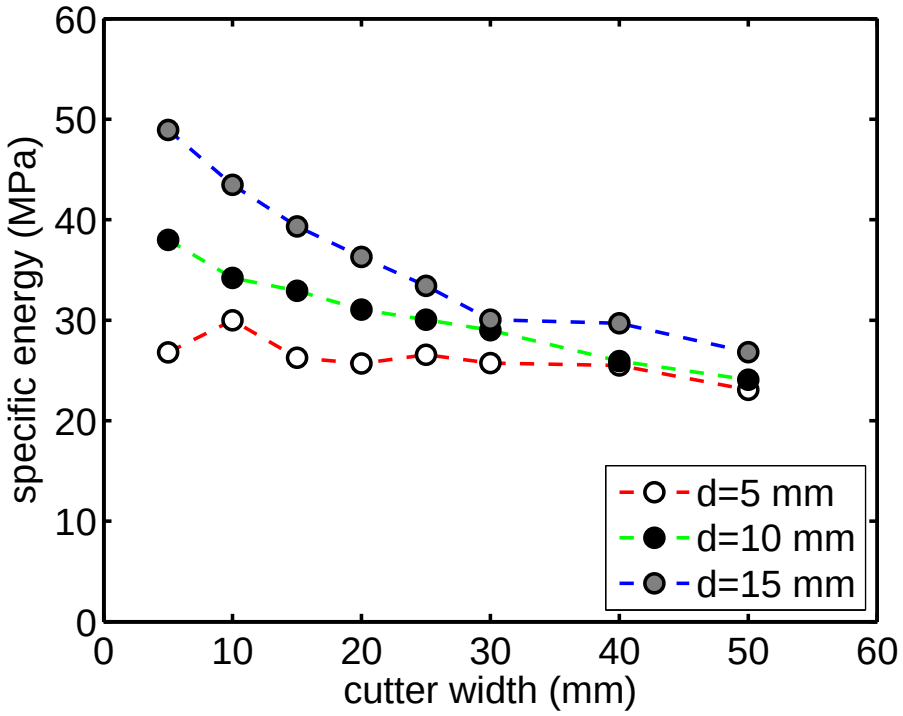

(a) specific energy

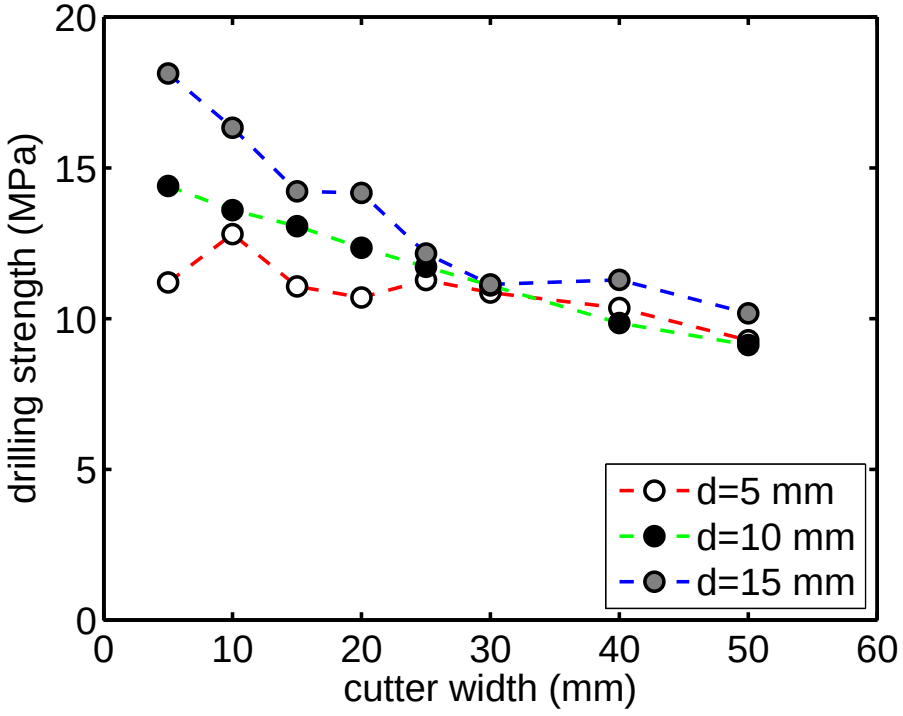

(b) drilling strength

Figure 5.20: Specific energy and drilling strength vs. cutter width for M1 L-shaped cutter.

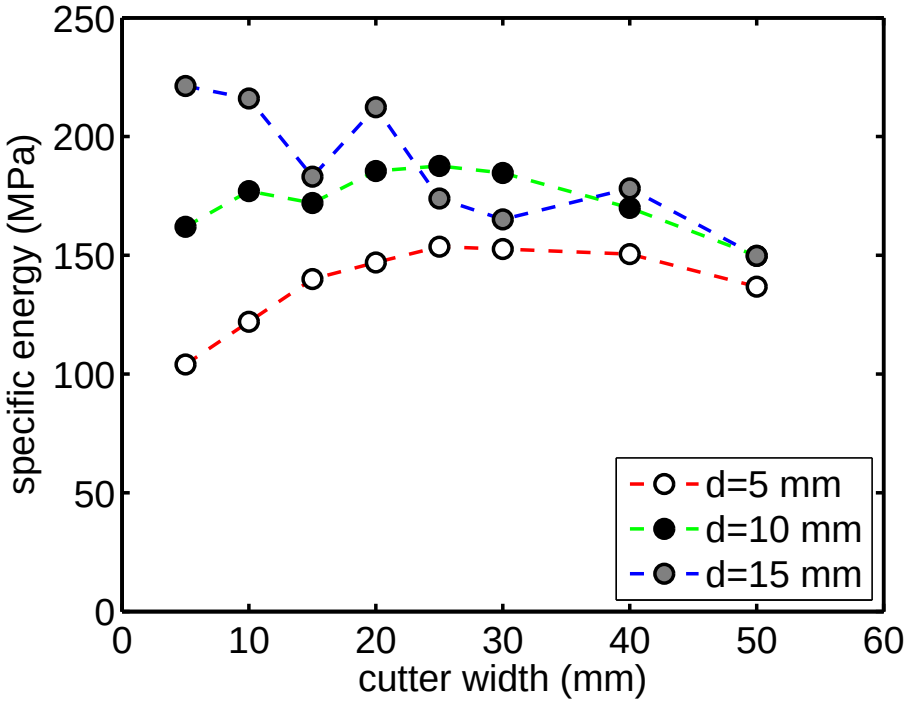

(a) specific energy

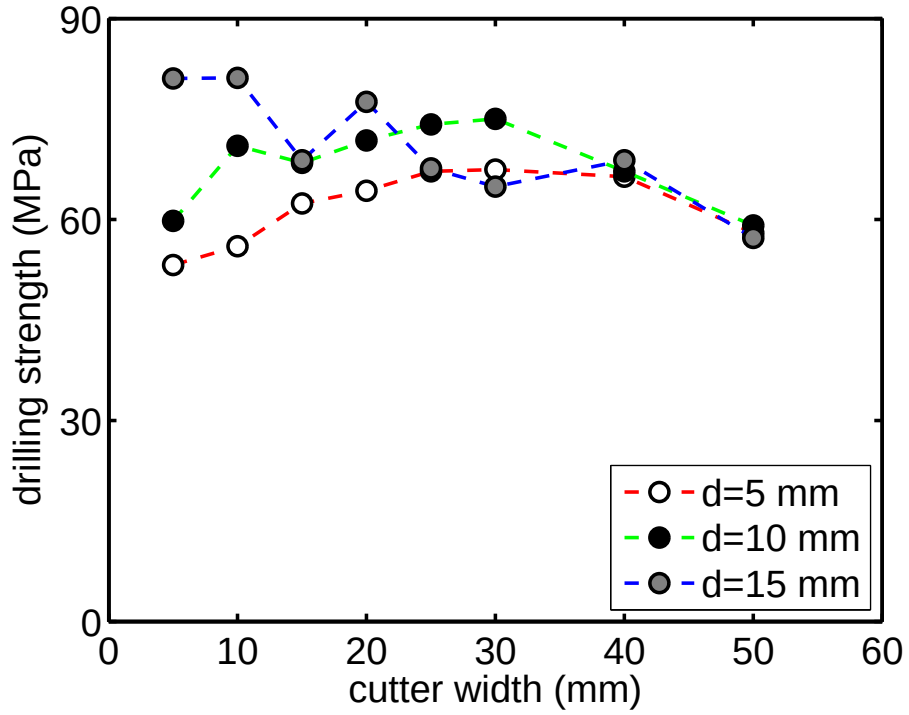

(b) drilling strength

Figure 5.21: Specific energy and drilling strength vs. cutter width for M2.

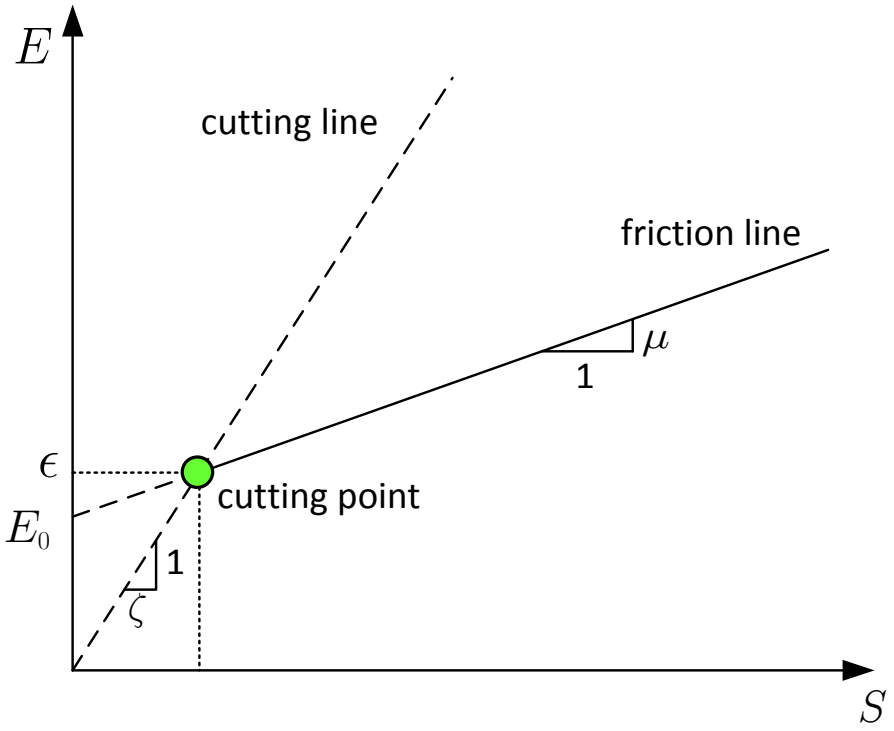

Figure 5.22: Theoretical $E - S$ diagram [35].

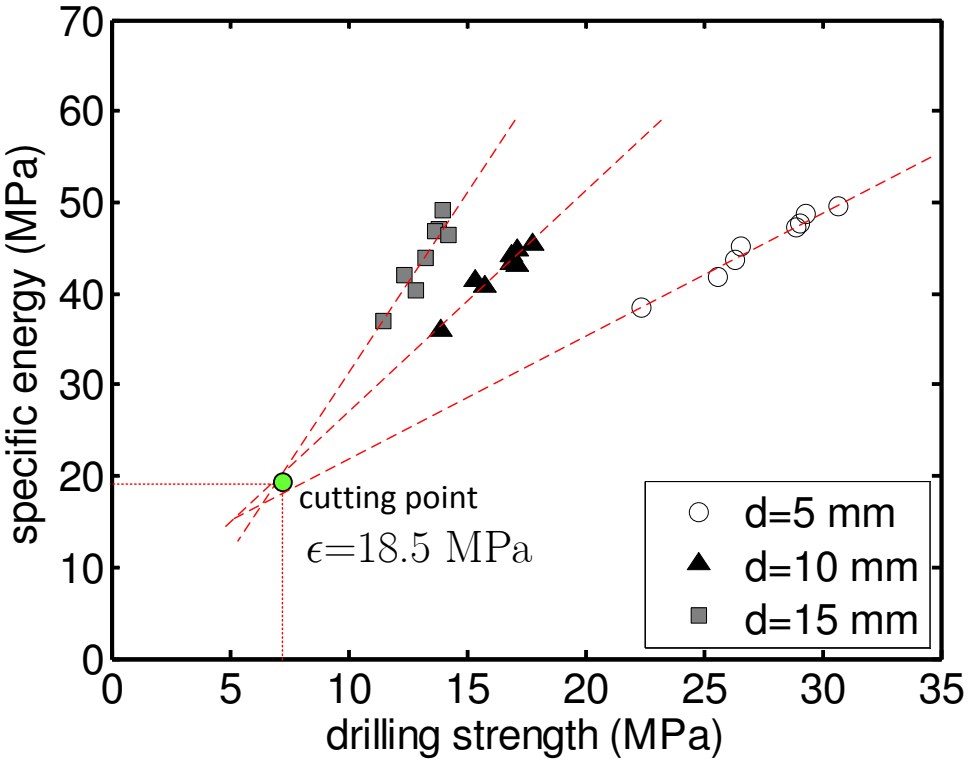

Figure 5.23: $E - S$ diagram for M1, box cutter.

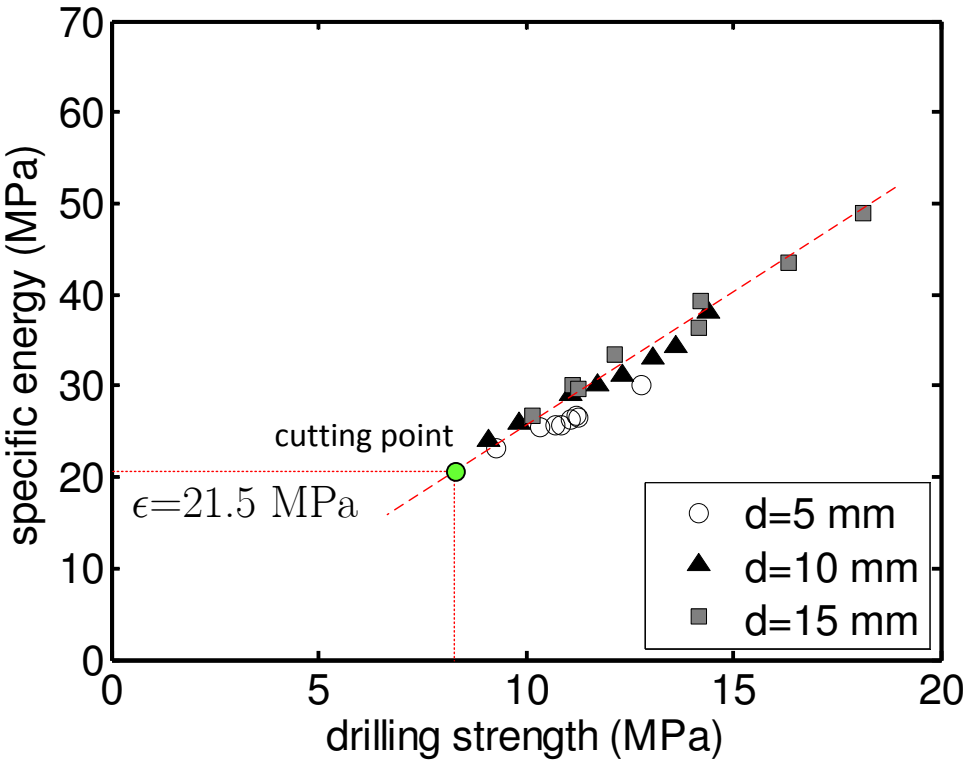

Figure 5.24: $E - S$ diagram for M1, L-shaped cutter.

cutter due to wear effect; in this study, all the cutters are modeled with rigid wall and no wear effect is considered. All the $E - S$ diagram shows the characteristics of blunt cutter as seen in experiments. On the basis of that, the numerical simulation results show that the friction on the side and front of the cutter is also a key factor influencing the cutting efficiency.

In the last group of cutting tests, the cutter is modeled using a box with six walls. The tests are performed on M2, which is a much stronger material compared to M1. The results with $d = 5$ mm is off the trend compared to the other two groups. The cutting point determined from $d = 10$ mm and $d = 15$ mm shows that $\epsilon = 142$ MPa, which is much lower compare to $\sigma_c = 231.06$ MPa.

Based on all the cutting test results, when cutter depth $d = 5$ mm, the depth is only about 5 times of the average grain radius. In other words, the cutter may have contacts with no more than 3 grains during the cutting process (neglect particles with broken bonds). As a result, both the horizontal and vertical cutting forces are significantly dependent on

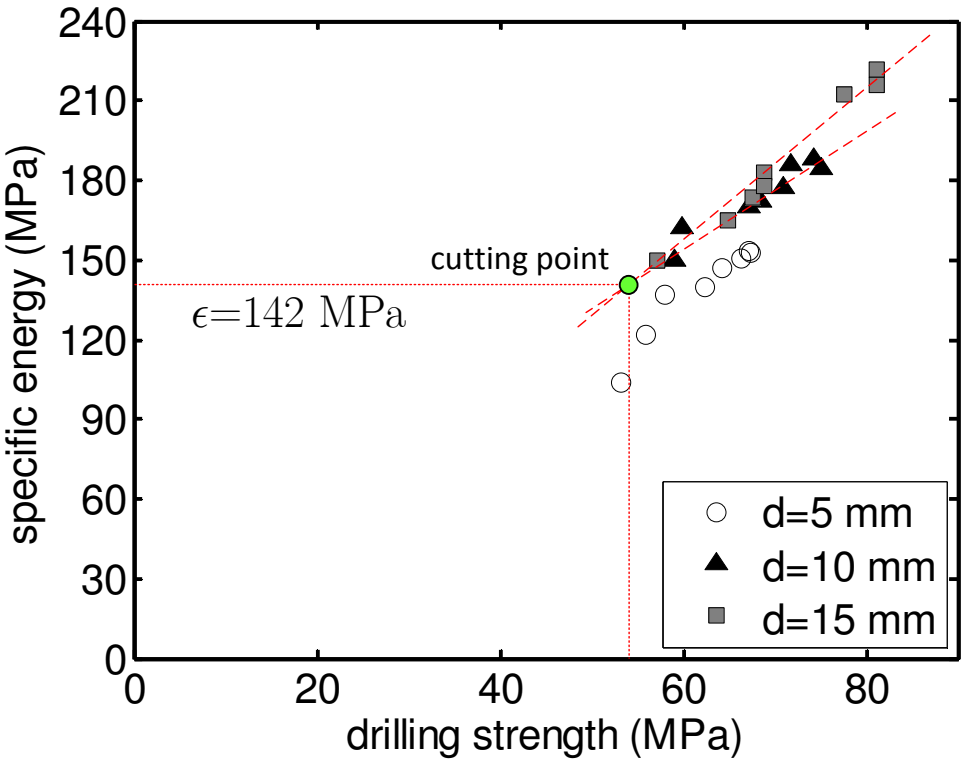

Figure 5.25: $E - S$ diagram for M2, box cutter.

the interactions of the side walls, as well as the particles piled up in front of the cutter. Therefore, the cutting force is not representative of the overall cutting behavior.

Simulation results show that the cutter geometry has a great impact to the rock cutting behavior. The energy required to cut a unit volume of rock is increasing first, then it would decrease with cutter width. For shallow depth cut, the pile-up effect is dominant to the overall cutting force signal. Besides, it will cause more energy requirement during the cutting process. So in order to improve the cutting efficiency, certain technique should be used to remove the loose materials to minimize the pile-up effect. Besides, the cutter width should be carefully chosen to lower the energy consumption.

5.6 Probing Rock Heterogeneity

5.6.1 Numerical Model

Cutting force signal is considered a direct reflection of the material property. In this section, this testing method is used to estimate material properties, as well as to probe rock heterogeneity.

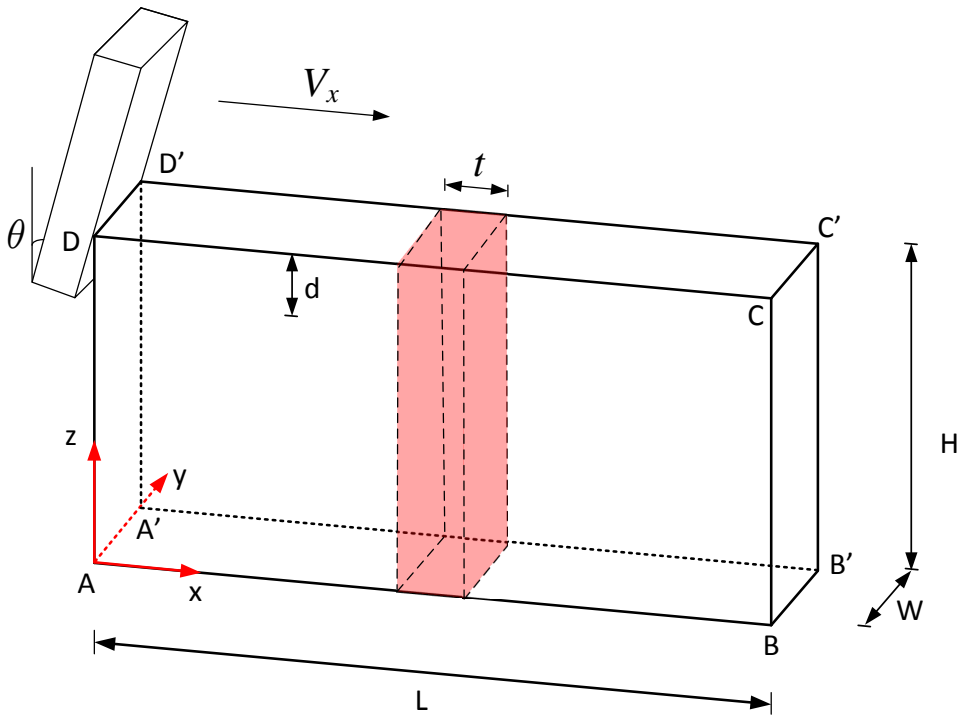

Figure 5.26: Schematic of numerical model.

First of all, a homogeneous baseline particle assembly is modeled using DEM, the micro-scale parameters are listed in Table 5.7 (under baseline Sample S1). Then, two additional numerical samples consisting of three vertical layers are also constructed by modifying the mechanical properties in the middle layer with the particle assembly configuration remaining the same as Sample S1, see Figure 5.26. Note that the thickness of the middle layer is t. The micro-scale parameters and the corresponding macro-scale mechanical properties for the middle layer are listed in Tables 5.7 and 5.8 under Samples M1 and M2. The bond strengths of the interfaces between the layers are the same as the middle layers. The compressive strengths of Samples M1 and M2 are around 157% and 42% of that of Sample S1, respectively. While the baseline material properties are similar to those of sandstone [70], the middle layer properties are chosen to be similar to those of the hard and soft North Sea shale as given in [57].

Table 5.7: Micro-scale parameters of the particle assemblies (Unit: MPa).

Micro-scale parameters	Baseline (Sample S1)	Middle layer (Sample M1)	Middle layer (Sample M2)
Point contact modulus E_c	5000	2800	7200
Parallel bond modulus $\bar{E}_c$	5000	2800	7200
Normal bond strength $\bar{\sigma}_c$	30	14	52
Shear bond strength$\bar{\tau}_c$	300	140	520

Table 5.8: Macro-scale properties of the particle assemblies.

Mechanical properties	Baseline (Sample S1)	Middle layer (Sample M1)	Middle layer (Sample M2)
Compressive strength σ_c (MPa)	62.55	98.4	26.53
Tensile strength σ_t (MPa)	11.92	20.0	5.52
Elastic modulus E (GPa)	6.92	9.79	3.77
Poisson's ratio ν	0.20	0.16	0.16
Friction angle ϕ (deg)	21.71	20.97	23.04

5.6.2 Effect of Heterogeneity

The two numerical samples, Samples M1 and M2, are utilized to probe the effect of heterogeneity by maintaining the same geometrical configuration as the baseline Sample S1 and modifying only the micro-scale properties in a middle layer of thickness t within $50 - t/2 < x < 50 + t/2$ mm according to Table 5.7. The material properties within $0 < x < 50 - t/2$ mm and $50 + t/2 < x < 100$ mm remain the same as those in Sample S1. The effect of heterogeneity is investigated from two aspects: (I) the contrast in the mechanical properties between the middle layer and the baseline; and (II) the effect of the thickness of the middle layer. Two series of simulations are performed. In the first series, the middle layer in Samples M1 and M2 has a thickness $t = 20$ mm. The compressive strength in the baseline sample is lower than the strength of the middle layer in Sample M1, but higher than that in Sample M2. In the second series, the middle layer thickness in Sample M2 is varied with the location remaining within $50 - t/2 < x < 50 + t/2$ mm.

Comparison of the force signals from Samples S1, M1 and M2 in Figure 5.27(a) indicates

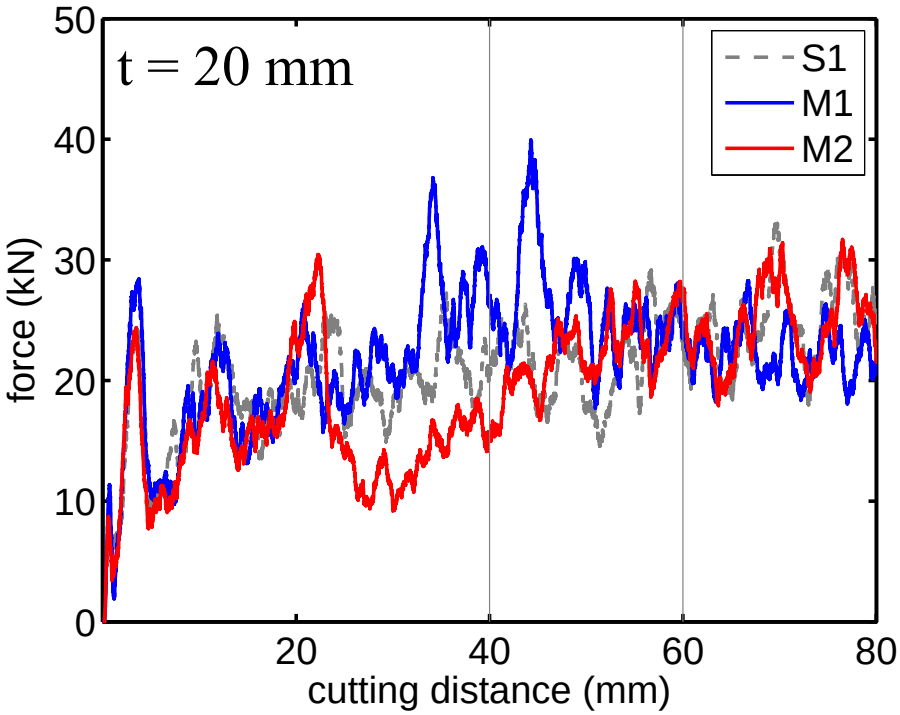

(a) sample S1 with middle layer M1 and M2, $t = 20$ mm

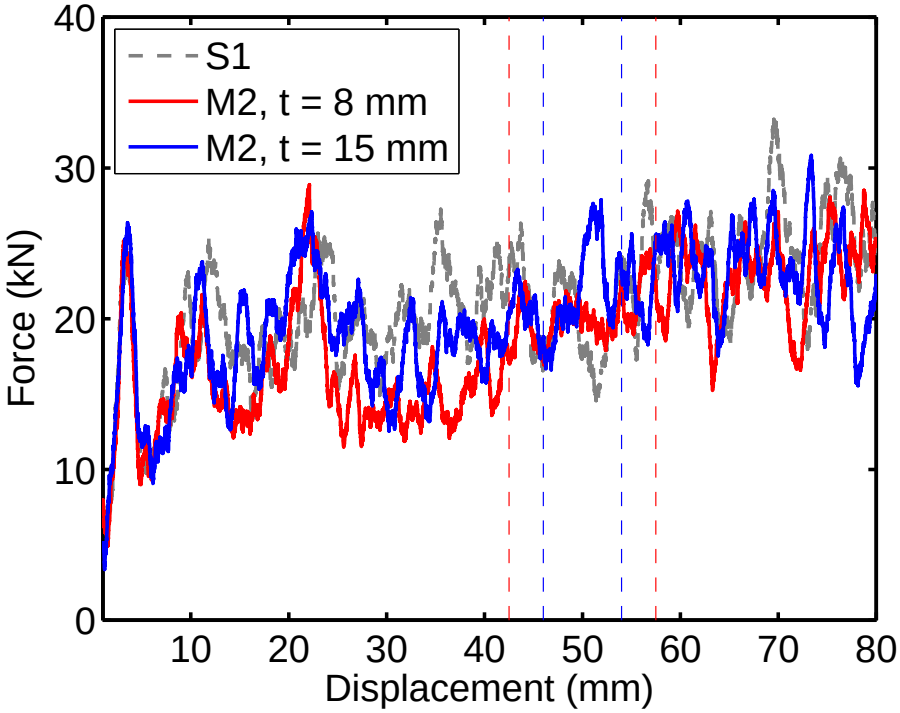

(b) sample S1 with middle layer M2, $t = 8$ and 15 mm

Figure 5.27: Cutting force signals with different middle layers.

that the existence of the middle layer is reflected in the force signals before the cutter has advanced to the layer. However, there is little influence for $s < 20$ mm and $s > 50$ mm. Within the range of $20 \leq s \leq 50$ mm, the mean force level reflects the strength magnitude in the middle layer for each case. The range of $20 \leq s \leq 40$ mm may therefore be considered as the transition zone. The size of this transition zone is about twice the depth of cut in these cases. As can be seen from Figure 5.27(b), the effect of heterogeneity diminishes as the middle layer thickness decreases. When $t = 20$ mm, the difference in the mean cutting force $\bar{F}_c$ between the baseline Sample S1 and Sample M2 averaged within $10 \leq s \leq 80$ mm is about 10%. The difference decreases to 2% when the middle layer thickness in Sample M2 decreases to $t = 8$ mm.

Dependence of the size of the transition zone on the depth of cut can be explained by examining the micro-scale failure mechanisms before and after the cutter scratches through the middle layer (see Figures 5.28 & 5.29). Apart from a few minor stable downward growing cracks, the dominant failure mechanisms in the simulations are ductile. An important failure characteristic shown in Figure 5.28 is that the plastic failure in the ductile mode is uncontained. In other words, the plastic zone grows to reach the free surface and is not enclosed by the domain in elastic deformation. Consequently, the response to the mechanical loading imposed by the cutter is mainly in form of plastic deformation and the elastic deformation is negligible. The cutting force therefore reflects rather local material properties, limited to the region near the cutter, which is of the size of the plastic zone and about a few times the depth of cut.

The numerical observations from this analysis justify that the scratch test is ideally suited to probe rock heterogeneity. If the thickness of a heterogeneous layer is at least an order larger than the depth of cut, the scratch test could capture the existence of the heterogeneity. In laboratory experiments on sedimentary rocks, at a depth of cut no more than 1 mm, the cutting force or the specific energy could already accurately reflect the strength of the rock [102, 103]. That means the resolution of the scratch test in identifying a heterogeneous layer could be as small as $O(10)$ mm.

In this work, the scratch test is modeled using the three-dimensional distinct element

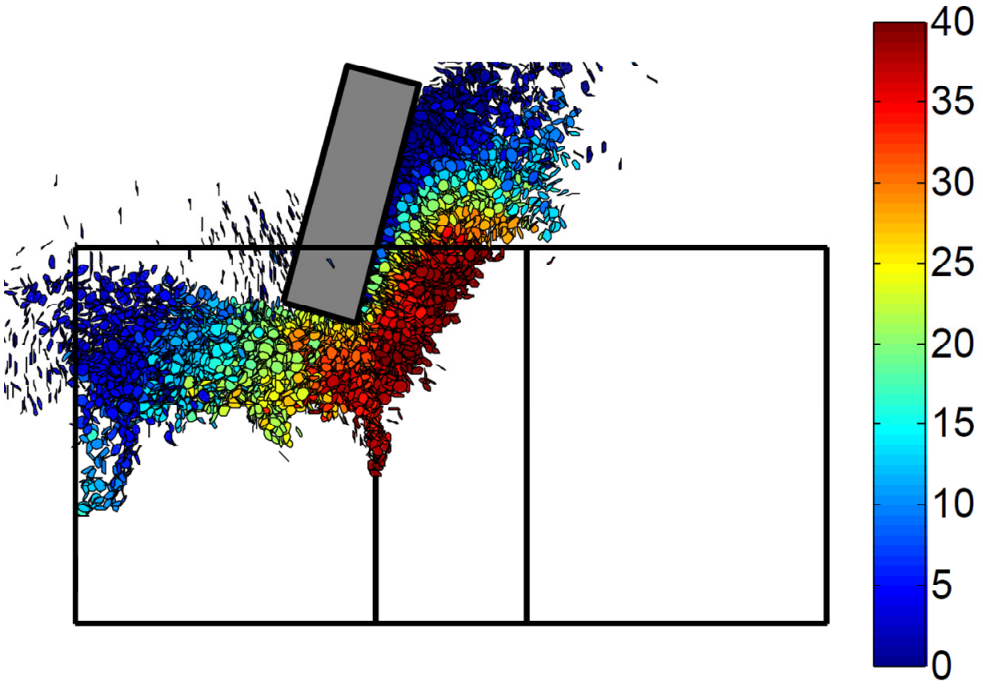

(a) M1, $s = 40$ mm

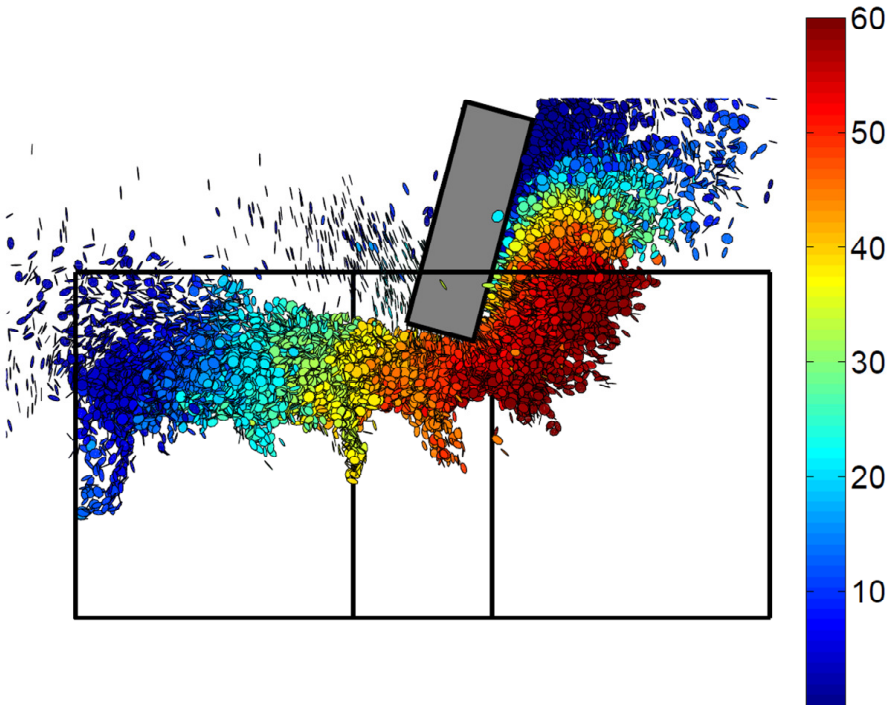

(b) M1, $s = 60$ mm

Figure 5.28: Micro-scale failure mechanism in Sample M1.

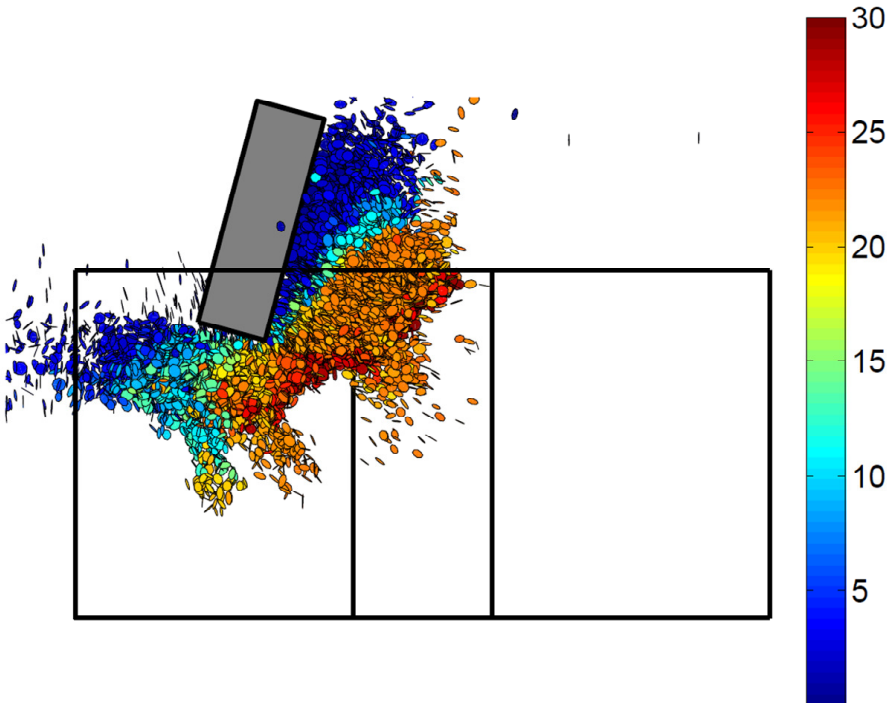

(a) M2, $s = 30$ mm

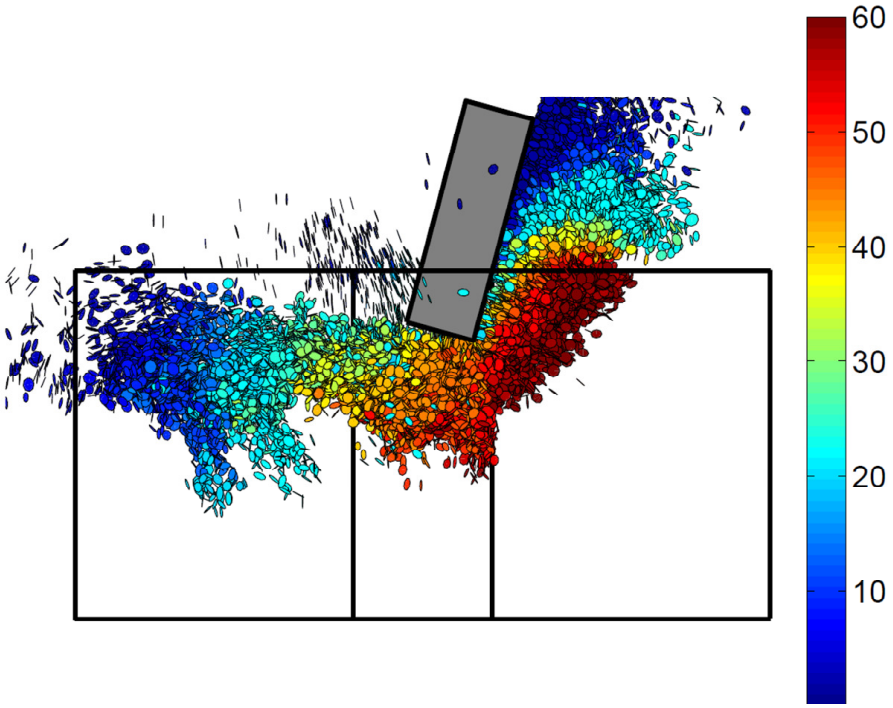

(b) M2, $s = 60$ mm

Figure 5.29: Micro-scale failure mechanism in Sample M2.

method. The numerical analysis is able to reproduce many characteristics in the cutting force signals that have been observed experimentally, e.g., the trends in the histograms of the cutting forces. However, the numerically obtained force signals lack high frequency content. A possible rate effect when the cutter speed is in the range of $V_x/V_P \tilde{} O(10^{-4}) - O(10^{-3})$ is observed numerically. Further comparison with experiments is needed in order to clarify whether the observed rate effect is a numerical artifact. The numerical analysis with the multi-layered samples shows that the scratch test is ideally suited to probe rock heterogeneity. The uncontained nature in the ductile mode of failure means that the reactions on the cutter are sensitive only to local material properties. From a practical standpoint, the resolution of the scratch test in identifying a heterogeneous layer on sedimentary rocks could be as small as $O(10)$ mm.

5.7 Fractal Analysis

5.7.1 Spectrum Analysis

Cutting force signal can be considered as a time series, which is also a self-affine fractal, thus the power spectrum $P(f)$ has a power law dependence on frequency f [116]. Peitgen *et al.* [92] showed that the continuous Fourier transform $F_T(f)$ of a signal T in relation to a statistical self similar signal Y is given by

$$F_T(f) = \int_0^X T(x)e^{-2\pi i f x}dx = \frac{1}{r^H}\int_0^{rX} Y(s)e^{-2\pi i (f/r)s}ds/r \tag{36}$$

in which X is the re-sampled length of T, rX is the total length of Y, and H is the Hurst exponent. By substituting $s/r = x$ and $ds/r = dx$, it can be expressed as:

$$F_T(f) = \frac{1}{r^{H+1}}F_Y(\frac{f}{r}) \tag{37}$$

Then transform Eq. 37 to a power spectrum. Given the fact that T and Y are statistically indistinguishable, i.e., $P_T = P_Y$, we have:

$$P_Y(f) = \frac{1}{r^{2H+1}}P_Y(\frac{f}{r}) \tag{38}$$

from which it can be shown that

$$P_Y(f) \propto \frac{1}{r^{2H+1}} = \frac{1}{f^{\beta}} \tag{39}$$

from there, researchers [92, 116] proved that

$$D = \frac{5-\beta}{2}$$

By applying the concept of Brownian noise, they obtained that the Hurst exponent is related to the slope β by

$$H = \frac{\beta - 1}{2}$$

The value of H determines what kind of process the fractal Brownian motion is:

- if $H = 1/2$, then the process is in fact a Brownian motion;
- if $H > 1/2$, then the increments of the process are positively correlated;
- if $H < 1/2$, then the increments of the process are negatively correlated;

Researchers [81] claimed that the Hurst exponent describes the raggedness of the resultant motion, with a higher value leading to a smoother motion. Based on the above statement, the power spectral density (PSD) for the cutting tests with $d = 10$ mm is demonstrated in Figure 5.30. The slope of the PSD curve is roughly equal to 1/2, which means that all the cutting force signals can be categorized as Brownian motion.

5.7.2 Identify Middle Layer Thickness

It has been observed that as the middle layer thickness decreased, the divergence of the force signal will be reduced as well. For the purpose of identifying the presence of the middle layer, a minimum layer thickness is predicted. Due to the oscillation of the force signal in time domain, the characteristics of the curve cannot be discovered. However, this problem can be solved in frequency domain by carrying out the Discrete Fourier Transform (DFT). The frequency components are corresponding to the cutting process, specifically, related to chip size [108]. Frequency spectrum of the cutting force is illustrated in Figure 5.32, from

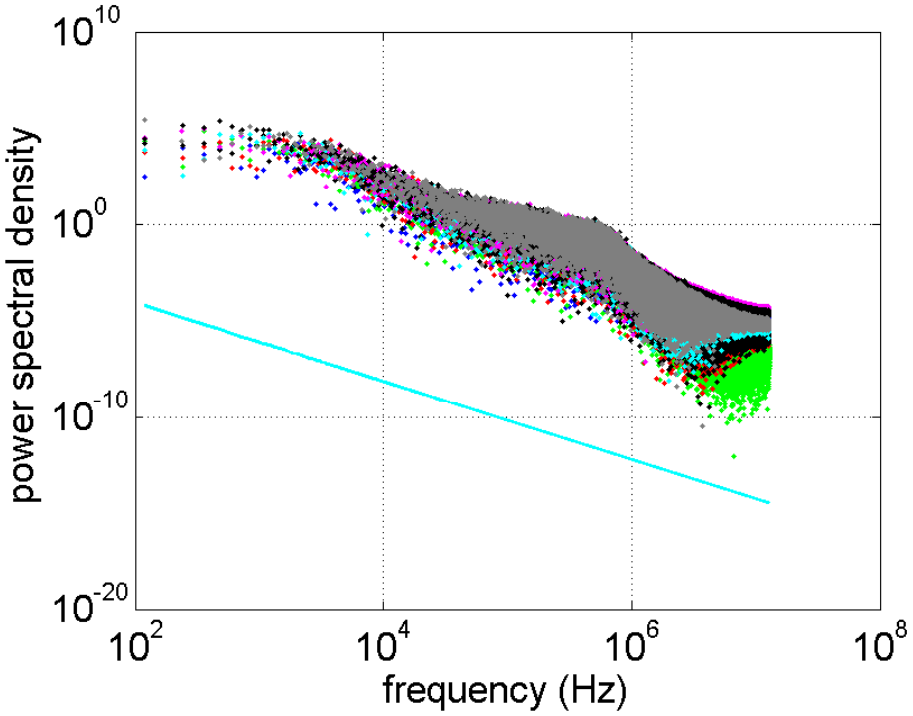

Figure 5.30: Power spectrum of signals from cutting tests $d = 10$ mm.

which we can see that the dominant components are mainly distributed in low frequency range, which corresponds to the chip formation and particle debonding process in cutting. On the basis of that, the high frequency components are useless in probing the heterogeneity from force signal. So a low pass filter is used to get rid of that part of force signal, as shown in Figure 5.33(middle). After performing the low pass filter, the oscillation related to high frequency components are eliminated and the shape of the signal is preserved. Afterwards, all of the filtered data are compared with each other under different middle layer thickness. The results are summarized in Figure 5.31.

In the frequency domain, the amplitude of different frequency components are very similar among cutting simulation trials. As an example, the specific result of $t = 20\,\text{mm}$ and baseline are shown in Figure 5.32. The power spectral density function $S(f) = 1/f$ is plotted as well, which is a straight line in log-log scale and the slope is -1, indicates pink noise characteristics.

Now take $t = 20\,\text{mm}$ as an example, the data of cutting distance from $x = 10\,\text{mm}$ to $x = 70\,\text{mm}$ is used to perform the analysis. The peaks and valleys of the force signal allow

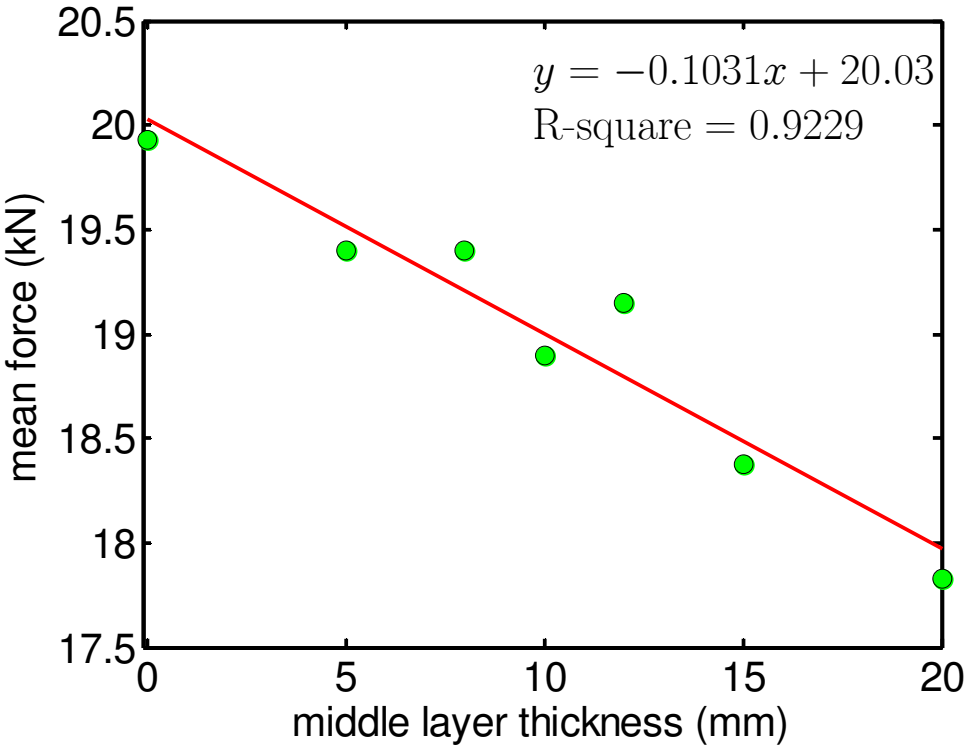

(a) average force vs. middle layer thickness

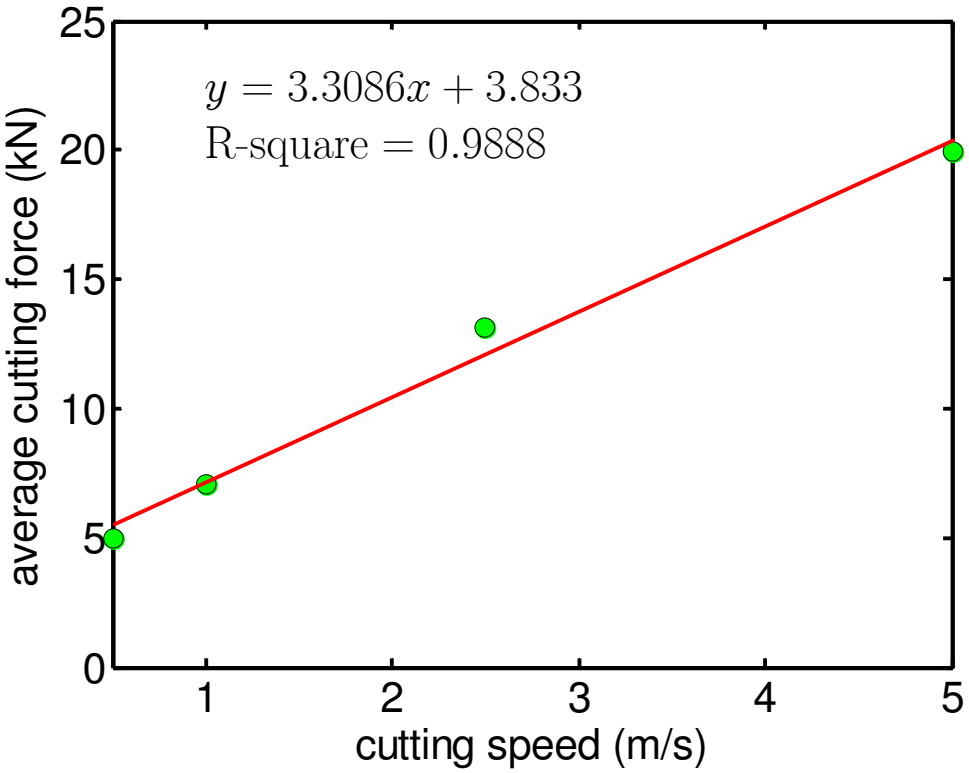

(b) average cutting force vs. cutting speed

Figure 5.31: Average cutting force variation.

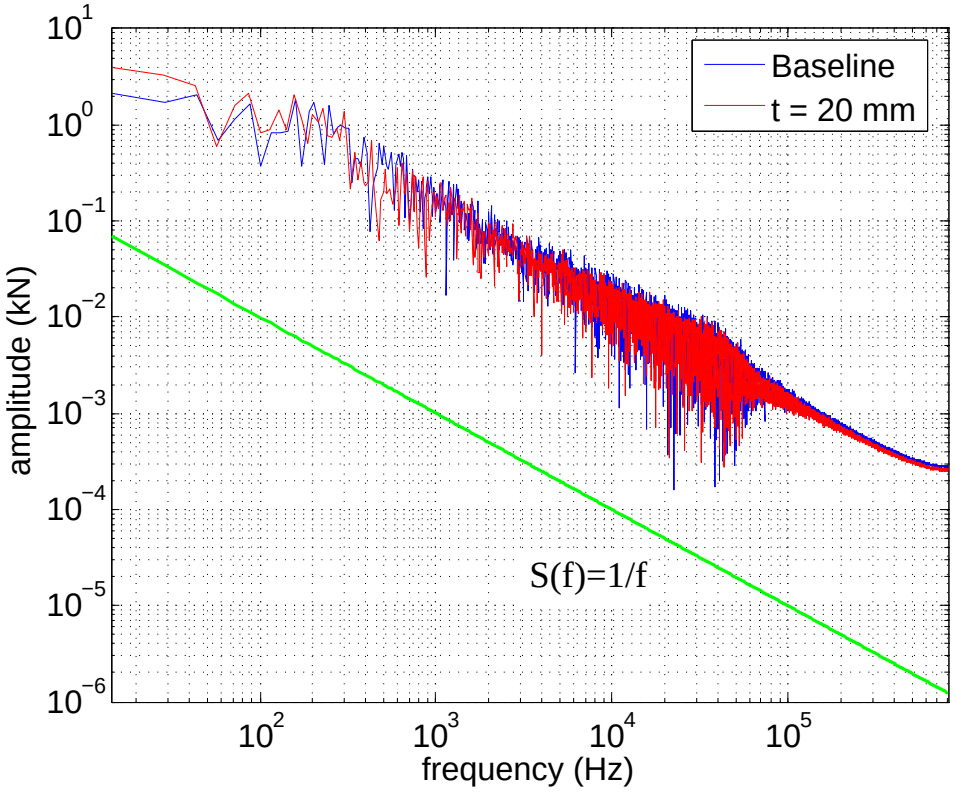

Figure 5.32: Amplitude vs. frequency after DFT.

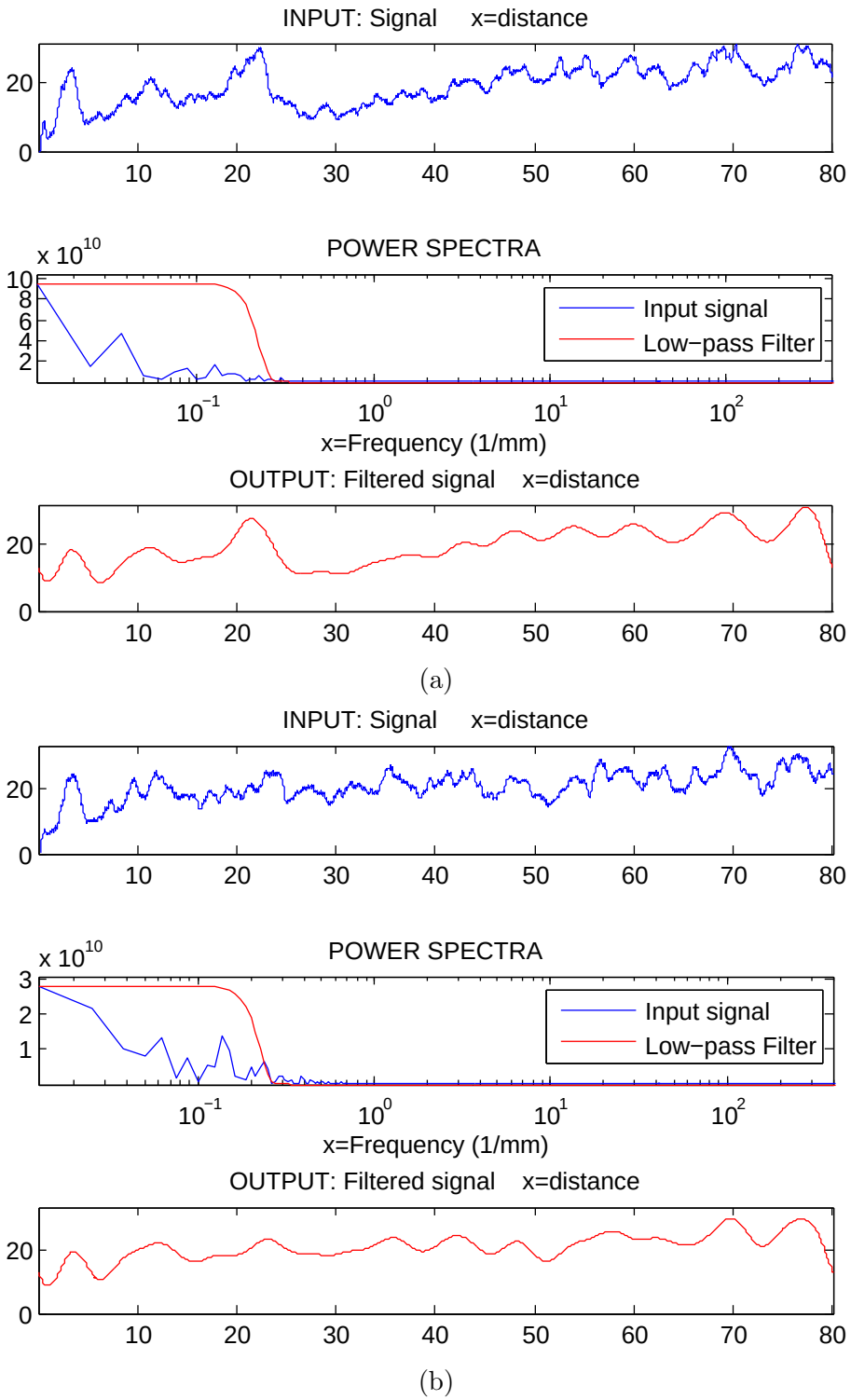

Figure 5.33: Divergence of cutting force signal. (up) original force signal without data filtering; (middle) low-pass filter; (down) data after passing the filter. (a) S1 with M1 middle layer, $t = 20$ mm; (b) S1 without middle layer.

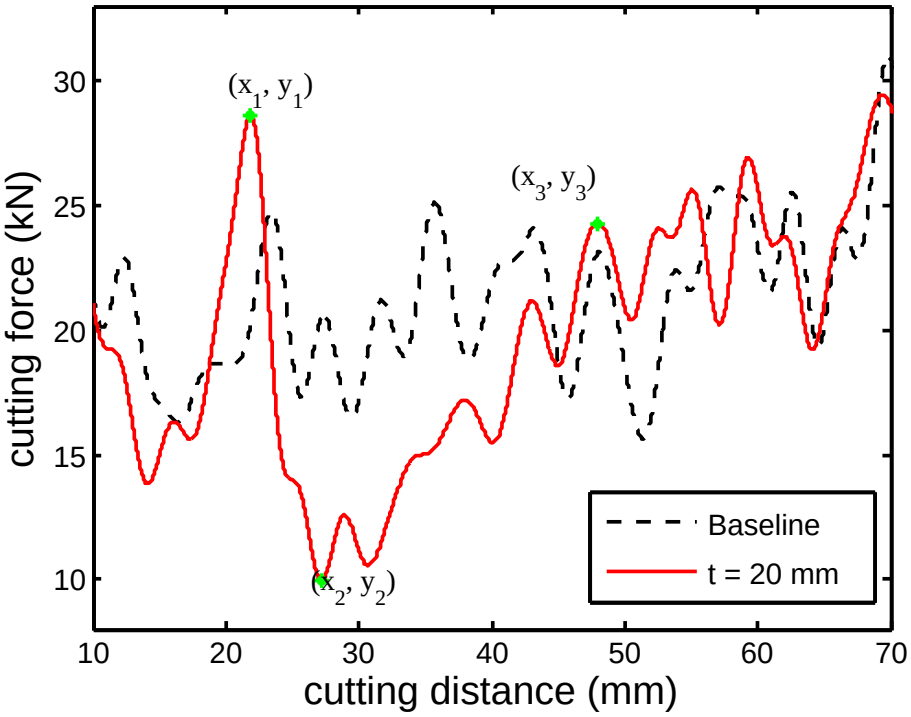

Figure 5.34: Identify peak and valley from the force signal.

us to estimate the middle layer thickness. Define the dip as $dip = \frac{1}{2}[(y_1 - y_2) + (y_3 - y_2)]$, length $l = (x_3 - x_1)$. The softening behavior, including dip and length of the valley, is caused by the bond breaking process in the middle layer during the cutting simulation. However, it is not necessary that the start point as $(x_1,\ y_1)$, shown in Figure 5.34, is identical to the left boundary of the middle layer. Instead, it is always $1t \sim 2t$ ahead of that. When the cutter reaches the boundary of the soft layer, the particles with broken bonds are compressed against each other, which makes the stiffness of that layer increase and thus the cutting force increases as well.

On the other hand, the distances between peaks and valleys on the cutting force signal of baseline material are considered a reflection of the materials intrinsic property.

5.7.3 Identify Failure Mechanism

As discussed in previous sections, the rock fails in brittle mode when $V_x = 5$ m/s, and ductile mode when $V_x = 0.5$ m/s. It has been shown experimentally that the PSD of the cutting signal is a white noise, $\beta = 0$, if the rock fails in ductile mode; or a pink noise,

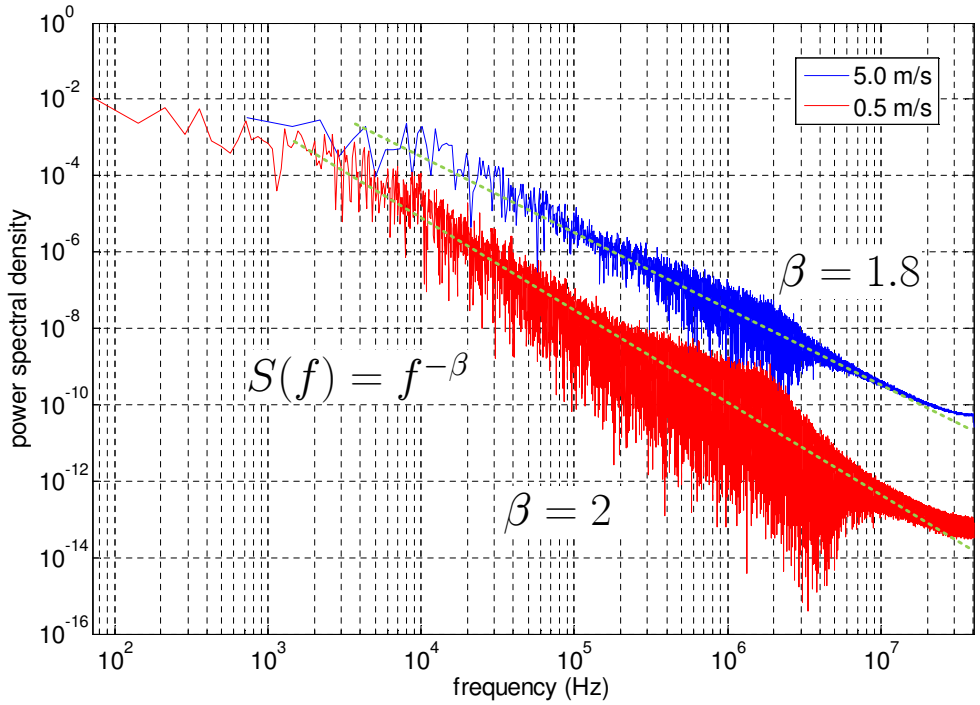

Figure 5.35: Identify peak and valley from the force signal.

$\beta = 1$, if the rock fails in brittle mode. In the simulations, the cutting force signal only shows the characteristics of Brownian noise, see Figure 5.35, in which $\beta = 2$ because high frequency components are inadequate in DEM models. However, when the rock fails in the transitioning zone from ductile to brittle, β is increasing from 1.8 to 2 in this study, which means that β could be considered as a failure mechanism indicator in rock cutting tests.

In this study, a signal analysis method is proposed to identify the presence of a middle layer in homogeneous baseline material. First of all, the ductile failure mode must be guaranteed in order to relate the cutting force with UCS of the material. Second, cutting force signal can be considered as an indicator of the material strength by identifying the local peaks and valleys. Third, it has been shown that the characteristic length and dip identified from the force signal are linearly correlated with middle layer thickness. Last but not least, the force signals from cutting tests satisfies the requirements of Brownian signal, that the power spectrum satisfy $S(f) = 1/f^{\beta}$ and $\beta = 2$ in frequency domain, and β could be considered as an indicator of the failure mechanism. In practice, the heterogeneity of rocks is a much more complex issue compared to the numerical model stated in this paper.

Further investigations are needed to solve complex problems such as rock with multiple middle layers, the effects of middle layer spacing, etc.

5.8 Conclusion

In this chapter, rock cutting tests are numerically modeled with discrete element method.

First, the 3D effect of cutter geometry is investigated. It shows that the failure mechanism observed in this study is mainly dominated by ductile failure. Due to the influence of the boundary condition at two ends of the sample, the average cutting force is obtained from the stable cutting process, which is related to the parameter λ. In this study, $\lambda = 4$ gives a good approximation of the cutting force. Then, the correlation between specific energy and cutter width w is analyzed. The results show that the pile-up effect has a significant impact to the energy consumption in the cutting process. Besides, when using L-shaped cutter to minimize this effect, the specific energy would decrease monotonically with cutter width. The $E - S$ diagrams obtained from the simulations verified D&D model and showed that the rock cutting tests in this study involved frictional interaction between the cutter and the sample.

Rock cutting tests can also be used to probing rock properties, such as strength. In this part, layered samples are used to perform the tests. First of all, the effect of cutting velocity is studied. The results show that when velocity is as small as $V_x = 0.5$ m/s, then the failure mechanism is dominated by brittle failure. However, if the cutting velocity is increased to $V_x = 5$ m/s, then the failure mechanism is dominated by ductile failure. Second, the properties of the middle layer material is changed from baseline to M1 and M2, respectively. In both cases, the cutting force signals show certain characteristics to represent the property change.

It has been shown by researchers that the rock cutting signals represents the failure mechanism. In this study, the signals satisfy the definition of Brownian noise. Besides, when the failure mechanism changes from ductile to brittle, the force signal also inclined to pink noise. By monitoring the parameters of the cutting force, a linear correlation with middle layer thickness is observed. As a result, this empirical correlation could be further

used to identify rock heterogeneity.

CHAPTER VI

CONCLUSIONS AND FUTURE WORK

6.1 Conclusions

Brittle-ductile failure mechanism transitions in various rock destruction processes are studied comprehensively using the DEM code PFC2D/3D in this work. Both two and three dimensional simulations are conducted to investigate the connections among the nominal material strengths, the sample size and the failure mechanisms in laboratory strength tests.

A novel displacement-softening contact model is first proposed and implemented in the DEM code PFC2D/3D to model the failure behaviors of quasi-brittle materials. The numerical analyses show that the displacement-softening contact model is capable of reproducing a realistic strength ratio UCS/UTS as commonly seen in quasi-brittle materials, while properly capturing the macro-scale failure mechanism. By adjusting the softening coefficient β, the strength ratio effectively increases from ~ 4, typical for a perfect brittle contact model, to as high as ~ 30, which could be considered as the upper bound of quasi-brittle materials. A series of confined compression and extension tests is performed to calibrate the softening model against two commonly studied rocks, Lac du Bonnet granite and Berea sandstone. The numerically obtained failure envelopes show excellent agreements with those obtained from the experiments. The brittle-ductile failure mechanism transition from the failure mode dominated by an opening mode tensile crack under low confinement, to the failure mode governed by shear bands under high confinement, is properly modeled.

As consistent with experimental observations, two failure scenarios are reproduced in the intact Brazilian test, namely, diametrical splitting failure from a center crack (Scenario I) and indentation-type of failure (Scenario II). The simulation results show that the failure mechanisms in the Brazilian test are governed by the strength ratio of the material. If the strength ratio is low, the indentation-type of failure is more likely to occur. The nominal

Brazilian tensile strength (BTS) decreases with the sample diameter and reaches an asymptote. The asymptote nevertheless could be as low as about only 0.5 times of uniaxial tensile strength. On the other hand, if the strength ratio is relatively high, while the size effect in BTS becomes negligible, the BTS in fact overestimates the intrinsic tensile strength. The nominal strength based on the crack initiation load, instead of the peak load, yields a better prediction of the tensile strength. The ratio of the BTS/UTS based on the crack initiation load from the numerical analysis falls in between about 0.5–1.36, comparable to those obtained experimentally in the literature. From the point of view of DEM material properties calibration, our analysis suggests that the Brazilian test is not a suitable index test to obtain the tensile strength for a DEM model. For the conventional perfect brittle contact models, only the indentation type of failure is possible and the UTS could potentially be underestimated. From the laboratory testing point of view, the implications of our numerical analysis are that failure mechanisms in the Brazilian test are critical to the reliability of test results and incorporating monitoring techniques to determine the crack initiation load could be beneficial to improve the test reliability.

The failure mechanism transition from ductile shear (shear band or damaged zone) to brittle shear (shear crack) is studied by performing numerical simulations of uniaxial compression, three-point bending with the tensile failure mode suppressed, and four-point bending tests. Both the ductile and brittle shear failure modes are reproduced in the simulations. In ductile shear failure mode, the macro-crack is formed by the coalesces of the micro-cracks and no clear crack tip can be identified during the failure process. On the other hand, brittle shear is associated with the progressive development of the shear crack. Propagation of the crack tip can be observed during the loading process. Size effect is observed if the sample fails in a brittle shear mode. For three-point and four-point bending tests, the strength decay is governed by the shear zone size to sample size ratio. Uniformity of the stress field plays a critical role in dictating the micro- and macro-scale failure mechanisms.

In the scratch test, dependence of the critical depth of cut, which governs the transition from a ductile shear failure mode to a brittle tensile fracture mode, on the strength ratio

is verified. The numerical simulations confirm that the scratch test in the ductile shear failure mode could be a non-destructive alternative for measuring the uniaxial compressive strength. The numerical analysis with the multi-layered samples shows that the scratch test is ideally suited to probe rock heterogeneity. The uncontained nature in the ductile mode of failure means that the reactions on the cutter are sensitive only to local material properties. From a practical standpoint, the resolution of the scratch test in identifying a heterogeneous layer on sedimentary rocks could be as small as $O(10)$ mm.

6.2 Future Work

With the basic failure characteristics such as the strength ratio and the nonlinear failure envelope being properly reproduced by the displacement-softening contact model, a new venue is open for us to explore the rock behaviors under more complex loading conditions. Additional benchmarks of the numerical models with experimental observations, especially those with acoustic emission measurements, and under other testing configurations, e.g., thick-walled cylinder test, could help improve the digital rock to become true representations of real rocks. Complexities at the contact level (e.g., the shear component of the contact, which has be largely neglected in this study, long-range particle interactions, etc.) and related to the grain size and shape could also be introduced to enrich the model behaviors. Moreover, the numerical simulations could help improve the reliability of laboratory tests such as the Brazilian test through quantitative modeling of specific rock types as well as more accurate descriptions of the test conditions, for example, how the BTS will be affected by the jaws of a certain curvature, and whether the Brazilian test under dynamic loading or cyclic loading conditions could be used to measure the dynamic tensile strength or to describe the fatigue behaviors.

APPENDIX A

FRACTURE PROCESS ZONE CHARACTERISTICS IN MICRO-SCALE

A.1 Introduction

Physical phenomenon of quasi-brittle material, such as rock fracturing and fragmentation, is related to the process of crack initiation, propagation, and coalescence. Since it has been accepted that the initiation and accumulation of crack damage is a necessary precursor to all rupture modes for rock [36], it is essential to have a thorough understanding of the fundamental mechanism behind the initiation and propagation of cracks.

In quasi-brittle material, the fracture process zone grows near the fracture tip consisting of micro cracks, some of which later coalesce and grow into a macro fracture as the fracture propagates. The fracture initiation and propagation process are associated with the energy dissipation in the form of elastic strain energy, namely, AE waves. As a result, many researchers believe that recording acoustic emissions during standard laboratory tests provides significant additional data that is crucial in revealing intrinsic material properties and failure mechanisms. Using this technique, Zietlow and Labuz [131] determined the intrinsic fracture process zone size which is significantly dependent on rock types but not related to specimen size, by measuring the area that covers 90% of the AE events locations. Similar technique is also used by other researchers [79, 87, 90], and Lin [74, 75] refined the results by post-processing the AE results using a digital imaging approach. Besides, using AE locations to study micro-crack initiation and coalescence is useful to gain a better understanding of the earthquake mechanisms [122, 77].

Not only spatial information of AE signals reveal intrinsic failure mechanisms, but also the AE signals allow the opportunities of calculating magnitudes of energy [45]. It has been shown that by using the energy levels quantified from the signals [90], the characteristics of the fracture evolution process are captured. Also, an attempt was made to find the

correlation between AE energy and fracture toughness by Vidya Sagar [119], indicating that the magnitude of AE energy is related to material properties. Furthermore, the magnitude, as well as distribution of AE energy levels have shown to be a possible assessment of material damage [28, 111].

Meanwhile, DEM models have been applied to simulate the fracture evolution, as well as failure mechanism, in brittle materials [16, 80, 114]. However, limited success was achieved in capturing the characteristic pattern of AE energy distribution. Later, Hazzard [50, 51] proposes a model using kinetic energy of particles in a random area (2D model) to simulate the AE event magnitudes, as well as locations. Shortly, this technique is improved by using moment tensor to represent kinetic energy, and is proved to be more robust and realistic [48]. However, this model requires that the damping ratio of the model must be small enough to reproduce adequate seismic events, which is not accurate for static simulations. Since experimental evidences [30] show that the softening behavior may be reflected in AE data, a softening contact law was implemented into a discrete element code [32] to gain a better understanding of the fracture process zone in their study. During the loading process of a three point bending beam with a center notch, location and magnitude of acoustic emission signals are recorded and analyzed.

Most of the investigations about fracture process zone are conducted on mode I type of failure. However, pure mode I fracturing is not commonly seen in nature. Instead, a mixed-mode fracturing is essential in determining the evolution of the cracks. Lin [74, 73] has used digital imaging techniques quite successfully to identify the mixed-mode process zone by monitoring the displacement field. But information such as vertical displacement field is inadequate due to the restriction of the experimental equipment. Also the relatively low resolution of this technique clouds researchers understanding of the crack growth at the tip.

In this chapter, both two and three dimensional simulations are conducted to investigate the characteristics of fracture process zone in mode I fracture. A series of three dimensional models are used to perform a parametric study. Besides, the effect of the micro-scale parameters to the macro-scale properties of the material is addressed. Then, a two dimensional

model of three-point bending with a center notch is used to investigate the evolution of tensile cracks. At last, the mixed-mode fracture is simulated by implementing a biased notch at the bottom of the beam. The simulations are designated to explore how the characteristics of the fracture process zone are affected by micro-scale parameters of the sample, including the geometry of the defects. The energy dissipation in fracture process zone, as well as the evolution of micro-cracks near fracture tip are also discussed.

A.2 Constitutive Model

Each AE signal corresponds to elastic energy released by an AE event. In macro-scale, the AE events are usually located in the process zone of a localized fracture due to damage. In this study, the softening contact law is an analog of the cohesive zone model. The tip of the traction free zone is considered as the crack tip. In the cohesive zone, the bond between particles is still able to carry traction; however, a certain amount of damage is taken into consideration characterized by the softening coefficient, as shown in Figure 2.3. The dimensions of the fracture process zone are then related to the cluster of damaged bonds.

Based on the constitutive law implemented in this model, the AE signal energy is related to the bond status. When the equivalent distance between two particles is within $\bar{\delta}_1$, all the input energy is converted into elastic energy. In other words, no energy is dissipated during the loading process. But when the distance exceeds $\bar{\delta}_1$, a certain amount of elastic energy is released, which can be expressed as a function of the maximum δ_m in the loading history:

$$\Delta E = \frac{\bar{k}_n \bar{\delta}_1^2}{2} + \frac{2\bar{k}_n\bar{\delta}_1 - \beta\bar{k}_n(\delta_m - \bar{\delta}_1)}{2} \cdot (\delta_m - \bar{\delta}_1) - \frac{[\bar{k}_n\bar{\delta}_1 - \beta\bar{k}_n(\delta_m - \bar{\delta}_1)]^2}{2\alpha\bar{k}_n} \tag{40}$$

where $\bar{k}_n$ is stiffness [F/L], $\bar{\delta}_1$ is displacement corresponding to peak force [L], $\bar{\delta}_*$ is displacement when bond breaks [L], δ_m is the max displacement in loading history [L], β is softening coefficient, and α is a dimensionless variable related to material properties. For simplification, $\alpha = 1$ and $\beta = 0.1$ or ∞ in this study.

At a specific time step during the loading process, ΔE is recorded at each bond location.

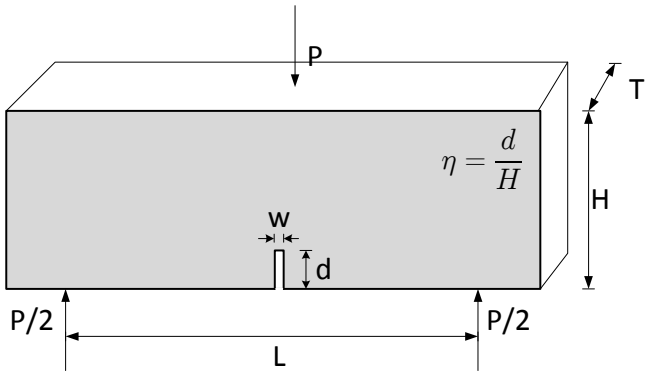

Figure A.1: Three-point bending test.

When the distance exceeds $\bar{\delta}_*$, the bond breaks and all the stored elastic energy is released.

A.3 Three-point Bending with Center Notch in 3D

Three-point bending test is performed to examine mode I fracture. In order to properly control the crack initiation and propagation, a notch that considered as a stress concentrator is installed at the bottom center of the beam.

The three-point bending test is a simple and effective method to develop a mode I fracture, as shown in Figure A.1. The fracture initiates from the preexisting notch and propagates towards the loading point. A 3D numerical model is used to study the properties of the FPZ ahead of the crack tip, including both the width and depth. The micro-scale parameters for this particle assembly are listed in Table A.1, dimension of the sample is $L \times H \times T = 104 \times 30 \times 25$ mm^3, $L/H = 3.47$. A sufficiently large L/H is applied to guarantee the mode I failure mechanism. In this study, the span depth ratio L/H is kept constant. Meanwhile, the notch size is set to be $d = 4 \sim 10$ mm and $w = 3 \sim 6$ mm.

The macro-scale properties of the synthetic rock are investigated by performing direct tension and uniaxial compression tests. The results are summarized in Table A.2. By introducing the softening coefficient into the model, we can see that the tensile strength is decreasing from 10.42 to 3.87 by 63% while the compressive strength decreases by 85%. As a result, the strength ratio σ_c/σ_t is increasing while softening coefficient is decreasing. The trend is shown in Figure A.2. When $\beta = 0.05$, the strength ratio reaches its maximum value 12.86. Note that the relationship between strength ratio σ_c/σ_t and β shown in Figure A.2

Table A.1: Micro-scale parameters of the baseline particle assembly.

Test Parameters	Particle	Parallel Bond
Density $\rho\left(\mathrm{kg/m^3}\right)$	2630	-
Average grain size $\overline{d}_m$ (mm)	1.60	-
Elastic Modulus E (GPa)	5.0	5.0
Bond Stiffness Ratio $\overline{k}_n/\overline{k}_s$	-	1.0
Contact Stiffness Ratio k_n/k_s	2.5	-
Normal Bond Strength $\overline{\sigma}_n$ (MPa)	-	$10.0 \pm 1.0)$
Shear Bond Strength $\overline{\sigma}_s$ (MPa)	-	$100.0 \pm 10.0)$
Friction Coefficient μ	0.5	-
Radius Multiplier λ	-	1.66
Moment Contribution Factor	-	1.0

Table A.2: Macro-scale mechanical properties.

Softening coefficient β	0.01	0.02	0.05	0.1	1.0	∞
Compressive strength σ_c (MPa)	100.65	99.57	96.21	87.28	31.40	17.03
Tensile strength σ_t (MPa)	10.42	9.11	7.48	7.24	4.12	3.87
Elastic Modulus E (GPa)	6.06	6.06	6.05	6.02	5.68	5.42
Poisson's ratio ν	0.22	0.22	0.22	0.21	0.15	0.12
Strength ratio σ_c/σ_t	9.66	10.93	12.86	12.06	7.62	4.40

is different to Figure 2.13, because the normal bond strength is not scaled and thus shear cracks govern the strength at lower β.

A.3.1 Evolution of FPZ Dimensions

In discrete element models, micro-cracks are simulated by debondings between adjacent particles, as represented by red disks in 3D in Figure A.4. A complete force vs. crack mouth opening distance (CMOD) curve is shown in Figure A.3, and the size of the process zone can be determined as shown in Figure A.4, in which the gray disks represent damaged bonds. During the loading process, both the position and orientation of the micro-scale events, including softening and breakage, are recorded. After the examinations of the crack pattern at specific loading stages, it is observed that the size of the process zone evolves with loading process, as demonstrated in Figure A.5.

The force vs. CMOD curve can be divided into several regions:

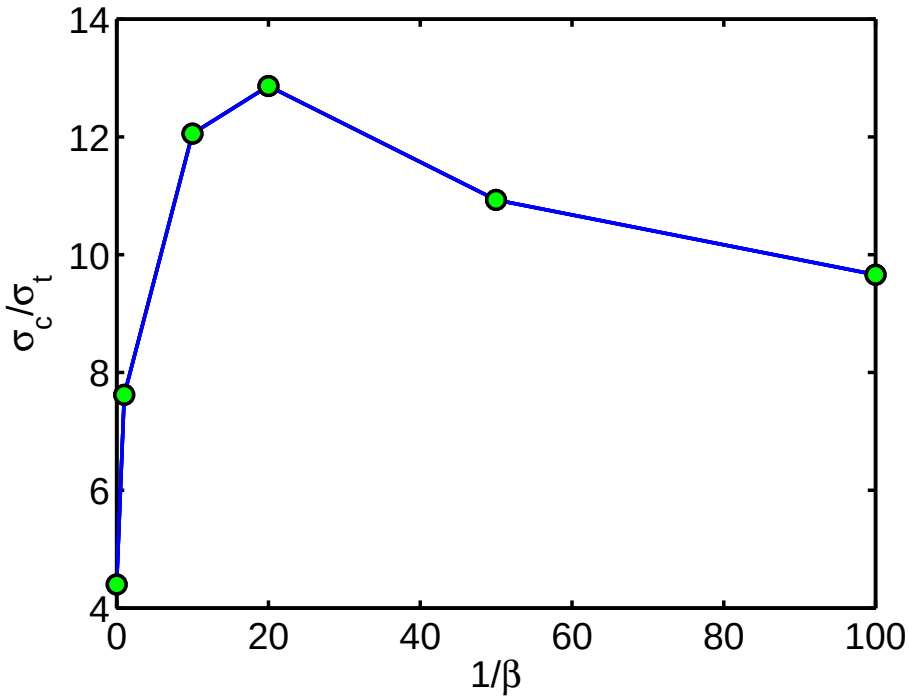

Figure A.2: Strength ratio vs. softening coefficient β.

- from origin to stage C: the whole sample deforms in elastic while crack initiates between stage B and C;
- from stage C to E: micro-cracks interact with each other to form a macro-crack.
- at stage F: the load reaches the peak;
- after stage F: crack propagates in a stable manner, though kinks are observed between stage G and H.

Before crack initiates, both width and length of the process zone increase more or less linearly with CMOD. However, when the peak force is reached, the process zone width becomes a constant. On the other hand, the process zone length increases linearly at first, then it remains a constant. The sudden drop of process zone length after stage F is caused by the difference of evolution speed between the fracture and process zone. When the cracks coalescence together, the macro-crack propagates forward faster than the growth of the process zone, resulting in a decrease of distance between crack tip and process zone tip. It is expected that the process zone length will approach a constant in stable crack growth

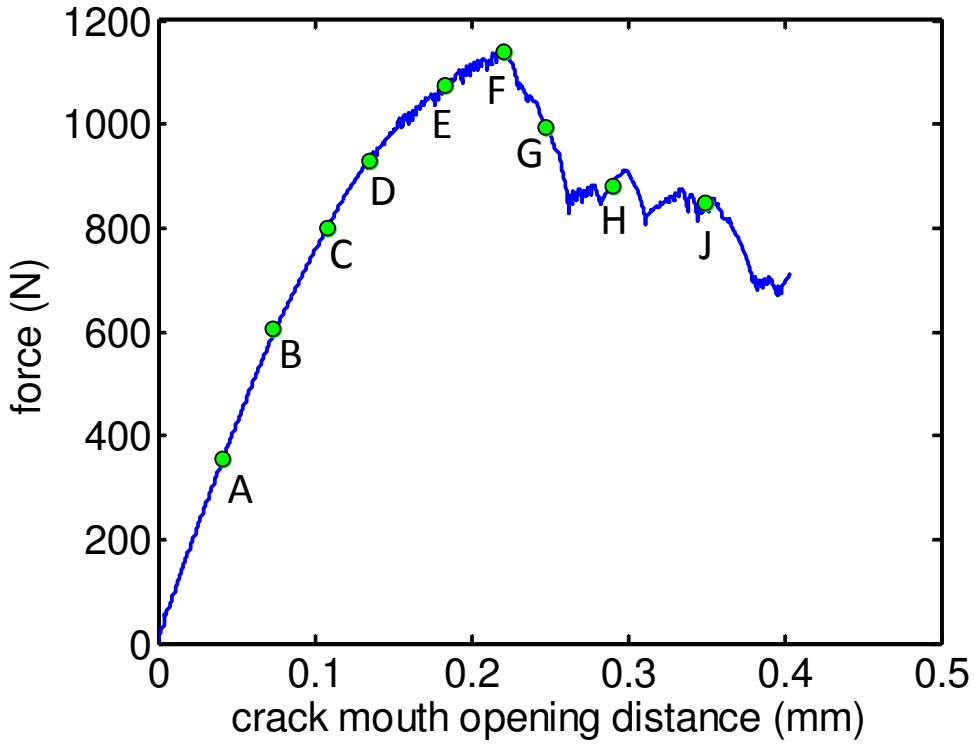

Figure A.3: Force vs. crack mouth opening distance.

stage. The constant process zone size around the peak could be considered an intrinsic length scale related to material properties.

From the displacement field shown in Figure A.6, the presence of the center notch does not change the symmetry very much; besides, the parallel vertical contour lines indicate where the mode I fracture is. On the other hand, the point where the contour lines tend to converge represents the process zone, whose length could be approximated from Figure A.6(a). During the loading process, the growth of the process zone is stable in the post-peak

Table A.3: Process zone size at different loading stage (Unit: mm).

Stage	Crack tip	FPZ length	FPZ width	CMOD
A	NA	2.30	3.36	0.044
B	NA	3.70	5.92	0.074
C	NA	5.07	8.99	0.109
D	NA	5.30	11.40	0.130
E (crack initiation)	12.95	7.55	14.60	0.199
F (peak)	14.00	7.74	15.20	0.227
G	14.98	7.84	14.24	0.252
H	14.98	7.78	13.60	0.287

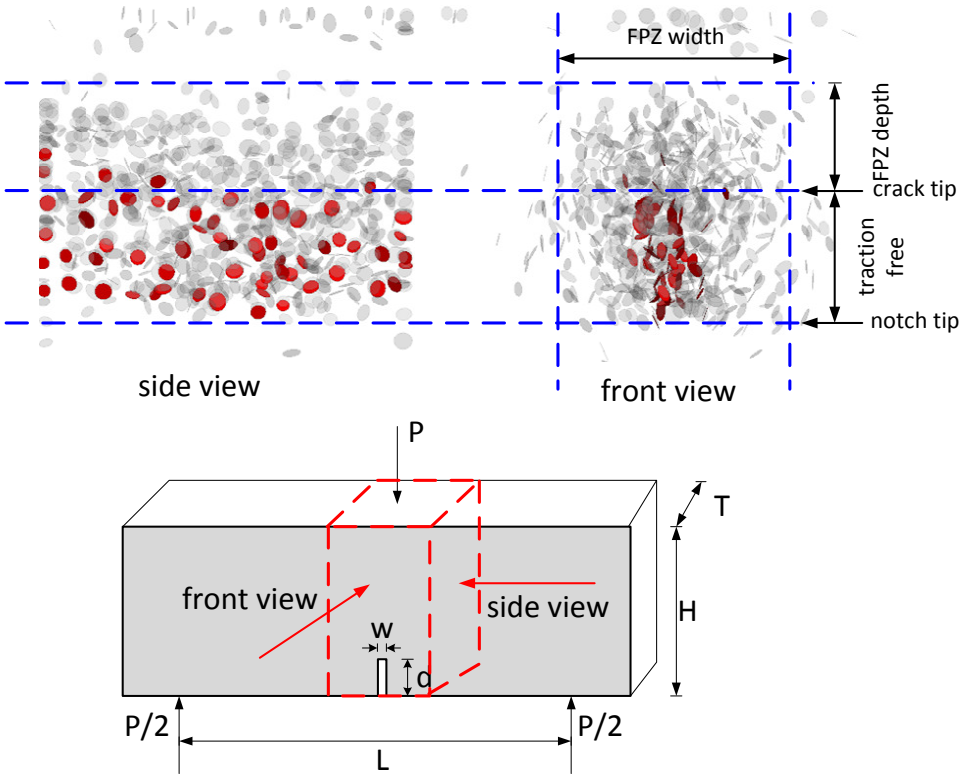

Figure A.4: FPZ in three-point bending. Red and grey disks represent the micro-cracks and damaged bonds, respectively.

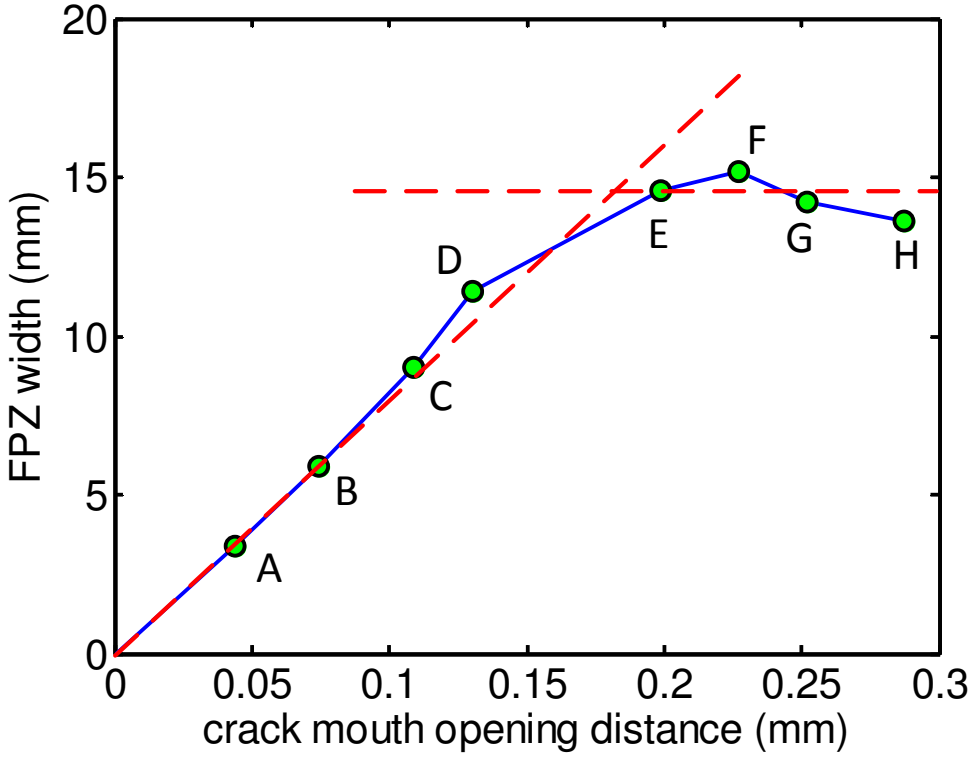

(a)

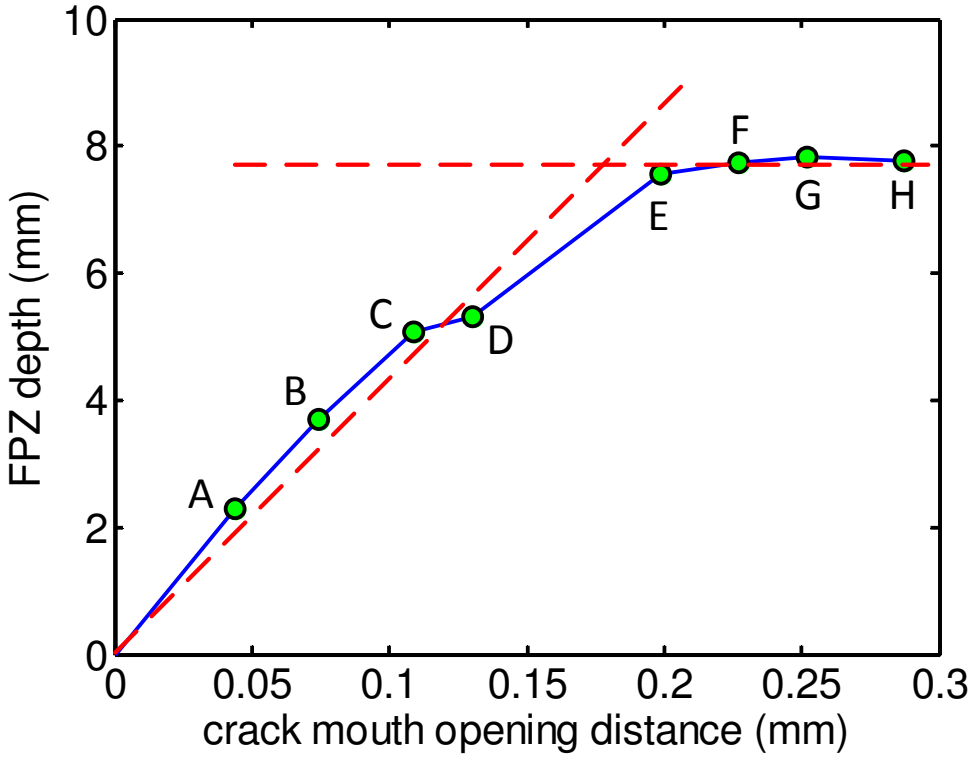

(b)

Figure A.5: Dimension of FPZ vs. CMOD.

stage.

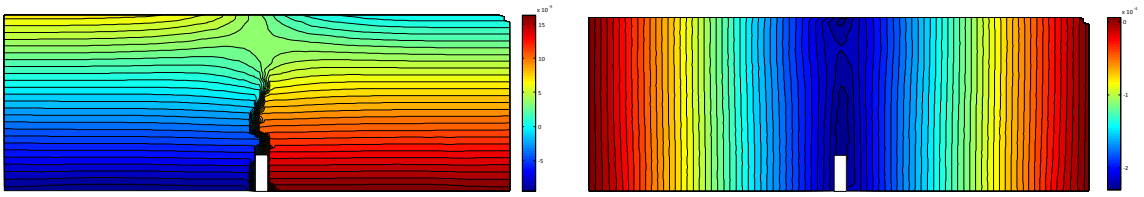

(a) horizontal displacement field (b) vertical displacement field

Figure A.6: Displacement field at peak.

A.3.2 Influence of Bond Strength Ratios

In DEM models, the crack initiation and coalescence of the particle assembly are governed by the bond strength. In this study, a parametric study is carried out to investigate the effect of shear to normal bond strength ratio, as well as normal bond strength, on the variation of FPZ width. In three-point bending test, a FPZ is observed at the tip of the notch. Then it propagates upwards at a nearly constant velocity as shown by the constant slope in Figure A.5 until the notch starts to extend. Afterwards, the crack grows as the load keeps increasing. If the bond strength is large enough in shear direction than in normal direction, the whole failure mechanism is dominated by tensile failure. However, at low shear to normal bond strength ratio, shear cracks are observed at the loading point rather than at the notch tip. Nevertheless, the failure of the sample is still governed by the tensile fracture developed near the notch tip. As the shear to normal bond strength ratio increases from 0.5 to 10, the strength ratio σ_c/σ_t will increase as pointed out in [60]. Consequently, more energy is required to propagate the fracture. Thus the width of the FPZ increases as expected, see Table A.4.

Table A.4: FPZ size at peak load while keeping normal bond strength constant.

Shear to normal bond strength ratio	FPZ width (mm)
10	14.90
5	14.20
2	13.30
1	7.90
0.5	6.66

On the other hand, three groups of simulations are performed with a constant bond strength ratio while the normal bond strength varies. The results are listed in Table A.5, showing that the FPZ width is more or less a constant, too. Since the FPZ is simulated by softening behaviors defined by the constitutive model with softening coefficient β, the size of the process zone is dependent on the elastic to input energy ratio, instead of the absolute value.

Table A.5: Dimensions of FPZ at peak load while keeping strength ratio constant.

Normal bond strength (MPa)	FPZ width (mm)
10	14.30
20	14.40
50	14.85

The width of the fracture process zone is usually considered a material constant. The intrinsic width w_* is defined as,

$$w_* \sim Rf\left(\frac{R}{\delta_1^n}, \frac{\delta_2^n}{\delta_1^n}, \frac{\delta_1^s}{\delta_1^n}, \cdots\right) \tag{41}$$

where R is the average particle radius; δ_1^n is the displacement between particles in normal direction at the peak; δ_2^n is the ultimate displacement between particles; δ_1^s is the ultimate displacement in shear direction. As such, the ratio δ_2^n/δ_1^n represents the softening behavior characterized by softening coefficient β. When the normal bond strength is fixed and the

shear to normal bond strength ratio increases, the ratio δ_1^s/δ_1^n increases. Thus the intrinsic fracture process zone width increases, as shown in Table A.4. When the shear to normal bond strength ratio is a constant, changing the normal bond strength won't change the ratio of δ_2^n/δ_1^n and δ_1^s/δ_1^n. Meanwhile, when the sample size is relatively large, the ratio R/δ_1^n becomes negligible. Thus the intrinsic fracture process zone width w_* remains roughly a constant, as shown in Table A.5.

A.3.3 Influence of Notch Geometry

In this section, the location of the preexisting notch is fixed at the bottom-center of the beam, while the dimensions, including width and length, of the notch vary in a range of $w \in [0,\ 6]$ mm and $d \in [4,\ 10]$ mm. Since the process zone size evolves with respect to loading stages, we pick the peak stage as a reference, at which the width can be considered as a constant (see Figure A.5(a)). A perfect line cutting notch ($w = 0$ mm) is obtained by removing the bonds on the notch plane. The results are summarized in Table A.6.

Table A.6: Process zone size at peak load (Unit: mm).

Index	Notch width	Notch length	FPZ width
0	0	10	14.90
1	4	10	15.20
2	4	8	15.36
3	4	6	16.30
4	4	4	16.80
5	3	8	15.20
6	5	8	14.90
7	6	8	15.20

The results suggest that the FPZ width is nearly independent of the notch length and width. Since it has been shown that the FPZ size is independent of sample size, as well as the defect geometry, we could argue that the FPZ dimensions could be considered as a material constant that only relate to the mechanical properties of the material.

A.4 Three-point Bending with Refined Region in 2D

A.4.1 Model Setup

In previous section, it has been shown that the proposed numerical model with softening coefficient is capable of capturing the characteristics of fracture evolution in quasi-brittle materials. In this section, a 2D discrete element model is used to study the development of FPZ from energy point of view. For calculation efficiency considerations, we use a 2D model instead to construct the simulations.

The numerical simulation of three point bending test is conducted with a rectangular shaped sample with length $L = 160$ mm, height $H = 60$ mm, and span $L_s = 146.8$ mm, see Figure A.7. The numerical domain is divided into two zones: first, the baseline zone is densely packed with 4237 randomly generated particles (cylinders in 2D) with the radii uniformly distributed in the range of $1.2 \leq R \leq 1.99$ mm; second, particles located in the "refine zone" are replaced with smaller particles in order to capture the characteristics of the crack region and intrinsic fracture process zone. In order to alleviate the size effect stemmed from pre-exist crack width, an initial crack with infinitesimal width is installed by removing bonds crossing the line segment at the bottom center of the refined zone. The loading process is modeled by imparting a constant velocity $v = 0.04$ m/s to the top center of the beam with a circular rigid wall.

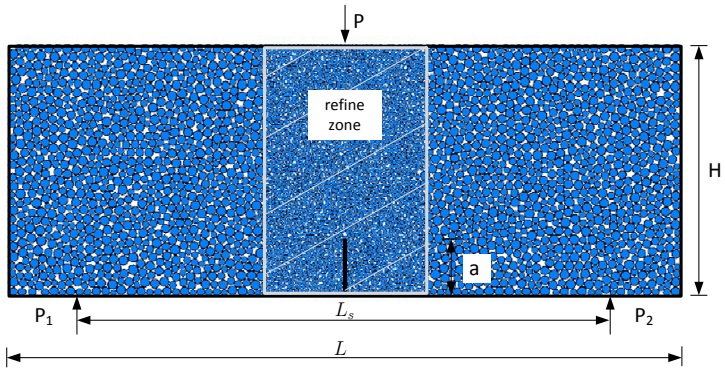

Figure A.7: Three point bending model setup.

It has been noted in [42] that the size of process zone in quasi-brittle material is dependent upon the specimen size. Moreover, the dependency disappears when the ratio of

specimen size to grain size is large enough. So in this study, particles adjacent to the notch are refined to smaller sizes in order to make sure that the apparent fracture toughness is equal to the true material toughness. To be more specific, the original particle is deleted and then replaced by two new ones while the total area (in 2D, volume in 3D) is equivalent during the refine process. Meanwhile, the radius ratio after the refinement is set to be no greater than that of the baseline material. On the basis of the two criteria, the new particles radius r_1 and r_2 can be expressed as:

$$r_1 = s_1 + \varphi(s_2 - s_1),\ \varphi \in [0, 1] \tag{42}$$

$$r_2 = (r_0^2 - r_1^2)^{1/2} \tag{43}$$

with $s_1 = r_0(1 + \xi^{(2/l)})^{-1/2}$ and $s_2 = r_0 \cdot 2^{-1/2}$. Where r_0 is the original particle size, ξ is the particle-size ratio of the baseline material, l is refinement level, and φ is a refinement parameter that in the range from zero to one. If $\varphi = 1$, then $r_1 = r_2$ and the size ratio of the replaced material will be equal to that of the base material. If $\varphi < 1$, then $r_1 \neq r_2$ and the ball size ratio will be greater than that of the base material.

Micro-scale parameters for the baseline and refined assembly are listed in Table A.7. Unless otherwise noted, the rest of the parameters are chosen as follows: the radius multiplier, $\bar{\lambda}$=1; the stiffness ratios, k_n/k_s=1 and $\bar{k}_n/\bar{k}_s$=1; the inter-particle friction coefficient, μ=0.5; the particle density, ρ=2630 kg/m^3; in order to obtain a relatively brittle material (Huang, 1999), the average normal and shear bond strength ratio is chosen to be 1/100; and the standard deviation of both the normal and shear bond strengths is chosen to be 1% of the mean value.

Before performing the tests, an additional group of numerical samples without refined zone are used to verify that the existence of the refined zone will not impact the macro-scale properties of the sample. Table A.8 shows that the difference between baseline and refined sample is acceptable.

Table A.7: Micro-scale parameters.

Micro-scale parameters	Baseline	Refined zone
Minimum radius R_{min} (mm)	0.5 (0.8)*	0.38
Ball-size ratio R_{max}/R_{min}	2.21 (1.28)*	1.71
Average ball radius $\bar{R}$ (mm)	1.02	0.51
Elastic Modulus E_c (GPa)	50	-
Stiffness ratio K_n/K_s	4	-
Friction coefficient μ	0.5	-
Density ρ (kg/m^3)	2630	-
Bond modulus $\bar{E}_c$ (GPa)	50	-
Radius multiplier $\bar{\lambda}$	1	-
Bond Stiffness ratio $\bar{K}_n/\bar{K}_s$	4	-
Normal Bond Strength (MPa)	$\bar{\sigma} = 5$, $\bar{\delta} = 1\%\bar{\sigma}$	-
Shear Bond Strength (GPa)	$\bar{\tau} = 320$, $\bar{\delta} = 1\%\bar{\tau}$	-
Softening coefficient		

*Number in parentheses is the ball radius initially assigned when generating the assembly.

Table A.8: Macro-scale mechanical properties.

Mechanical properties	Baseline	Refined	Error (%)
Compressive strength σ_c (MPa)	34.33	33.45	2.5
Tensile strength σ_t (MPa)	3.02	2.97	1.6
Elastic Modulus E_c (GPa)	50.9	51.5	1.2
Poisson's ratio ν	0.31	0.29	6.4
Strength ratio σ_c/σ_t	11.37	11.26	1.0

A.4.2 Simulation Results

Figure A.8 shows the load history of the previously described particle assembly under three point bending test. The first AE event (including bond breakage or bond damage) is recorded at approximately 30% load ratio, where load ratio is defined at the percentage of the maximum load, but continuous AE productions do not start until the load ratio reaches 70%, marked as stage A in the figure. This ratio is realistic when compared with experimental results, showing the ratio is about 80% [87]. At this stage, several parallel bonds located at the bottom center of the beam near notch tip start entering the softening regime, and FPZ begins to grow. Before fracture occurs, the size of the FPZ is not fully developed. In other words, the FPZ grows in both vertical and horizontal directions as load keeps increasing. Meanwhile, the number of AE events increases in a stable manner. When load increases to 90% of peak, namely stage B, fracture is initiated at the notch tip, surrounded by a process zone. At this point, the shape of the process zone is mostly fixed, only the size changes in the following steps. Besides, the number of AE events is still increasing in a continuous way. When the load reaches the peak, the size of the process zone is almost at its limit and the fracture starts to grow unstably. A sudden increase of AE events is also observed right at the peak. However, the ratio of AE event number to number of cracks is decreasing; see Figure A.9. In the pre-peak stage, the size of the FPZ keeps growing in a relatively faster pace than that of the cracks. As a result, the AE events ratio goes up as high as 12 then suddenly drops when new cracks forms. This process repeats several times and the average AE events ratio keeps going down as the size of FPZ approaching a constant. In the post-peak stage, the loading force drops quickly corresponding to a sudden growth of the fracture. The number of softening events jumps from 200 to almost 400, however, the AE event number ratio is more or less a constant, which indicates that the size of the process zone is stable and growing with fracture.

Figure A.9 also shows that in post-peak stage, the crack propagates in a creeping pattern rather than what is commonly known as stable growth. When the loading force reaches 90% post-peak, the FPZ size is roughly fully developed. Consequently, the fracture propagates towards the tip of the FPZ. Since fracture grows much faster than plastic zone does, so the

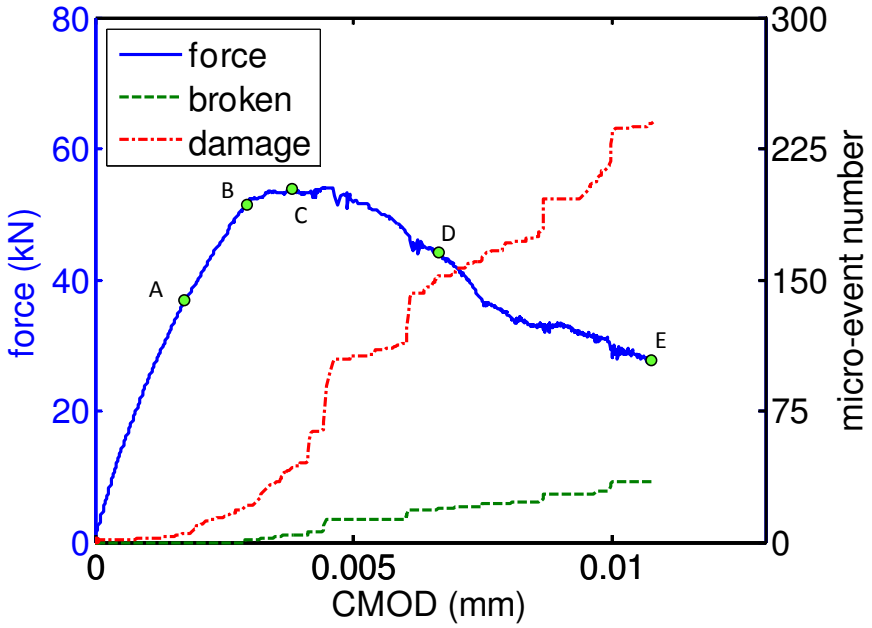

Figure A.8: Load vs. CMOD and the corresponding AE event numbers.

ratio of AE events drops quickly to about 6.5, at which point, the energy stored in FPZ is released to generate new fracture. Then the plastic zone ahead of the fracture tip hampers the continuous propagation of the fracture. Consequently, the FPZ starts to grow ahead of the fracture tip until the stored energy is enough to propagate the fracture. Therefore, even in stable fracture propagation phase, the FPZ length increases and then decreases repeatedly corresponding to the growth of fracture. On the other hand, once the FPZ is fully developed, its width becomes a constant which is determined by mechanical properties of the material. In this simulation, for example, the size independent FPZ width is related to the softening coefficient of the contact law.

Magnitude of energy dissipated in FPZ is recorded, as shown in Figure A.10. In pre-peak stage, total energy dissipated from generating fracture is lower than that in FPZ. However, when passing stage E (80% post-peak), the cumulative energy dissipated by bond breaking grows faster than in FPZ, indicating that the energy released during the loading process is mostly used to propagate the fracture. Meanwhile, the amount of energy dissipated in FPZ is about 40% of the total energy.

Figure A.11 shows the development of the FPZ and fracture in the overall loading

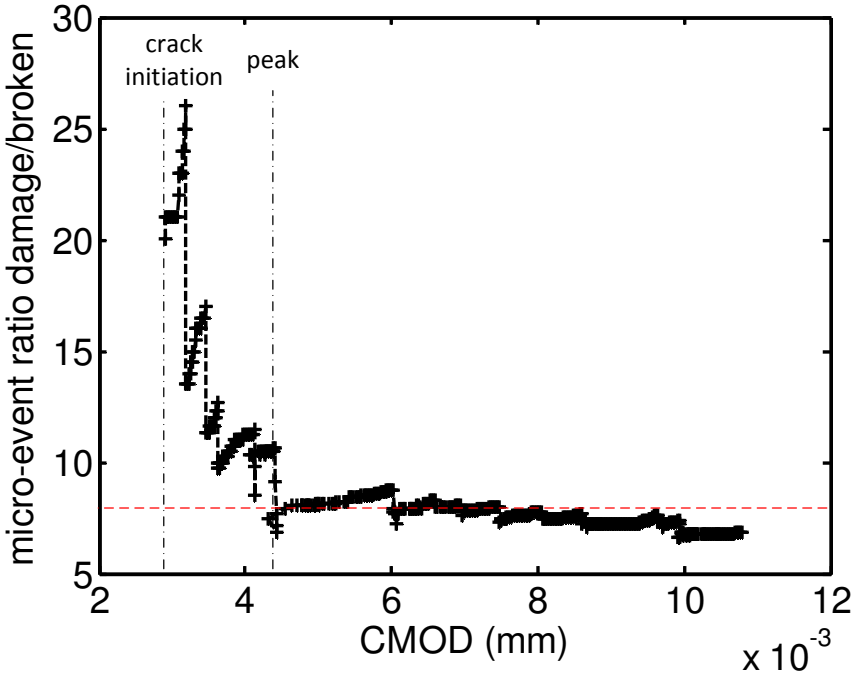

Figure A.9: Micro-events ratio vs. CMOD.

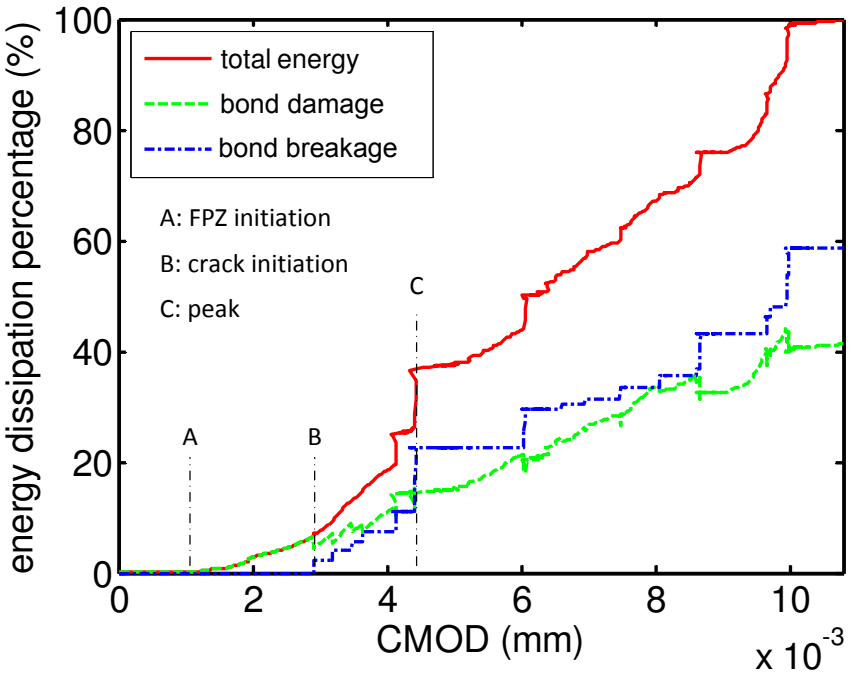

Figure A.10: Cumulative energy.

process. The left column of the figure shows the AE signal locations while the right column shows the energy density cloud. These figures suggest that the FPZ width remains unchanged during the whole process while the fracture length changes as described previously. Meanwhile, the energy density indicates where the potential fracture tip is. In Figure A.11(e), the energy density cloud shows a branching crack at the top which cannot be observed from the AE locations figure. The reason is the "branching crack" is actually not formed because the energy stored in FPZ is not high enough to create a new fracture. Energy magnitude of the AE signals in that region is in the intermediate level between plastic zone and micro-crack. Other than that, the energy density figures also show a clear boundary of the FPZ, which makes it easier to measure the size of the FPZ. The energy level adjacent to the path of the fracture is approximately in the range from 1.5–4.5 mJ, while at the FPZ boundary, the energy level is as low as $O(10^{-3})$ mJ. The difference in AE energy levels is considered as a material property, which is related to the micro-scale damage model and force-displacement law. Also it has been noticed by many researchers that there are various approaches to classify AE energy levels [97, 19]. In this study, the AE energies are grouped into three categories, namely: low energy, intermediate energy, and high energy, as shown in Figure A.12.

In Figure A.12(a), each blue dot represents an AE event. Then all the AE events are sorted based on its energy magnitude in ascending order and illustrated using red dots, see also in Figure A.12(a). Then all the AE events are automatically divided into three groups: low energy AE events, where $E < E_1$ and E_1 is approximately 0.07 mJ; high energy AE events, where $E > E_2$ and E_2 is approximately 0.4 mJ; and intermediate zone in between, where $E_1 < E < E_2$. In [58], the author defines the high energy zone as inner zone, or in other words, fracture core zone; the low energy zone, together with the intermediate energy zone, is called outer micro-scale fracture zone. Usually, E_2 is defined one order higher than E_1. From Figure A.12(b), it is observed that the number of AE event occurrence at low and intermediate energy levels take 70.83% of the total AE events, but the total energy dissipated is only 15.85%. High energy level corresponds to fracture core zone in macro-scale, and the number of event occurrence is about 29.17%, however, the total energy

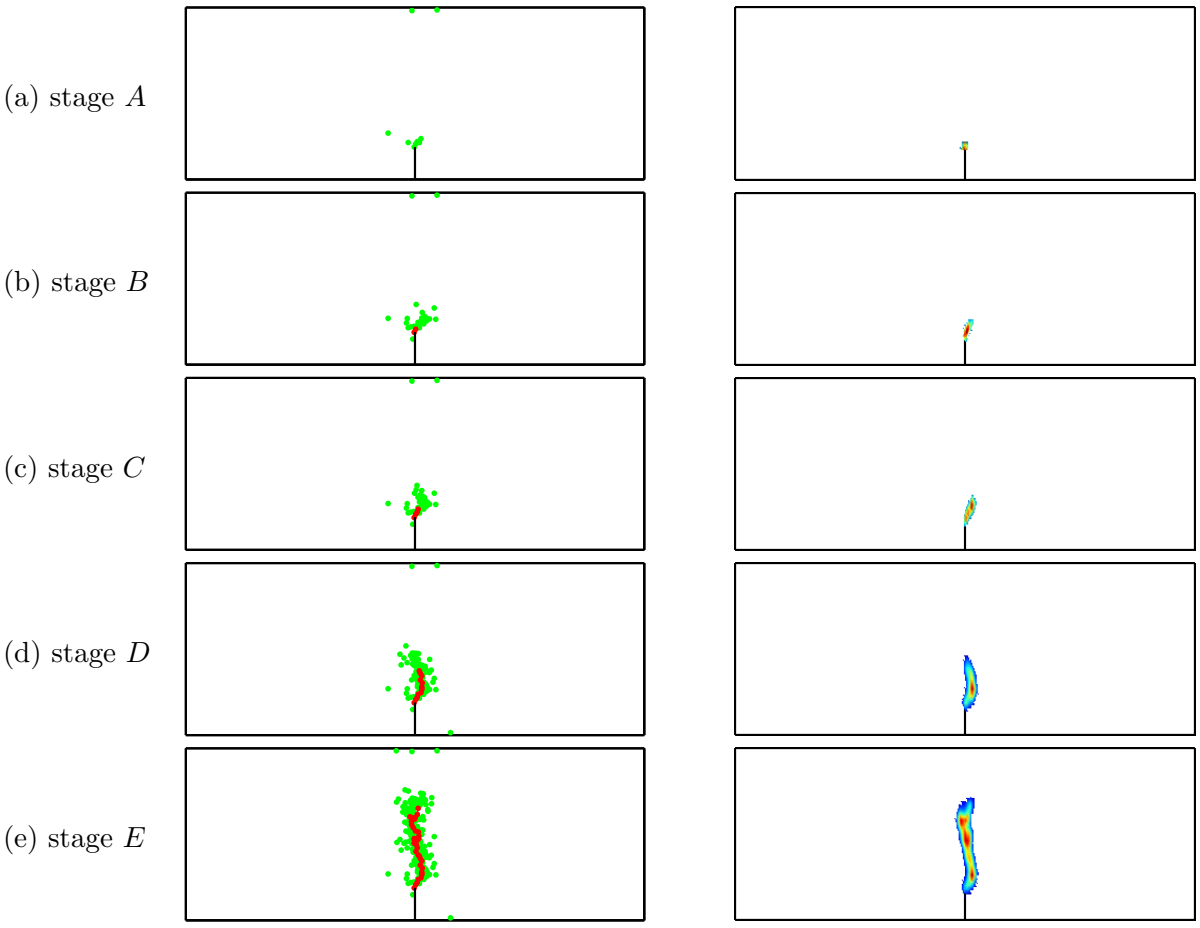

Figure A.11: Micro-event locations and energy distribution at different stages. Stage A: FPZ initiation, stage B: crack initiation, stage C: peak, stage D: post-peak 80%, stage E: post-peak 60%. Green and red dot represent bond damage and breakage, respectively.

dissipated is as high as 84.15%. The histogram also shows that the occurrence of AE signal is five times more frequent in FPZ than on the fracture path, which indicates that the size of the FPZ is about $4 \sim 5$ times of average grain diameter. A summary of the AE events occurrence and energy can be found in Table A.9.

Table A.9: Micro-event energy classification.

	Number of Occurrence		Energy	
	absolute	relative (%)	absolute (mJ)	relative (%)
Low energy ($E < E_1$)	56	23.33	1.73	1.18
Intermediate ($E_1 < E < E_2$)	114	47.50	21.44	14.67
High energy ($E > E_2$)	70	29.17	122.99	84.15
Summation	240	100.0	146.16	100.0

Researchers usually use the locations of the acoustic emission signals to identify the dimensions of FPZ. This study shows that the distribution of signals is closely related to the energy levels, too. In DEM, we define that the width of FPZ equals to one average grain size for one individual micro-scale event. Then at a specific time-step, we divide the total length of the micro-events cloud into several buckets. The width of FPZ in each bucket is determined accordingly and then averaged to estimate the overall width of FPZ. The results are summarized in Figure A.14. The width of FPZ is determined based on all the micro-scale events that has a energy level higher than a specific value. When the specific energy level is low, the width is as high as about 15 mm, i.e. about 6$\sim$7 times of the average grain diameter. However, if the energy level is high, the width of FPZ is about 2 mm, representing a single crack that involves only two grains. We can also see that the width of FPZ is discretized based on different energy levels. If we use E_1 and E_2 as critical

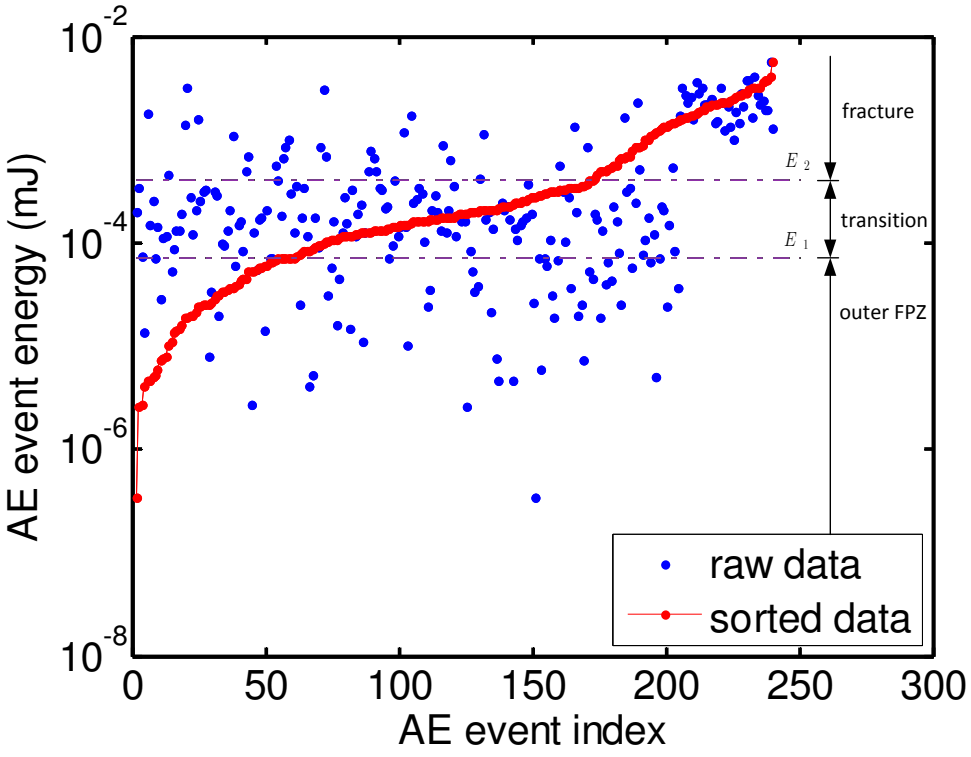

(a) micro-event energy levels

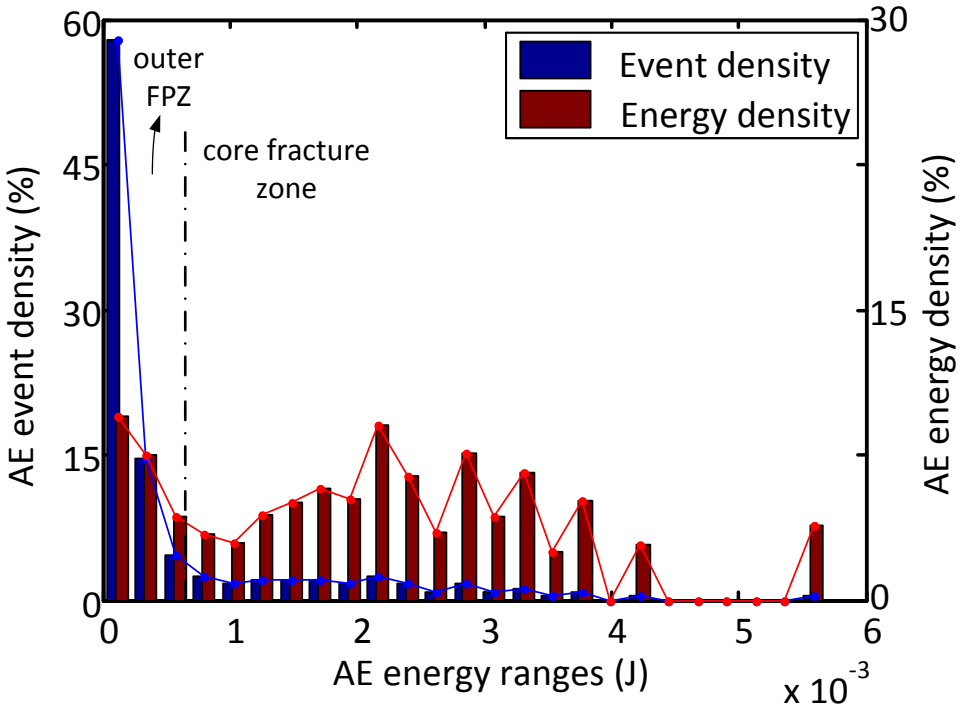

(b) micro-event and energy density

Figure A.12: Micro-event energy at final stage.

energy levels, the dimension of FPZ can be divided into three regions. In low energy region, the size represents the outer FPZ width, while the high energy represent the core fracture. The FPZ is located between these two regions. Therefore, the width of the FPZ is about 11 mm.

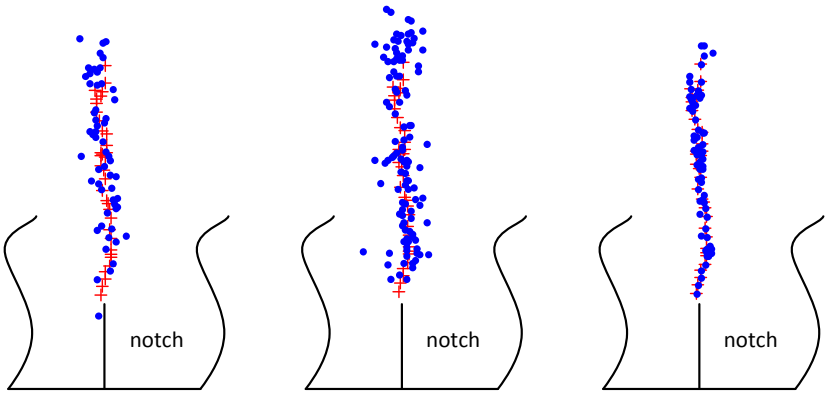

(a) low energy (b) intermediate energy (c) high energy

Figure A.13: AE locations at different energy levels.

The histogram in Figure A.15 shows the AE events and energy distribution along the mid-span depth of the specimen, and reflects the whole process of fracture initiation and propagation. Both number of events and energy dissipated near the notch tip increase consistently as FPZ grows. As the load continues increasing, the histogram shows a zigzag pattern, and the variation of energies clearly follows the trend of AE events occurrence until the end. As mentioned previously, the variation is caused by the stepwise pattern of fracture growth, see Figure A.9. However, many researchers [87] have noticed that in laboratory AE tests, the number of events occurrence remains constant for a certain distance along the ligament length. The possible explanations are: in real experiments, the resolution of data obtaining system is not high enough to acquire high frequency AE signals in post-peak stage; and the fracture propagation process is so fast that the loading equipment cannot precisely accommodate. On the other hand, the loading speed and time steps are optimized in this numerical simulation to capture the post-peak behaviors of the fracture, which indicates that the fracture, as well as the FPZ, grows in a stepwise pattern.

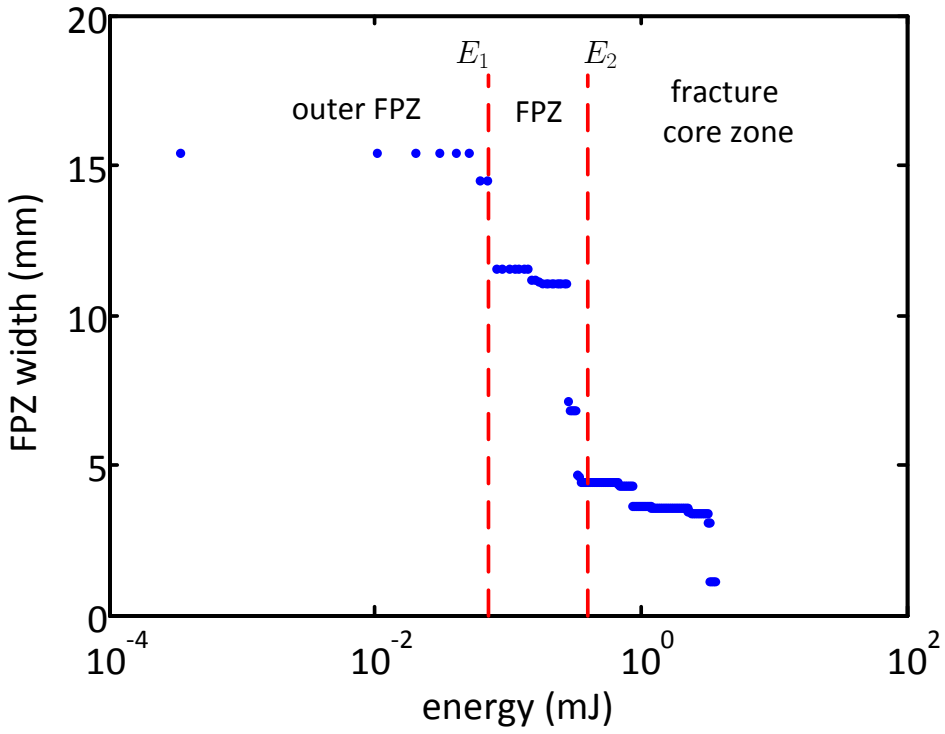

Figure A.14: FPZ width at different energy levels

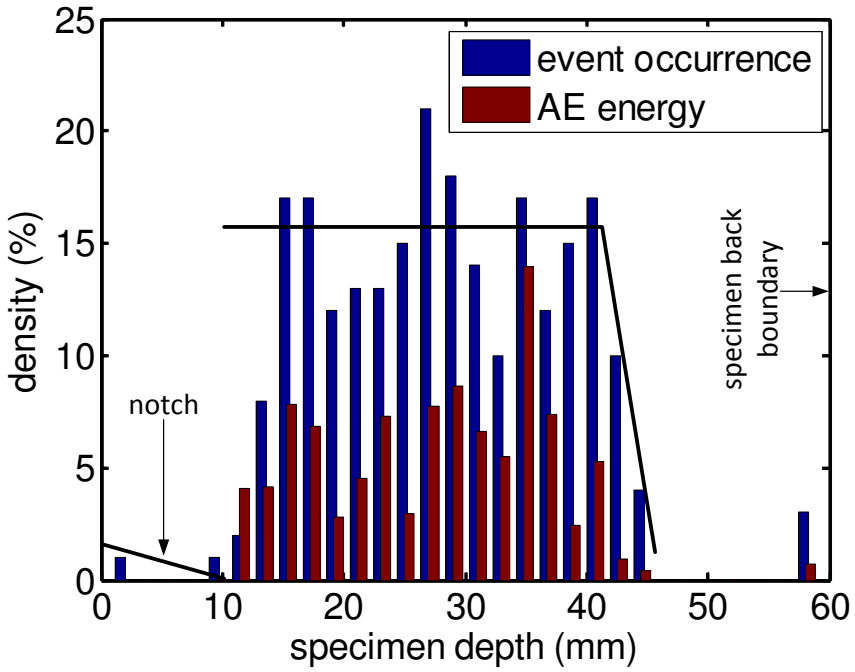

Figure A.15: AE events density and energy levels along mid-span.

During the simulation, FPZ width and length are determined on statistical basis. At

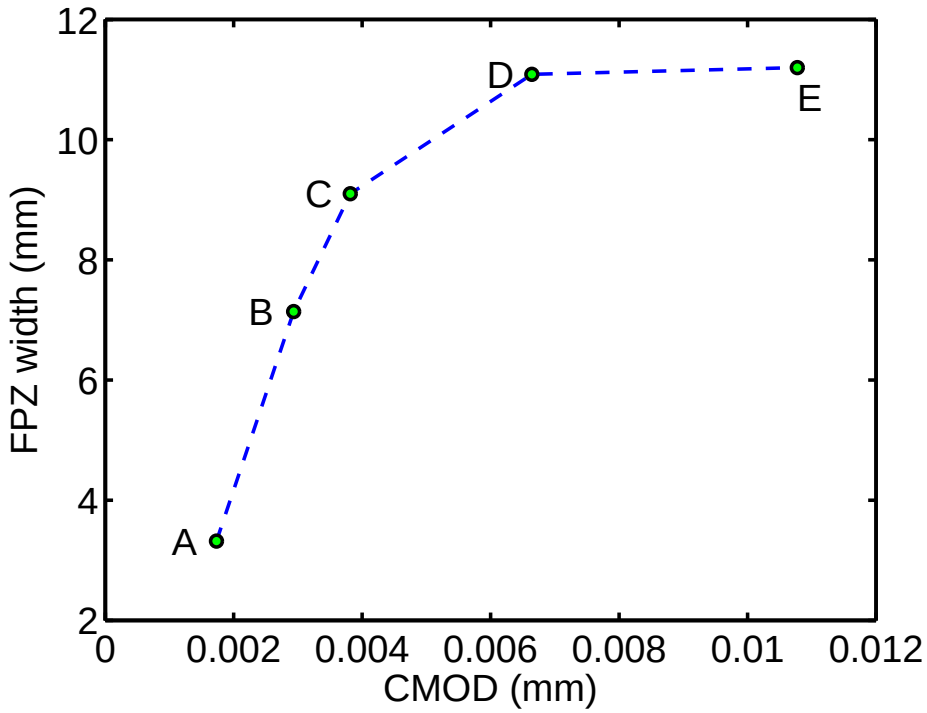

Figure A.16: FPZ dimensions

each stage, the FPZ area is determined by including all AE events having energy range between E_1 and E_2, and then the width are measured accordingly, see Figure A.16. Before fracture propagation happens (stage C), the FPZ width is monotonically increasing. As the fracture propagates, the width becomes roughly a constant, which is also shown in Figure A.11.

A.4.3 Discussion

According to the Griffith theory, a crack could propagate when the critical strength is reached at the tip. From energy point of view, the amount of energy required for crack propagation equals to the strain energy released when crack extends. The strain energy release rate, G_I, is defined as the derivative of crack energy, U_c, with respect to crack area, A_c, as shown in Eq. 44.

$$G_I = \frac{\mathrm{d}U_c}{\mathrm{d}A_c} = \frac{\mathrm{d}(U_t - U_s)}{\mathrm{d}A_c} \tag{44}$$

where U_c is defined as

$$U_c = U_t - U_s \tag{45}$$

where U_t is total work done by the load bearing stripes and U_s is the strain energy stored in the point contact and bond before it breaks. A_c is defined as the accumulative crack area (length in 2D) that can be calculated based on the following equation:

$$A_c = \begin{cases} \pi\lambda^2 \sum_{i=1}^{N_c} \min(R_i^{(1)},\ R_i^{(2)})^2 & \text{3D} \\ 2\lambda \sum_{i=1}^{N_c} \min(R_i^{(1)},\ R_i^{(2)}) & \text{2D} \end{cases} \tag{46}$$

where N_c is the total number of breaking bonds, λ is bond radius multiplier, $R_i^{(1)}$ and $R_i^{(2)}$ are the radius of grains at two ends of the ith bond, respectively.

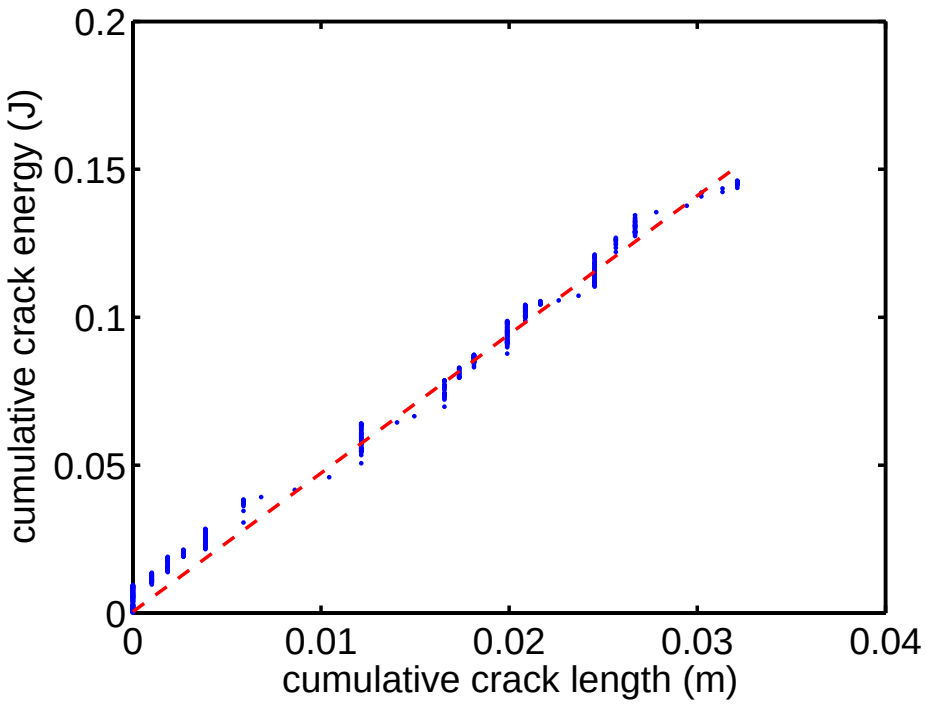

Figure A.17: Cumulative crack energy vs. crack length

Figure A.17 shows the relationship between cumulative crack energy and crack length. The slope of the curve is equivalent to G_{IC}:

$$G_{IC} = 4.68\,\text{N·m/m}^2 \tag{47}$$

According to linear elastic fracture mechanics, the correlation between critical energy release rate and fracture toughness is stated as follow:

$$K_{IC} = \sqrt{EG_{IC}} = 0.49\,\text{MPa}\sqrt{\text{m}} \tag{48}$$

where E is elastic modulus. Given that:

$$K_{IC} = \sigma_t \sqrt{\pi a} \tag{49}$$

where σ_t is uniaxial tensile strength and a is intrinsic length scale. We can estimate $a \simeq 9$ mm, a consistent number compared to the FPZ width, $w \simeq 11$ mm, when fracture grows.

A.5 Three-point Bending with Eccentric Notch

Three-point bending tests performed on numerical samples with an eccentric notch is a common approach that used for studying mixed-mode fracture. At the notch tip, a different combination of normal and shear stress can be achieved from the applied load by changing the notch position along the bottom of the beam. Thus, the mixed-mode crack can be obtained from this relatively simple loading configuration, as shown in Figure A.18. The geometry and position of the notch are quantified by parameters $\eta = \dfrac{d}{H}$ and $\zeta = \dfrac{s}{L/2}$, respectively. The size of the specimen is: span $L = 146.8$ mm, height $H = 60$ mm, thickness $T = 26$ mm, notch width $w = 4$ mm, and notch length $d = 6$ mm.

It is shown that the failure mechanism is not only highly dependent of these geometric parameters, but also closely related to the load velocity. Since the dynamic effect will cause a different pattern of damage initiation and propagation, in the following simulations, the loading velocity is adjusted after each cycle to make sure that the total force applied to the top of the beam is within a tolerance compared to the total reaction forces on the supports.

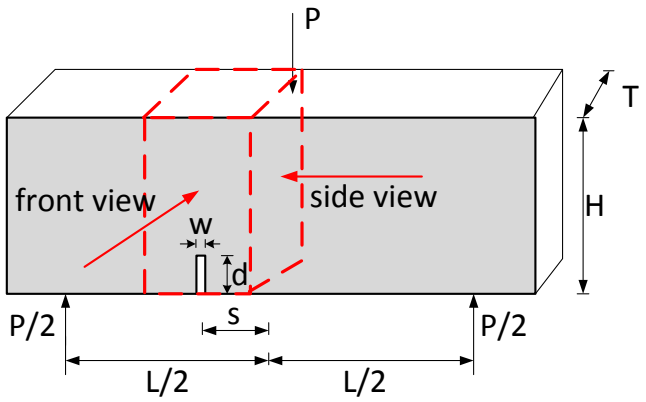

Figure A.18: Three-point bending test with an eccentric notch.

Three groups of specimen are examined with different geometric parameters. (1) Group 1: $\eta = 0.1$, and $\zeta = 0.33$; (2) Group 2: $\eta = 0.2$, and $\zeta = 0.33$; (3) Group 3: $\eta = 0.2$, and $\zeta = 0.66$;

The force on top of the beam is applied using a cylindrical wall and a small initial overlap is allowed. During the loading process for group 1, three stages are clearly identified from the force-displacement curve. At the beginning, the beam deforms elastically and the curve is a straight line without oscillations, see Figure A.19. At stage b, both local tensile and shear cracks started to appear at the loading point, and the support as well, causing the oscillations on the force-displacement curve. The first significant drop is associated to the localization of shear cracks at the loading point on top of the beam. A plastic zone forms and grows while increasing the load. The next sudden drop, however, is resulted from the development of the mixed-mode fracture, as shown in Figure A.20(a). The numerical results are post-processed by illustrating a micro-crack, namely, a broken parallel bond, using a filled circle, drawn perpendicular to the contact axis with the size equal to the mean diameter of the two particles previously in contact.

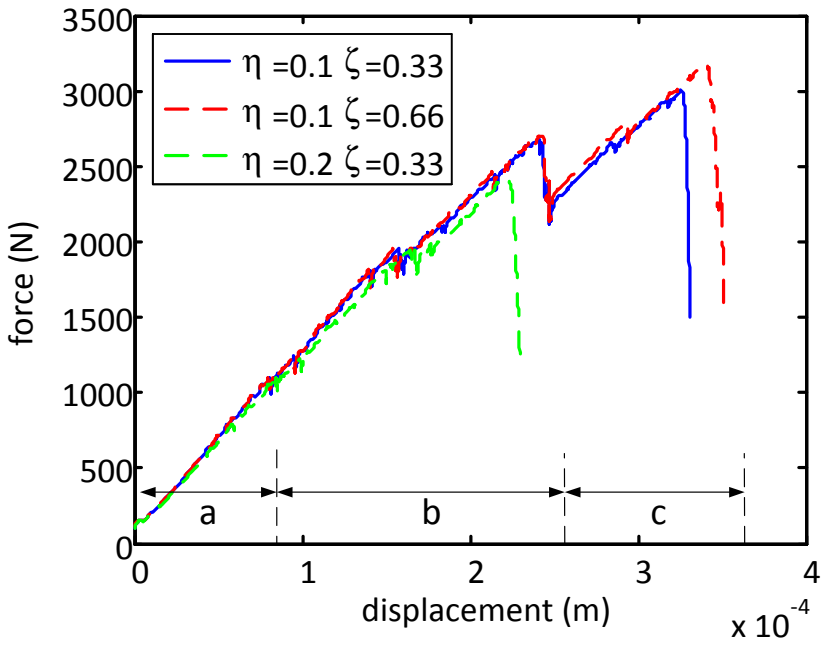

Figure A.19: Three-point bending test with an eccentric notch.

Mixed-mode loading configuration creates a non-symmetric pattern of deformation, which causes a combination of mode I and mode II failure mechanism, as shown in Figure A.20(b). Both shear and tensile cracks are observed at the fracture path (red and blue filled circles), combined with a softening zone (green filled circles) surrounding the main fracture. The length of the process zone is hard to estimate, because the evolution of the mixed-mode fracture is too fast than that in mode I. In Figure A.20 (c), the color of the micro-cracks represents the time sequence when they are generated. Blue means the micro-cracks are generated earlier while red means later. The sequence of the micro-crack events can therefore be inferred from the color bar. As it shows, the plastic zone at the loading point developed in a stable manner as it grows with increasing load. Meanwhile, the mixed-mode fracture propagates in an unstable way that it grows towards the loading point in a very short period of time. Thus, unlike in three-point bending test with a center notch, the process zone length in mixed-mode fracture cannot be accurately estimated. Nevertheless, the width of the process zone, approximately $3 \sim 5$ grain size, keeps a constant during the whole process.

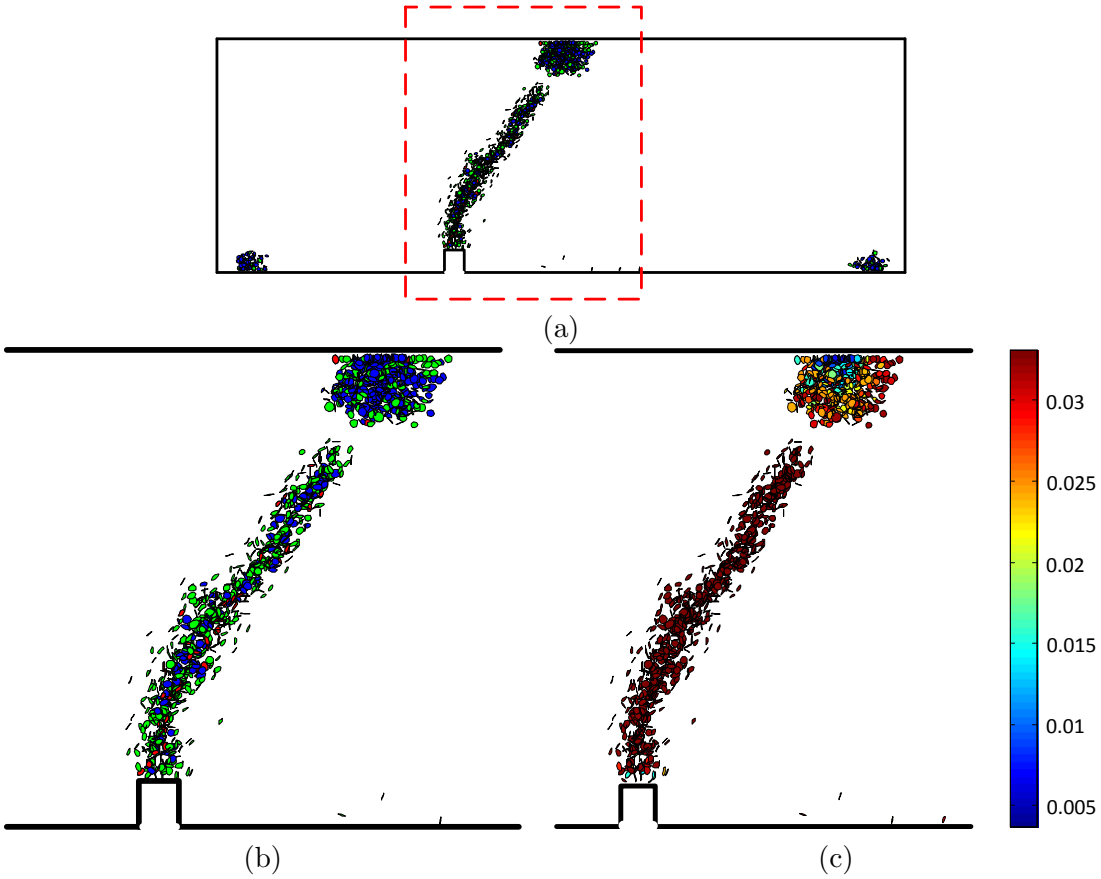

Figure A.20: Crack pattern in post-peak stage: (a) crack distribution in the whole specimen; (b) crack types in the fracture, red: tensile failure, blue: shear failure, green: softening bond; (c) crack age when it is generated.

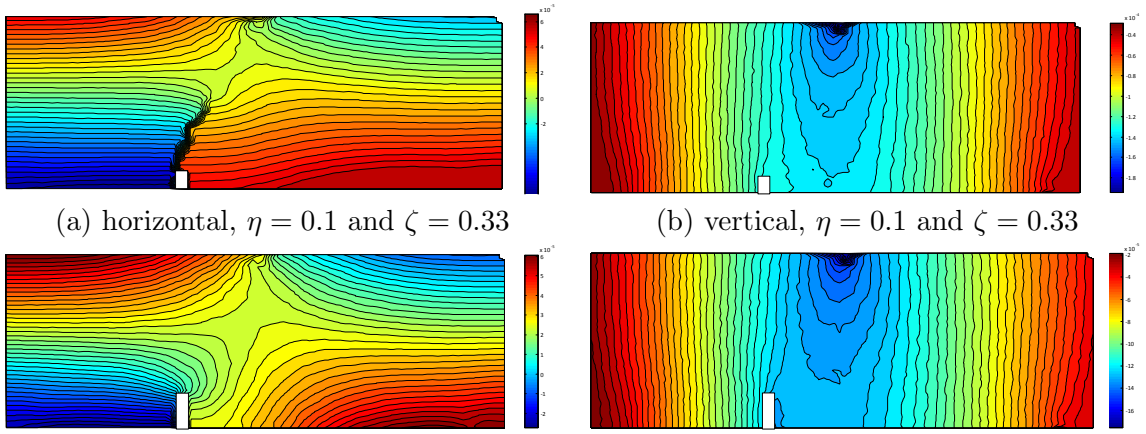

(a) horizontal, $\eta = 0.1$ and $\zeta = 0.33$

(b) vertical, $\eta = 0.1$ and $\zeta = 0.33$

(c) horizontal, $\eta = 0.2$ and $\zeta = 0.33$

(d) vertical, $\eta = 0.2$ and $\zeta = 0.33$

Figure A.21: Displacement fields at peak.

For group 2, the failure mechanism remains the same as in group 1, but total lose of the strength happens earlier, as shown in Figure A.19. The horizontal displacement field shows that the contour lines tend to converge at the crack tip, as shown in Figure A.21(a). According to the numerical results, the zero horizontal displacement is somewhere near the center of the fracture. As the fracture grows upwards, the neutral axis of the beam moves upward as well, which could be tracked by monitoring the zero horizontal displacement contour line. Because of the eccentric notch, the horizontal displacement field is twisted leftwards, instead of being symmetric as in center notch case. Meanwhile, the vertical displacement field is more or less symmetric, despite being distorted by the notch near the tip.

When the notch length increases to 12 mm, in other words, $\alpha = 0.2$, the vertical displacement field is not influenced very much. However, at about 85%∼90% of the peak, the mixed-mode fracture cannot be obtained, except a small region ahead of the crack tip exhibits the characteristics of FPZ. In Figure A.21(c), the zero horizontal displacement line is located somewhere next to the notch, close to the center of the beam, indicating the existence of a process zone.

As the load increases to post-peak stage, a displacement discontinuity is observed from the displacement fields, as shown in Figure A.22. The length of the notch does not make much difference in the displacement field at this stage. The beam fails when the mixed-mode

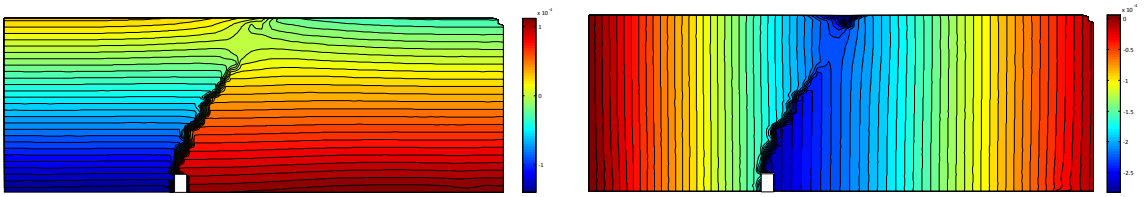

(a) horizontal, $\eta = 0.1$ and $\zeta = 0.33$ (b) vertical, $\eta = 0.1$ and $\zeta = 0.33$

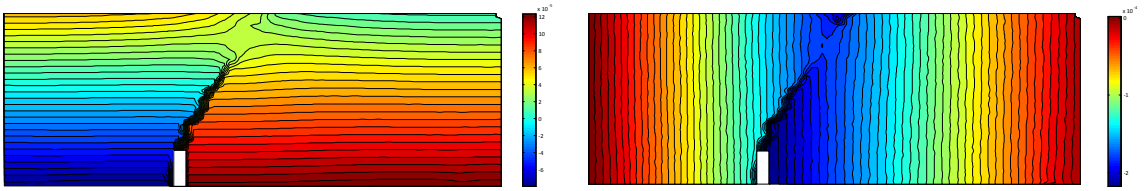

(c) horizontal, $\eta = 0.2$ and $\zeta = 0.33$ (d) vertical, $\eta = 0.2$ and $\zeta = 0.33$

Figure A.22: Displacement fields at post-peak.

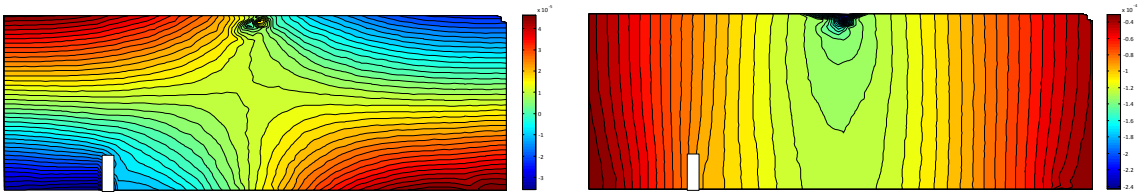

(a) horizontal, $\eta = 0.2$ and $\zeta = 0.66$ (b) vertical, $\eta = 0.2$ and $\zeta = 0.66$

Figure A.23: Displacement fields at post-peak.

fracture coalescence with the plastic zone under the loading point.

In group 3, the notch is moved away from the bottom center of the beam, and located at 66% of the half span. When the beam fails, no clear process zone is formed near the notch tip or midspan; instead, it fails due to the local plastic deformation under the loading point, as indicated by Figure A.23. However, the presence of the notch causes more horizontal displacement on the left. In the meantime, the zero displacement horizontal contour line is located in the center of the beam, implying that the first process zone is most likely to initiate in the midspan, rather than the notch tip.

A.6 Conclusion

In this study, a three point bending test with a central and eccentric notch is modeled using both the 2D and 3D discrete element method with a softening contact law. The numerical analysis is capable of reproducing many characteristics of quasi-brittle material in the form of acoustic emission signals that have been observed in experiments, e.g., the AE energy

pattern, and histogram along specimen mid-span depth. Though, the resolution of AE results is dependent on grain size; in this study, the dependency is reduced by introducing a refined zone in the middle of the specimen without sacrificing computational efficiency. Meanwhile, the bond strength across the whole sample is simplified as a constant to reduce the random nature of the particle assembly. The reason not to introduce random bond strength into the model is to find out the intrinsic characteristic of the material and the overall fracture process, as well as the FPZ size. A detailed fracture propagation process is described, furthermore, supported by the simulation results.

The numerical model proposed in this paper is capable of reproducing characteristic behaviors of quasi-brittle material, including the FPZ growth and crack initiation and propagation. The acoustic emission signals simulated using the softening model are comparable with experimental results. For example, the first continuous production of AE events happen at 70% of peak load, which is close to the result reported in [87]. However, the absolute number of AE event occurrence is too low due to limitations of grain size resolution. But the relative density at different energy levels shows good consistency with laboratory tests. The magnitude of AE energy is calculated based on the energy dissipated from softening bonds. Because of the two dimensional nature of the numerical model, the results are only meaningful when compared qualitatively to experiments. So the magnitude of energy at each individual AE events shows that 70.83% low and intermediate energy AE events take only 15.85% of the total energy, while 29.17% high AE events take up to 84.15% of total energy. Zones of low energy events consists of localized micro-cracks around the notch tip, and the locations of high energy events indicate where the fracture path is. Based on the ratio of softening to crack events, the results suggest that the FPZ, as well as the macro fracture, creeps as the load increases. This conclusion is corroborated by the histogram of AE events along the mid-span of the specimen, as consistent with experimental results reported in [87].

The energy magnitude gradient clearly identifies the FPZ and the inner core of the fracture. Using AE energy levels as a criterion allows us to measure the FPZ size. The softening model proposed in this study, combined with the process zone model, is valid

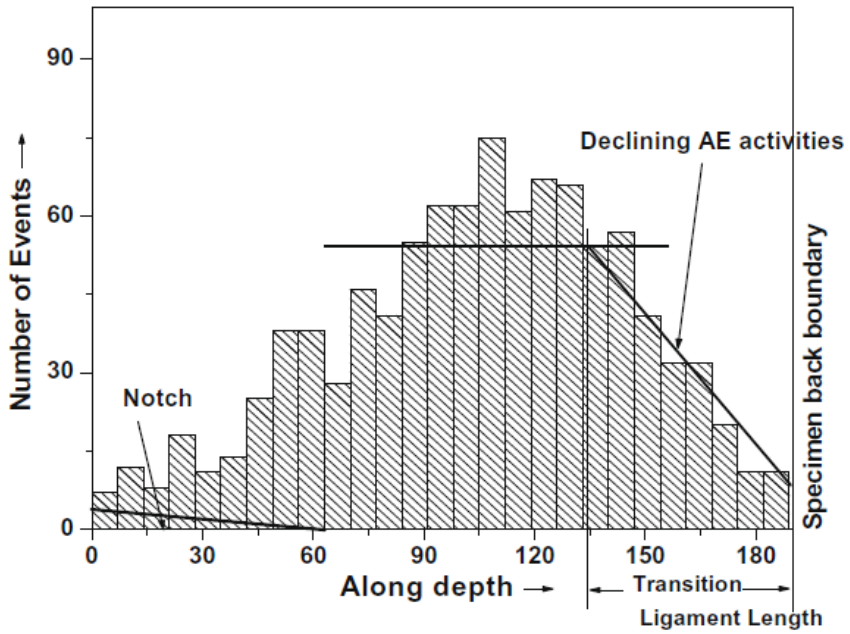

Figure A.24: Number of micro-events along mid-span [87].

in simulating mode I and mixed-mode fracturing. The mode I fracture is obtained by performing three-point bending test with a center notch. During the loading process, the process zone boundary is clearly identified by monitoring the distribution of damaged bonds. The average process zone width is about $4 \sim 9$ average grain size; on the other hand, the process zone length only remains constant at peak and post-peak stages. Besides, the crack tip and the damage zone can be visualized by examining the displacement field. The parallel contour lines in the center of the sample indicates a displacement discontinuity, stemmed from the presence of a fracture. At the crack tip, the contour lines have a trend to converge at a point, which proves the existence of a damage zone. Moreover, the region that consists of the gradually converging contour lines is the process zone. Since how the geometries of the notch can influence the process zone was not clear before, so in this study, the effect of notch sizes on FPZ size is investigated. Based on the simulation results, the process zone width remains more or less constant at the peak. Consequently, we believe that the notch geometry plays a role similar to a stress concentrator, which is important during the crack initiation stage, but when the crack starts to grow, it does not have much impact to the behavior of the FPZ.

In order to capture the essence of mixed-mode fracturing, three groups of three-point bending test with an eccentric notch are carried out. First, the notch is implemented at different positions along the bottom of the beam. When it is at 33% of the half span, the displacement field is distorted because of the notch and is no longer symmetric. The zero displacement contour line is located somewhere close to the fracture center, and on top of the notch, the contour lines are parallel to each other, indicating a displacement discontinuity. The simulation results also prove that the failure mechanism is not affected by the geometry of the notch, except fracture initiation and propagation happens earlier. In the post-peak stage, all cases yield a similar result that the vertical displacement at the bottom of the fracture is increasing enormously caused by the sliding on both sides of the fracture.

Interestingly, when the notch is placed at 66% of the half span, no mixed-mode fracture is observed. Instead, the process zone is developed at the bottom mid-span. More horizontal displacement is observed on the left of the notch, which is not significant enough to initiate the crack at the notch tip. As the load increases, the beam fails due to the presence of localized plastic zone. In mixed-mode fracturing, the length of the process zone is not a constant. From the observation, the fracture develops in an unstable manner. As such, only the width of the process zone could be identified as a constant.

REFERENCES

[1] Ai, J., Chen, J.-F., Rotter, J. M., and Ooi, J. Y., "Assessment of rolling resistance models in discrete element simulations," *Powder Technology*, vol. 206, no. 3, pp. 269–282, 2011.

[2] Akono, A.-T., *Scratch tests: a new way of evaluating the fracture toughness of materials.* PhD thesis, Department of civil and environmental engineering, massachusetts institute of technology, 2011.

[3] Akono, A.-T. and Ulm, F.-J., "Scratch test model for the determination of fracture toughness," *Engineering Fracture Mechanics*, vol. 78, no. 2, pp. 334–342, 2011.

[4] Akono, A., Reis, P., and Ulm, F., "Scratching as a fracture process: From butter to steel," *Physical review letters*, vol. 106, no. 20, p. 204302, 2011.

[5] Andreev, G., "A review of the brazilian test for rock tensile strength determination. part i: calculation formula," *Mining Science and Technology*, vol. 13, no. 3, pp. 445–456, 1991.

[6] Andreev, G., "A review of the brazilian test for rock tensile strength determination. part ii: contact conditions," *Mining Science and Technology*, vol. 13, no. 3, pp. 457–465, 1991.

[7] Ashby, M. F. and others, "The failure of brittle solids containing small cracks under compressive stress states," *Acta Metallurgica*, vol. 34, no. 3, pp. 497–510, 1986.

[8] ASTM, "D3967. standard test method for splitting tensile strength of intact rock core specimens," *Annual Book of ASTM Standards, American Society for Testing and Materials, West Conshohocken, PA*, 1995.

[9] Bard, R. and Ulm, F.-J., "Scratch hardness–strength solutions for cohesive-frictional materials," *International Journal for Numerical and Analytical Methods in Geomechanics*, vol. 36, no. 3, pp. 307–326, 2012.

[10] Bažant, Z. P., "Size effect in blunt fracture: concrete, rock, metal," *Journal of Engineering Mechanics*, 1984.

[11] Bažant, Z. P., "Size effect on structural strength: a review," *Archive of applied Mechanics*, vol. 69, no. 9-10, pp. 703–725, 1999.

[12] Bažant, Z. P., *Scaling of structural strength*. Butterworth-Heinemann, 2005.

[13] Bazant, Z. P., Kazemi, M. T., Hasegawa, T., and Mazars, J., "Size effect in brazilian split-cylinder tests: measurements and fracture analysis," *ACI Materials Journal*, vol. 88, no. 3, pp. 325–332, 1991.

[14] Bazant, Z. P. and Kim, J.-K., "Size effect in shear failure of longitudinally reinforced beams," *ACI Journal*, vol. 81, no. 5, pp. 456–468, 1984.

[15] Bažant, Z. and Pfeiffer, P., "Shear fracture tests of concrete," *Materials and Structures*, vol. 19, no. 2, pp. 111–121, 1986.

[16] Blair, S. C. and others, "Statistical model for rock fracture," in *The 33th US Symposium on Rock Mechanics (USRMS)*, American Rock Mechanics Association, 1992.

[17] Bobet, A. and Einstein, H., "Fracture coalescence in rock-type materials under uniaxial and biaxial compression," *International Journal of Rock Mechanics and Mining Sciences*, vol. 35, no. 7, pp. 863–888, 1998.

[18] Bobich, J. K., "Experimental analysis of the extension to shear fracture transition in berea sandstone," Master's thesis, Texas A&M University, 2005.

[19] Bourchak, M., Farrow, I., Bond, I., Rowland, C., and Menan, F., "Acoustic emission energy as a fatigue damage parameter for cfrp composites," *International Journal of Fatigue*, vol. 29, no. 3, pp. 457–470, 2007.

[20] Brace, W. F., *Brittle fracture of rocks*. Massachusetts Institute of Technology, Industrial Liaison Program, 1963.

[21] Broch, E. and Franklin, J., "The point-load strength test," in *International Journal of Rock Mechanics and Mining Sciences & Geomechanics Abstracts*, vol. 9, pp. 669–676, Elsevier, 1972.

[22] Caley, E. R. and Richards, J. F., "Theophrastus on stones: Introduction, greek text, english translation, and commentary," 1956.

[23] Carpinteri, A., Chiaia, B., and Ferro, G., "Size effects on nominal tensile strength of concrete structures: multifractality of material ligaments and dimensional transition from order to disorder," *Materials and Structures*, vol. 28, no. 6, pp. 311–317, 1995.

[24] Chen, L. and Labuz, J., "Indentation of rock by wedge-shaped tools," *International Journal of Rock Mechanics and Mining Sciences*, vol. 43, no. 7, pp. 1023–1033, 2006.

[25] Chen, W. F. and Yuan, R. L., "Tensile strength of concrete: double-punch test," *Journal of the Structural Division*, vol. 106, no. 8, pp. 1673–1693, 1980.

[26] Cho, N., Martin, C., and Sego, D., "A clumped particle model for rock," *International Journal of Rock Mechanics and Mining Sciences*, vol. 44, Oct. 2007.

[27] Colback, P. and others, "An analysis of brittle fracture initiation and propagation in the brazilian test," in *1st ISRM Congress*, International Society for Rock Mechanics, 1966.

[28] Colombo, I. S., Main, I., and Forde, M., "Assessing damage of reinforced concrete beam using "b-value" analysis of acoustic emission signals," *Journal of materials in civil engineering*, vol. 15, no. 3, pp. 280–286, 2003.

[29] Coviello, A., Lagioia, R., and Nova, R., "On the measurement of the tensile strength of soft rocks," *Rock Mechanics and Rock Engineering*, vol. 38, no. 4, pp. 251–273, 2005.

[30] Cox, S. and Meredith, P., "Microcrack formation and material softening in rock measured by monitoring acoustic emissions," in *International journal of rock mechanics and mining sciences & geomechanics abstracts*, vol. 30, pp. 11–24, Elsevier, 1993.

[31] Cundall, P., "A computer model for simulating progressive large movements in blocky rock systems," *Proceedings of the Symposium of the International Society of Rock Mechanics*, vol. 1, 1971.

[32] Cundall, P. A. and Strack, O. D., "A discrete numerical model for granular assemblies," *Geotechnique*, vol. 29, no. 1, pp. 47–65, 1979.

[33] Dagrain, F., Detournay, E., and Richard, T., "Influence of the cutter geometry in rock cutting," in *Proceedings of the Rock mechanics in the national interest*, pp. 927–934, 2001.

[34] Deisman, N., Mas Ivars, D., and Pierce, M., "Pfc2d smooth joint contact model numerical experiments," *Proceedings of the GeoEdmonton*, vol. 8, 2008.

[35] Detournay, E. and Defourny, P., "A phenomenological model for the drilling action of drag bits," in *International journal of rock mechanics and mining sciences & geomechanics abstracts*, vol. 29, pp. 13–23, Elsevier, 1992.

[36] Diederichs, M. S., *Instability of hard rockmasses: the role of tensile damage and relaxation*. PhD thesis, 1999.

[37] Diederichs, M., "Manuel rocha medal recipient rock fracture and collapse under low confinement conditions," *Rock Mechanics and Rock Engineering*, vol. 36, no. 5, pp. 339–381, 2003.

[38] Efimov, V., "The rock strength in different tension conditions," *Journal of mining science*, vol. 45, no. 6, pp. 569–575, 2009.

[39] Evans, B., Saeedi, A., Rasouli, V., Liu, K., and Lebedev, M., "Predicting co2 injectivity properties for application at ccs sites," *A report to ANLEC, Project Number 3-1110*, vol. 122, p. 83pp, 2012.

[40] Fairhurst, C., "On the validity of the brazilian test for brittle materials," in *International Journal of Rock Mechanics and Mining Sciences & Geomechanics Abstracts*, vol. 1, pp. 535–546, Elsevier, 1964.

[41] Fairhurst, C. and Cook, N., "The phenomenon of rock splitting parallel to the direction of maximum compression in the neighborhood of a surface," in *Proceedings of the first congress on the international society of rock mechanics*, vol. 1, pp. 687–692, 1966.

[42] Fakhimi, A. and Tarokh, A., "Process zone and size effect in fracture testing of rock," *International Journal of Rock Mechanics and Mining Sciences*, vol. 60, pp. 95–102, 2013.

[43] Fuenkajorn, K. and Klanphumeesri, S., "Laboratory determination of direct tensile strength and deformability of intact rocks," 2010.

[44] Hakala, M. and Heikkilä, E., "Summary report-development of laboratory tests and the stress-strain behaviour of olkiluoto mica gneiss," tech. rep., Posiva Oy, 1997.

[45] Hanks, T. C. and Kanamori, H., "A moment magnitude scale," *Journal of Geophysical Research B*, vol. 84, no. B5, pp. 2348–2350, 1979.

[46] Hardy, H. and Jayaraman, N., "An investigation of methods for the determination of the tensile strength of rock," tech. rep., 1970.

[47] Hasegawa, T., Shioya, T., and Okada, T., "Size effect on splitting tensile strength of concrete," in *Proceedings Japan Concrete Institute 7th Conference*, pp. 309–312, 1985.

[48] Hazzard, J. F. and Young, R. P., "Moment tensors and micromechanical models," *Tectonophysics*, vol. 356, no. 1, pp. 181–197, 2002.

[49] Hazzard, J. F., Young, R. P., and Maxwell, S., "Micromechanical modeling of cracking and failure in brittle rocks," *Journal of Geophysical Research: Solid Earth (1978–2012)*, vol. 105, no. B7, pp. 16683–16697, 2000.

[50] Hazzard, J., Maxwell, S., Young, R., and others, "Micromechanical modelling of acoustic emissions," in *SPE/ISRM Rock Mechanics in Petroleum Engineering*, Society of Petroleum Engineers, 1998.

[51] Hazzard, J. and Young, R., "Simulating acoustic emissions in bonded-particle models of rock," *International Journal of Rock Mechanics and Mining Sciences*, vol. 37, no. 5, pp. 867–872, 2000.

[52] Hobbs, D., "The tensile strength of rocks," in *International Journal of Rock Mechanics and Mining Sciences & Geomechanics Abstracts*, vol. 1, pp. 385–396, Elsevier, 1964.

[53] Hoek, E. and Martin, C., "Fracture initiation and propagation in intact rock–a review," *Journal of Rock Mechanics and Geotechnical Engineering*, vol. 6, no. 4, pp. 287–300, 2014.

[54] Hoek, E. and Bieniawski, Z., "Brittle fracture propagation in rock under compression," *International Journal of Fracture Mechanics*, vol. 1, no. 3, pp. 137–155, 1965.

[55] Hoek, E., Carranza-Torres, C., and Corkum, B., "Hoek-brown failure criterion-2002 edition," *Proceedings of NARMS-Tac*, pp. 267–273, 2002.

[56] Hondros, G., "The evaluation of poisson¡¯s ratio and the modulus of materials of a low tensile resistance by the brazilian (indirect tensile) test with particular reference to concrete," *Aust J Appl Sci*, vol. 10, no. 3, pp. 243–268, 1959.

[57] Horsrud, P., Sønstebø, E., and Bøe, R., "Mechanical and petrophysical properties of north sea shales," *International Journal of Rock Mechanics and Mining Sciences*, vol. 35, no. 8, pp. 1009–1020, 1998.

[58] Hu, X.-Z. and Wittmann, F., "Fracture energy and fracture process zone," *Materials and Structures*, vol. 25, no. 6, pp. 319–326, 1992.

[59] Huang, H., Lecampion, B., and Detournay, E., "Discrete element modeling of tool-rock interaction i: rock cutting," *International Journal for Numerical and Analytical Methods in Geomechanics*, 2012.

[60] Huang, H., *Discrete Element Modeling of Tool-Rock Interaction*. PhD thesis, UNIVERSITY OF MINNESOTA, 1999.

[61] Huang, H. and Detournay, E., "Intrinsic length scales in tool-rock interaction 1," *International Journal of Geomechanics*, vol. 8, no. 1, pp. 39–44, 2008.

[62] Huang, H. and Detournay, E., "Discrete element modeling of tool-rock interaction ii: rock indentation," *International Journal for Numerical and Analytical Methods in Geomechanics*, 2012.

[63] Hudson, J., Brown, E., and Rummel, F., "The controlled failure of rock discs and rings loaded in diametral compression," in *International Journal of Rock Mechanics and Mining Sciences & Geomechanics Abstracts*, vol. 9, pp. 241IN1245–244IN4248, Elsevier, 1972.

[64] ISRM, "Suggested methods for determining tensile strength of rock materials," *International Journal of Rock Mechanics and Mining Sciences & Geomechanics Abstracts*, vol. 15, no. 3, pp. 99 – 103, 1978.

[65] Jaeger, J., "Failure of rocks under tensile conditions," in *International Journal of Rock Mechanics and Mining Sciences & Geomechanics Abstracts*, vol. 4, pp. 219–227, Elsevier, 1967.

[66] Kemeny, J. M. and Cook, N. G., "Crack models for the failure of rocks in compression," tech. rep., Lawrence Berkeley Lab., CA (USA), 1986.

[67] Kim, J.-K., "Size effect in concrete specimens with dissimilar initial cracks," *Magazine of Concrete Research*, vol. 42, no. 153, pp. 233–238, 1990.

[68] Labuz, J. and Biolzi, L., "Characteristic strength of quasi-brittle materials," *International journal of solids and structures*, vol. 35, no. 31, pp. 4191–4203, 1998.

[69] Labuz, J. F., Cattaneo, S., and Chen, L.-H., "Acoustic emission at failure in quasi-brittle materials," *Construction and building Materials*, vol. 15, no. 5, pp. 225–233, 2001.

[70] Lama, R. and Vutukuri, V., *Handbook on Mechanical Properties of Rocks: Testing Techniques and Results, Vol. II*, vol. 3. Trans Tech, 1978.

[71] Lavrov, A., Vervoort, A., Wevers, M., and Napier, J., "Experimental and numerical study of the kaiser effect in cyclic brazilian tests with disk rotation," *International journal of rock mechanics and mining sciences*, vol. 39, no. 3, pp. 287–302, 2002.

[72] Li, D. and Wong, L. N. Y., "The brazilian disc test for rock mechanics applications: review and new insights," *Rock mechanics and rock engineering*, vol. 46, no. 2, pp. 269–287, 2013.

[73] Lin, Q., Fakhimi, A., Haggerty, M., and Labuz, J., "Initiation of tensile and mixed-mode fracture in sandstone," *International Journal of Rock Mechanics and Mining Sciences*, vol. 46, no. 3, pp. 489–497, 2009.

[74] Lin, Q., *Identification of Rock Fracture by Imaging Techniques.* PhD thesis, UNIVERSITY OF MINNESOTA, 2010.

[75] Lin, Q. and Labuz, J. F., "Identifying quasi-brittle fracture by ae and digital imaging," *J. Acoustic Emission*, pp. 68–77, 2011.

[76] Lin, Q. and Labuz, J. F., "Fracture of sandstone characterized by digital image correlation," *International Journal of Rock Mechanics and Mining Sciences*, vol. 60, pp. 235–245, 2013.

[77] Lockner, D., "The role of acoustic emission in the study of rock fracture," in *International Journal of Rock Mechanics and Mining Sciences & Geomechanics Abstracts*, vol. 30, pp. 883–899, Elsevier, 1993.

[78] Lundborg, N., "The strength-size relation of granite," in *International Journal of Rock Mechanics and Mining Sciences & Geomechanics Abstracts*, vol. 4, pp. 269–272, Elsevier, 1967.

[79] Maji, A. and Shah, S., "Process zone and acoustic-emission measurements in concrete," *Experimental mechanics*, vol. 28, no. 1, pp. 27–33, 1988.

[80] Malan, D. and Napier, J., "Computer modelling of granular material microfracturing," *Tectonophysics*, vol. 248, no. 1, pp. 21–37, 1995.

[81] Mandelbrot, B. B. and Van Ness, J. W., "Fractional brownian motions, fractional noises and applications," *SIAM review*, vol. 10, no. 4, pp. 422–437, 1968.

[82] Martin, C. and Chandler, N., "The progressive fracture of lac du bonnet granite," in *International Journal of Rock Mechanics and Mining Sciences & Geomechanics Abstracts*, vol. 31, pp. 643–659, Elsevier, 1994.

[83] Martin, C. D., *The strength of massive Lac du Bonnet granite around underground openings*. PhD thesis, University of Manitoba Manitoba, 1993.

[84] Martino, J. and Chandler, N., "Excavation-induced damage studies at the underground research laboratory," *International Journal of Rock Mechanics and Mining Sciences*, vol. 41, no. 8, pp. 1413–1426, 2004.

[85] McGarr, A. and Gay, N., "State of stress in the earth's crust," *Annual Review of Earth and Planetary Sciences*, vol. 6, p. 405, 1978.

[86] Mellor, M. and Hawkes, I., "Measurement of tensile strength by diametral compression of discs and annuli," *Engineering Geology*, vol. 5, no. 3, pp. 173–225, 1971.

[87] Muralidhara, S., Prasad, B. R., Eskandari, H., and Karihaloo, B. L., "Fracture process zone size and true fracture energy of concrete using acoustic emission," *Construction and Building Materials*, vol. 24, no. 4, pp. 479–486, 2010.

[88] Murrell, S. A. F., "The effect of triaxial stress systems on the strength of rocks at atmospheric temperatures," *Geophysical Journal of the Royal Astronomical Society*, vol. 10, no. 3, pp. 231–281, 1965.

[89] Okubo, S. and Fukui, K., "Complete stress-strain curves for various rock types in uniaxial tension," in *International journal of rock mechanics and mining sciences & geomechanics abstracts*, vol. 33, pp. 549–556, Elsevier, 1996.

[90] Otsuka, K. and Date, H., "Fracture process zone in concrete tension specimen," *Engineering Fracture Mechanics*, vol. 65, no. 2, pp. 111–131, 2000.

[91] Pandey, P. and Singh, D., "Deformation of a rock in different tensile tests," *Engineering geology*, vol. 22, no. 3, pp. 281–292, 1986.

[92] Peitgen, H.-O., Jürgens, H., and Saupe, D., *Chaos and fractals: new frontiers of science*. Springer Science & Business Media, 2006.

[93] Pena, C., "An experimental study of the fragmentation process in rock cutting," Master's thesis, UNIVERSITY OF MINNESOTA, 2010.

[94] Perras, M. A. and Diederichs, M. S., "A review of the tensile strength of rock: concepts and testing," *Geotechnical and geological engineering*, vol. 32, no. 2, pp. 525–546, 2014.

[95] Pierce, M., Cundall, P., Potyondy, D., Ivars, D. M., and others, "A synthetic rock mass model for jointed rock," in *1st Canada-US Rock Mechanics Symposium*, American Rock Mechanics Association, 2007.

[96] Pollard, D. D. and Aydin, A., "Propagation and linkage of oceanic ridge segments," *Journal of Geophysical Research: Solid Earth*, vol. 89, no. B12, pp. 10017–10028, 1984.

[97] Pollock, A., "Acoustic emission-2: acoustic emission amplitudes," *Non-destructive testing*, vol. 6, no. 5, pp. 264–269, 1973.

[98] Potyondy, D. and Cundall, P., "A bonded-particle model for rock," *International journal of rock mechanics and mining sciences*, vol. 41, no. 8, pp. 1329–1364, 2004.

[99] Potyondy, D. and others, "A flat-jointed bonded-particle material for hard rock," in *46th US Rock Mechanics/Geomechanics Symposium*, American Rock Mechanics Association, 2012.

[100] Ramsey, J. M. and Chester, F. M., "Hybrid fracture and the transition from extension fracture to shear fracture," *Nature*, vol. 428, no. 6978, pp. 63–66, 2004.

[101] Read, R., "20 years of excavation response studies at aecl's underground research laboratory," *International Journal of Rock Mechanics and Mining Sciences*, vol. 41, no. 8, pp. 1251–1275, 2004.

[102] Richard, T., "Determination of rock strength from cutting tests," Master's thesis, University of Minnesota, 1998.

[103] Richard, T., Dagrain, F., Poyol, E., and Detournay, E., "Rock strength determination from scratch tests," *Engineering Geology*, 2012.

[104] Roberto, S.-R., Jørn, S., and Fabrice, D., "Continuous scratch testing on core allows effective calibration of log-derived mechanical properties for use in sanding prediction evaluation," in *SPE/ISRM Rock Mechanics Conference*, 2002.

[105] Rocco, C., Guinea, G., Planas, J., and Elices, M., "The effect of the boundary conditions on the cylinder splitting strength," *Fracture Mechanics of Concrete Structures, Wittmann FH (ed.). Aedificatio Publishers: Freiburg, Germany*, pp. 75–84, 1995.

[106] Rocco, C., Guinea, G. V., Planas, J., and Elices, M., "Mechanism of rupture in splitting test," *Materials Journal*, vol. 96, no. 1, pp. 52–60, 1999.

[107] Rocco, C., Guinea, G. V., Planas, J., and Elices, M., "Size effect and boundary conditions in the brazilian test: experimental verification," *Materials and Structures*, vol. 32, no. 3, pp. 210–217, 1999.

[108] Rojek, J., Onate, E., Labra, C., and Kargl, H., "Discrete element simulation of rock cutting," *International Journal of Rock Mechanics and Mining Sciences*, vol. 48, no. 6, pp. 996–1010, 2011.

[109] Sabnis, G. M. and Mirza, S. M., "Size effect in model concretes," *Journal of the Structural Division*, vol. 105, no. 6, pp. 1007–1020, 1979.

[110] Scholtès, L. and Donzé, F.-V., "A dem model for soft and hard rocks: Role of grain interlocking on strength," *Journal of the Mechanics and Physics of Solids*, 2012.

[111] Shigeishi, M., Colombo, S., Broughton, K., Rutledge, H., Batchelor, A., and Forde, M., "Acoustic emission to assess and monitor the integrity of bridges," *Construction and building materials*, vol. 15, no. 1, pp. 35–49, 2001.

[112] Standard, A., "D7012–14 (2014)," *Standard test method for compressive strength and elastic moduli of intact rock core specimens under varying states of stress and temperatures, ASTM International, West Conshohocken, Pa., doi*, vol. 10, 2014.

[113] Stirling, R. A., Simpson, D. J., and Davie, C. T., "The application of digital image correlation to brazilian testing of sandstone," *International Journal of Rock Mechanics and Mining Sciences*, vol. 60, pp. 1–11, 2013.

[114] Tang, C., "Numerical simulation of progressive rock failure and associated seismicity," *International Journal of Rock Mechanics and Mining Sciences*, vol. 34, no. 2, pp. 249–261, 1997.

[115] Thuro, K., Plinninger, R., Zäh, S., and Schütz, S., "Scale effects in rock strength properties. part 1: Unconfined compressive test and brazilian test," *EUROCK 2001: Rock Mechanics-A Challenge for Society*, pp. 169–174, 2001.

[116] Turcotte, D. L., *Fractals and chaos in geology and geophysics*. Cambridge university press, 1997.

[117] Ulm, F.-J. and James, S., "The scratch test for strength and fracture toughness determination of oil well cements cured at high temperature and pressure," *Cement and Concrete Research*, vol. 41, no. 9, pp. 942–946, 2011.

[118] Van Vliet, M. R. and Van Mier, J. G., "Experimental investigation of size effect in concrete and sandstone under uniaxial tension," *Engineering Fracture Mechanics*, vol. 65, no. 2, pp. 165–188, 2000.

[119] Vidya Sagar, R., "An experimental study on acoustic emission energy and fracture energy of concrete," 2009.

[120] Weibull, W., *A statistical theory of the strength of materials*. No. 151, Generalstabens litografiska anstalts förlag, 1939.

[121] Wijk, G., Rehbinder, G., and Lögdström, G., "The relation between the uniaxial tensile strength and the sample size for bohus granite," *Rock mechanics*, vol. 10, no. 4, pp. 201–219, 1978.

[122] Yamada, I., Masuda, K., and Mizutani, H., "Electromagnetic and acoustic emission associated with rock fracture," *Physics of the Earth and Planetary Interiors*, vol. 57, no. 1, pp. 157–168, 1989.

[123] Yanagidani, T., Sano, O., Terada, M., and Ito, I., "The observation of cracks propagating in diametrically-compressed rock discs," in *International Journal of Rock Mechanics and Mining Sciences & Geomechanics Abstracts*, vol. 15, pp. 225–235, Elsevier, 1978.

[124] Zhang, Q. and Zhao, J., "Determination of mechanical properties and full-field strain measurements of rock material under dynamic loads," *International Journal of Rock Mechanics and Mining Sciences*, vol. 60, pp. 423–439, 2013.

[125] Zhang, Q., Zhu, H., Zhang, L., and Ding, X., "Study of scale effect on intact rock strength using particle flow modeling," *International Journal of Rock Mechanics and Mining Sciences*, vol. 48, no. 8, pp. 1320–1328, 2011.

[126] Zhang, Z., Kou, S., Jiang, L., and Lindqvist, P.-A., "Effects of loading rate on rock fracture: fracture characteristics and energy partitioning," *International Journal of Rock Mechanics and Mining Sciences*, vol. 37, no. 5, pp. 745–762, 2000.

[127] Zhang, Z., Kou, S., Yu, J., Yu, Y., Jiang, L., and Lindqvist, P.-A., "Effects of loading rate on rock fracture," *International Journal of Rock Mechanics and Mining Sciences*, vol. 36, no. 5, pp. 597–611, 1999.

[128] Zhou, Y. and Lin, J.-S., "Modeling the ductile–brittle failure mode transition in rock cutting," *Engineering Fracture Mechanics*, vol. 127, pp. 135–147, 2014.

[129] Zhou, Z., Li, X., Zou, Y., Jiang, Y., and Li, G., "Dynamic brazilian tests of granite under coupled static and dynamic loads," *Rock mechanics and rock engineering*, vol. 47, no. 2, pp. 495–505, 2014.

[130] Zhou, Z., Ma, G., Li, X., and others, "Dynamic brazilian splitting and spalling tests for granite," in *11th ISRM Congress*, International Society for Rock Mechanics, 2007.

[131] Zietlow, W. K. and Labuz, J., "Measurement of the intrinsic process zone in rock using acoustic emission," *International Journal of Rock Mechanics and Mining Sciences*, vol. 35, no. 3, pp. 291–299, 1998.